TIME-DEPENDENT WAVE PACKET DYNAMICS OF THE H+HLi REACTION

A THESIS

SUBMITTED FOR THE DEGREE OF

DOCTOR OF PHILOSOPHY

BY

RAMANATHAN PADMANABAN

SCHOOL OF CHEMISTRY

UNIVERSITY OF HYDERABAD

HYDERABAD - 500 046

INDIA

December 2005

STATEMENT

I hereby declare that the matter embodied in this thesis is the result of investigations carried out by me in the School of Chemistry, University of Hyderabad, Hyderabad, under the supervision of Dr. Susanta Mahapatra.

In keeping with the general practice of reporting scientific observations, due acknowledgements have been made wherever the work described is based on the findings of other investigators.

Hyderabad-46 (Ramanathan Padmanaban)

December 2005

CERTIFICATE

Certified that the work contained in this thesis entitled "Time-dependent wave packet dynamics of H+HLi reaction"has been carried out by Mr. Ramanathan Padmanaban under my supervision and the same has not been submitted elsewhere for a degree.

Hyderabad-46 (Dr. Susanta Mahapatra)

December 2005 Thesis Supervisora

Dean

School of Chemistry

University of Hyderabad

Hyderabad 500 046

INDIA

ACKNOWLEDGEMENTS

I wish to express my deep sense of gratitude and indebtedness with profound respect to my supervisor Dr. Susanta Mahapatra for his constant encouragement throughout my research work. I have learnt a lot from his meticulous planning and implementation, dedication and hard work. I must add that I have benefited immensely, both academically and personally through my association with him.

I express my sincere gratitude to Prof. N. Sathyamurthy, IIT Kanpur, for his interest and valuable suggestions to carry out a part of the present work.

I thank sincerely to Prof. G. R. Desiraju, Prof. E. D. Jemmis and Prof. M. Periasamy, Deans, School of Chemistry, for providing all facilities to carry out my research work. I also thank all the faculty members of the school for their help and guidance on various occasions.

I express my heartily thanks to my lab mates T. S. Venkatesan, Subhas Ghosal, B. Jayachander Rao, R. Rajesh Kumar, V. Sivaranjana Reddy and Rakesh Sengupta for many fruitful discussions and their nice company in lab. I would like to express my special thanks to former research project student Gireesh M. K. for his wonderful company in the initial days of my research work. Their association will remain forever in my memory. I also thank the present project students Tanmoy Mandal and Susanta Ghanta.

I am very thankful to all the research scholars in School of Chemistry for their timing help and useful discussions in various regards of my research work.

I would like to thank Mrs. Gitashri Mahapatra, Anusha Mahapatra and Mrs. Jayachander Rao for providing me a homely atmosphere and for their delightful company on the various occasions.

I will take this opportunity to thank all of my friends - Vairaprakash, Venky, Sundaram, 'history'Senthil, 'thambi'Balaram, 'singam'Selva, 'iyer'Arumugam, 'gaja'Vijayan, Kanna, Arun, and Drs. 'idhayakoil'Mari, Philip, Anbazhagan - made my stay a pleasant one and given me a cheerful atmosphere in the campus.

My special thanks to Dr. K. Senthil Kumar (Naats-Geets), Dr. Perumal, Siva-Chair, Madhu, '7G'Prakash, Gnanam, 'sound' Xavier, Sankar and 'mams'Jagan for their "Royal" company during the stay in A-208, NRS hostel.

Thanks are also due to my seniors Drs. VSS, JK, Ashok, GVK-Siva and Balaji for their

support and I extend this to all the past and present tamil friends in the campus for their enjoyable company (particularly at the time of Tamil New Year celebrations).

I thank my M.Sc. friends Maha, 'prof'Arumugam, 'savukku'Senthil, 'kabali' Saravanan, 'parattai'Bangaru, 'kadi'Madhu, 'keity'Velusamy, Bagya, 'machi'Durai, 'ice' Thenmozhi, Mrs. Jayasri and all for their useful discussions and friendship. I also extend my thanks to my seniors Ayya, Senthil, Perusu, Venkat, Suresh, Aravindan sir, and all for their kind words and help during my M.Sc. course in University of Madras, Chennai.

I should thank my M.Sc. teachers, Professors. Balakrishnan, Meenakshi Marudhamuthu, Padmamalar, Santhanalakshmi, Vijayaragavan and Srinivasan for their motivation to do the research.

I should recall here, the kind of training I received from my college and schoolteachers that laid a strong foundation for whatever I am today. I am thankful to them forever.

I wish to thank all my B.Sc., and School friends, particularly RameshBanu, Nizam, Sundaram, Kumar, 'boy'Ahmed, Babu, Udhayan who shared my joys and feelings and also for their encouragement.

I would like to extend my thanks to the University authorities for providing necessary facilities, Centre for Modelling Simulation and Design (CMSD), University with Potential for Excellence (UPE) programme and high performance computational facility program (HPCF) of the University of Hyderabad.

Financial assistance from Department of Science and Technology (DST), University of Grants Commission (UGC) and Council of Scientific and Industrial Research (CSIR) are gratefully acknowledged. I also acknowledge the Volkswagen Foundation, Germany for the financial support.

Last, but not least, I take immense pleasure in thanking my parents (Narayanan Ramanathan and Chinnamani), brothers (Sivakumar, Sridhar, Sankar, Sabapathi) and sister (Sumathi) for their constant encouragement and support throughout my life. I also thank to my brother-in-laws, sister-in-laws and kutties (Gokul, Sedhu, 'cute' Praveena, Raji, Dhandapani and Priya) for their love and affection.

R. Padmanaban

List of Abbreviations

BF	-	Body-fixed
BO	-	Born-Oppenheimer
CC	-	Coriolis coupling
CP	-	Chebyshev polynomial
CRP	-	Cumulative reaction probability
CS	-	Centrifugal sudden
DMJ	-	Dunne, Murrell and Jemmer
DVR	-	Discrete variable representations
FBR	-	Finite basis representations
FC	-	Franck-Condon
FD	-	Finite difference
FFT	-	Fast Fourier transform
FGH	-	Fourier grid Hamiltonian
FT	-	Fourier transform
FWHM	-	Full-width at half-maximum
GWP	-	Gaussian wave packet
MP2	-	Second order Møller-Plesset perturbation theory
NIP	-	Negative imaginary potential
PES	-	Potential energy surface
QCT	-	Quasiclassical trajectory
RPO	-	Resonant periodic orbit
SCF	-	Self-consistent field
SF	-	Space-fixed
SI	-	Symplectic integrator
SIL	-	Short-iterative Lanczos
SO	-	Split operator
SOD	-	Second-order difference
SQM	-	Spectral quantization method
TDSE	-	Time-dependent Schrödinger equation
TISE	-	Time-independent Schrödinger equation
TDWP	-	Time-dependent wave packet
TS	-	Transition state
WP	-	Wave packet
ZPE	-	Zero-point energy

Contents

Chapter 1

Introduction

The study of molecular reaction dynamics is very important in understanding the fundamental physical and chemical processes occurring on earth as well as in the upper atmosphere. The recent developments in this field has greatly enhanced our understanding of the nature of unimolecular and bimolecular chemical reactions and the underlying intramolecular motions and intermolecular collisions including the molecule-surface encounters. An understanding of the dynamical behavior of a system at a molecular (*microscopic*) level is the key to the interpretation of the "macroscopic" kinetics of the bulk system [1–5]. The particular focus here is to study these fundamental processes of small molecular systems, for instance, atom-molecule and ion-molecule reactions in the gas phase by a time-dependent wave packet (TDWP) dynamical approach.

The experimental and theoretical research in molecular reaction dynamics has undergone a revolution during the past few decades [6]. Revolution in the experimental research is largely due to the major technological developments in molecular beams and pump-probe femtosecond spectroscopy [7]. Rotational cooling of polar diatomic molecules by supersonic jet expansion [8], followed by the application of electric or magnetic field perpendicular to the beam flow, has created molecules in hybrid states [9,10]. Crossed molecular beam experiments [11], laser-induced-fluorescence studies [12], coherent anti-stokes Raman spectroscopy [13], Doppler methods and Rydberg atom time-

of-flight spectroscopy [14] have increased the understanding of the mechanism of the gas phase reactions. Laser multiphoton ionization-time-of-flight mass spectrum of a beam containing strongly bound clusters, for example, C_n and C_nLa cluster molecules, (n=60, 70) have been studied by Heath *et al.* [15]. Using the pump-probe technique, it has become possible to "clock" the transition state (TS) of a chemical reaction ($\sim$ 10-100 fs) in real time and subsequently follow the nuclear motion [16–19]. The term transition state, refers to all configurations the system acquires while passing from the reactant to the product valley. With this experimental setup, one can also study the product state distributions, collision cross sections, rate coefficients and the reaction mechanism in detail.

Recent developments in the theoretical study of reaction dynamics has made it possible to understand the properties of a chemical reaction in relation to the topography of the *ab initio* potential energy surface (PES) of the collision system. The theoretical results can be obtained very close to the experimental findings with the help of high performance computing facility and computer softwares. Theoretical studies of the elementary chemical reactions can be carried out either by a classical or quantum mechanical methods. The classical or quasiclassical trajectory (QCT) method [20–22] of studying the reactions involves the integration of classical Hamilton's equations, which gives the mechanistic insights of the encounter viewed in terms of classical trajectories and yields the state-to-state dynamical informations. During the collision event, the understanding of the tunneling behavior and resonances at the reaction threshold are very important, but these are quantum mechanical in nature. So a subsequent method called semiclassical method [23, 24] is developed to incorporate quantum features in the classical framework. In recent years, full quantum mechanical treatments of bimolecular chemical reactions have become possible. Here the treatments are based either on a time-independent [25, 26] or a time-dependent [27–32] approach. The latter is more fashionable, because it allows to view the fate of reagents during the course of the reaction in terms of the wave packet (WP) snapshots. With these developments,

the underlying accuracy of the PES [33–36] is better tested in conjunction with the molecular beam results for a chemical reaction. A qualitative understanding of main topological features of the PES provides the route from the reactants "valley" to that of the products, termed the *minimum energy path* or the "reaction coordinate" [36]. Once the PES is obtained, the next step is the investigation of the internuclear motion on the PES by solving the equations of motion (either classical or quantum mechanical). It is possible to calculate the dynamical quantities such as reaction probabilities, reaction cross sections, temperature dependent reaction rate constants, and transition states in chemical reactions [37–44]. It has useful applications in describing the molecular encounter in the interstellar clouds and combustion processes. Considerable progress has been made in the past years to develop new quantum mechanical methods for performing calculations of full three-dimensional atom-diatom reactive encounters [2, 29, 30]. The results of these calculations can be directly compared with those obtained from the molecular beam experiments.

The most promising time-dependent method to do the state-to-state dynamics is based on the reactant product decoupling (RPD) approach, introduced by Zhang and coworkers in 1996 [45]. In this approach, the WP is absorbed at the starting point of the product channel and the same is re-emitted into the product channel, where the propagation is carried out using product Jacobi coordinates. This yields the state-to-state S-matrix elements. Subsequently, Kouri *et al.* [46] have proposed an extended RPD method that uses another absorbing potential to separate the reagent channel in an analogous way to the product channel. Althorpe *et al.* [44,47] have implemented this method efficiently, by decoupling the reagent channel using artificial reflecting potential. This method yields the fully converged differential and integral reaction cross sections in state-to-state reactive scattering for a bimolecular chemical reaction [47], using either a time-independent or time-dependent WP approach. In practice, the exact quantum dynamical calculations in full dimensions are computationally very expensive and cumbersome when the Coriolis coupling (CC) is included. Meijer and Goldfield [48–51] have

performed the extensive WP calculations to calculate the initial state-selected reaction cross sections in a parallel computing architecture for H+O_2 reaction and suggested that the CC plays a vital role in gas phase reactive scattering, particularly for higher values of the total angular momentum.

Complete descriptions of full-dimensional time-dependent scattering theory are well documented in the literature [29,30,37,52–56,146]. In general, a full-dimensional quantum dynamical study can be performed for a reactive scattering system by solving the nuclear Schrödinger equation on a given Born-Oppenheimer (BO) PES. Such a task is undertaken in the present thesis. In what follows, full-dimensional treatment of the dynamics of H+HLi reacting system is carried out systematically, starting from reduced dimensionality models. The integral reaction cross section and thermal rate constant are calculated and the details of the reaction mechanism is discussed.

1.1 Lithium-Hydrogen Reactions

The cooling of the primordial matter and its collapse are controlled by the presence of trace amount of gas molecules in it. Way back in 1984, the preliminary study of Lepp and Shull [57] have indicated that a large fraction of primordial lithium exists as LiH. Subsequently, the effects of presence of these species in the "Early Universe" have been discussed by various researchers [58]. The formation and depletion of LiH and its ionic counterparts were believed to play rather important role in the Steller evolution and galactic lithium production [59]. Furthermore, the presence of such molecular species may cause significant anisotropy of the cosmic background radiation by undergoing Thompson scattering with the emitted photon [60]. Recently, Dalgarno and coworkers [61] have carried out a detailed study and pointed out the possible pathways for the formation and depletion of LiH via collisions with H^+ and H in the interstellar cloud.

In gas phase, the collision of H atom with HLi diatom is one of the most important

reactions in the chemistry of the upper atmosphere. This collision may proceed via the following two reactive and one nonreactive paths:

$$\mathrm{H + HLi} \longrightarrow \mathrm{H_2 + Li} \qquad \text{(R1)}$$

$$\mathrm{H + HLi} \longrightarrow \mathrm{LiH + H} \qquad \text{(R2)}$$

$$\mathrm{H + HLi} \longrightarrow \mathrm{HLi + H} \qquad \text{(NR)}$$

While the path (R1) is highly exothermic and considered to be one of the events contributing to LiH depletion, the hydrogen exchange path (R2) is mostly of thermoneutral type leading to the retention of LiH. In addition, there is another path leading to the retention of LiH via the non-reactive collisions with H (NR). The possibility of the reverse endothermic process of the reaction (R1), contributing to the LiH formation has also been pointed out [61] and studied in the literature [62–65]. The rates of the reaction (R1) in the temperature range of interest have been estimated qualitatively by Dalgarno and coworkers [61]. To date, however, very little is known (both theoretically and experimentally) about the H+HLi collision dynamics.

A few theoretical studies on the reaction of

$$\mathrm{Li}(2^2P) + \mathrm{H_2} \longrightarrow \mathrm{LiH}(X^1\Sigma^+) + \mathrm{H} \qquad \text{(R3)}$$

elucidating various aspects of the collision on the ground and low-lying excited electronic states have been reported elsewhere [65–68]. Chen *et al.* [65] have provided insight into the dynamical behavior for the $\mathrm{Li}(2^2P_J)$ + $\mathrm{H_2}$ reaction. They have reported the rotational populations of LiH ($v = 0$) by using the pump-probe technique. The *ab initio* PES data for this reaction [64] indicate that the HLi formation reaction is dominated by the insertion type of mechanism near C_{2v} geometry. The LiH formation reaction (R3) is highly endothermic ($\sim$ 1680 $\mathrm{cm^{-1}}$), so that, it is only feasible when the Li atom is in its excited electronic state. The activation energy has also been esti-

mated for this reaction by temperature dependence measurement [65]. The total and state-to-state cross sections for this reaction are calculated by McCaffery *et al.* [66], using the Monte-Carlo simulation of trajectories. McCaffery [69] have also reported the rotational distributions of ($X^1\Sigma^+$) LiH($v = 0$) from the reaction (R3) using the reactive angular momentum (AM) model. Their results are in very good agreement with the experimental findings of Chen *et al.* [65].

Recently, Bililign *et al.* [70] have performed laser excitation of LiH_2 collision pairs in the gas cell environment for a study of the (R3) reaction. Following to this work, Grimpe *et al.* [71] have reported the differential cross sections for optical collision processes of Li atom with H_2 or D_2 molecules in a differential scattering experiment and by quantum scattering calculations using rotational sudden approach, probing ground and lower excited PESs of the LiH_2 or LiD_2 collisional molecules. Their findings reveal the oscillatory structures in the cross section results, and a mutual agreement between the theory and experiment has been found for optical collision cross sections [71].

Martínez has reported the first *ab initio* multi-electronic state molecular dynamics (AIMSMD) calculation using the ultrafast spectroscopy [72] and collision-induced ionization [73] of NaI as example, and extended the AIMSMD simulation around a conical intersection, and investigated the effects of conical intersection in realistic molecules. The term "conical intersection" is a generic feature in polyatomic molecules where the two PESs intersect in f-2 dimension (f is the number of internal degrees of freedom). Such intersections, lead to a breakdown of the BO approximation and initiate new mechanisms ensuing different nonadiabatic couplings [74]. The author has illustrated this AIMSMD simulation around a conical intersection with the collision-induced electronic quenching of Li(^2p) by an H_2 molecule [75] [see Fig. 1.1].

Murrell *et al.* [76] have carried out the accurate potential energy calculations to search for bound levels of the van der Waals molecules like H_2 and LiH in its lowest

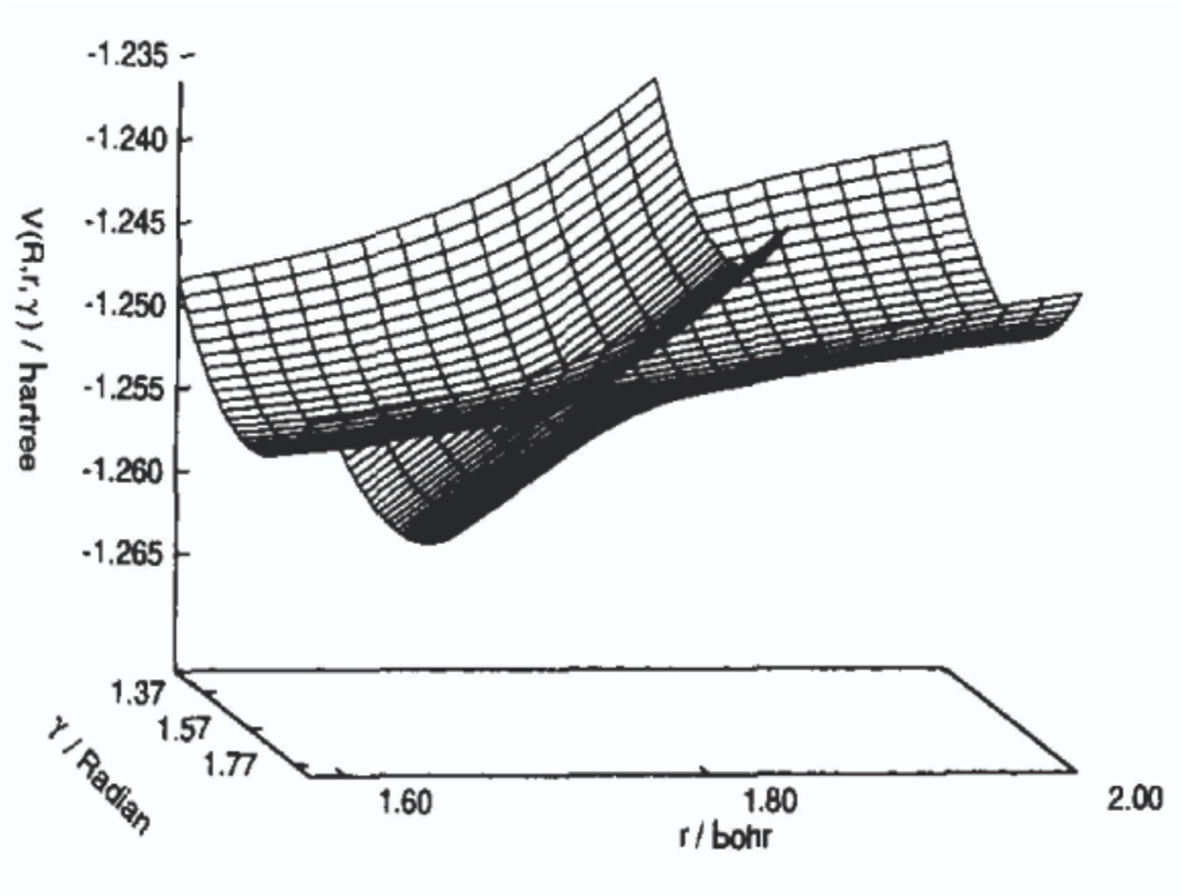

Figure 1.1: PESs in the adiabatic representation in the vicinity of the conical intersection for fixed Li-H_2 distance, R, (2.8 bohr). Notice the sharply sloped nature of the intersection in the H-H distance, r, which occurs because the intersection is located in the repulsive well. [Reproduced from Fig. 1 of Ref. [73]]

triplet states ($a^3\Sigma^+$) and then reported the high quality potentials for H_2 and Restricted Coupled-Cluster Singles-Doubles (Triples) (RCCSD(T)) potentials over a long range distances for LiH. They found that the triplet LiH have a bound levels for all commonly occurring isotopomers and the triplet H_2 is unbound for all isotopes.

A few related Lithium-Hydrogen reactions e.g.,

$$\mathrm{LiH} + \mathrm{He} \longrightarrow \mathrm{LiHe} + \mathrm{H} \qquad \text{(R4)}$$

$$\mathrm{LiH}^+ + \mathrm{H} \longrightarrow \mathrm{H}_2 + \mathrm{Li}^+ \qquad \text{(R5)}$$

$$\mathrm{LiH} + \mathrm{H}^+ \longrightarrow \mathrm{H}_2^+ + \mathrm{Li} \qquad \text{(R6)}$$

are studied by Bodo and coworkers [67, 68, 77, 78], in order to understand the microscopic energy redistribution processes in the lithium chemistry. These authors have calculated the excitation/relaxation rates of LiH with different partners, like He [67], H and H^+ [68], which are the most abundant atomic species in the primordial medium. They have analyzed the reaction dynamics of some of the relevant neutral and ionic partners by carrying out the detailed calculations for their PESs [77] and the reaction pathways for the LiH_2/LiH_2^+ systems in order to derive informations on the reactive processes between H_2, H_2^+, LiH, LiH^+ and the atomic counterparts. Their analysis revealed that the H-H-Li configuration leads to an extremely exoergic pathway (exothermicity $\sim$ 4.24 eV) due to the large difference in the binding energies between the reactants and the products [77]. Their further investigation on the collinear dynamics of $LiH^+ + H$ reaction on its low-lying electronic PESs, using a TDWP approach, yielded the collision-induced dissociative probabilities for the elastic and inelastic state-to-state transitions. The probabilities thus obtained, reveal oscillating pattern as a function of energy [78]. Following to this work, very recently Bulut *et al.* [79] have reported the state-to-state and state-selected inelastic probabilities for the $Li+H_2^+$ collision using a TDWP method and the J-shifting approximations. Their findings reveal that the integral cross section decreases monotonically with collision energy as expected for a barrierless reaction [79].

More recently, the integral reaction cross sections and thermal rate constants are reported for the inelastic He+LiH collisions using a three-dimensional PES constructed within a rigid rotor approximation, by Taylor and Hinde [80]. These authors report that both the quantum close-coupling and the coupled states calculations yield the smaller cross section than the experimental values. The vibrational excitation as well as vibrational relaxation rate constant for the He-LiH collisions also plays significant roles in the cooling of the primordial matter. The collision of Li atom with HF molecule has also been studied and the reaction cross section [81], transition state spectroscopy [82], and the scattering at ultracold temperatures [83] are examined.

In the following, we focus on the collision dynamics of H with HLi molecule on its electronic ground state.

1.2 Electronic Structure of the LiH_2 system

In 1984, Hobza and Schleyer [85] have carried out the geometry optimizations of the (^{2}S) Li - H_2 as well as (^{2}P) Li* - H_2 systems at the second-order Møller-Plesset perturbation (MP2) level of theory employing the 6-311G(2d,2p) basis set. They have also examined the possible interactions between Li^+ and H_2, LiH and H. Their findings reveal that the binding energy of H-H$\cdots$Li is very low $\sim$ 13 kcal/mol (0.056 eV) at a distance of 6.03 Å in linear geometry, however, no binding is found for the C_{2v} geometry. Whereas in case of Li^+ and H_2 interaction, the linear approach has been shown to be less favorable than the C_{2v} approach. Their results are found to be in good agreement with the experimental data derived from high-temperature calorimetry and ionization potential measurements [86].

Earlier theoretical studies on the LiH_2 system have focused on various aspects of its electronic structure. Boldyrev and Simon [87] have reported the vertical and adia-

batic ionization potentials of LiH_2^- at the MP2 level of theory employing a triple-zeta plus polarization and 6-311++G* diffuse basis set. Their study revealed a stable $D_{\infty h}$ structure ($1\sigma_g{}^2 1\sigma_u{}^2$) of LiH_2^- and the detachment of the extra electron from the highest occupied molecular orbital ($1\sigma_u$) leads to the formation of LiH_2 in its $^2\Sigma_u^+$ electronic state with a vertical ionization potential of ~ 3.06 eV [87]. The latter is in close agreement with that reported by Senekowitsch and Rosmus [88] calculated at the coupled electron pair approximation (CEPA) level and by Boldeyrev and Niessen [89] calculated at the Green's function level. LiH_2 in its $^2\Sigma_u^+$ state is reported to possess an imaginary bending frequency of $277i\,\mathrm{cm}^{-1}$ indicating the absence of a local minimum [87]. On the other hand, a local minimum along the bending mode for the bent (C_{2v}) geometry of LiH_2 correlating to a $^2B_2$ species has been discovered [87]. This structure is reported to be more stable with respect to H + HLi dissociation but unstable with respect to Li + H_2 dissociation. At the optimal geometry of this $^2B_2$ state, a low-lying $^2A_1$ state correlating with the Li(^2S) + $H_2(^1\Sigma_g^+)$ asymptote is also reported to exist [87]. This $^2A_1$ state can undergo nonadiabatic crossings with the $^2B_2$ state and therefore can form a conical intersection [63, 64]. Such an intersection with a minimum lying only ~ 2.40 kcal mole^{-1} above the minimum of the $^2B_2$ state has been found, which causes an indirect dissociation of the $^2B_2$ state into Li + H_2. This reveals the importance of the non-collinear configuration of LiH_2 in the H+HLi collision dynamics. The detachment of an electron from the $1\sigma_g$ molecular orbital of LiH_2^- leads to the formation of LiH_2 in the $^2\Sigma_g^+$ state. The latter supports a local minimum at the $D_{\infty h}$ configuration. The corresponding vertical and adiabatic ionization potentials were found to have nearly the same value of ~ 3.35 eV [87].

1.3 Potential Energy Surface (PES) and Dynamics of H+HLi Reaction

The reactive PES of H+HLi reaction on its ground electronic state for the collinear arrangements of the three nuclei (HHLi or HLiH) has been reported by Clarke *et al.* [90]. They have obtained this PES through extensive valence bond calculations using non-orthogonal, spin-coupled wavefunctions with optimized orbitals. These authors have also calculated [90] the initial state-selected reaction probabilities for the forward and the reverse processes of (R1) for the collinear arrangements of the three nuclei by a QCT as well as a TDWP approach. Their findings revealed a strong exothermicity of (R1) with an energy gain of ~ 2.024 eV including the zero-point energy (ZPE) correction, and a small early barrier of ~ 0.036 eV [90]. The dynamical results mostly indicated a direct nature of the reaction proceeding without any transition state. A sharp resonance feature, very sensitive to the initial most probable translational energy, has been observed in the threshold region of the reaction probability curve. Furthermore, it is reported that low translational energy of the reagent fragments favors the depletion process and vibrational excitation of LiH does not have any noticeable effects on it [90]. These findings therefore indicate that "cold" primordial LiH molecules can be depleted efficiently by reactive encounters with H-atom even at a very low value of translational energy. Their study also indicated that much of the reagent translational energy emerge as the product vibrational energy in the exothermic LiH depletion path [90].

A global three-dimensional analytical PES for the H + HLi system is reported by Dunne, Murrell, and Jemmer (hereafter will be referred to as DMJ PES) [91] (see Fig. 1.2). These authors have derived this PES by fitting analytically a many-body expansion function to energies obtained by performing high quality *ab initio* configuration interaction calculations using augmented correlation consistent valence double zeta basis set. The resulting PES did not reveal the existence of any barrier to the reaction [91]. Apart from this minor difference, the collinear surface of Clarke *et al.* [90]

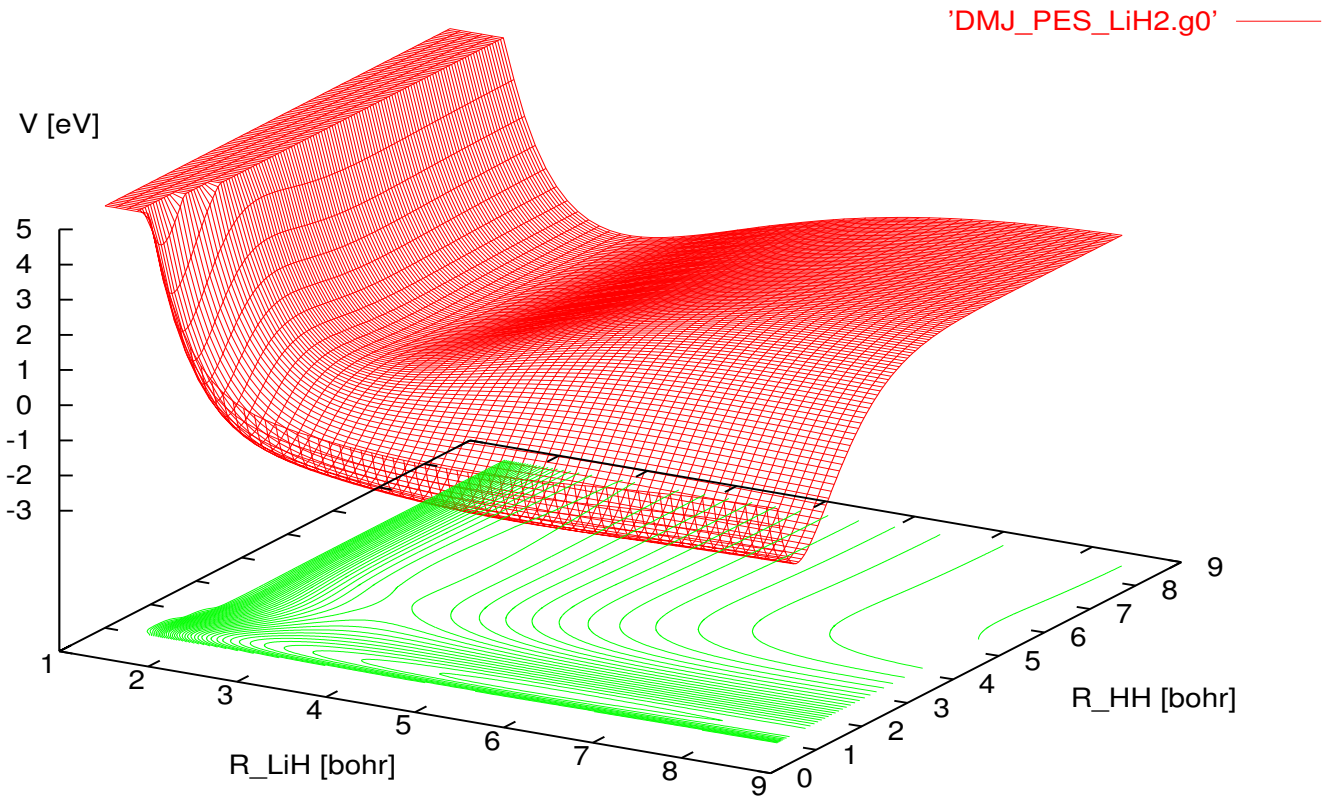

Figure 1.2: The three-dimensional view of the DMJ PES for the collinear approach of H to HLi in terms of HH and HLi internal coordinates. Minimum energy of the potential energy contour occur at -2.28 eV and the contour levels are 0.2 eV energy spaced for this collinear ($\gamma = 0^\circ \rightarrow$ HHLi) approach.

is well reproduced by the global analytical DMJ PES [91]. The latter authors have also studied the temperature dependence of the rate of the depletion reaction (R1) and provided a satisfactory analytical fit with respect to this rate [91].

Recently, Kim *et al.* [92] have performed the complete-active space self-consistent-field (SCF) calculations to calculate the potential energy data and numerically represented the PES in three-dimensions using the interpolant moving least square /Shepard interpolation scheme. These authors have performed QCT calculations on the resulting interpolated PES. Their findings indicated a direct nature of the reaction (R1) and the internal energy of the reagent HLi does influence the reaction dynamics [92]. The DMJ PES [91] as well as the one reported by Kim *et al.* [92] did not reveal the existence of the small early barrier as reported by Clarke *et al.* [90]. Using the DMJ PES, Defazio *et al.* [93] recently carried out the quantum dynamical calculations of H+HLi collisions and reported the state-to-state reaction cross section (vibrationally resolved), thermal product distributions, and rate constants for both the channels (R1) and (R2) using the real WP method [94] and the J-shifting (JS) approximation [95]. Their findings reveal that the LiH depletion (R1) rate is larger than the H-exchange (R2) rate (upto $\sim$ 40 K) and then the latter predominates at higher temperatures. The rate constant results for both the processes are reported to deviate from the Arrhenius type of behavior.

1.4 Overview of the Thesis

In the present thesis, we investigate the H+HLi collision dynamics (via the reactive paths: (R1) and (R2)) theoretically with the aid of a TDWP method and by employing the DMJ PES [91]. This *ab initio* three-dimensional PES [91] is used in the entire theoretical studies described in this thesis. The rest of the thesis is organized in the following way.

In Chapter 2, we present a detailed theoretical framework of a TDWP method to

study the nuclear dynamics in full-dimensions. The numerical grid method, to solve the time-dependent Schrödinger equation (TDSE) for an explicitly time-independent Hamiltonian of a triatomic system, is briefly reviewed. The relation between body-fixed (BF) and space-fixed (SF) Jacobi coordinates utilized in the numerical solution of the TDSE for the scattering problems is illustrated through the rotation by three Euler angles (ϕ, θ, χ). Numerically the solution is achieved in three steps: (i) preparation of the initial WP corresponding to the reactants, (ii) propagation of the WP on the potential grid, and (iii) final analysis of the WP to calculate the reaction attributes viz., reaction probability, integral reaction cross section and thermal rate constant. Each of these steps are discussed at length in this chapter. The quantum flux method to calculate the initial state-selected and energy resolved reaction probability and integral reaction cross section is discussed. An averaging of the latter over the collision energy at a given temperature yields the thermal rate constants. In addition to the full dimensional WP calculations (i.e., including the CC), various approximate schemes viz., JS and centrifugal sudden (CS) approximations to perform the scattering calculations in reduced dimensions are also discussed.

In Chapter 3, we report the initial state-selected and energy resolved channel specific reaction probabilities of the H+HLi reaction for $J = 0$ [101] by using a TDWP method which is discussed in Chapter 2. The reaction probabilities are reported for both the collinear (investigated only for the R1 channel) and the three-dimensional arrangements (investigated both for the R1 and R2 channels) of the reacting system. Our findings reveal that the scattering occurs via resonance formation at low energies and the dynamics follow a more direct path at high energies, for both the arrangements. Examination of channel specific reaction probabilities reveal that R2 channel is more favored over R1 channel at any given energy. The onset of both the channels occurs at the zero-point vibrational energy of LiH, indicating the barrierless behavior, consistent with the topography of the DMJ PES [101]. The effect of the rotationally and vibrationally excited reactant LiH molecule on the dynamics is discussed. The importance

of non-collinear configuration of the reacting system on the LiH depletion dynamics is also examined.

In Chapter 4, we investigate the dynamics of H+HLi scattering for $J \neq 0$. We present here the effect of CC on the initial state-selected and channel specific energy-resolved integral reaction cross sections and thermal rate constants and compared with those obtained from the JS and CS models. The reaction cross section is obtained by summing up all the partial wave contributions upto J_{max} to the reaction probabilities, and further averaging the results yields the thermal rate constant. Within the reduced dimensionality (CS and JS) models, $J_{max} = 74$ is considered [102], whereas in the CC model $J_{max} = 30$ and $K_{max} = 4$ are considered [103], to converge the reaction cross section results upto the collision energy 1.0 eV and 0.75 eV, respective to the models. The resonance features in the cross section results average out with various partial wave contributions, when compared to the same observed in the individual reaction probability curve. The overall variation of reaction cross sections obtained from the various (JS, CS and CC) models correspond well to the behavior of a barrierless reaction. Within the CS model [102], except near the onset of the reaction, the vibrational and rotational excitation of the reagent HLi, in general, does not dramatically influence the reactivity of either channel. The thermal rate constant (with the temperature range 150-4000 K) decreases with vibrational excitation of the reagent HLi, indicating that the cold HLi molecules are efficiently depleted in the reactive encounter with H at relatively low temperatures [102].

The overall pattern of variation of the cross section results is similar in both the CS and CC models which indicates no dramatic influence of the CC on the reaction mechanism [103]. The weak resonance features seen in the CS results near the onset of both the channels are absent in the CC results. The variation of initial state-selected rate constants with temperature (100-1200 K range) reveal a non-Arrhenius type of behavior within the temperature range [103]. The rate constants for the R1 channel

are generally lower than that of R2 channel at a given temperature. The CC increases the rate constant of both the channels when compared to the CS results at low temperatures and the reverse holds at high temperatures for initial ($v = 0, j = 0$) state of the reagent HLi [103].

In Chapter 5, we examine the resonances in H+HLi scattering for both the total angular momentum $J = 0$ and $J \neq 0$ [104, 105]. The theoretical method to calculate resonances with the aid of a TDWP approach is discussed. The resonances are identified and characterized in terms of their energy eigenvalues, eigenfunctions and lifetime. The findings of this chapter are related to those in Chapters 3 and 4, where the signature of resonances is observed in terms of oscillations in the reaction probability curves. They are identified here from a set of pseudospectrum calculated for different initial locations of a carefully chosen stationary GWP in the interaction region of the DMJ PES [91]. The peaks in the spectrum correspond to the quasibound states and the peak maxima describes the energy eigenvalue of the resonances of H+HLi system. Each of the peaks are identified and assigned by computing their eigenfunctions through spectral quantization algorithm. They are identified in terms of three quantum numbers n_R, n_r and n_γ representing the number of nodes along these three Jacobi coordinates, respectively. Both the line-width as well as decay lifetime of these resonances are reported [104]. Our investigation of the resonances by using the CS and the CC models (i.e., including the three-body rotation), reveal that the resonances tend to become broader and this effect becomes more prominent in the CC model [105]. The resonances tend to disappear at higher values of J. This supports the absence of resonances in the integral reaction cross section near the onset in the CC model.

Summary of the findings is presented in each chapter and finally, the outlook of the thesis is given in Chapter 6.

Chapter 2

Time-dependent Wave Packet Approach To Reactive Scattering Dynamics

2.1 Introduction

The time-dependent WP approach provides a more realistic way to treat the dynamics of chemical reactions in a theoretical study. With the availability of improved algorithms and fast computing machines, this is currently the method of choice. This approach is now well established to investigate the bimolecular reactive collisions and has been very successfully applied to numerous atom-diatom, diatom-diatom and atom-polyatomic gas phase chemical reactions in recent years [for example, see Refs. [37, 40–42, 106–109]]. With the aid of this approach, one can carry out nearly exact quantum mechanical calculations for chemical reactions and can investigate the detailed mechanism of the process by looking at the WP snapshots on the potential grid during the course of the reaction.

In a full dimensional investigation of A+BC scattering dynamics, the physical wave-

function can be expanded in terms of body-fixed translational, vibrational, rotational basis, and the three Euler angles, (θ, ϕ, χ), describing the overall orientation of the body-fixed axes with respect to the space-fixed axes. The first application of a TDWP technique to three-dimensional quantum reactive scattering in the gas phase was demonstrated by Neuhauser, Baer, Kouri, and coworkers [110, 111]. In their study, the whole configuration space is divided into three regions: (1) the reagent arrangement, (2) the interaction region and (3) the product arrangement. The initial WP was prepared in the region 1 and then propagated through region 2 and analyzed in region 3. With the aid of this scheme, one can calculate the total reaction probability by analyzing the reactive flux of the WP as it enters the product channel. The latter is carried out beyond the strong interaction region. Once the analysis is performed, the time-evolved WP is absorbed by activating a suitable absorber to prevent the WP reflections or wrap around from the grid boundaries [112–116].

In quantum WP propagation, the BF Jacobi coordinates corresponding to the reactant arrangement channel are commonly used for calculating the initial-state selected observables. This is convenient as the kinetic energy operator has a very simple structure in this coordinate system. The calculations of state-to-state observables are far more cumbersome. In this case, one needs to transform the WP into the product coordinates to perform the analysis [37, 106, 117]. The method is also convenient for ascertaining the total reaction probabilities and has been successful in carrying out the accurate full six-dimensional calculations of the total reaction probabilities for polyatomic reactions [106–108, 118, 119]. Billing and Marković have formulated the full atom-diatom reactive scattering problem in terms of coupled three-dimensional WPs in hyperspherical coordinates [120]. Zhang *et al.* [106] have reported the initial state-selected integral cross sections for the atom-triatom, H+H_2O and H+D_2O reactions, using a TDWP method within the centrifugal sudden approximation. They tested the accuracy of this approximation by carrying out the accurate calculations including the Coriolis coupling (coupled channel method) and compared these results with the ex-

perimental findings. Rigorous quantum mechanical treatment of four-body problems (AB+CD) requires six degrees of freedom. The dynamics of H_2+OH reaction and its isotopic variants are investigated by Neuhauser [118] and Zhang & Zhang [121,122] and the state-selected reaction cross sections, are reported.

The computational cost of the time-dependent WP method scales much lower than that of the time-independent method, which scales as N^3 with the number of basis functions, N. For example, the time-dependent method is computationally more viable for three-atom reactions that require large number of basis functions owing to the presence of deep wells in the reaction path. Such systems usually require a full inclusion of the Coriolis coupling between different projections of the total angular momentum quantum number, J, and this may be treated very efficiently using parallel algorithms [48, 123, 124]. The discrete variable representation (DVR) method, for evaluating multidimensional eigenvalues, has contributed to the progress indirectly and discussed elsewhere [117, 125–130]. A new methodology called the S-matrix Kohn variational method which directly evaluates the thermal rate constants has also been devised [131–134]. Using the TDWP approaches, quite a few triatomic reactions, for example, H^++H_2 [135], H^-+H_2 [136], He+H_2^+ [137], C+H_2 [138], N^++H_2 [139], O+H_2 [51, 140], H+O_2 [49, 50], N+O_2 [141], Cl+H_2 [142–144], and Li+HF [81, 83, 145], LiH+He [67], H+LiH^+ [68], have been studied.

In a TDWP approach, the nuclear motion on the electronic PES is monitored by solving the time-dependent Schrödinger equation.

$$i\hbar\frac{\partial\Psi}{\partial t} = \hat{H}\Psi \tag{2.1}$$

where, $\hat{H}$ $(= \hat{T} + \hat{V})$ defines the Hamiltonian operator of the collision system. For an

explicitly time-independent Hamiltonian, the solution of the TDSE reads

$$|\Psi(t)\rangle = \exp\left[\frac{-i\hat{H}t}{\hbar}\right]|\Psi(t=0)\rangle, \tag{2.2}$$

where, $|\Psi(t=0)\rangle$ and $|\Psi(t)\rangle$ are the wavefunction of the reacting system at time 0 and t, respectively.

Usually, the *grid method* is used to solve the TDSE in the discrete Hilbert space [112, 146]. The discrete grid is usually constructed in the coordinate space, with each grid point being characterized by a finite value of interaction potential. Once this grid is set up, the overall solution is accomplished in next three steps: (i) preparation of initial WP ($\Psi(t=0)$) on the grid, (ii) its evolution in space and time and (iii) the final state analysis to calculate the dynamical observables.

2.2 Spatial Grid

Let us consider that the coordinate space, (x), is discretized into a set of N discrete points with a spacing between two successive points, Δx, then the eigenvalue of the position operator $\hat{x}$ at each point on the grid is given by [146]

$$x_i = (i-1)\Delta x, i = 1, ..., N \tag{2.3}$$

On this discrete grid, the eigenvectors $|x_i\rangle$, are given by the orthogonality and the completeness relations,

$$\sum_{i,j}\Delta x\langle x_i|x_j\rangle = \delta_{ij} \tag{2.4}$$

and

$$\hat{I}_x = \sum_{i=1}^{N}|x_i\rangle\Delta x\langle x_i|, \tag{2.5}$$

where, $\hat{I}_x$ is the identity operator. The wavefunction for an arbitrary physical state at the grid points is given by

$$\phi(x_i) = \langle x_i|\phi\rangle \tag{2.6}$$

The normalization integral of the wavefunction becomes $\int_{-\infty}^{+\infty} \phi^\star(x)\phi(x)dx = 1$. The maximum length of the grid ($L = N\Delta x$) along the spatial coordinate x, determines (Δk) the spacing between two successive points in the momentum space:

$$\Delta k = \frac{2\pi}{N\Delta x}. \tag{2.7}$$

In the momentum space (k), the grid is centered at zero and all other points are distributed symmetrically on either side of it. If the maximum momentum $p_{max}(= \hbar k_{max})$ represented in the k space then the momentum ranges from $-p_{max}$ to $+p_{max}$ and the total length (volume) of the phase space becomes, $Vol = 2L|p_{max}| = Nh$. Now the sampling spacing Δx read as:

$$\Delta x = \frac{\pi}{|k_{max}|}. \tag{2.8}$$

The maximum energy on this discretized grid is given by: [147]

$$\begin{aligned} E_{max} &= T_{max} + V_{max} \\ &= \frac{p_{max}^2}{2m} + V_{max} \\ &= \frac{\hbar^2|k_{max}^2|}{2m} + V_{max} \\ &= \frac{\pi^2\hbar^2}{2m(\Delta x)^2} + V_{max}, \end{aligned} \tag{2.9}$$

where, m is the mass of the particle and V_{max} is the maximum potential energy. The minimum energy, E_{min}, is equal to the minimum value of potential energy, V_{min}, on the grid.

2.3 Coordinate System

In reactive scattering, the different arrangements of the collisional system are generally described by the Jacobi coordinates corresponding to a particular arrangement channel (either reactant or product). Let us consider the simple Jacobi coordinates to represent the A+BC scattering system in the space-fixed [148] or the body-fixed [149] frame. For a triatomic molecule, there are totally three sets of Jacobi coordinates (by considering BC, AB, and AC as diatoms). It is often convenient to use the mass-scaled Jacobi coordinates, (R, r, γ), which is defined, e.g. for the A+BC arrangements by

$$R' = R\lambda \text{ and } r' = r/\lambda,$$

where, $\lambda = \sqrt{\frac{\mu}{\mu_{BC}}}$, is the scaling factor. The Jacobi distances R and r are the distance of atom A from the center of mass of the BC diatom and the internuclear distance of BC, respectively and γ is the Jacobi angle between $\vec{R}$ and $\vec{r}$ in the BF frame. The scaled three body reduced mass, (μ), and the diatomic reduced mass, (μ_{BC}), of the system are given by

$$\mu_{BC} = \frac{m_B m_C}{m_B + m_C} \tag{2.10}$$

$$\mu = \sqrt{\frac{m_A m_B m_C}{m_A + m_B + m_C}}, \tag{2.11}$$

where, m_A, m_B and m_C are the masses of the atom A, B and C, respectively.

2.3.1 Transformation Between Space-fixed and Body-fixed Bases

There are two equivalent and widely used formalisms to expand the wavefunction in the coupled-angular momentum representations. One is the SF and another one is the BF frame belonging to the same center-of-mass coordinate system. The total angular momentum, $\boldsymbol{J} = L + j$, is conserved in both the frames. In the SF frame, the coordinate is stationary and orientation of its axes are fixed, whereas in the BF frame,

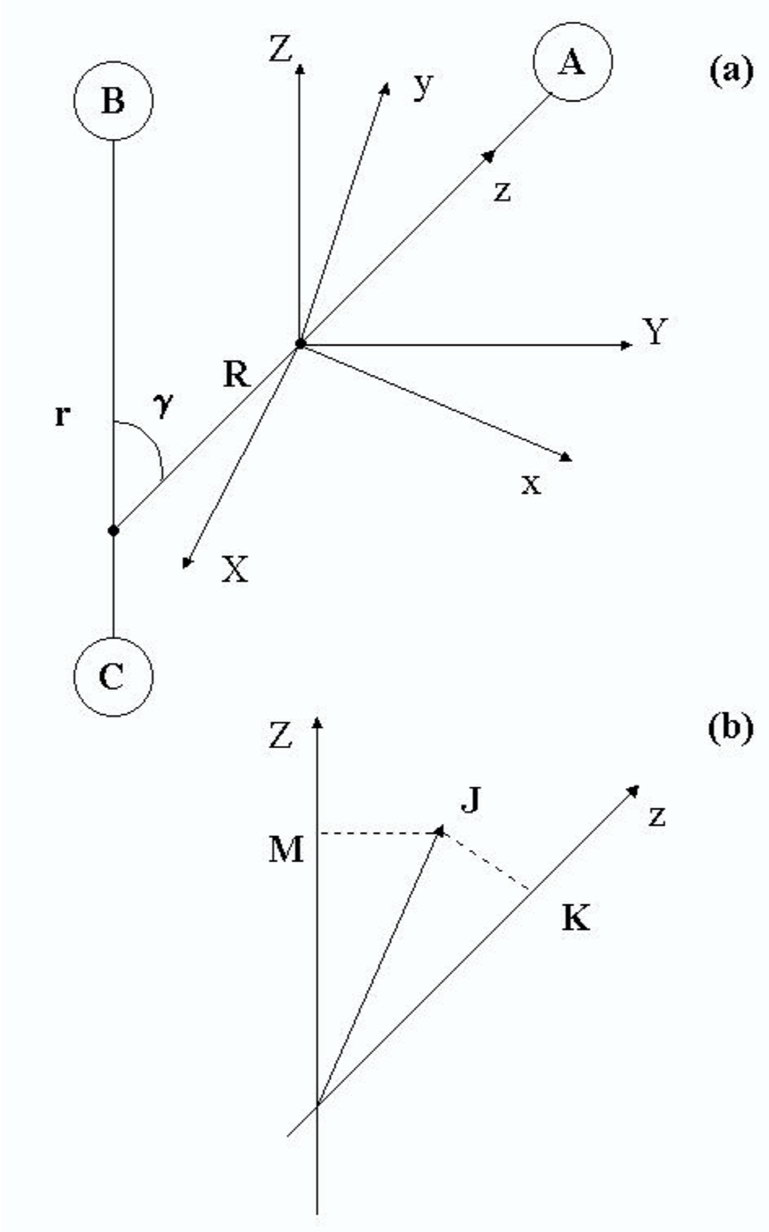

Figure 2.1: The panel (a) shows the center-of-mass coordinates for the A+BC collisions used in the space-fixed and the body-fixed frame are represented as XYZ and xyz axes, respectively. The coordinate origin is the center of mass of the atom-diatom system. The panel (b) shows the vector model picture for the rotation of the state function $|JM\rangle$ from SF-Z axis to $|JK\rangle$ of the BF-z axis.

the coordinate is rigidly fixed in the body with its axes rotating to maintain a fixed relative orientations of the particles. As shown in Fig. 2.1, the SF and the BF frame are

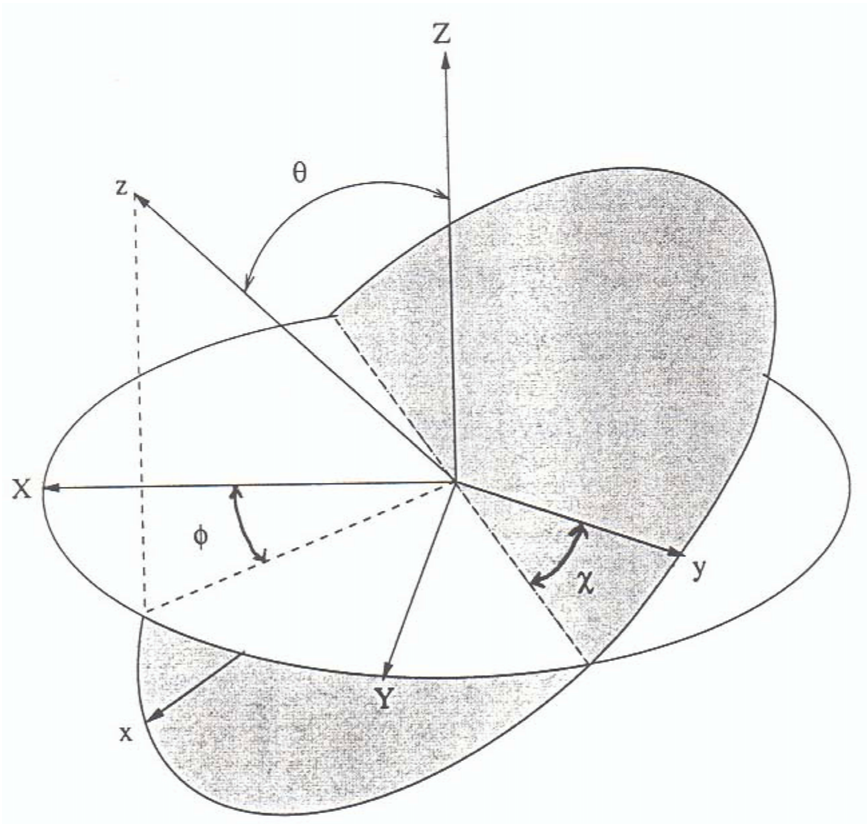

Figure 2.2: Euler angles ϕ, θ, and χ relating the SF (XYZ) and the BF (xyz) frames.

represented by (X, Y, Z) and (x, y, z) axes, respectively. The BF coordinate system is obtained through a rotation of the SF coordinate system by three Euler angles (ϕ, θ, χ) (cf. Fig. 2.2). Thus, the rotation of the physical system from the SF $\rightarrow$ BF frame can be carried out using a rotation matrix

$$\boldsymbol{R}(\phi, \theta, \chi) = e^{-i\phi J_Z} e^{-i\theta J_Y} e^{-i\chi J_Z}, \tag{2.12}$$

where, J_Z and J_Y are the projections of the total angular momentum on the Y and Z axes in the SF frame. A general multidimensional expansion of the eigenfunctions of a triatomic molecule for the motion along Jacobi distances $\Psi(R, r)$ and the rotational angular momentum wavefunction for the motion along γ in the SF frame is obtained

from the unrotated one using an orthogonal transformation [37, 151]

$$\Psi_{jl}^{JM}(\hat{R},\hat{r}) = \sum_{K} D_{KM}^{J}(\phi,\theta,\chi)\psi_{jl}^{JK}(\hat{R},\hat{r}). \tag{2.13}$$

where, J and M are the quantum numbers related to the total angular momentum and its SF Z-component, respectively. Here, the orbital angular momentum operator l in the BF representation is defined by [152],

$$\begin{aligned} l &= l_x\hat{e}_x + l_y\hat{e}_y + l_z\hat{e}_z \\ l &= \boldsymbol{R}\times p = R\hat{e}_z \times \boldsymbol{p}_R \\ &= R\hat{e}_z \times \{(p_R)_x\hat{e}_x + (p_R)_y\hat{e}_y + (p_R)_z\hat{e}_z\}. \end{aligned} \tag{2.14}$$

where, $\hat{e}_z$ is the unit vector along the body oriented z-axis. One can easily find from Eq. (2.14) that $l_z = 0$. As a result, $J_z = j_z$, because the projection (l_z) of $\boldsymbol{l}$ along the $\boldsymbol{R}$ axis is zero.

The angular momentum eigenstate, $|JK\rangle$, of $\boldsymbol{J}^2$ and J_z operators is given by

$$|JK\rangle = \boldsymbol{R}(\phi,\theta,\chi)|JM\rangle. \tag{2.15}$$

In Eq. (2.13), $D_{KM}^{J}(\phi,\theta,\chi)$ represents the rotation matrix which is defined by the angular momentum eigenstate, [151]

$$\begin{aligned} D_{KM}^{J}(\phi,\theta,\chi) &= \langle JK|\boldsymbol{R}(\phi,\theta,\chi)|JM\rangle \\ &= e^{-i\phi K} d_{KM}^{J}(\theta) e^{-i\chi M}. \end{aligned} \tag{2.16}$$

These are the elements of a $(2J+1)\times(2l+1)$ unitary matrix for the rotation $\boldsymbol{R}$. The reduced form of the rotation matrix, $d_{KM}^{J}(\theta)$, introduced by Wigner [151, 153, 154], is explicitly given in Appendix, A.1.

The SF total angular momentum wavefunction can be written explicitly [37] with the unit vectors $\hat{R} = (\theta_R, \phi_R)$ and $\hat{r} = (\theta_r, \phi_r)$ as:

$$\Psi_{jl}^{JM}(\hat{R}, \hat{r}) = \sum_m \langle jml(M-m)|JM\rangle \Psi_j^m(\hat{r}) \Psi_l^{M-m}(\hat{R}), \tag{2.17}$$

According to the BF formalism, z-axis coincides with the unit vector $\hat{R}$ and all three atoms lie in the xz-plane. Thus, $\hat{R} = (0,0)$ and $\hat{r} = (\gamma, 0)$ and γ in practice can be equated to the Euler angle θ. Now the unrotated wavefunction reads as

$$\begin{aligned} \psi_{jl}^{JK}(00,\theta 0) &= \sum_m \langle jml(K-m)|JM\rangle \psi_j^m(\theta,0)\psi_l^{K-m}(00) \\ &= \sqrt{\frac{2l+1}{4\pi}} \langle jKl0|JK\rangle \psi_j^m(\theta,0), \end{aligned} \tag{2.18}$$

for this particular choice of BF frame $l_z = 0$, $J_z = j_z$, and $K = m$. Therefore, the rotated angular momentum wavefunction can be written as

$$\Psi_{jl}^{JM}(\hat{R}, \hat{r}) = \sqrt{\frac{2l+1}{4\pi}} \sum_K \langle jKl0|JK\rangle D_{KM}^J(\phi,\theta,\chi)\psi_j^m(\theta,0). \tag{2.19}$$

Now we can define the BF angular momentum function by

$$Y_{jK}^{JM} = \tilde{D}_{KM}^J P_{jK}, \tag{2.20}$$

where,

$$\tilde{D}_{KM}^J = \sqrt{\frac{2J+1}{8\pi^2}} D_{KM}^J \tag{2.21}$$

and

$$P_{jK} = \sqrt{2\pi}\psi_j^m(\theta,0) \tag{2.22}$$

are the normalized rotation matrices and normalized associated Legendre polynomials,

respectively. Denoting the orthogonal transformation matrix by

$$C_{lK} = \sqrt{\frac{2l+1}{2J+1}} \langle jKl0|JK\rangle, \tag{2.23}$$

the angular wavefunction in terms of angular momentum function can be expressed as

$$\Psi_{jl}^{JM} = \sum_{K} C_{lK} Y_{jK}^{JM}. \tag{2.24}$$

By inverting the above equation and including the parity, the BF angular momentum function becomes

$$\begin{aligned} Y_{jK}^{JM} &= \sum_{l} C_{lK} \Psi_{jl}^{JM} \qquad (2.25) \\ \hat{p} Y_{jK}^{JM} &= \sum_{l} C_{lK} \hat{p} \Psi_{jl}^{JM} \\ &= \sum_{l} C_{lK} (-1)^{j+l} \Psi_{jl}^{JM} \\ &= (-1)^{J} \sum_{l} C_{l-K} \Psi_{jl}^{JM} \\ &= (-1)^{J} Y_{j-K}^{JM}. \qquad (2.26) \end{aligned}$$

We made use of the symmetry relations of C_{lK}, the Clebsch-Gordon coefficients, which are also referred to as vector coupling coefficients, vector addition coefficients, or Wigner coefficients, in the literature [151, 153–156]. It is clear that the BF angular momentum function, Y_{jK}^{JM}, is not an eigenfunction of the parity operator.

When the parity is considered in the angular functions, Eq. (2.20), the normalized parity-adapted angular momentum wavefunctions, Y_{jK}^{JMp}, is written as a linear combination of the Wigner rotation matrix elements, D_{KM}^{J}, [157, 158]

$$Y_{jK}^{JMp} = [2(1+\delta_{K,0})]^{-1/2} \sqrt{\frac{2J+1}{8\pi^2}} \left[D_{K,M}^{J} + (-1)^{P} D_{-K,M}^{J} \right]. \tag{2.27}$$

These matrix elements are written in the passive zyz notation of rotation and using the Condon-Shortley phase convention [155, 156]. In Eq. (2.27), the parity, P, is given by $J + K + p$, where p defines the parity and can have the value either 0 (even) or 1 (odd), depending on the values of J. The D^J_{KM} matrix elements corresponding to the same absolute value, but different signs, of K must be combined to form parity-adapted angular functions. For instance, odd J states will have odd parity ($p = 1$) and even J states will have even parity ($p = 0$) [48]. In addition to the parity term in Eq. (2.27), note that $(-1)^K$ term is also exists in the expansion of $D^J_{-K,M}$.

By the choice of BF frame for a triatomic system, the rotation of a state vector $|JK\rangle$ can be accomplished by rotation of the BF frame by three Euler angles $(0, \theta, 0)$, as the three atoms are always in the xz plane. In other words, the rotation of the $|JK\rangle$ equivalent to the rotation of the vector $\boldsymbol{R}$ in the xz plane, i.e. the Euler angle θ converges to the angle between the vector $\boldsymbol{R}$ and $\boldsymbol{r}$. This results in the projection of J for the final state $|JK'\rangle$ on the BF z-axis, $J_z(= K') = 0$. Therefore, the rotation matrix $D^J_{KK'}$ of Eq. (2.16) reduces to the associated Legendre polynomials:

$$D^J_{K0}(0, \theta, 0) = d^J_{K0}(\theta) = (-1)^K \sqrt{\frac{(J-K)!}{(J+K)!}} P^K_J(\cos\theta). \tag{2.28}$$

Hence, the BF total angular momentum eigenfunction of Eq. (2.20) is reduced to the associated Legendre polynomial [Eq. (2.28)].

The reduced rotation matrix satisfy some useful symmetry relations:

$$d^J_{KM}(\theta) = d^J_{-K,-M}(\theta) \tag{2.29}$$

$$\begin{aligned} d^J_{KM}(-\theta) &= d^J_{MK}(\theta) \\ &= (-1)^{K-M} d^J_{KM}(\theta). \end{aligned} \tag{2.30}$$

It also shows that $d^J_{KM}(0) = \delta_{KM}$ and $d^J_{KM}(\pi) = (-1)^{J+K}\delta_{K,-M}$.

Now, the physical wavefunction of the system satisfying the TDSE [Eq. (2.2)] and depending on the total angular momentum J, its projection onto the SF Z-axis, M, and parity under inversion of nuclear coordinates in the SF frame, p, can be expanded in terms of six coordinates: three internal Jacobi coordinates (R, r, γ) and three Euler angles $(\omega \equiv \theta, \phi, \chi)$ defining the orientation of the BF axes with respect to the SF axes, [37, 49, 98–100, 117],

$$|\Psi^J_M(R, r, \gamma, \omega, t)\rangle = \frac{1}{Rr} \sum_{K=-J}^{J} Y^{JMp}_{jK}(\omega) |\Psi^J_K(R, r, \gamma, t)\rangle, \tag{2.31}$$

where, K is the quantum number for the projection of $\boldsymbol{j}$ (and also of $\boldsymbol{J}$) on the BF z axis.

2.4 The Hamiltonian

The present thesis deals with an atom-diatom scattering problem. Therefore, we describe here the general situation of A+BC scattering in the reactant (A+BC) channel mass-scaled Jacobi coordinates R, r and γ (as introduced above) in the BF frame. With this set of coordinates, the Hamiltonian of the A+BC reacting system for the total angular momentum $J \neq 0$ can be expressed as [84, 98, 99, 121, 125, 126, 157, 159]

$$\hat{H} \;=\; -\frac{\hbar^2}{2\mu}\left[\frac{\partial^2}{\partial R^2} + \frac{\partial^2}{\partial r^2}\right] + \frac{\hat{l}^2}{2\mu R^2} + \frac{\hat{j}^2}{2\mu r^2} + V(R, r, \gamma), \tag{2.32}$$

where, μ is the three-body reduced mass [Eq. (2.11)] and $V(R, r, \gamma)$ is the interaction potential of the A+BC system.

In Eq. (2.32), the quantity $\hat{l}^2$ denotes the orbital angular momentum operator, and $\hat{j}^2$ denotes the rotational angular momentum operator of the BC diatom in the BF frame. The BF z-axis is defined to be parallel to Jacobi vector $\boldsymbol{R}$ and the diatom lies in the (x, z) plane. The angle γ defines the polar angle of the diatomic axis in the rotating

frame.

By this choice, the orbital angular momentum operator in the BF representation is given in Eq. (2.14). Now, the quantity $\hat{l}^2$ associated with R can be expressed as [37,160]

$$\hat{l}^2 \equiv (\hat{J} - \hat{j})^2 = \hat{J}^2 + \hat{j}^2 - 2\hat{J}_z\hat{j}_z - \hat{J}_+\hat{j}_- - \hat{J}_-\hat{j}_+. \tag{2.33}$$

Here the operators $\hat{J}_z$ and $\hat{j}_z$ are the respective BF z components and the total angular momentum operator $\hat{J}^2$ commutes with the operators $\hat{J}_z$ and $\hat{J}_\pm$. The corresponding raising (lowering) operators $\hat{J}_+(\hat{J}_-)$ and $\hat{j}_+(\hat{j}_-)$ are defined as

$$J_\pm = J_x \pm iJ_y, \tag{2.34}$$

$$J_\mp = J_X \mp iJ_Y. \tag{2.35}$$

The operator $J_\pm$ in the BF frame behave like the operator $J_\mp$ in the SF frame [150]. Since the total angular momentum operator $\hat{J}^2$ commutes with the operators $\hat{J}_z$ and $\hat{J}_\pm$ and thus the eigenvalues of these operators corresponding to the eigenvectors, $|J, K, M\rangle$ and $|J, K \pm 1, M\rangle$, are given respectively as

$$\hat{J}^2|J, K, M\rangle = \hbar^2 J(J+1)|J, K, M\rangle \tag{2.36}$$

$$\hat{J}_z|J, K, M\rangle = \hbar K|J, K, M\rangle \tag{2.37}$$

$$\hat{J}_\pm|J, K, M\rangle = \hbar\lambda^\pm_{JK}|J, K \pm 1, M\rangle, \tag{2.38}$$

where, J=0,1,2,... and $K = -J, ..., 0, ..., +J$, and $\lambda^\pm_{JK} = \sqrt{J(J+1) - K(K \pm 1)}$ [151]. M is the projection of J on the SF z axis and K is the projection of J and also j on the BF z axis.

One can express the matrix elements for the $\hat{l}^2$ operator in the BF frame which is

obtained in a tridiagonal matrix form as [37, 151, 161]

$$\begin{aligned} W^{Jj}_{K,K'} &= \left[J(J+1)+j(j+1)-2K^2\right]\delta_{K,K'} - \lambda^{+}_{JK}\lambda^{+}_{jK}\sqrt{1+\delta_{K0}}\delta_{K,K'+1} \\ &\quad -\lambda^{-}_{JK}\lambda^{-}_{jK}\sqrt{1+\delta_{K1}}\delta_{K,K'-1} \end{aligned} \tag{2.39}$$

A detailed derivation of these matrix elements of $\hat{l}^2$ operator in the BF frame is explicitly given in Appendix, A.2.

By substituting the total Hamiltonian [Eq. (2.32)] and the wavefunction of Eq. (2.31), in the TDSE, and after some algebra, the effective Hamiltonian in the BF frame operating on the time-dependent wavefunction becomes [49, 51, 121, 131, 132]

$$\begin{aligned} \hat{H} &= \left[-\frac{\hbar^2}{2\mu}\left(\frac{\partial^2}{\partial R^2}+\frac{\partial^2}{\partial r^2}\right)+\frac{\boldsymbol{j}^2}{2I}+\frac{\hbar^2}{2\mu R^2}\left[\boldsymbol{J}^2-2K^2\right]+V(R,r,\gamma)\right]\delta_{K,K'} \\ &\quad -\frac{\hbar^2}{2\mu R^2}\lambda^{+}_{JK}\left(\frac{\partial}{\partial\gamma}-K\cot\gamma\right)\delta_{K,K'+1} \\ &\quad -\frac{\hbar^2}{2\mu R^2}\lambda^{-}_{JK}\left(-\frac{\partial}{\partial\gamma}-K\cot\gamma\right)\delta_{K,K'-1}, \end{aligned} \tag{2.40}$$

$$\text{where, } I = \frac{\mu R^2 r^2}{R^2+r^2}, \tag{2.41}$$

is the three-body moment of inertia of the scattering system. The last two off-diagonal terms couples the various K states in the BF frame and are known as the Coriolis coupling terms [48, 124]. Hereafter, we refer the first term in the right hand side of Eq. (2.40) as $\hat{T}(R,r)$, the second and third terms as $\hat{T}_{dia}(\gamma)$ and the fifth and sixth terms as $\hat{T}_{off}(\gamma)$.

2.4.1 Centrifugal Sudden (CS) Approximation

While neglecting the Coriolis coupling terms in Eq. (2.40), one arrives at the well-known coupled-states or centrifugal sudden approximation [98,99]. Within this approximation, K is a good quantum number and it is conserved in the BF frame. It assumes that

the internal angular motion of a triatomic system is "frozen" throughout the collision. While the interaction potential is diagonal in the BF frame, the centrifugal potential arising from J is tridiagonal in the K states. In this approximation, one neglects inter-multiplet couplings due to $\hat{l}^2$ (i.e. the K-coupling) to obtain a diagonal representation of the Hamiltonian in the K quantum number. This is often found to be a very good approximation. In doing so, Eqs. (2.33) and (2.39) reduce to

$$\begin{aligned} \hat{l}^2 &= \hat{J}^2 + \hat{j}^2 - 2\hat{J}_z\hat{j}_z \\ W^{Jj}_{K,K'} &= \left[J(J+1) + j(j+1) - 2K^2\right]\delta_{K,K'} \end{aligned} \tag{2.42}$$

For a given value of J and parity of the system, K states will manifold either $J+1$ or J times. Decoupling of K-states also reduces the computation time significantly in the diagonalization of the Hamiltonian matrix. This approximation greatly simplifies $J \neq 0$ calculations by reducing the dimensionality of the problem from four to three and provides reasonably accurate results for many bimolecular reactions [162–166].

2.4.2 Diatomic Hamiltonian

The ro-vibrational motion excluding the center-of-mass motion of a diatomic molecule BC consists of three degrees of freedom. The Hamiltonian for a diatomic molecule of reduced mass, μ', can be written as [152]

$$\hat{H}_{BC} = -\frac{\hbar^2}{2\mu'}\frac{\partial^2}{\partial r'^2} + \frac{\boldsymbol{j}^2}{2\mu' r'^2} + V(r'), \tag{2.43}$$

where, $r' = r(\mu/\mu')^{1/2}$ is the unscaled internuclear distance of the BC molecule and $V(r')$ is its potential energy obtained from the *ab initio* PES by setting $R \to \infty$. The rotational angular momentum operator is defined as

$$\boldsymbol{j}^2 = -\frac{\hbar^2}{\sin^2\gamma}\left[\sin\vartheta\frac{\partial}{\partial\vartheta}\left(\sin\vartheta\frac{\partial}{\partial\vartheta}\right) + \frac{\partial^2}{\partial\varphi^2}\right]. \tag{2.44}$$

Here ϑ and φ are the angles associated with $\boldsymbol{r}$ representing the orientation of diatom.

The diatomic eigenfunctions, $\phi_{vj}(r)$, corresponding to a vibrational and rotational states satisfy the Schrödinger equation

$$\left[-\frac{\hbar^2}{2\mu'}\frac{d^2}{dr'^2} + V(r') + \frac{j(j+1)\hbar^2}{2\mu' r'^2}\right]\phi_{vj}(r') = \epsilon_{vj}\phi_{vj}(r'). \tag{2.45}$$

Here ϵ_{vj} is the energy eigenvalue. This eigenvalue equation is solved by using the sine-DVR approach of Colbert and Miller [130] which is discussed in Sec. 2.5.2.4.

2.5 Numerical Solution of TDSE

The TDSE equation [Eq. (2.2)] is solved for the first time in 1959 for a model collinear exchange reaction by Mazur and Rubin [167]. Several years later, numerical solution of the WP motion in one dimension was carried out by Goldberg *et al.* [168] and then McCullough and Wyatt [169] used a finite difference (FD) scheme combined with an implicit propagator to study the collinear H+H_2 exchange reaction. The FD method scales as $O(N^2)$ which was improved to $O(N)$ by Askar and Cakmak [170] using a second-order-differencing (SOD) propagator. In 1976, Feit *et al.* [171] had introduced a Fourier method to solve the TDSE numerically on a grid, and Kosloff *et al.* [112] made it more practicable to deal with the problems in chemical dynamics. This method [112, 172] is extremely efficient and accurate due to the fast Fourier transform (FFT) algorithm, which scales as $O(N \log N)$ [173, 174]. Moreover, with the use of modern computers in parallel architecture the scaling can be further reduced to $O(\log N)$ [175].

The evolution of the WP on a given PES involves both space and time. The discrete Hilbert space enable to represent the Hamiltonian operator which is partitioned as a sum of kinetic ($\hat{T}$) and potential energy ($\hat{V}$) operator. The action of $\hat{H}$ operator on Ψ should be done for these two noncommuting operators separately, since their

local spaces are different. The operator $\hat{V}$ is local in the coordinate space and it is a function of coordinates only, however, the operator $\hat{T}$ is local in the momentum space and therefore, a transformation of the two spaces is required to carry out a simultaneous operation of these two operators on the wavefunction. As stated earlier, the grid is constructed in the coordinate space and therefore, the potential energy operator is local in this space and its operation is accomplished by multiplying the value of the potential energy with the wavefunction at each grid point. Evaluation of $\hat{T}\Psi$ in the coordinate space then becomes a bottleneck in all time-dependent WP calculations as the kinetic energy operator is nonlocal in this space. A similar problem arises with the potential energy operator in the momentum space, because the kinetic energy operator, $\left[\hat{T} = \frac{\hat{p}^2}{2m} = \frac{\hbar^2 k^2}{2m}\right]$, is local in this space and hence its operation becomes a multiplication of the wavefunction by the discrete kinetic energy spectrum at each grid point and the space transformation is required to evaluate the action of the potential energy operator on the momentum grid.

In the present study, we construct the grid in the coordinate space and therefore, the action of the potential energy operator is carried out locally. The action of the kinetic energy operator is carried out by means of the FFT method as described below.

2.5.1 The Fourier Method

The Fourier method is a special case of the orthogonal collocation scheme to construct the discrete Hilbert space. The collocation method determines the expansion coefficients (a_n) of the orthogonal basis functions $(g_n(x_i))$ by matching the solution on a set of N grid points:

$$\Psi(x_i) \equiv \overline{\Psi}(x_i) = \sum_{n=0}^{N-1} a_n g_n(x_i), \tag{2.46}$$

where, $(g_n(x_i))$ is chosen as the plane wave basis functions [171, 176]

$$g_n(x_i) = \exp\left[i2\pi kx/L\right], \quad k = -(N/2-1), \ldots, 0, \ldots, N/2. \tag{2.47}$$

Now the wavefunction in this basis is given by

$$\Psi(x) \approx \sum_{k=-(N/2-1)}^{N/2} a_k \exp\left[i2\pi kx/L\right], \tag{2.48}$$

where, a_k is becomes the Fourier expansion coefficient and it represents the amplitude of the wavefunction in momentum space, which is obtained by inverting the above relation using the orthogonality relation of the Fourier functions, i.e.

$$a_k = \frac{1}{N} \sum_{i=1}^{N} \Psi(x_i) \exp\left[-i2\pi kx_i/L\right]. \tag{2.49}$$

The above discrete summations [Eqs. (2.48) and (2.49)] can also be represented by integrals as

$$\Psi(x) = \frac{1}{\sqrt{2\pi}} \int_{-\infty}^{\infty} \overline{\Psi}(k) e^{ikx} dk \tag{2.50}$$

and

$$\overline{\Psi}(k) = \frac{1}{\sqrt{2\pi}} \int_{-\infty}^{\infty} \Psi(x) e^{-ikx} dx. \tag{2.51}$$

In general, Fourier transform performs the transformation from one domain to another domain connected through the uncertainty relation (for example, the coordinate-momentum or the time-energy mapping space). In this scheme, the action of the kinetic energy operator $\hat{T}$ on the wavefunction involves transformation of the coordinate space wavefunction to the momentum space, by multiplying the kinetic energy discrete spectrum, $T(k)$, at each grid points,

$$\hat{T}\Psi(x) = \frac{\hbar^2 k^2}{2m} \overline{\Psi}(k) = \frac{\hbar^2 k^2}{2m} a_k, \tag{2.52}$$

and then by transforming back the result in the right-hand side (RHS) of the Eq. (2.52) to the coordinate space.

Kosloff and Kosloff [112] have described the utility of a FFT algorithm and its

application to the numerical solution of Schrödinger equation on a grid. The Fourier method becomes exact for wavefunctions which obey the periodic boundary condition and they are band-limited functions with finite support. The support of a function is defined by a non-zero set of values. Usually, the wavefunctions (except semilocalized wavefunctions) are not band-limited with finite-support as they can not be confined simultaneously both in coordinate and momentum spaces. The boundary conditions for the WPs can be made by using the absorbing boundaries and reducing their amplitude to zero at the grid edges. A FFT method scales as $N \log N$ when compared to a finite difference (FD) scheme (of similar accuracy) which scales as $O(N^2)$ with the number of grid points, N. Therefore, a FFT algorithm is computationally more useful and used here.

2.5.2 The Discrete Variable Representation (DVR) Method

The discrete variable representation is another example of the orthogonal collocation method which utilizes the basis functions and the coordinate points. In a DVR, the desired eigenstates are usually obtained by diagonalizing the relevant Hamiltonian matrix. The matrix elements are determined by the orthogonal transformation relation between the points and the basis functions using a finite basis representation (FBR). The DVR is a basis consisting of N discrete points, whereas the FBR is a basis consisting of N^2 integrable functions appropriate to the DVR coordinates. Both the basis are designed to evaluate the action of operators in their respective local representations. The potential matrix elements are calculated by the numerical quadrature functions and points using the DVR-FBR transformation. A few decades ago, following to the Harris *et al.* work [177], Dickinson and Certain [178] proposed the use of orthogonal polynomial basis functions (e.g., the Hermite polynomials), corresponding to the Gaussian quadrature to carry out an orthogonal transformation between the N quadrature points and N basis functions. Light and coworkers [125–127] applied the DVR-FBR transformation to evaluate the Hamiltonian matrix elements, and it has been used ex-

tensively thereafter [117, 127–129, 179, 180]. In the following, we discuss some of the DVRs' used to treat the problems in chemical dynamics.

2.5.2.1 Quadrature DVR

Let us assume that the mixed grid representation of the function $\Psi(x)$, $\{\Psi(x_i),\ i = 1, 2, ..., N\}$ is used then it is multiplied by the corresponding diagonal value of any local operator at the particular grid point. The action of a non-local operator is evaluated by switching from the grid (DVR) to the basis representation (FBR). The transformation matrix needs to be unitary, therefore an orthonormal basis set of some basis functions $(\phi_n(x_\alpha))$ are used on a set of quadrature points x_α, associated with the quadrature weights w_α.

$$\langle \phi_n | x_\alpha \rangle = \phi_n^\star(x_\alpha) \tag{2.53}$$

In the pseudospectral approximations one can write

$$\Psi(x) = \sum_n c_n \phi_n(x) \tag{2.54}$$

The orthonormal property of $\phi_n(x)$ is utilized to evaluate the expansion coefficients,

$$c_n = \int \phi_n^\star(x)\Psi(x)dx. \tag{2.55}$$

For the N discrete quadrature points on a grid the above integrals can be approximated as

$$c_n = \sum_\alpha w_\alpha \phi_n^\star(x_\alpha)\Psi(x_\alpha) \tag{2.56}$$

Now, the basis functions $\Psi(x)$ can be evaluated at the quadrature points through

$$\begin{aligned} \Psi(x) &= \sum_n \sum_\alpha w_\alpha \phi_n^\star(x_\alpha)\Psi(x_\alpha)\phi_n(x) \\ &= \sum_\alpha \Psi_\alpha \psi_\alpha(x) \qquad (2.57) \\ \text{where, } \psi_\alpha(x) &= \sqrt{w_\alpha}\sum_\alpha \phi_n^\star(x_\alpha)\phi_n(x) \qquad (2.58) \end{aligned}$$

here the transformation matrix $T^\dagger_{n\alpha}$ is introduced between the N Gaussian quadrature points (DVR) and N orthogonal polynomials (FBR) in the discrete Hilbert space with the weight functions w_α:

$$T^\dagger_{n\alpha} = \sqrt{w_\alpha}\phi_n^\star(x_\alpha) \qquad (2.59)$$

This matrix ensures the orthonormality of the basis functions, i.e. T matrix is column orthogonal, $(T^\dagger T)_{nm} = \delta_{nm}$, and it is also unitary. In the discrete representation, the overlap matrix is given by

$$\triangle_{\alpha\beta} = \langle\alpha|\beta\rangle = (TT^\dagger)_{\alpha\beta} \qquad (2.60)$$

This overlap integral will have a value of either zero or one and hence, $T^\dagger_{n\alpha}$ is orthonormal and unitary ($T^\dagger T = TT^\dagger = 1$). Therefore, T corresponds to the transformation matrix from the DVR to the FBR.

2.5.2.2 Diagonalization DVR

The DVR-FBR transformation also provides the elements of potential matrix, which is diagonal in the DVR on the Gaussian quadrature points as

$$\langle\alpha|\hat{V}^{DVR}|\beta\rangle = V_{\alpha\beta} = V(x_\alpha)\delta_{\alpha\beta} \qquad (2.61)$$

Substituting this diagonal potential matrix in the DVR of the Hamiltonian,

$$\begin{aligned}\langle\alpha|\hat{H}^{DVR}|\beta\rangle &= \langle\alpha|\hat{T}^{DVR}|\beta\rangle + \langle\alpha|\hat{V}^{DVR}|\beta\rangle \\ &= \sum_{nm} T^{\dagger}_{n\alpha}\hat{T}^{FBR}T_{\beta m} + V_{\alpha\beta} \\ &= (T^{\dagger}T^{FBR}T)_{\alpha\beta} + V_{\alpha\beta}. \end{aligned} \tag{2.62}$$

It is well known that the DVR scheme can be applied in multidimensions [126, 181] and in that case, it can be constructed as a direct product of one dimensional DVR by successive diagonalization, truncation and recoupling. Let us consider a three-dimensional Hamiltonian, it can be represented in a simple way by using the orthogonal coordinate system. The multidimensional DVRs are constructed as stated above [126, 181, 182]

$$\begin{aligned}\langle\alpha'\beta'\gamma'|\hat{H}^{DVR}|\alpha\beta\gamma\rangle &= K_{\alpha'\alpha}\delta_{\beta'\beta}\delta_{\gamma'\gamma} + K_{\beta'\beta}\delta_{\alpha'\alpha}\delta_{\gamma'\gamma} + K_{\gamma'\gamma}\delta_{\alpha'\alpha}\delta_{\beta'\beta} \\ &\quad + V(x_{\alpha}, y_{\beta}, z_{\gamma})\delta_{\alpha'\alpha}\delta_{\beta'\beta}\delta_{\gamma'\gamma} \end{aligned} \tag{2.63}$$

where, K is the kinetic energy matrix in one-dimension, and has the form $T^{\dagger}T^{FBR}T$.

Colbert and Miller [130] have proposed a novel DVR, introducing the L^2 basis set with a uniform grid, to evaluate the integrals of vibrational eigenvalue problem for quantum reactive scattering calculations. They pointed out that in Cartesian coordinates the DVR of kinetic energy matrix is extremely sparse (the potential energy matrix is diagonal as in all DVRs), i.e, it can be written as a sum of one-dimensional kinetic energy operators with $N \log N$ scaling . Following to this proposition, Corey *et al.* [129] pointed out that the non-Cartesian coordinate representation of the Hamiltonian matrix and the $(N \log N)$ scaling relation is due to the fact that the multi-dimensional Hamiltonian can be written as a sum of the local and nonlocal operators in a single coordinate.

2.5.2.3 Legendre DVR

The Legendre DVR is based upon a GLQ and the associated Legendre polynomial functions: The latter are eigenfunctions of the angular momentum operator [41]

$$\hat{j}^2 = -\hbar^2 \left(\frac{1}{\sin\gamma} \frac{\partial}{\partial\gamma} \sin\gamma \frac{\partial}{\partial\gamma} - \frac{K^2}{\sin^2\gamma} \right), \tag{2.64}$$

where, K $(-l, \ldots, 0, \ldots, +l)$ is the magnetic quantum number. The $\mathcal{L}^2$-normalized associated Legendre functions obtained by using the Condon-Shortley phase convention can be written as [155]

$$\tilde{P}_l^m(\cos\gamma) = (-1)^m \sqrt{\frac{2l+1}{2} \frac{(l-m)!}{(l+m)!}} P_l^m(\cos\gamma). \tag{2.65}$$

The angular grid points represent the nodes of a GLQ, which can be obtained by diagonalizing the matrix of $\cos\gamma$ operator in the basis of the associated Legendre polynomials for a fixed value of m, using the recursion relation,

$$c_{l+1}\tilde{P}_{l+1}^m(\cos\gamma) - \cos\gamma \tilde{P}_l^m(\cos\gamma) + c_l \tilde{P}_{l-1}^m(\cos\gamma) = 0, \tag{2.66}$$

where, the coefficients of the polynomials are given by

$$c_l = \sqrt{\frac{l^2 - m^2}{4l^2 - 1}}. \tag{2.67}$$

The matrix representation of transformed coordinate, $x = \cos\gamma$, exhibit a tri-diagonal structure. The diagonalization of $\hat{x}$ yields the eigenvalues (x_α) of this matrix, and the DVR grid points are then obtained as, $\gamma_\alpha = \arccos x_\alpha$. The eigenvector matrix defines the DVR-FBR transformation matrix, $T_{l\alpha}^m$. The resulting quadrature weights are given by [41]

$$w_\alpha^{1/2} = \sqrt{\frac{2^{m+1} m!}{(2m+1)!!}} \sin^{-m}(\gamma_\alpha) T_{1\alpha} \tag{2.68}$$

where, $T_{1\alpha}$ refers the first row of the eigenvector matrix. This method is most convenient

to evaluate the action of the angular kinetic energy operator in various coordinate system. For example, the action of the $\hat{l}^2$ operator [Eq. (2.64)] can be accomplished on a grid for a fixed value of m as

$$\hat{l}^2\Psi^m(\gamma_\alpha) = \sum_{l=|m|}^{l_{max}} T_{l\alpha}^{m\dagger}\left[\hbar^2 l(l+1)\right] T_{l\alpha}^{m}\Psi^m(\gamma_\alpha). \tag{2.69}$$

where, the number of angular basis functions, $l_{max} = (N_\gamma - 1)$, (N_γ being the number of angular grid points), is used and $T_{l\alpha}^{m\dagger}$ is the Hermitian conjugate of $T_{l\alpha}^{m}$. Here the wavefunction on the grid (DVR) is transformed to the angular momentum space (FBR), where the $\hat{l}^2$ operator is local, using the matrix $T_{l\alpha}^{m}$. Subsequently, it is multiplied by the eigenvalue of the operator and transformed back to the grid space using the matrix $T_{l\alpha}^{m\dagger}$ [128, 129, 132].

In case of a full-dimensional calculations, the action of rotational kinetic energy operators (for the both diagonal $\hat{T}_{dia}$ and off-diagonal $\hat{T}_{off}^{\pm}$) is carried out by transforming the DVR wavefunction to the angular momentum space FBR, multiplying it by the diagonal and off-diagonal value of the operators $\hat{T}_{dia}$ and $\hat{T}_{off}^{\pm}$, respectively and transforming it back to the DVR. Numerically, this can be accomplished in a single step as follows

$$\hat{T}_{dia}(\gamma)|\Psi_{lmn'}^{K}\rangle = \sum_{n}\left\{\sum_{j} \boldsymbol{U}_{n',j}^{K\ \dagger}\left[W_{dia}\right]\boldsymbol{U}_{j,n}^{K}\right\}|\Psi_{lmn}^{K}\rangle, \tag{2.70}$$

$$\hat{T}_{off}^{\pm}(\gamma)|\Psi_{lmn'}^{K}\rangle = \sum_{n}\left\{\sum_{j} \boldsymbol{U}_{n',j}^{K\pm1\dagger}\left[W_{off}^{\pm}\right]\boldsymbol{U}_{j,n}^{K}\right\}|\Psi_{lmn}^{K\pm1}\rangle, \tag{2.71}$$

where, W_{dia} and $W_{off}^{\pm}$ are the diagonal and off-diagonal values of the respective rota-

tional kinetic energy operators, given as (cf. Eqs. (2.39)),

$$W_{dia} = \frac{\hbar^2}{2}\left[\frac{j(j+1)}{I} + \frac{J(J+1)-2K^2}{\mu R^2}\right] \tag{2.72}$$

$$W^{\pm}_{off} = \frac{\hbar^2}{2\mu R^2}\left[\lambda^{\pm}_{JK}\lambda^{\pm}_{jK}\right]. \tag{2.73}$$

$\boldsymbol{U}^{\dagger}_{n,j}$ are the elements of the inverse transformation matrix, the Hermitian conjugate to $\boldsymbol{U}_{j,n}$. $\lambda^{\pm}_{JK}$ and $\lambda^{\pm}_{jK}$ are the CC terms.

2.5.2.4 Sine-DVR

This DVR, proposed by Colbert and Miller [130], uses the particle-in-a-box eigenfunctions as a basis on a coordinate grid. The coordinate x is restricted to the interval (a, b) and the length of the box is then given by $L = b - a$. The DVR grid points (x_i) are considered to be equally spaced and they are given by

$$x_i = a + iL/N, \quad i = 1, \ldots, N-1, \tag{2.74}$$

and the basis functions are given by

$$\phi_n(x) = \sqrt{\frac{2}{L}}\sin\left(\frac{n\pi(x-a)}{L}\right), \; n = 1, \ldots, N-1, \tag{2.75}$$

note that, $\psi_n(x_0 \equiv a) = \psi_n(x_N \equiv b) = 0$; and there are $(N-1)$ functions and points. The DVR or the grid-point representation of the kinetic energy is given by

$$T_{ii'} = -\frac{\hbar^2}{2m}\Delta x \sum_{n=1}^{N-1}\phi_n(x_i)\phi''_n(x_{i'}), \tag{2.76}$$

where, $\Delta x = L/N$ is the grid spacing. By substituting Eq. (2.75) in Eq. (2.76), the latter becomes

$$T_{ii'} = -\frac{\hbar^2}{2m}\left(\frac{\pi}{L}\right)^2\frac{2}{N}\sum_{n=1}^{N-1} n^2 \sin\left(\frac{n\pi i}{N}\right)\sin\left(\frac{n\pi i'}{N}\right). \tag{2.77}$$

The summation in the above expression can be analytically evaluated [130]

$$T_{ii'} = \frac{\hbar^2}{2m}\frac{(-1)^{i-i'}\pi^2}{2L^2}\left[\frac{1}{\sin^2(\pi(i-i')/2N)} - \frac{1}{\sin^2(\pi(i+i')/2N)}\right], \tag{2.78}$$

for $i \neq i'$, and

$$T_{ii'} = \frac{\hbar^2}{2m}\frac{\pi^2}{2L^2}\left[(2N^2+1)/3 - \frac{1}{\sin^2(\pi i/N)}\right], \tag{2.79}$$

for $i = i'$.

In case of the $(-\infty, +\infty)$ interval, the finite grid spacing, Δx, requires that $N \to \infty$, and $i + i' \to \infty$, but $i - i'$ is finite, thus Eq. (2.78) becomes

$$T_{ii'} = \frac{\hbar^2}{2m}\frac{(-1)^{i-i'}}{\Delta x^2}\left\{\begin{array}{ll} \pi^2/3, & i = i' \\ \frac{2}{(i-i')^2}, & i \neq i' \end{array}\right\} \tag{2.80}$$

and in that case, the grid is specified more conveniently as $x_i = i\Delta x$ $i = 0, \pm 1, \pm 2, ...$

In the same way, the kinetic energy matrices for other cases, specifically $(0, \infty)$, $(0, \pi)$, $(0, 2\pi)$ intervals, are also shown to be evaluated by this approach [130].

2.5.3 Time Evolution Operator

In quantum molecular dynamics, there are several approximate methods to propagate the WP in time. We described some of them in the following subsections. Various propagation methods of solving the TDSE have been developed by different researchers. These methods are the second-order difference (SOD) [112, 170], split-operator (SO) [171, 172], Chebyshev polynomials (CP) [183, 184], short-iterative Lanczos (SIL) [186], and symplectic integrator (SI) [187] applied explicitly to the time-independent Hamiltonians. Also, the methods are developed to deal with the explicitly time-dependent Hamiltonians [188, 189]. Leforestier *et al.* [190] have presented a comparative account of the four widely used propagation schemes (viz., the SOD, SO, CP and SIL), and examined them in terms of their performance and accuracy.

The general solution of the TDSE [Eq. (2.1)] is given by

$$\Psi(t) = \hat{P} \exp\left[-i\hbar \int_0^T \hat{H}(t')dt'\right] \Psi(0) \tag{2.81}$$

where, $\Psi(0)$ and $\Psi(t)$ are the wavefunction at time 0 and t, respectively. $\hat{P}$ is the time ordering operator. For an explicitly time-independent Hamiltonian, the solution reads as in Eq. (2.2). The exponential operator in the above is known as the time-evolution operator denoted by $\hat{U}(t, t_0)$ [191]. In quantum dynamical studies, the above equation [Eq. (2.1 or Eq. (2.2)] is numerically solved by approximating the exponential operator by a suitable WP propagation scheme as stated above. The time axis is divided into N segments with a step length Δt. The time-evolution for the entire range of time is then accomplished through:

$$\text{For } t = 0,\ \hat{U}(t, t_0) = e^{-i\hat{H}t/\hbar} \tag{2.82}$$

$$\hat{U}(t) = \Pi_{n=0}^{N_t-1} \hat{U}((n+1)\Delta t, n\Delta t) \tag{2.83}$$

where, N_t is the total number of time-evolution steps and $\Delta t = t/N_t$. The Eq. (2.83) can be expanded by considering the parameter t_0 as a variable, and the composition property of the $\hat{U}$ operator

$$\hat{U}(t_n, t_1) = \hat{U}(t_n, t_{n-1}) \ldots \hat{U}(t_3, t_2)\hat{U}(t_2, t_1) \tag{2.84}$$

where, $t_1, t_2, \ldots, t_n$ are arbitrary and assuming $t_1 < t_2 < \ldots < t_n$. If t_n's are not in ascending order, one should use *time-ordering operator* [146] which uses the *time-ordered product* [192], to evaluate $\hat{U}(t_n, t_1)$.

The norm conservation of the state leads to the probability conservation during time-evolution, which demands the operator $\hat{U}$ is linear and unitary:

$$\hat{U}\hat{U}^\dagger = \hat{U}^\dagger\hat{U} = 1. \tag{2.85}$$

For an infinitesimal time-step (dt) the time-evolution operator, $\hat{U}(t+dt,t)$, (which is also unitary) can be written as [192]

$$\hat{U}(t+dt,t) = 1 - \frac{i}{\hbar}H(t)dt. \tag{2.86}$$

2.5.4 Split-Operator (SO) Method

The kinetic energy and potential energy operators do not commute. Therefore, a straight forward splitting of the time evolution operator $e^{-i[\hat{T}+\hat{V}]t/\hbar}$ into $e^{-i\hat{T}t/\hbar} \times e^{-i\hat{V}t/\hbar}$ results into commutation error, which is first-order in $O(\Delta t^2)$. Fleck *et al.* [171, 172] showed that splitting of the time-evolution operator symmetrically reduces this error to third order in time. They called it as a second order SO scheme. The potential referenced second-order SO scheme is given by:

$$e^{-i\hat{H}\Delta t/\hbar} = e^{-i\hat{T}\Delta t/2\hbar}e^{-i\hat{V}\Delta t/\hbar}e^{-i\hat{T}\Delta t/2\hbar} + O(\Delta t^3). \tag{2.87}$$

The time evolution of the WP in this scheme is given by

$$\begin{aligned} \Psi(t+\Delta t) &= e^{-i\hat{T}\Delta t/2\hbar}e^{-i\hat{V}\Delta t/\hbar}e^{-i\hat{T}\Delta t/2\hbar}\Psi(t) \\ &= Q\Psi(t) \end{aligned} \tag{2.88}$$

where, $QQ^{\dagger} = 1$. It is clear from the above expression that the SO scheme is unitary and the norm of WP is therefore conserved. However, the energy conservation fails in this scheme due to the noncommutability of the potential and kinetic energy operators. To obtain comparatively accurate results, an optimum time step is selected based on the maximum potential energy on the grid [112, 172].

$$\Delta t < \frac{\pi}{3\Delta V_{max}}, \quad \Delta V_{max} = V_{max} - V_{min}. \tag{2.89}$$

The SO method also works well in the presence of negative imaginary potential

(NIP) that is added to the interaction potential to avoid reflection of WP from grid edges [114]. In presence of a NIP ($-iV_0$) Eq. (2.87) can be written as

$$Q' = e^{-i\hat{T}\Delta t/2\hbar} e^{-i\hat{V}\Delta t/\hbar} e^{-V_0\Delta t/\hbar} e^{-i\hat{T}\Delta t/2\hbar} + O(\Delta t^3). \tag{2.90}$$

It maintains the unitary relation and the expression will be given by

$$Q'Q'^{\dagger} = e^{i\hat{T}\Delta t/2\hbar} e^{-2V_0\Delta t/\hbar} e^{-i\hat{T}\Delta t/2\hbar}. \tag{2.91}$$

Using the above relation, the norm of the wavefunction at time $t + \Delta t$ can be written :

$$\langle \Psi(t+\Delta t)|\Psi(t+\Delta t)\rangle = e^{-2V_0\Delta t/\hbar}\langle \Psi(t)|\Psi(t)\rangle \tag{2.92}$$

It is clear that the norm of the WP decreases with increase in Δt.

2.5.5 Chebyshev Polynomial (CP) Scheme

Among the WP propagation methods mentioned in Sec. 2.5.3, the CP scheme is found to be one of the most accurate and efficient for the Hermitian Hamiltonians. Because, this method has exponential convergence property and the error (both in the amplitude and in the phase of the wavefunction) is distributed uniformly over all eigenvalues of the Hamiltonian. Though the method is not unitary and is neither norm nor energy conserving, it is so accurate that deviation of the norm from unitarity serves as a check for the accuracy of the scheme. Tal-Ezer and Kosloff [183] were the first to realize the superior numerical effectiveness of CP expansion, and introduced this as a global propagation scheme. The CPs are optimal for scalar function, $F(x)$, bounded in the interval (-1, 1). A function like e^{ax} can be expressed by

$$e^{ax} = \sum_{n=0}^{\infty} (2 - \delta_{n0}) J_n(\alpha) T_n(x) \tag{2.93}$$

where, $J_n(\alpha)$ and $T_n(x)$ are the Bessel functions and CPs of order n, respectively. δ_{n0} is a Kronecker delta and $\alpha = \Delta E \Delta t/2\hbar$.

CPs belong to a unique class of orthogonal polynomials based on the cosine function are satisfy the recursion relation

$$T_{n+1}(x) = 2xT_n(x) - T_{n-1}(x), \text{ for } n \geq 1 \tag{2.94}$$

with $T_0(x) = 1$ and $T_1(x) = x$. In case of Hamiltonian which is self-adjoint, the eigenvalues lie on a real axis. The latter can be bounded in the interval (-1,+1) by renormalizing the Hamiltonian $\hat{H}$ as follows:

$$\hat{H}_{norm} = \frac{2(\hat{H} - \hat{I}\overline{H})}{\Delta E} \tag{2.95}$$

where, $\overline{H} = (E_{max} + E_{min})/2$ and $\Delta E = E_{max} - E_{min}$. The E_{max} and E_{min} are maximum and minimum energy for the system. The maximum radial and rotational kinetic energies on a grid in Jacobi coordinates are given by [193],

$$T_{max}(R,r) = \frac{\pi^2\hbar^2}{2\mu}\left[\frac{1}{\Delta R^2} + \frac{1}{\Delta r^2}\right] \tag{2.96}$$

$$T^{dia}_{max}(\gamma) = \frac{\hbar^2}{2}\left[\frac{j_{max}(j_{max}+1)}{I_{min}} + \frac{J_{max}(J_{max}+1) - 2K^2_{max}}{\mu\Delta R^2}\right] \tag{2.97}$$

$$T^{off}_{max}(\gamma) = \frac{\hbar^2}{2\mu\Delta R^2}\left[\lambda^{\pm}_{J_{max}K_{max}}\lambda^{\pm}_{j_{max}K_{max}}\right] \tag{2.98}$$

where, ΔR and Δr are the grid spacings along the respective coordinates. I_{min} indicates the minimum value of three-body moment of inertia (cf. Eq. (2.41)), and j_{max} is the maximum rotational angular momentum quantum number given as $(N_\gamma - 1)$. $\lambda^{\pm}_{J_{max}K_{max}}$ and $\lambda^{\pm}_{j_{max}K_{max}}$ are the CC terms for the maximum value of J, j and K quantum numbers.

The time-evolution operator [Eq. (2.2)] can be written in terms of the renormalized

Hamiltonian as

$$\exp\left(-i\hat{H}\Delta t/\hbar\right) = \exp\left(-i\overline{H}\Delta t/\hbar\right)\exp\left(-i\alpha\hat{H}_{norm}\right) \tag{2.99}$$

where, the first term in the RHS of the above expression represents the phase shift due to the shift in the energy scale and $\hat{H}_{norm}$ is approximated by the Chebyshev series as

$$e^{-i\alpha\hat{H}_{norm}} = \sum_{n=0}^{\infty}(2-\delta_{n0})J_n(\alpha)\Phi_n(-i\hat{H}_{norm}) \tag{2.100}$$

where, Φ_n are the complex CPs of order n satisfying the recursion relation:

$$\Phi_{n+1} = -2i\hat{H}_{norm}\Phi_n + \Phi_{n-1} \tag{2.101}$$

where, $\Phi_0 = 1$ and $\Phi_1 = -iH_{norm}$. Therefore the evolution of the WP in the CP scheme on a discrete grid can be written as

$$\Psi(t+\Delta t) = \exp(-i\overline{H}\Delta t/\hbar)\sum_{n=0}^{\infty}(2-\delta_{n0})J_n(\alpha)\Phi_n(-i\hat{H}_{norm})\Psi(t). \tag{2.102}$$

The number of terms required in the above summation is estimated from the time-energy space volume α. CP scheme shows the good convergence for the larger number of recursion terms and for $n > \alpha$.

The instability of CP scheme becomes unstable in presence of a NIP. Mowrey *et al.* [194] noticed that this instability is caused by adding NIP to the global potential. Following to this observation, Mandershtam and Taylor [184] have made a simple analytic continuation of the CPs by using the exponential damping factor in the definition of CP without disturbing the Hamiltonian and keeping the properties of CP scheme

unaltered. They renormalized the Hamiltonian including a NIP, defining

$$\hat{U}(t) = \sum_{n=0}^{N} a_n(t) Q_n(\hat{H}_{norm;\hat{\gamma}}) \tag{2.103}$$

$$\text{where, } a_n(t) = (-1)^n (2 - \delta_{n0}) J_n(\Delta E t/\hbar) \exp(-i\overline{H}t/\hbar)) \tag{2.104}$$

$$\overline{H} = \frac{E_{max} + E_{min}}{2} - iV_0, \tag{2.105}$$

with $Q_n(\hat{H}_{norm;\hat{\gamma}})$ satisfying the recursion relation:

$$\exp(-\hat{\gamma}) Q_{n-1} + \exp(\hat{\gamma}) Q_{n+1} = 2\hat{H}_{norm} Q_n \tag{2.106}$$

where, $Q_0 = \hat{I};\ Q_1 = \exp(-\hat{\gamma})\hat{H}_{norm}$, and the operator γ is dimensionless and it defines the damping factor which has a value zero at the strong interaction region and rises to a maximum value at the asymptotic region.

2.6 Reactive Scattering Dynamics

2.6.1 Preparation of Initial Wave Packet and Propagation

The first step in the treatment of a reactive scattering problem involves the preparation of the initial WP appropriate to the reactants. In the immediate next step, this WP is propagated on the potential energy hypersurface using the methodology described above and finally, the propagated WP is analyzed in the product region of the PES to calculate the reaction attributes viz., the reaction probability, cross section and rate constant. Neuhauser and Baer have developed the strategy of dividing the configuration space into three regions consisting of (1) reagent channel, (2) interaction region, and (3) product channel. The initial vibrational-rotational state-selected and energy resolved reaction probabilities, $P^R_{vj}(E)$, have been calculated by computing the energy resolved flux of the WP across a dividing surface in the product channel.

In scattering studies, the initial WP is located in the asymptotic reactant channel (far away from the interaction region) where there is no influence of the interaction potential. Under such circumstances, the initial WP can be written as a product of the Gaussian WP (GWP) for the translational motion along R, $F(R)$, the rovibrational eigenfunction of the diatomic molecule, $\phi_{vj}(r)$, and $\mathcal{L}^2$-normalized associated Legendre polynomial $\tilde{P}_j^K(\cos\gamma)$ to describe the motion along the approach angle γ,

$$|\Psi_K^J(R, r, \gamma, t = 0)\rangle = F(R)\phi_{vj}(r)\tilde{P}_j^K(\cos\gamma). \tag{2.107}$$

The translational motion is best described by a minimum uncertainty GWP for $F(R)$ which is centered at R_0, (far away from the interaction region)

$$F(R) = \left(\frac{1}{2\pi\delta^2}\right)^{\frac{1}{4}} \exp\left[-\frac{(R - R_0)^2}{4\delta^2} - ik_0(R - R_0)\right]. \tag{2.108}$$

Here, δ_0 is the width of the GWP, R_0 and k_0 represents the location of its maximum in the coordinate and momentum space, respectively. This GWP is carefully chosen to ensure that the translational motion is properly represented over the entire energy range under investigation.

The rovibrational eigenfunction $\phi_{vj}(r)$ corresponding to a vibrational v, and rotational j states of the reagent diatom is obtained by solving the eigenvalue equation using the sine-DVR approach [see Eq. (2.45)]. This eigenfunction can also be computed by a Fourier grid Hamiltonian method [188, 189]. The $\mathcal{L}^2$-normalized associated Legendre polynomials are given by

$$\tilde{P}_j^K(\cos\gamma) = \sqrt{\frac{2j+1}{2}\frac{(j-K)!}{(j+K)!}} P_j^K(\cos\gamma) \tag{2.109}$$

which are the eigenfunctions of the $\hat{j}^2$ operator.

The coordinate grid consists of equally spaced points R_l and r_m along the Jacobi distances R and r, respectively. The initial wavefunction at each node (R_l, r_m, γ_n) of this grid is given by

$$|\Psi_K^J(R_l, r_m, \gamma_n, t=0)\rangle = |\Psi_{lmn}\rangle = \sqrt{w_n} F(R_l)\phi_{vj}(r_m)\tilde{P}_j^K(\cos\gamma_n). \tag{2.110}$$

The propagation of the WP is carried out by using the schemes described above. For example, in the present application the spatial propagation of the WP along the Jacobi distances R and r is carried out by the FFT method and along the Jacobi angle γ is carried out by the Gauss-Legendre DVR method. The time propagation of the WP is carried out by the second order SO method [172] or the CP scheme [183].

2.6.2 Final Analysis

2.6.2.1 Calculation of Reaction Probability

The initial state-selected and energy resolved reaction probability is calculated from the expectation value of the quantum flux operator, $\hat{F}$, in the basis of the energy normalized reactive scattering wavefunction

$$P_i^{JK}(E) = \sum_f |S_{fi}^{JK}|^2 = \langle\Phi(R, r, \gamma, E)|\hat{F}|\Phi(R, r, \gamma, E)\rangle|_{r=r_d}, \tag{2.111}$$

where, S_{fi}^{JK} is the reactive scattering matrix from an initial state i of the reactant to a final state f of the product. The flux operator $\hat{F}$ in terms of a dividing surface (at $r = r_d$ in the product arrangement) can be given as [161, 195, 196]

$$\hat{F} = -\frac{i\hbar}{2\mu}\left[\frac{\partial}{\partial r}\delta(r - r_d) + \delta(r - r_d)\frac{\partial}{\partial r}\right]. \tag{2.112}$$

With this the reaction probability in Eq. (2.113), is expressed as

$$P_i^{JK}(E) = \frac{\hbar}{\mu}\mathrm{Im}\left[\langle\Phi(R, r_d, \gamma, E)|\frac{\partial\Phi(R, r_d, \gamma, E)}{\partial r}\rangle\right]. \tag{2.113}$$

The quantity in the RHS of above equation is integrated over the entire range of R and γ. The quantity E is the total energy (relative translational + ro-vibrational) and μ is the three-body mass scaled reduced mass of the collisional system. The energy normalized time-independent reactive scattering wavefunction is calculated along the dividing surface at $r = r_d$ as

$$|\Phi(R, r_d, \gamma, E)\rangle = |\psi(R, r_d, \gamma, E)\rangle/\kappa_E. \tag{2.114}$$

The function $\psi(R, r_d, \gamma, E)$ is obtained by Fourier transforming the time-evolved WP, $\Psi(R, r, \gamma, t)$ along the dividing surface

$$\psi(R, r_d, \gamma, E) = \frac{1}{\sqrt{2\pi}} \int_{-\infty}^{+\infty} \Psi(R, r, \gamma, t) e^{iEt/\hbar} dt|_{r=r_d}. \tag{2.115}$$

The quantity κ_E in Eq. (2.114), is the weight of the translational energy component contained in the initial WP for a given total energy E:

$$\kappa_E = \left(\frac{\mu}{2\pi\hbar k_{vj}}\right)^{1/2} \int_{-\infty}^{+\infty} F(R) e^{ikR} dR, \tag{2.116}$$

$$= \left(\frac{\mu}{2\pi\hbar k_{vj}}\right)^{1/2} F(k). \tag{2.117}$$

where

$$k_{vj} = \sqrt{2\mu(E - \epsilon_{vj})}/\hbar, \tag{2.118}$$

with ϵ_{vj} being the initial rovibrational energy of the diatomic molecule. $F(k)$ is the translational GWP in momentum space centered at k_0. The factor $(\mu/\hbar k)^{1/2}$ in the above equation accounts for the energy normalization of $\Psi(R, r, \gamma, E)$. After some algebra, the energy dependent reaction probability is given by

$$P_{vj}^{JK}(E) = \left(\frac{\hbar^2 k}{\mu^2 |F(k)|^2}\right) \mathrm{Im}\left[\langle \Phi(R, r_d, \gamma, E)| \frac{\partial \Phi(R, r_d, \gamma, E)}{\partial r} \rangle\right]. \tag{2.119}$$

In A+BC collisions the reactive flux flowing into a specific reaction channel (AB+C

or AC +B) is estimated by comparing the internuclear distances of the product AB and AC molecules. The reactive flux in which the AB distance is smaller than the AC distance is considered to represent the (AB+C) channel and the rest is considered to represent the (AC+B) channel [197]. Finally, the channel specific reaction probabilities are obtained by integrating the flux in the respective channel.

The function $\Phi(R, r_d, \gamma, E)$ and its derivative with respect to r at the dividing surface can be computed as follows:

$$\Phi(R, r_d, \gamma, E) = \frac{\Delta E}{\sqrt{2\pi}} \sum_{n=0}^{\infty} \Phi(R, r, \gamma, n\Delta t) e^{iE_n \Delta t/\hbar}|_{r=r_d} \tag{2.120}$$

$$\frac{\partial \Phi(R, r_d, \gamma, E)}{\partial r}|_{r=r_d} = \frac{\Delta E}{\sqrt{2\pi}} \sum_{n=0}^{\infty} \frac{\partial \Phi(R, r, \gamma, n\Delta t)}{\partial r} e^{iE_n \Delta t/\hbar}|_{r=r_d} \tag{2.121}$$

Once the contribution from each time step are added to the values from previous step, the time evolved WP is damped out with the help of a masking function or a NIP.

2.6.2.2 Calculation of Integral Reaction Cross Section and Thermal Rate Constant

The integral reaction cross section is theoretically calculated by summing up all the partial-wave contributions of J to the reaction probability. This is given by

$$\sigma_{vj}(E) = \frac{\pi}{k_{vj}^2} N_{vj}(E). \tag{2.122}$$

Here, k_{vj} is the wave vector given in Eq. (2.118) with the initial rovibrational energy of the diatomic molecule, ϵ_{vj}. The quantity N_{vj} represents the cumulative reaction probability (CRP) for a specified initial (v, j) state and is given by

$$N_{vj}(E) = \sum_{K=0}^{j} \frac{g_K}{(2j+1)} \sum_{J \geq K}^{J_{max}} (2J+1) P_{vj}^{JK}(E), \tag{2.123}$$

where g_K is the degeneracy factor and will have the value 1 for $K = 0$ and 2 for $K \neq 0$. To calculate the reaction cross section for a given collision energy one needs to carry out the WP calculations for all contributing nonzero values of J. In case of higher J values one may need to extend the grid along R and locate the initial WP further out in the asymptotic reagent channel in order to avoid any overlap with the slowly decaying centrifugal potential. Alternatively, one may also use an adiabatic correction scheme as proposed by Meyer and coworkers [162].

The initial state-selected thermal rate constant can be calculated from the CRP as [131, 134]

$$k(T) = (2\pi\hbar Q_R(T))^{-1} \int_{-\infty}^{+\infty} dE e^{-E/k_B T} N_{vj}(E), \tag{2.124}$$

the quantity $Q_R(T)$ in the above equation defines the reagent (A+BC) partition function [198], can be expanded as

$$Q_R(T) = Q_{ele} Q_{tr} Q_{vib} Q_{rot} \tag{2.125}$$

In the present case

$$\begin{aligned} Q_{ele} &= 1, && \text{(2.126a)} \\ Q_{tr} &= \left(\frac{2\pi m k_B T}{\hbar^2}\right)^{3/2}, && \text{(2.126b)} \\ Q_{vib} &= \frac{1}{1 - \exp(\frac{h\nu}{k_B T})}, && \text{(2.126c)} \\ Q_{rot} &= \sum_{j}^{\infty} (2j+1) \exp(-j(j+1)B/k_B T). && \text{(2.126d)} \end{aligned}$$

are the electronic, translational, vibrational and rotational partition functions, respectively. k_B being the Boltzmann constant. At high temperatures, Eq. (2.126c) and Eq. (2.126d) becomes $Q_{vib} = \frac{k_B T}{h\nu}$ and $Q_{rot} = \frac{8\pi^2 I_{BC} k_B T}{\hbar^2}$.

2.6.3 J-Shifting (JS) Approximations

One of the most important and simple approximation to calculate the reaction cross section and thermal rate constant is the J-shifting (JS) approximation. This approximation is computationally cheaper when compared to the rigorous/accurate quantum dynamics calculations for $J \neq 0$. The $J \neq 0$ reaction probabilities are approximated by simply shifting the collision energy in the reaction probability for $J = 0$, as follows

$$P_{vj}^{J}(E) \approx P_{vj}^{J=0}(E - E_J^{\ddagger}), \quad J = 0, 1, 2, \ldots, J_{max}, \tag{2.127}$$

where, $E_J^{\ddagger}$ is the triatomic (ABC) rotational energy at the transition state (TS). $B^{\ddagger}$ is the rotational constant of the collision complex at the TS. These are given by

$$E_J^{\ddagger} = B^{\ddagger} J(J+1) \tag{2.128}$$

$$B^{\ddagger} = \frac{\hbar}{4\pi I c}. \tag{2.129}$$

The bottleneck of the JS approximation lies in the extraction of a reasonable value of $B^{\ddagger}$ for the TS species at a given temperature T.

In the standard JS approach [95], the rotational constant B is treated as a fixed quantity, whereas in the uniform JS approach B is optimizing at a given temperature and for a range of J values. In case of the standard JS approach, thermal rate constant can be rewritten as

$$k_s(T) = \frac{Q_{rot}^{\ddagger}(T)}{2\pi\hbar Q_R(T)} \int_0^{\infty} dE e^{-E/k_B T} P_{vj}^{J=0}(E) \tag{2.130}$$

where,

$$Q_{rot}^{\ddagger}(T) = \sum_J (2J+1) \exp(-BJ(J+1)/k_B T), \tag{2.131}$$

is the rotational partition function of the collision complex at the TS and $Q_R(T)$ is the total partition function of the TS species (cf. Eq. (2.125)).

In this case the final rate constant results often suffer from numerical uncertainties because the temperature and also J dependence of B is not included in the model. Following to Mielke and coworkers work [96], Zhang and Zhang [97] proposed a modified JS approach, called the uniform JS, whereby the constant B is uniquely determined through an optimization procedure at a given temperature. In this case the reaction probability for a few non-zero values of J are calculated by accurate quantum dynamical method. The optimized value of B at a given temperature T for a range of J values is extracted from these accurate probability functions, given as

$$B_i(T) = \frac{k_B T}{J_{i+1}(J_{i+1}+1) - J_i(J_i+1)} ln(Q^{J_i}/Q^{J_{i+1}}),\ (i = 1, 2, ...). \tag{2.132}$$

In the above equation, the temperature dependent rotational constant also called the *shifting constant* can be written in a simple form [96, 97]

$$B(T) = \frac{k_B T}{J(J+1)} ln(Q^0/Q^J), \tag{2.133}$$

where, Q^0 and Q^J are the partition-like functions defined as

$$Q^J = \int P^J(E) e^{-E/k_B T} dE. \tag{2.134}$$

In the uniform JS approach [96, 97], the shifting constant $B(T)$, is extracted to calculate the thermal rate constant from the accurate probability functions, $P^J(E)$. In this case the rate constant is given by

$$k_u(T) = \frac{Q^0(T)}{2\pi\hbar Q_R(T)} \sum_J (2J+1) \exp(-B(T)J(J+1)/k_B T). \tag{2.135}$$

The J- and K-shifting can also be used to estimate the initial state-resolved reaction cross sections. In addition to the energy shift approximation, the harmonic, adiabatic-bend, and bend-energy shift approximations (called as collinear exact quantum bend (CEQB)) are also used to calculate the reaction probabilities $P_{vj}^{JK}(E)$ with $K \neq 0$

[95, 199, 200]. As we mentioned earlier, many versions of the JS approach [95–97, 201–203] are proposed in the literature and have been successfully applied to a wide variety of bimolecular collisions [204–209]. In the present work, we applied both the standard [95] and the uniform [97] JS approximations, to calculate the temperature dependent rate constants. In order to assess the accuracy of these approximations, more involved quantum scattering calculations within the CS and CC models are performed [48, 51, 125, 129, 204].

Chapter 3

H+HLi Scattering for the total angular momentum $J = 0$: Reaction Probability

3.1 Introduction

The available literature on the experimental and theoretical studies on the lithium-hydrogen reactions are reviewed in Chapter 1. In this chapter, we concentrate on the study of H+HLi reaction for the total angular momentum $J = 0$. A TDWP method (as discussed in Chapter 2) is employed to calculate the energy resolved reaction probabilities.

We report here, the initial state-selected and energy resolved channel specific reaction probability of H+HLi collisions in three-dimensions for the total angular momentum, $J = 0$. The DMJ PES [91] of the H+HLi reaction is employed for the purpose. In addition to reporting the three-dimensional reaction probabilities, we have also shown the results obtained for the HLi depletion path for the collinear configurations of the system, in order to check the consistencies of the present results with those of Clarke

et al. [90]. Furthermore, these calculations for the collinear arrangements enable us to optimize the grid parameters more carefully for this reaction, which proceeds on a steep down-hill path. Apart from these, it can also be seen that the collinear results have no real significance when compared with the three-dimensional results. The sharp resonance features seen at the onset of the collinear reaction survive in the three-dimensional results. The channel specific reaction probabilities show a preference of the reactive path R2 over R1 in H+HLi collision dynamics for any given energy. Finally, the effect of the rotational and vibrational excitation of the reagent LiH molecule on the reaction dynamics is discussed.

3.2 Methodology and Computational Details

The time-dependent WP approach to treat the reactive scattering dynamics is discussed in Chapter 2. For $J = 0$, the Hamiltonian of Eq. (2.32) reduces to

$$\hat{H} = -\frac{\hbar^2}{2\mu}\left[\frac{\partial^2}{\partial R^2} + \frac{\partial^2}{\partial r^2}\right] + \frac{\boldsymbol{j}^2}{2I} + V(R, r, \gamma). \tag{3.1}$$

For the H+HLi scattering, $\mu = \sqrt{m_{\rm H}^2 m_{\rm Li}/(2m_{\rm H} + m_{\rm Li})}$, ($m_{\rm H}$ and $m_{\rm Li}$ are the masses of H and Li, respectively) is the three-body reduced mass and $I = \mu R^2 r^2/(R^2 + r^2)$. The DMJ PES of the H+HLi collision system is used for $V(R, r, \gamma)$ [91].

The initial wavefunction $|\Psi(t = 0)\rangle$ of the H+HLi reacting system at time, $t = 0$, is prepared in the asymptotic reactant channel (i.e. $R \to \infty$) where there is no influence of the interaction potential. This wavefunction is taken as the product of the H-HLi translational wavefunction and HLi ro-vibrational wavefunction as illustrated in Sec. 2.6.1. This initial wavefunction at each node of an equally spaced potential grid points along the three Jacobi coordinates R_l, r_m and γ_n (the Jacobi angle is chosen as the

node of a n-point GLQ), for $J = 0$ is represented as

$$|\Psi(R_l, r_m, \gamma_n, t = 0)\rangle = |\Psi_{lmn}\rangle = \sqrt{w_n} F(R_l)\phi_{vj}(r_m)\sqrt{\frac{2j+1}{2}} P_j(\cos\gamma_n), \tag{3.2}$$

where, w_n is the weight of the GLQ associated with the grid point n. The functions, $\phi_{vj}(r)$, along with the normalized Legendre polynomials ($P_j(\cos\gamma)$) represent the rovibrational eigenfunction corresponding to a vibrational v and rotational j state of the HLi molecule, and these are obtained by solving the eigenvalue equation for the free HLi molecule. We used the sine-DVR approach, which is discussed in Sec. 2.5.2.4 [130], to solve the eigenvalue equation of the HLi molecule (cf. Eq. (2.45)). The potential energy of the free HLi molecule, $V(r')$, is obtained from the DMJ PES [91] by setting $R \to \infty$.

We have used the SO propagation method to calculate the action of the time-evolution operator, $\exp[-i\hat{H}t/\hbar]$, on the wavefunction. This is accomplished by dividing the total propagation time t into N steps of length Δt. The exponential operator at each time step Δt is more specifically splitted as [172]

$$\begin{aligned} \exp\left[\frac{-i\hat{H}\Delta t}{\hbar}\right] &= \exp\left[\frac{-i\hat{V}\Delta t}{2\hbar}\right]\exp\left[\frac{-i\boldsymbol{j}^2\Delta t}{4I\hbar}\right]\exp\left[\frac{-i\hat{T}\Delta t}{\hbar}\right] \\ &\quad \times\exp\left[\frac{-i\boldsymbol{j}^2\Delta t}{4I\hbar}\right]\exp\left[\frac{-i\hat{V}\Delta t}{2\hbar}\right] + O[(\Delta t)^3], \end{aligned} \tag{3.3}$$

where, T represents the total radial kinetic energy operator along the Jacobi coordinates R and r. Equation (3.3) is used in conjunction with the FFT method [112], to evaluate the action of the exponential containing the radial kinetic energy operator and the DVR method [117, 125, 127–129], to evaluate the action of the exponential containing the rotational kinetic energy operator ($\boldsymbol{j}^2/4I$) on the wavefunction.

The action of the rotational kinetic energy operator is carried out by transforming

the DVR wavefunction, $|\Psi_{lmn}\rangle$, [Eq. (3.2)] to the angular momentum space (FBR), multiplying it by the diagonal value of the operator ($e^{-ij(j+1)\Delta t\hbar/4I}$), and transforming it back to the DVR representation. Numerically this is accomplished in a single step [117, 128]:

$$\exp\left[\frac{-i\boldsymbol{j}^2\Delta t}{4I\hbar}\right]|\Psi_{lmn'}\rangle = \sum_n \left\{\sum_j \boldsymbol{T}^{\dagger}_{n',j} e^{-ij(j+1)\Delta t\hbar/4I}\boldsymbol{T}_{j,n}\right\}|\Psi_{lmn}\rangle, \tag{3.4}$$

where, j is the rotational quantum number of the HLi molecule. The coefficients $\boldsymbol{T}_{j,n}$ are the elements of the DVR-FBR transformation matrix, constructed in terms of Legendre polynomials (eigenfunctions of the $\boldsymbol{j}^2$ operator for $\boldsymbol{J}=0$) [117, 125, 129]:

$$\boldsymbol{T}_{j,n} = \sqrt{w(n)}\sqrt{\frac{2j+1}{2}}P_j(\cos\gamma_n), \tag{3.5}$$

and $\boldsymbol{T}^{\dagger}_{n,j}$ are the elements of the inverse transformation matrix, i.e., the Hermitian conjugate to $\boldsymbol{T}_{j,n}$.

Once the TDSE (Eq. (2.2)) is solved the initial state i (vj state of reactant HLi molecule) selected and energy resolved reaction probability is calculated from the expectation value of the flux operator $\hat{F}$ as discussed in Sec. 2.6.2.1.

In dynamical studies involving scattering systems, as the WP moves forward in time, its fast moving components approach the grid boundaries and are no longer relevant for the rest of the dynamics [113]. Therefore, to avoid unphysical reflections or wrap around of these components from the boundaries of a finite sized grid, the WP at each time step is multiplied by a damping function [114]

$$f(X_i) = \sin\left[\frac{\pi}{2}\frac{(X_{mask}+\Delta X_{mask}-X_i)}{\Delta X_{mask}}\right], \qquad X_i \geq X_{mask} \tag{3.6}$$

which is activated outside the dividing line in the product channel and also in the

Table 3.1: Numerical grid parameters and properties of the initial wavefunction used in the calculations of reaction probabilities.

Parameter	Value	Description
$N_R/N_r/N_\gamma$	128/64/64	Number of grid points
R_{min}/R_{max} (a_0)	1.0/18.78	Extension of the grid along R
r_{min}/r_{max} (a_0)	1.0/8.56	Extension of the grid along r
$\Delta R/\Delta r$ (a_0)	0.14/0.12	Grid spacings along R and r respectively
r_I (a_0)	5.44	Location of the dividing surface in the product channel
R_{mask}/r_{mask} (a_0)	14.72/5.8	Starting point of the masking function
R_0 (a_0)	12.0	Initial location of the center of the GWP in the coordinate space
V_{cut} (eV)	4.0	Maximum potential energy cut-off
δ (a_0)	0.3	Initial width parameter of the GWP
Δt (fs)	0.1347	Length of the time step used in the WP propagation
T (fs)	413.76	Total propagation time

asymptotic reactant channel. X_{mask} is the point at which the damping function is initiated and $\Delta X_{mask}(= X_{max} - X_{mask})$ is the width of X over which the function decays from 1 to 0, with X_{max} being the maximum value of X in that direction, in a particular channel.

The properties of the initial WP and the grid parameters used for the numerical calculations are listed in Table 3.1. The properties of the DMJ PES [91] of H+HLi reaction are discussed in Sec. 3.3.1. The dynamical calculations are carried out using these grid parameters and the convergence of the results is explicitly checked by varying them. The reaction probabilities are calculated at an energy interval of 0.005 eV and the most probable collision energy of 0.55 eV. The energy distribution of the initial GWP is shown in Fig. 3.6. The total energy E is measured relative to the minimum of the HLi potential. The WP is time evolved for a total of 413.76 fs and the norm ($\langle\Psi|\Psi\rangle$) of the WP goes down to 9.17×10^{-3} at the end of the time evolution.

3.3 Results and Discussion

3.3.1 Topography of the PES

In the following we used the analytical DMJ PES [91] to calculate the channel specific (R1 and R2) reaction probabilities of the H+HLi reaction. Dunne *et al.* [91] have derived this PES by fitting the *ab initio* (including configuration interaction, employing a double-zeta basis set) calculated potential energy values to a many-body expansion function in the following way. The two-body terms appearing in this expansion were fitted to the extended Rydberg function with parameters derived from the spectroscopic data on LiH($X,^1\Sigma^+$) and $H_2(X,^1\Sigma_g^+)$, in order to impose the correct dissociation limits of these diatomic species and to reproduce the experimental exothermicity of the reaction R1 [210]. The three-body energies were obtained by subtracting the atomic terms and the two-body potential energies from the calculated *ab initio* energies and were fitted to an analytical equation of the form [91]

$$V(R_1,R_2,R_3) = V_{AB}^{(2)}(R_1) + V_{BC}^{(2)}(R_2) + V_{CA}^{(2)}(R_3) + V_{ABC}^{(3)}(R_1,R_2,R_3), \tag{3.7}$$

where,

$$V^{(2)} = -D_e(1 + a_1\rho + a_2\rho^2 + a_3\rho^3)\exp(-a_1\rho), \tag{3.8}$$

$$V^{(3)} = V_0\left[1 + \sum_{ijk} C_{ijk}(S_1)^i(S_2)^j(S_3)^k\right]\left[1 - \tanh(\gamma_1 S_1/2 + \gamma_3 S_3/2)\right]. \tag{3.9}$$

Here, $S_1 = R_1 + R_2 - 2R^0_{\mathrm{LiH}}$; $S_2 = R_1 - R_2$ and $S_3 = R_3 - R^0_{\mathrm{HH}}$ (with R_1 and R_2 representing two LiH distances and R_3 the HH distance). The parameters in the above function were obtained by the authors [91] using a least-square fit with 21 coefficients (C_{ijk}) to represent the PES in the entire configuration range satisfactorily.

In order to demonstrate the microscopic details of the dynamics of R1 and R2, we briefly discuss on the salient features of the above PES. In Fig. 3.1 we show the mini-

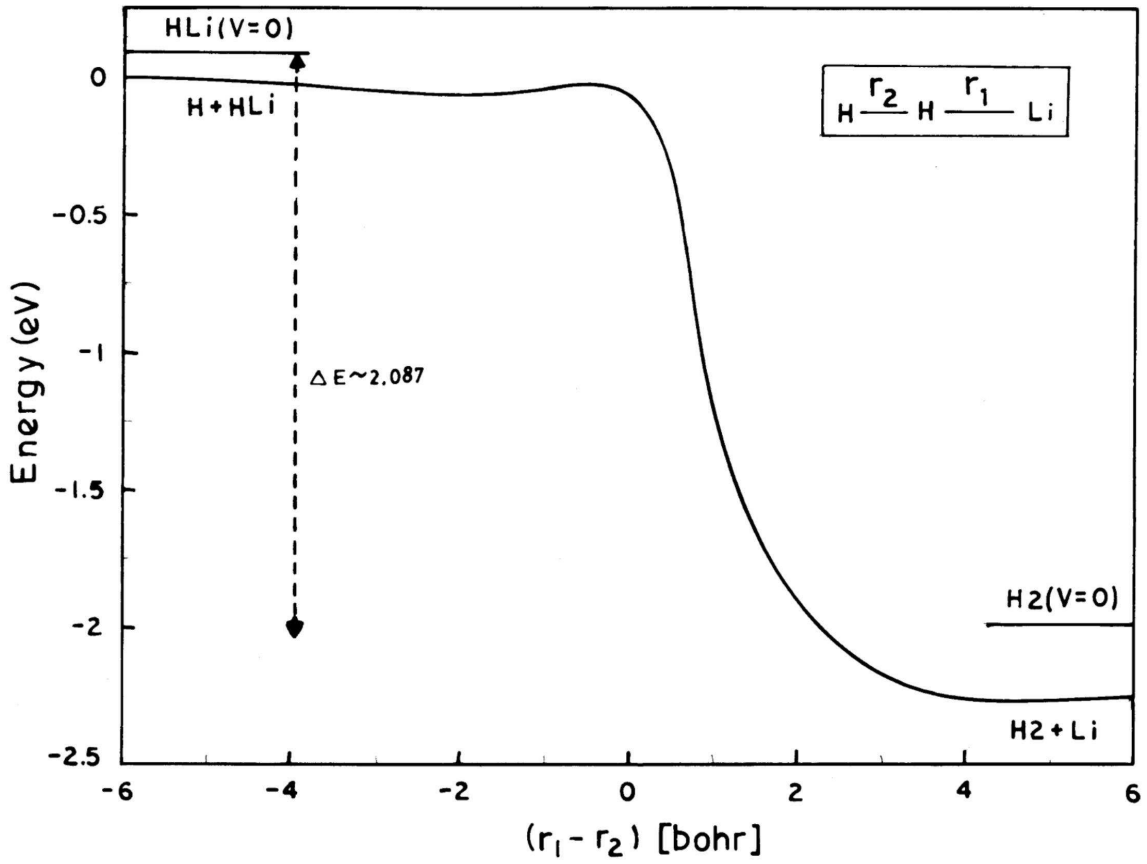

Figure 3.1: The minimum energy path for the H + HLi $\rightarrow$ H_2 + Li depletion reaction for the collinear approach. Energy is measured relative to the minimum of HLi potential. The zero point vibrational energies of the reactant HLi and the product H_2 molecules are indicated in the figure. The magnitude of the reaction exothermicity is $\sim$ 2.09 eV. The height of the diffuse barrier-like structure occurring for nearly equal LiH and HH distances is $\sim$ -0.028 eV.

mum energy path for the depletion reaction (R1) for the collinear configuration. The zero of the energy scale corresponds to the minimum of the LiH potential occurring for $R \rightarrow \infty$ in the reactant channel. The zero-point vibrational level of the reactant LiH as well as the product H_2 is also shown in the figure. The highly exothermic nature of the depletion reaction leading to Li + H_2 formation is clearly revealed by Fig. 3.1. The reaction exothermicity is $\sim$ 2.09 eV including the zero-point energy (ZPE) corrections. The height of the diffuse barrier-like structure apparently occurring for nearly equal HH and LiH distances is $\sim$ -0.028 eV [101].

The contour level diagrams of the above PES in the (R, r) plane are shown in Fig. 3.2 for $\gamma = 0$, and in Fig. 3.3 for various values of γ (indicated in each panel). The steep decrease in the potential energy while going from the reagent to the product channel revealing the attractive nature observed from the contour plots. For $\gamma \leq 90^\circ$ the equilibrium LiH (reactant) distance is smaller in small-R region than in the large-R region, which indicates a weak excitation of LiH vibration in the interaction region and hence low reaction probability to both the R1 and R2 channels. The topography of the PES for $\gamma \geq 90^\circ$, however indicates a relatively large vibrational excitation of the reactant LiH in the interaction region and hence high probability for the reactions to take place. Therefore, it is expected that the non-collinear collisions may make significant contribution to the reaction dynamics of H+HLi.

This view is further supported by investigating the cuts of the above PES along the Jacobi angle γ for fixed values of R and keeping the reactant LiH molecule at its equilibrium configuration. Such cuts are shown in Fig. 3.4. The meaning of different line types is indicated in the panel. It can be seen from Fig. 3.4 that at smaller values of the Jacobi distance R the potential exhibits an asymmetric double-well shape. This asymmetry results from the asymmetric nature of the reactant LiH molecule. The collisions at the bent geometry (near C_{2v}) of LiH_2 seem to be more favorable at small values of R. Therefore, an insertion type of mechanism appears to be more likely at such

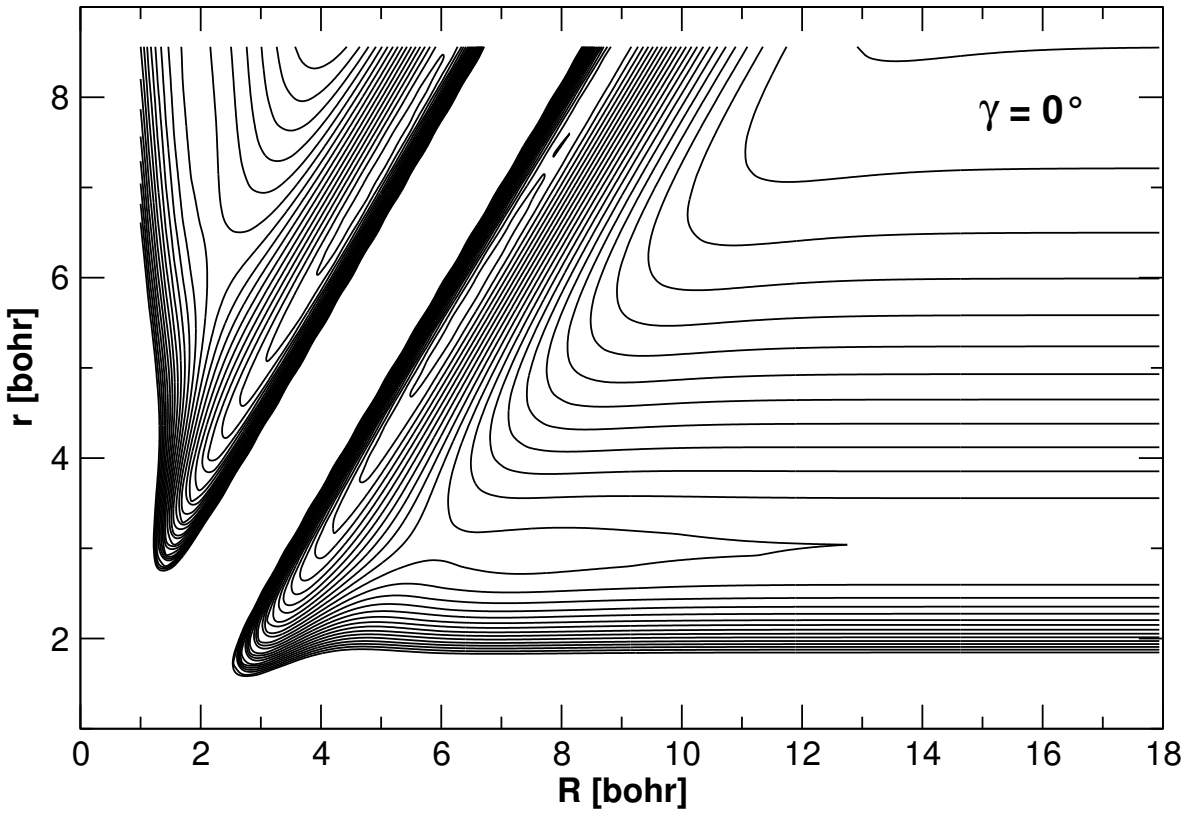

Figure 3.2: Potential energy contour diagram of the DMJ PES of the H+HLi system, plotted in the (R, r) plane for $\gamma = 0°$. The minimum of the contour occurs at -2.281 eV and the spacing between the successive contour lines is 0.2 eV. The zero of the energy corresponds to $R \to \infty$.

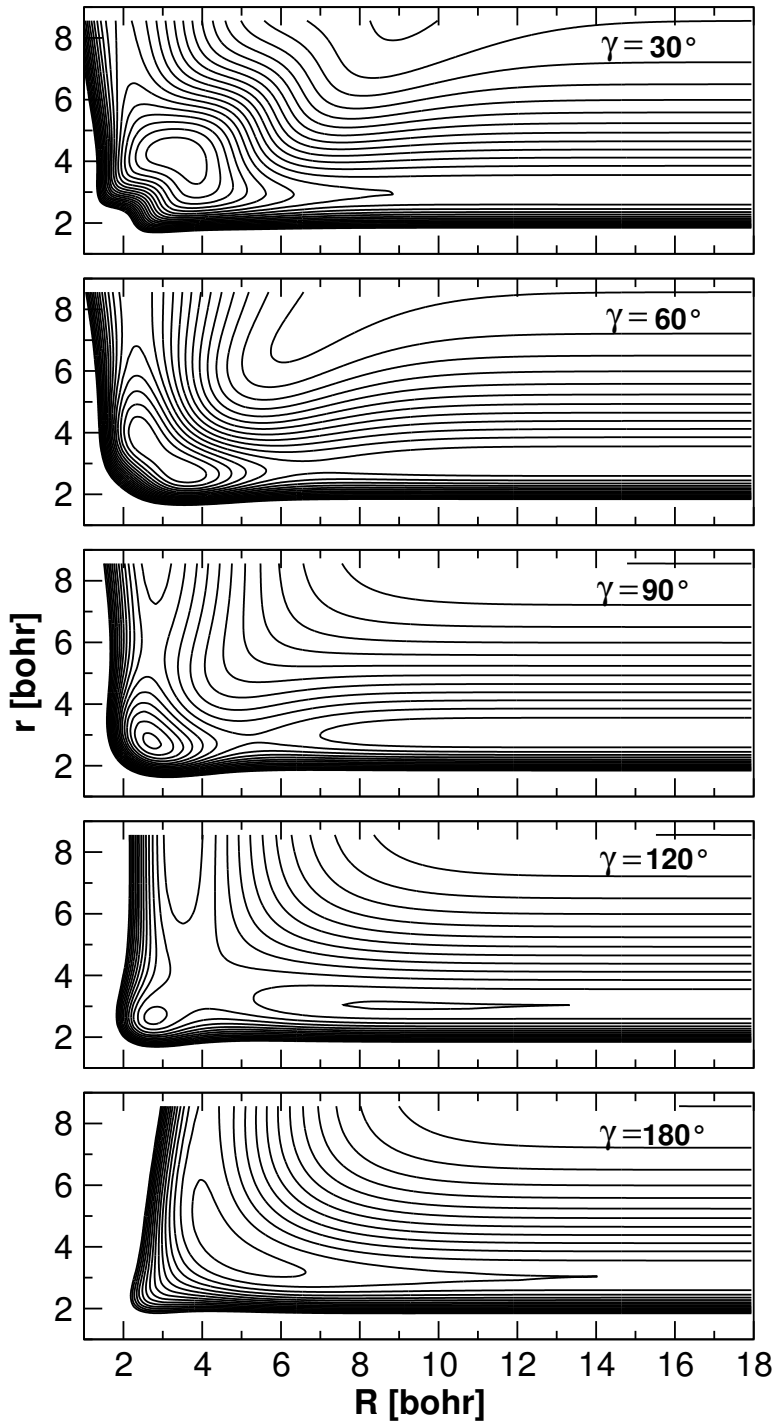

Figure 3.3: Contour line diagrams of the DMJ PES plotted in the (R, r) plane and for other values of γ indicated in the respective panel. The spacing between the successive contour lines is 0.2 eV and the minimum of the contour occurs at -1.363 eV, -0.991 eV, -0.866 eV, -0.0136 eV and -0.275 eV for $\gamma = 30°$, $60°$, $90°$, $120°$ and $180°$, respectively.

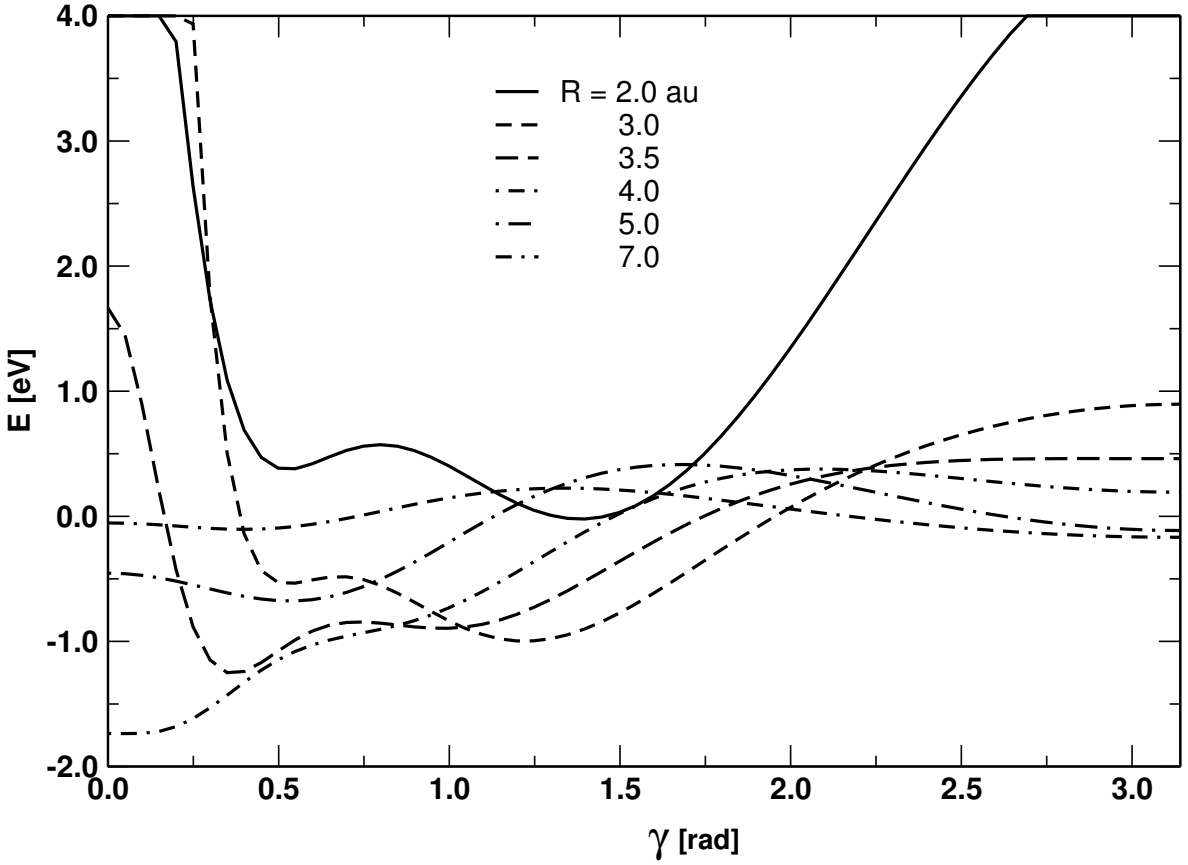

Figure 3.4: One-dimensional cuts of the DMJ PES along the H-HLi approach angle γ and for various values of R, indicated in the panel. The value of r is fixed at 3.015 a_0 corresponding to the equilibrium internuclear distance of the LiH molecule.

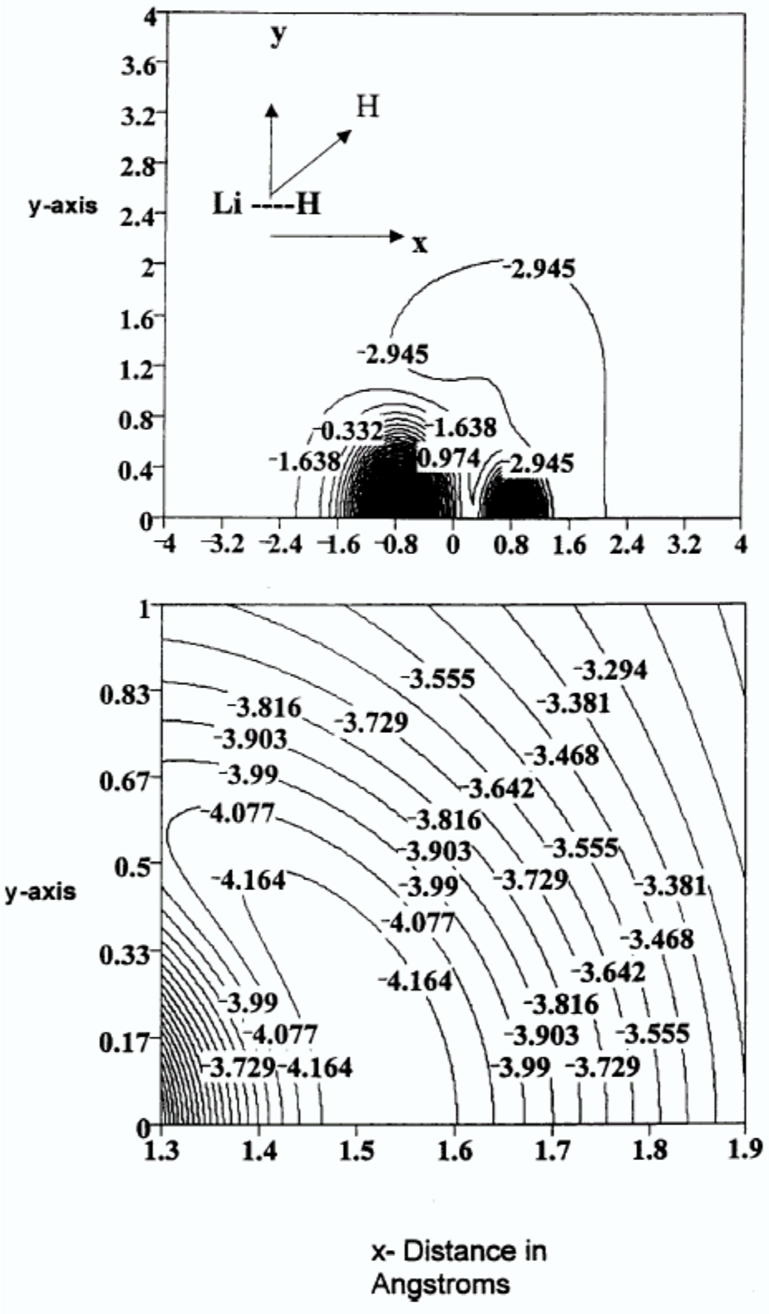

Figure 3.5: Contours of potential energy for a H atom moving around LiH at the equilibrium distance. The lower figure shows a 'blow up'of the lowest energy part of the surface. [Reproduced from Fig. 2 of Ref. [91]]

geometries. With increase in the approach distance R the well at the bent geometry transforms into a small barrier and the collisions at near collinear geometry appear to be more favorable. The polar plot presented in Fig. 3.5 [reproduced from Ref. [91]] clearly reveals a narrow "approach cone" for the H-abstraction from LiH by the incoming H atom, as a result of the steric hindrance caused by the relatively bulky Li atom [3].

3.3.2 Collinear Reaction Dynamics

The approach of the incoming H atom to the H end of the reactant LiH molecule is considered in the collinear model and the dynamical calculations are mathematically constrained to the (R, r) plane. In this configuration the depletion path (R1) is the only reactive channel and the dynamics takes place on the steep down-hill PES (cf. Fig. 3.1 and Fig. 3.2).

The total reaction probability for H + HLi($v = 0$) $\rightarrow$ $H_2(\Sigma v')$ + Li, for an initial most probable collision energy of 0.55 eV as a function of the total energy E (H-HLi translational + HLi vibrational) is shown in Fig. 3.7. It can be seen from Fig. 3.7 that the onset of the reaction occurs nearly at the ZPE ($\sim$ 0.087 eV) of HLi molecule indicating a zero reaction threshold and hence the absence of any barrier in the underlying PES. The pronounced oscillations in the reaction probability curve at low energies reveal the formation of resonances during the course of the reaction at these energies. These resonances correspond to the metastable excited vibrational levels of LiH_2. The resonance structures are less pronounced in the high energy part (>0.9 eV) of the reaction probability curve. Therefore, at high energies the collisions become more direct leading to the formation of the product. The main features of the above results are in fairly good agreement with the classical and quantum mechanical findings of Clarke *et al.* [90]. The remaining quantitative differences between the two may be attributed to the differences in the potential energy surfaces used in the two calculations.

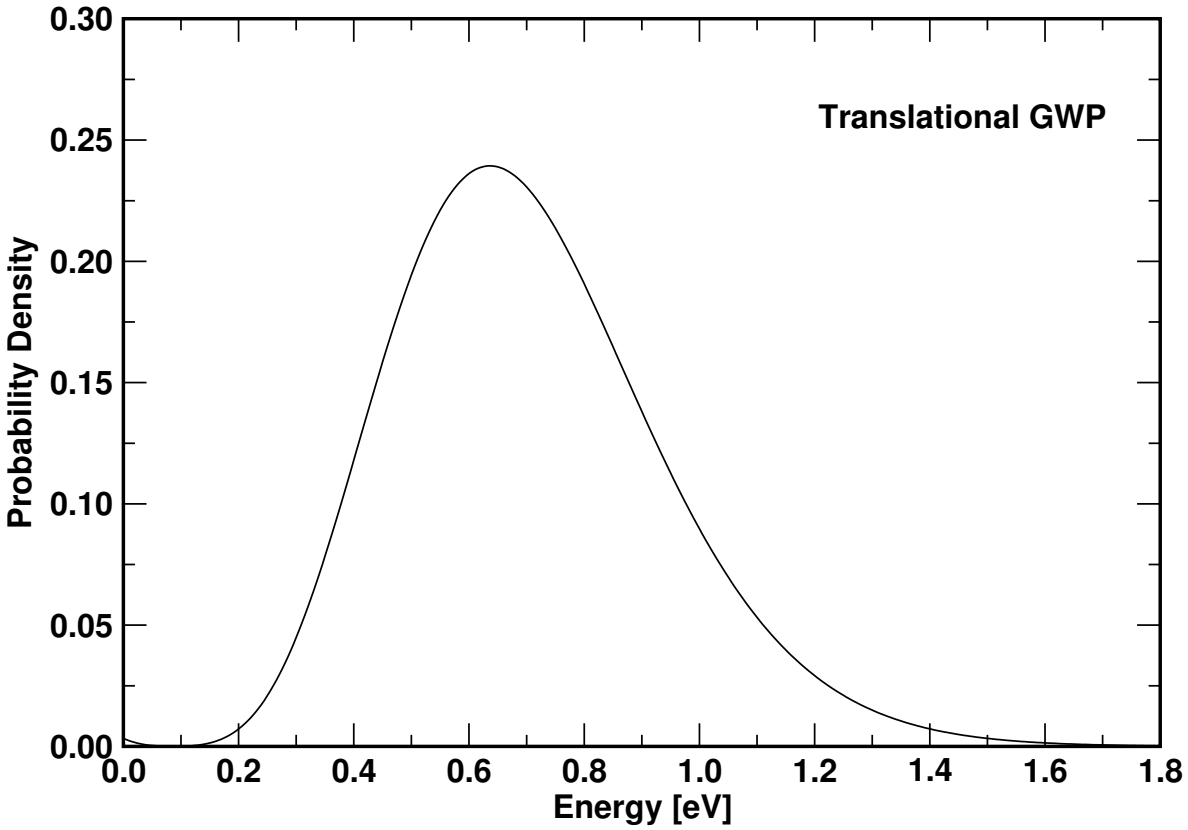

Figure 3.6: The probability density of the initial translational GWP in momentum space is plotted as a function of total energy for the H+HLi collisions. It shows clearly the energy distribution, $|\Delta E|^2$ of initial GWP.

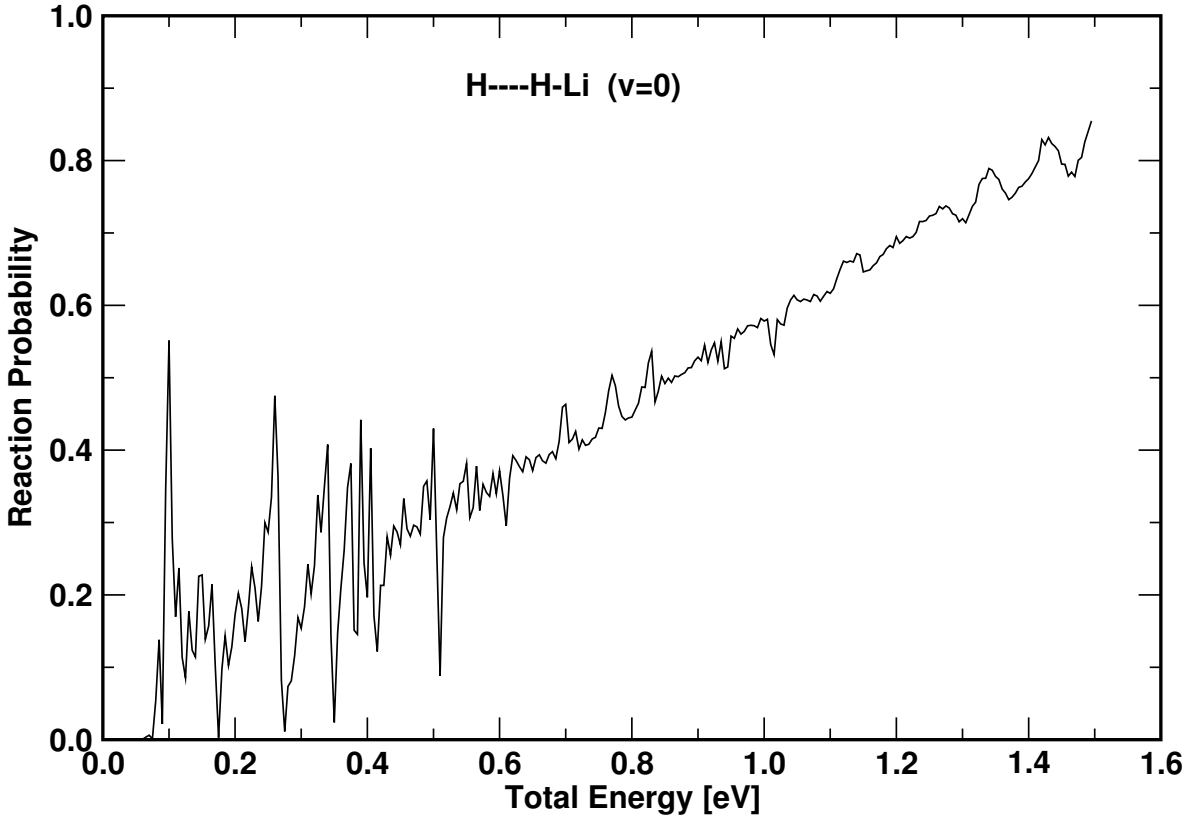

Figure 3.7: Total reaction probability as a function of total energy E (H, LiH translational + HLi vibrational) for the H + HLi ($v = 0$) $\rightarrow H_2$ ($\Sigma v'$) + Li depletion reaction in collinear configuration and for a initial most probable collision energy of 0.55 eV. The energy E is measured relative to the minimum of the HLi potential.

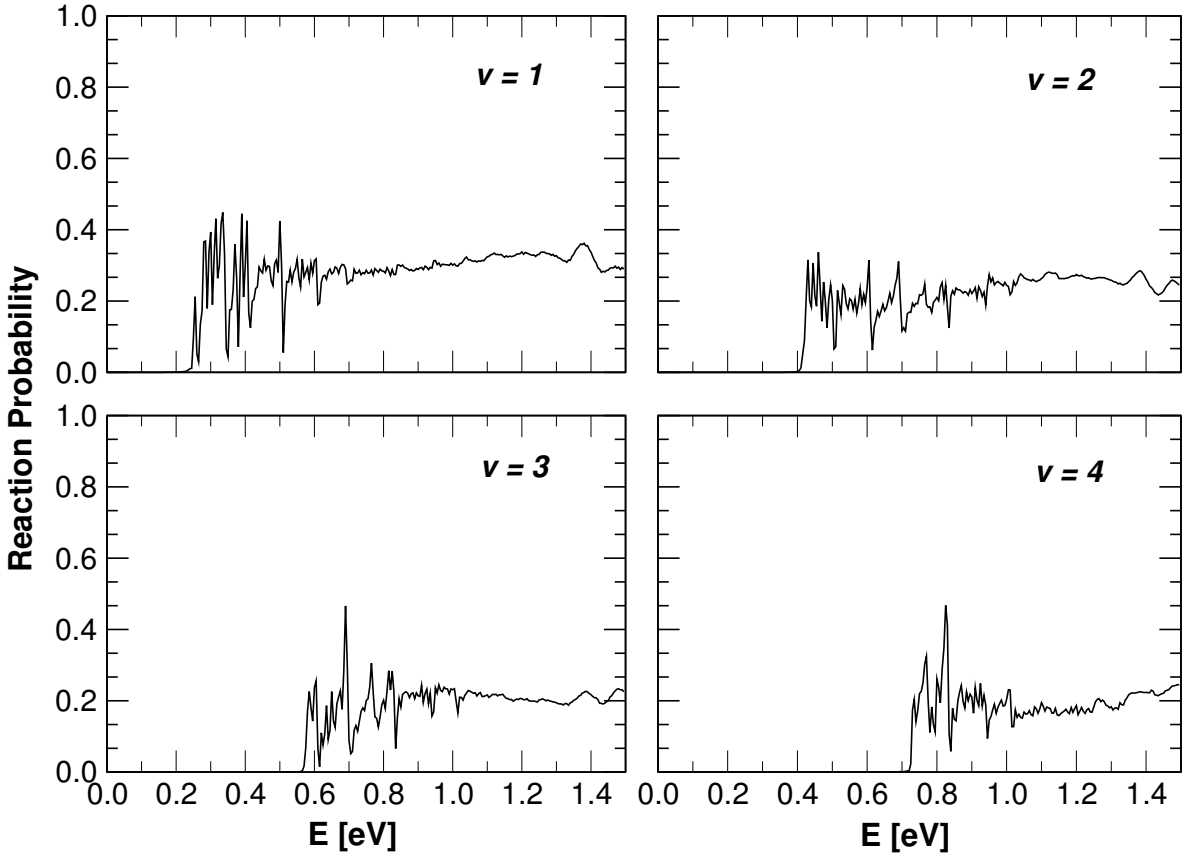

Figure 3.8: Same as in Fig. 3.7, obtained for the vibrationally excited reactant HLi (indicated in the panel) showing the effect of reagent vibration on the dynamics of the depletion reaction in collinear configuration.

In order to further check on the sensitivity of the above results, we have carried out calculations for different initial most probable collision energies, different width parameters of the GWP and also for different choices of the location of the dividing line at the product channel. We obtained consistent reaction probabilities calculated for initial most probable translational energies of 0.35 eV, 0.55 eV, 0.62 eV and 0.7 eV. Also the variation of the width parameter of the GWP in the range 0.25-0.35 a_0 is considered. We find some minor variation of the reaction probabilities for different choice of the dividing line at the product channel. For instance, the first sharp peak in the reaction probability curve disappears when this line is moved closer to the interaction region of the PES.

The reaction probability for the collisions of H atom with the vibrationally excited reactant HLi molecule is shown in Fig. 3.8. The initial vibrational quantum number of the HLi molecule is indicated in each panel. It can be seen from Fig. 3.8 that the onset of the reaction progressively shifts to the expected higher total energy. The exact location of this onset on the energy axis in each panel corresponds to the vibrational energy of the reactant HLi molecule. This, therefore, again supports the fact that the reaction has no threshold and the underlying PES is of early attractive nature. The sharp resonance structures at low energies also survive in collision with the vibrationally excited reactant molecule. It can also be seen that the reaction probability decreases with the vibrational excitation of the reactant HLi molecule, which is also indicated by the results of Clarke *et al.* [90].

3.3.3 Three-Dimensional Reaction Dynamics

In three-dimensional collisions both the reactive channels R1 and R2 are open. In order to calculate the reaction probability for R1 and R2 it is necessary to separately integrate the reactive flux flowing into these channels. As mentioned in Chapter 2, we distinguish these two channels by comparing the internuclear distances of the product H_2 and

LiH molecules. The calculations are carried out on the same (R, r) grid as employed for the collinear dynamics and a 64-point GLQ is used along the angle γ. The properties of the initial WP and other grid parameters are the same as those listed in Table 3.1.

The reaction probabilities for the H + HLi ($v = 0, j = 0$) collisions as a function of the total energy E are plotted in Fig. 3.9. The energy distribution of the initial GWP is the same as that shown in Fig. 3.6. The norm of the WP at the end of the time evolution goes down to 2.47×10^{-3} in this particular case. The probabilities for the H_2 + Li (R1) and LiH + H (R2) reactive channels are shown in the figure and the corresponding channels are indicated on the respective curves. These are the total reaction probabilities for the particular channel which resulted from the summation over all open vibrational (v') and rotational (j') levels of the corresponding product molecule at a given energy. The overall reaction probability considering both the channels together, obtained from a separate calculation, is included in the figure and is shown by the solid curve marked as R1+R2. To confirm the identity of the results the sum of the probabilities for R1 and R2 channels on a coarse energy grid is superimposed on it and is shown by the dots. It can be seen that the sum of the channel specific probabilities exactly converges to the overall reaction probabilities. The results of Fig. 3.9 reveal that, the hydrogen exchange probability is larger than the LiH depletion probability. Therefore, at any given energy the major portion of the reactive flux flows into the hydrogen exchange (R2) channel in three-dimensional collisions. This observation is consistent with the small value of the rate constant reported for the LiH depletion path by Stancil and Dalgarno [61] and also by Dunne *et al.* [91]. We note that, due to a relatively bulky nature of the Li atom, only a narrow cone available to the incoming H atom to approach to the H end of LiH (cf. Fig. 3.5) which in part reduces the probability of the LiH depletion [3,91].

It can be seen from Fig. 3.9 that the onset of both the reaction R1 and R2 occurs at the zero-point vibrational energy of LiH, indicating that these reactions proceed without any barrier. The oscillations in reaction probability curves indicate the exis-

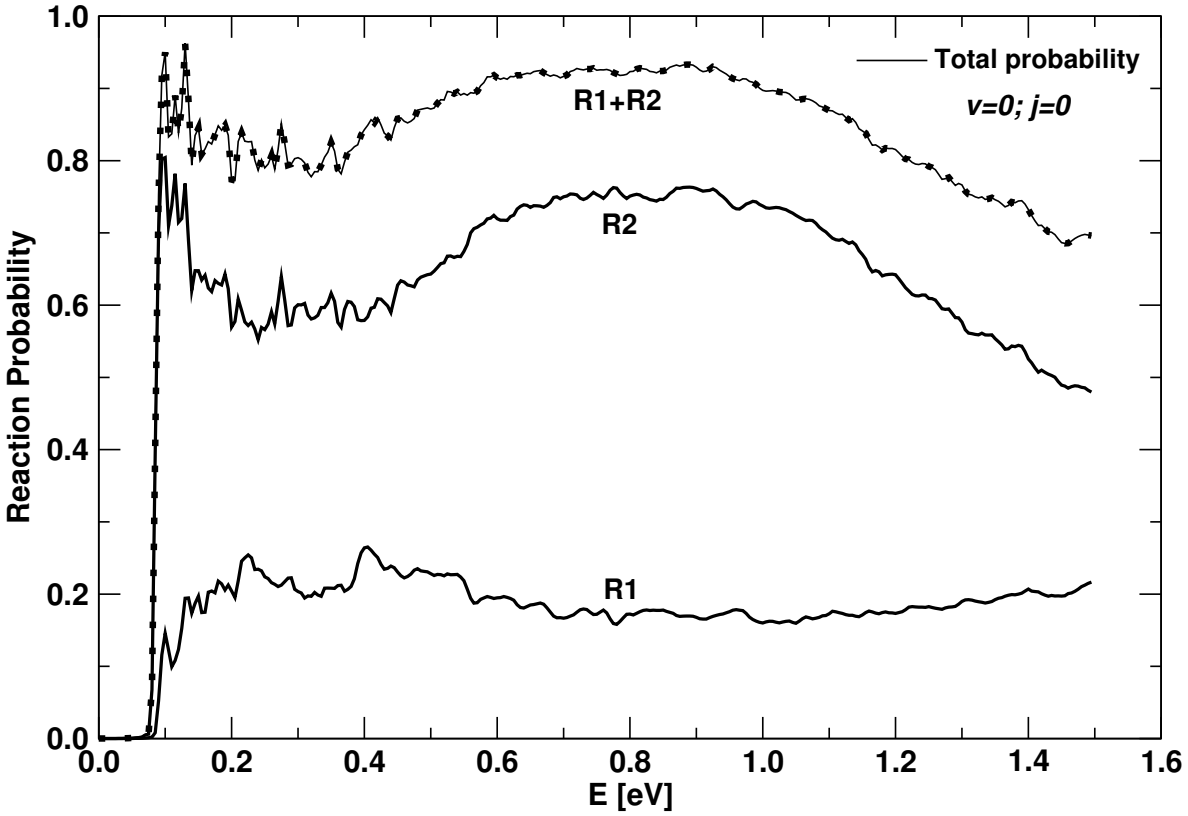

Figure 3.9: Total reaction probability as a function of the total energy E for the H + HLi ($v = 0, j = 0$) collision in three-dimensions and for total angular momentum $\boldsymbol{J}$=0. The total reaction probabilities for the (R1) and (R2) channels are shown separately and the corresponding curves are marked as R1 and R2, respectively. The overall reaction probability (considering both channels together) is shown by the solid curve marked as R1+R2 and the sum of the probabilities for (R1) and (R2) is superimposed on it on a coarse energy grid and is shown by the dots.

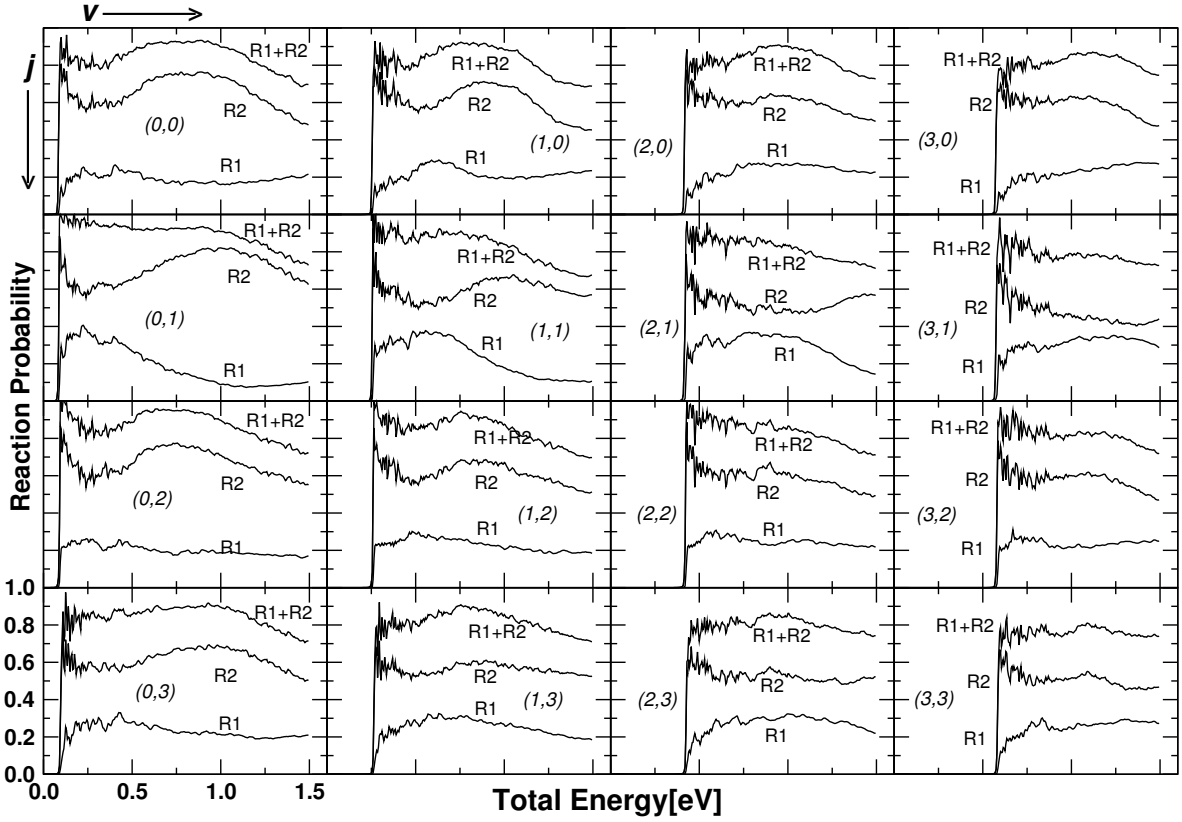

Figure 3.10: Same as in Fig. 3.9, obtained with different vibrational and rotational (v, j) states of the reactant LiH, illustrating the effect of reagent vibration and rotation on the H + HLi collision dynamics. In this case the solid curve marked as R1+R2 represents the sum of the two probability curves R1 and R2.

tence of short-lived resonances at low energies. On the other hand, a relatively smooth variation of the reaction probability reveals a direct nature of the collision dynamics at high energies. It can be seen by comparing the above reaction probability for the HLi depletion channel (R1) to the same obtained for the collinear configuration (cf. Fig. 3.7) that, despite an overall qualitative agreement the collinear model does not provide the realistic description of the dynamics of this system. Mechanistically, both the collinear as well as the three-dimensional reaction probabilities reveal the existence of resonances and therefore an indirect nature of the scattering at low energies and a more direct nature of the same at high energies [101]. A quantitative comparison of the two reaction probability curves clearly indicate the importance of the non-collinear collisions in the dynamics which is also revealed by the topological characteristics of the PES (cf. Fig. 3.3 and 3.4).

In order to study the effect of the reagent vibration and rotation on the dynamics, in Fig. 3.10 we show the reaction probability curves obtained with the vibrationally and rotationally excited reactant LiH molecule. The initial vibrational and rotational (v, j) quantum state of the latter is indicated in each panel. The overall trend of variation of reaction probabilities in each panel is similar to that observed for the reaction with LiH $(v = 0, j = 0)$ (which is again included in the figure for clarity). The onset of the reaction with the vibrationally and rotationally excited, reactant LiH occurs at the internal energy of the corresponding (v, j) state, indicating the absence of any barrier to the reaction. The sharp resonance structures near the onset of the reaction also show up in all the probability curves, which confirms an indirect nature of the dynamics at low energies. The resonance structures disappear at high energies and the dynamics is more direct at those energies. It can also be seen that for any (v, j) state the LiH depletion probability is lower than the H exchange probability for any given energy.

Unlike in the collinear case for the reaction (R1) the three-dimensional reaction probability results do not show any systematic variation with the vibrational excitation

of the reactant LiH. However, the reaction probabilities for (R2) show a slight decrease with the vibrational excitation of the reactant LiH. The rotational excitation of the reactant LiH, on the other hand, do not cause any systematic variation of the reaction probabilities of either (R1) or (R2) and appears to play only a minor role in the corresponding dynamics.

3.4 Summary

We reported in this chapter the initial state-selected and channel specific energy resolved reaction probabilities of the H+HLi system for the total angular momentum $J = 0$ by employing the DMJ PES [91]. The reaction probabilities are calculated by a TDWP approach which is presented in Chapter 2.

The reaction probability curves for both the LiH depletion channel (R1) as well as the hydrogen exchange channel (R2) exhibit sharp resonance structures at low energies. This therefore indicates an indirect nature of the scattering at those energies. The resonances are less pronounced at further high energies and the scattering becomes more direct. An examination of the probability results at the onset of the reactions indicates a zero threshold energy, in agreement with the absence of any barrier in the underlying PES. The channel specific reaction probability values indicate that H + HLi collision dynamics predominately follow the hydrogen exchange path (R2) at any given energy [101] which is consistent with the very small rate constant reported by Stancil and Dalgarno [61] and also by Dunne *et al.* [91] for the LiH depletion. This finding can be partly attributed to the steric effects associated with the bulky Li atom, which hinders the incoming H atom to approach to the H end of the LiH molecule to react via the path (R1).

A careful examination of the reaction (R1) for the collinear configuration revealed a decrease of probability with the vibrational excitation of the reactant LiH molecule.

Such a general trend however, is not revealed by the corresponding three-dimensional reaction probabilities. The probability for the exchange path (R2) in three-dimension, on the other hand, decreases slightly with the vibrational excitation of the reactant LiH. The rotational excitation of the reactant LiH molecule, however, does not show any such systematic variation of reaction probabilities either for (R1) or (R2).

A comparison of the reaction probabilities for (R1) for the collinear and the three-dimensional configuration clearly revealed the importance of the non-collinear collisions in the corresponding dynamics. In the three-dimensional collisions a substantial amount of reactive flux is pushed away from the collinear path. The dynamics at the bent geometry of LiH_2 is most likely to follow an insertion type of mechanism. This anticipation is further strengthened by the observation of a conical intersection in the bent geometry of LiH_2 [87]. A further detailed analysis of the energy disposal mechanism and the H+HLi dynamics for the total angular momentum $J \neq 0$ is presented in the next chapter. using various approximations to calculate the integral reaction cross section and thermal rate constant are discussed in the next chapter.

Chapter 4

H+HLi Scattering for the total angular momentum $J \neq 0$: Integral Reaction Cross Section and Thermal Rate Constant

4.1 Introduction

Reaction cross sections and thermal rate constants are the two most important dynamical quantities of a chemical reaction [2,3,5,37]. The reaction cross section is calculated by summing up all partial wave contributions of the total angular momentum J to the reaction probability discussed in the previous chapter. A further averaging of the energy-dependent reaction cross sections at a given temperature yields the thermal rate constant. In an atom-diatom reactive scattering, the reaction probability for $J \neq 0$ is best obtained by carrying out the explicit quantum dynamical simulations [37], which involve four degrees of freedom - three to describe the relative orientation of the atom and diatom in a plane and the fourth one, the projection, K, of the total angular momentum J, defining the orientation of this plane. A commonly employed approach in the

BF frame is called the centrifugal sudden or the coupled states approximation [98–100] introduced in Chapter 2, in which K is a good quantum number and is treated as a parameter. This reduces the dimensionality of the problem to three. Such an approximation has been widely used to determine the reaction cross sections and thermal rate constants in bimolecular chemical reactions [138, 162–166, 211] and in many cases this approximation turned out to be quite accurate. An even simpler approach called the J-shifting (JS) approximation [95] (also discussed at length in Chapter 2) has also been widely used to calculate the thermal rate constant. In this approach, the reaction probabilities for $J \neq 0$ are calculated from the corresponding $J = 0$ reaction probabilities (cf. results of Chapter 3) by simply shifting the collision energy by an amount corresponding to the rotational energy of the "transition state". Many versions of the JS approximation are proposed in the literature and have been successfully applied to a wide variety of bimolecular reaction [95–97, 201–203].

In this chapter, we finally present a detailed full-dimensional quantum scattering calculations of the reaction cross section and thermal rate constant for the H+HLi scattering. In these calculations, we consider the Coriolis coupling terms of the Hamiltonian of Eq. (2.40), where the neighboring K states couples each other and thereby the dimensionality of the problem becomes four. Our findings reveal that inclusion of the partial-wave contribution upto $J = 30$ is necessary to obtain the reaction cross sections upto a collision energy of ~ 0.75 eV. The projection quantum number K upto 4 is included in the dynamics. The CC results are reported and compared with those obtained in the reduced dimensionality models using the JS and CS approximations.

In the reduced dimensionality models, the dynamical calculations for $J \neq 0$ are carried out by invoking either the CS [98–100] or the JS [95–97] approximations, and the integral reaction cross sections and the temperature dependent rate constants. For the present problem, within the CS approximation, the partial wave contributions upto $J = 74$ was necessary to obtain the converged initial state-selected integral reaction

cross sections for the R1 and R2 channels upto a collision energy of 1.0 eV. The resonance oscillations seen in the reaction probability curves (e.g., the results presented in Chapter 3) average out with many partial wave contributions in the integral reaction cross section results. Vibrational and rotational excitation of the reagent HLi does not have any dramatic effect on the cross sections except at the onset of the reaction. The HLi depletion channel (R1) is found to be preferred over the H-exchange channel (R2) for higher values of collision energies and higher J values. The thermal rate constant values over the entire temperature range are larger for the R2 channel than the R1 channel, in par with the much larger cross sections for the R2 channel at low and moderate collision energies. The rate constant values for the vibrationally cold HLi molecules are much larger than the vibrationally hot ones (within the CS approximation) revealing that the cold HLi molecules can be efficiently depleted in collisions with the H atom at low temperatures.

The dynamical results of both the CS and CC models reveal that the exchange channel is generally preferred over the depletion channel. The reaction cross sections does not have a threshold indicating the feature of a barrierless reaction which is again reflected in substantial deviation of the thermal rate constant results from the Arrhenius behavior. The integral reaction cross sections are generally lower in the CC model when compared to the CS results, for both the channels. The CC leads to an increase of the reaction rate at low temperatures, and a decrease at high temperatures, when compared to the CS results for both the channels.

4.2 Methodology and Computation Details

The detailed theoretical framework of a TDWP approach to treat the reactive scattering is outlined in Chapter 2. We describe here only the essentials to treat the $J \neq 0$ dynamics to obtain the the reaction cross sections and the thermal rate constants of H+HLi collisions [37, 40–42, 146]. The details of the WP propagation here is similar to

that discussed in Chapter 3. We add that for the calculations, within the JS and CS approximations the SO method is employed, however, the CP scheme is employed in the full-dimensional calculations.

Within the CS approximation, the WP calculations are carried out by treating K as a fixed parameter, and therefore, the dimensionality of the problem reduced to three. Whereas in the CC calculations the adjacent K states are coupled together (i.e. K with $K \pm 1$). Therefore, in addition to the three BF coordinates K also adds to the overall dimensionality, and the resulting problem becomes four dimensional. For the latter, the choice of the grid along γ, in principle depends on the J and K values. In practice, the choice of different γ grid in a single numerical calculation is impossible. To avoid this difficulty, we used the grid points corresponding to $J = 0$ and $K = 0$ throughout the calculations, however, we used appropriate eigenvector matrix corresponding to a particular K value to set up the DVR-FBR transformation matrix [125, 128] (as discussed in Chapter 2). In the following, the nodes of a 48-points GLQ [212] are used for the grid points along γ. We note here that the SO algorithm [172] is not particularly straight forward for the CC calculations because of the numerical difficulty in dealing with the off-diagonal coupling elements of the Hamiltonian matrix. The CP method [183, 184] or a symplectic integrator [187] are the better alternatives for the time propagation of the WP in this case. We used the CP method [183] in the CC calculations and this method is discussed in Sec. 2.5.5.

In the CC calculations, the parity (p) selection in Eq. (2.31) depends on the odd or even values of J and K is restricted to non negative values. For instance, odd J states will have odd parity ($p = 1$) and even J states will have even parity ($p = 0$). In case of $J = 2$, for example, the four-dimensional calculations are carried out for each K values varying from 0 to 2 and even value of parity ($p = 0$). Within the CS approximation, the parity is not considered and the value of K is varying from 0 to $+\min(J, j)$.

In order to ensure the convergence of the SO and CP propagation schemes, we show the initial state-selected and energy-resolved reaction probabilities in H+HLi collisions both for the collinear and three-dimensional arrangements, calculated using these WP propagation schemes in Fig. 4.1(a-b). The identity of the results confirms their convergence.

The remaining details of the WP propagation is same as discussed in previous two chapters. The details of the numerical grid parameters and properties of the initial wavefunction used in this study are given in Table 4.1.

The detailed theory to calculate the J-dependent reaction probabilities within the CS and CC models, integral reaction cross sections and thermal rate constants are discussed in Sec. 2.6.2.1 and Sec. 2.6.2.2. The rotational constant value of HLi molecule used in the calculation of rate constant [Eq. 2.126d] is B=7.5131 cm^{-1} [91]. In the CC model, the initial state-selected integral reaction cross sections and thermal rate constants of the H+HLi reaction for a specified initial ($v = 0, j = 0$) state of HLi are evaluated using the following expressions, (cf. Eqs. (2.122) and (2.124)),

$$\sigma_{00}(E) = \frac{\pi}{(2j+1)k_{vj}^2} \sum_{K=0}^{K_{max}} \sum_{J \geq K}^{J_{max}} (2J+1) P_{00}^{JK}(E), \tag{4.1}$$

$$k(T) = (2\pi\hbar Q_R(T))^{-1} \int_{-\infty}^{+\infty} dE e^{-E/k_B T} \sigma_{00}(E). \tag{4.2}$$

where, the maximum allowed value of K, i.e., K_{max} is considered upto 4.

In this chapter, we also discuss the cross section and thermal rate constant results obtained using the uniform JS [97] as well as the standard [95] approximations. The latter are discussed in Chapter 2 (Sec. 2.6.3). Within the JS approximation, the reaction probability for $J \neq 0$ is obtained from that for $J = 0$ [101] using Eq. (2.127). In Eq. (2.127), $E_J^{\ddagger}$ and $B^{\ddagger}$ are the rotational energy and the rotational constant, respec-

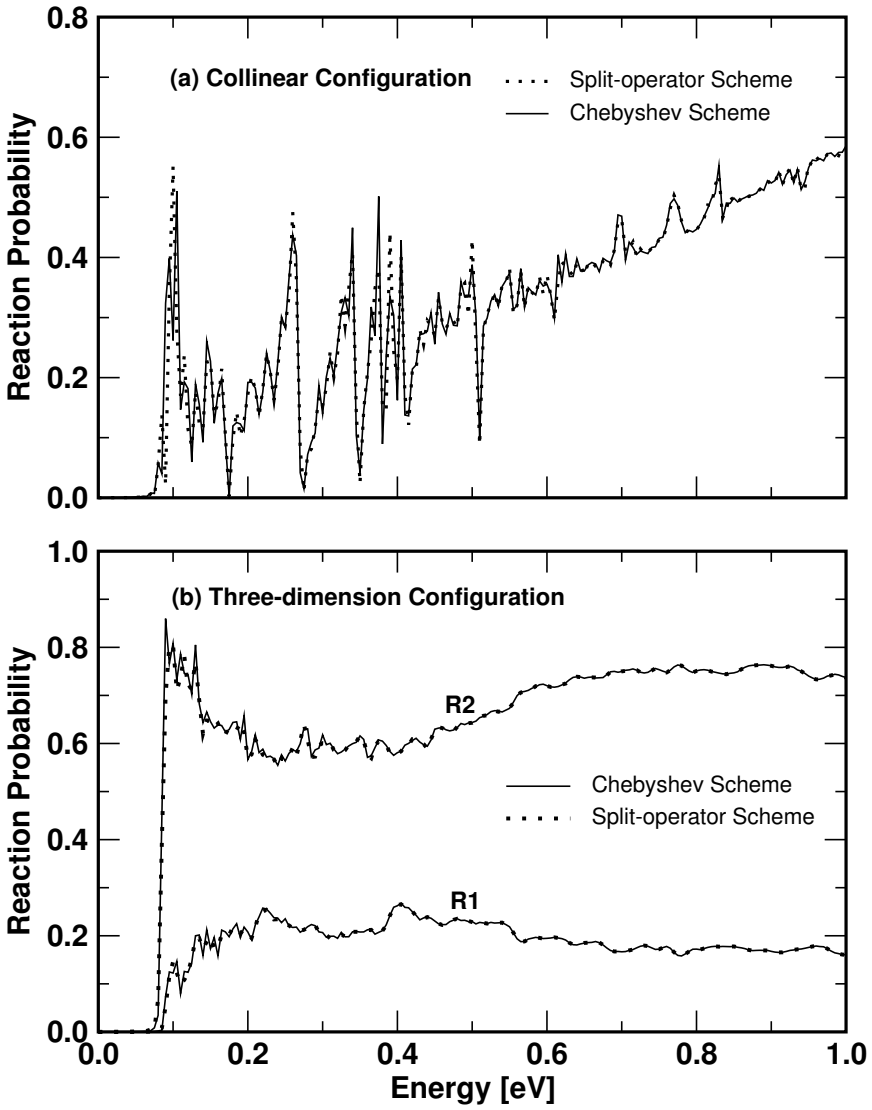

Figure 4.1: The initial state-selected and energy-resolved reaction probabilities as a function of the total energy in H+HLi collisions for the collinear (panel a) and three-dimensional (panel b) arrangements of the nuclei. The results obtained by employing the SO and CP schemes are shown as dotted and solid lines, respectively.

Table 4.1: Numerical grid parameters and properties of the initial wavefunction used in the calculation of integral reaction cross section and thermal rate constant using the JS, CS and CC models.

Parameter	Value	Description
$N_R/N_r/N_\gamma$	128 (256^a)/64/64 (48^b)	Number of grid points
R_{min}/R_{max} (a_0)	1.0/18.78 (36.7^a)	Extension of the grid along R
r_{min}/r_{max} (a_0)	1.0/8.56	Extension of the grid along r
$\Delta R/\Delta r$ (a_0)	0.14/0.12	Grid spacings along R and r
r_d (a_0)	5.44	Location of the dividing surface in the product channel
R_{mask}/r_{mask} (a_0)	14.58 (28.3^a) (13.46^b)/5.68	Starting point of the masking function
R_0 (a_0)	12.0 (25.0^a)	Initial location of the center of the GWP in the coordinate space
V_{cut} (eV)	4.0 (3.0^b)	Maximum potential energy cut-off
E_{trans} (eV)	0.55	Initial translational kinetic energy
δ (a_0)	0.3	Initial width parameter of the GWP
Δt (fs)	0.135	Length of the time step used in the WP propagation
T (fs)	414 (552^a) (276^b)	Total propagation time

[a] the parameters related to the extended R grid used for higher values of J in the CS model.

[b] the parameters used in the CC calculations.

tively for the $[HHLi]^{\ddagger}$ transition state species. The latter is obtained by optimizing the transition state species of H+HLi reaction using the MP2 level of theory employing a correlation consistent polarized valence triple-ζ (cc-pVTZ) basis set [213]. This yields a value $\sim 1.874\times10^{-4}$ eV (1.512 cm^{-1}) for the $B^{\ddagger}$ for the HHLi transition state.

The detailed discussion of these approximations in the calculation of thermal rate constant can be found in Sec. 2.6.3.

4.3 Results and Discussion

4.3.1 CS Approximation

4.3.1.1 $J \neq 0$ Reaction Probabilities

The initial state-selected and energy resolved total reaction probabilities of H+HLi system calculated within the CS approximation are shown in Fig. 4.2 for the total angular momentum $J = 0 - 74$ [102]. It can be seen that the oscillations in the reaction probability curves gradually disappear, and therefore the resonances are seem to be less pronounced at higher energies and higher values of J.

In Fig. 4.3, we plotted the channel specific reaction probability values as a function of the total energy E computed within the CS approximation for a few representative values of the total angular momentum, J=10, 30, 40 and 70 and for $K = 0$ for different (v, j) levels of the reagent HLi (indicated in the respective panel). The reaction probabilities for both the HLi depletion channel and the H-exchange channel are shown in each panel and are indicated by thin and thick lines, respectively. The initial most probable collision energy of the GWP is chosen to be 0.55 eV. The total energy E is measured relative to the minimum of the HLi potential. The WP is time evolved for a total of 551.68 fs and the norm ($\langle\Psi|\Psi\rangle$) of the WP at the end of the time evolution in each calculation goes down to a very small value. Reaction probability pertinent to a

channel is calculated by integrating the reactive flux flowing into it. The two channels R1 and R2 are distinguished by comparing the internuclear distances of the product H_2 and HLi molecules. The reaction probabilities reported here are calculated at an energy interval of 0.005 eV. We note here that for higher values of J we used a larger grid along R and located the initial WP further out in the reagent channel in order to avoid any overlap with the slowly decaying centrifugal potential. The centrifugal potential term, $\hbar^2[J(J+1)-2K^2]/2\mu R^2$ [see Eq. (2.40)] adds a barrier to the PES and the height of this barrier increases with increasing J (cf. Fig. 4.4). For a very large value of J, the effective potential becomes repulsive because the centrifugal barrier acts fully against the approach of the colliding particles [3]. The reaction probabilities presented in Fig. 4.2, represent the total reaction probabilities, i.e., summed over all open vibrational (v') and rotational (j') levels of the product molecule at a given energy. The channel specific reaction probabilities for $J = 0$ case is discussed in Chapter 3, where the results indicated sharp resonance structures at low energies for both the R1 and R2 channels. The resonances are found to be less pronounced at high energies revealing a more direct nature of the reaction. Some of these resonances are identified and characterized in terms of their energy eigenvalue, eigenfunction and lifetime and are discussed in detail in Chapter 5. The $J = 0$ probability results indicated a preference for the R2 path over the R1 path in the collision dynamics [101].

Examination of the probability results of Figs. 4.3(a-d) indicate that the resonances survive at lower energies near the onset of the reaction even for higher values of J (although less prominent compared to the $J = 0$ results, see Chapter 3). The reaction is intrinsically barrierless and proceeds without any threshold, which is explicitly indicated in the $J = 0$ reaction probabilities. However, for $J \neq 0$ collisions the reaction acquires a threshold energy due to the presence of the centrifugal barrier [see Fig. 4.4], which shows up in the probability results presented in Figs. 4.3(a-d). Interestingly, the HLi depletion reaction dominates over the H-exchange reaction for higher values of J (for example, for $J = 30, 40, \ldots$). On the average the reaction probabilities for higher

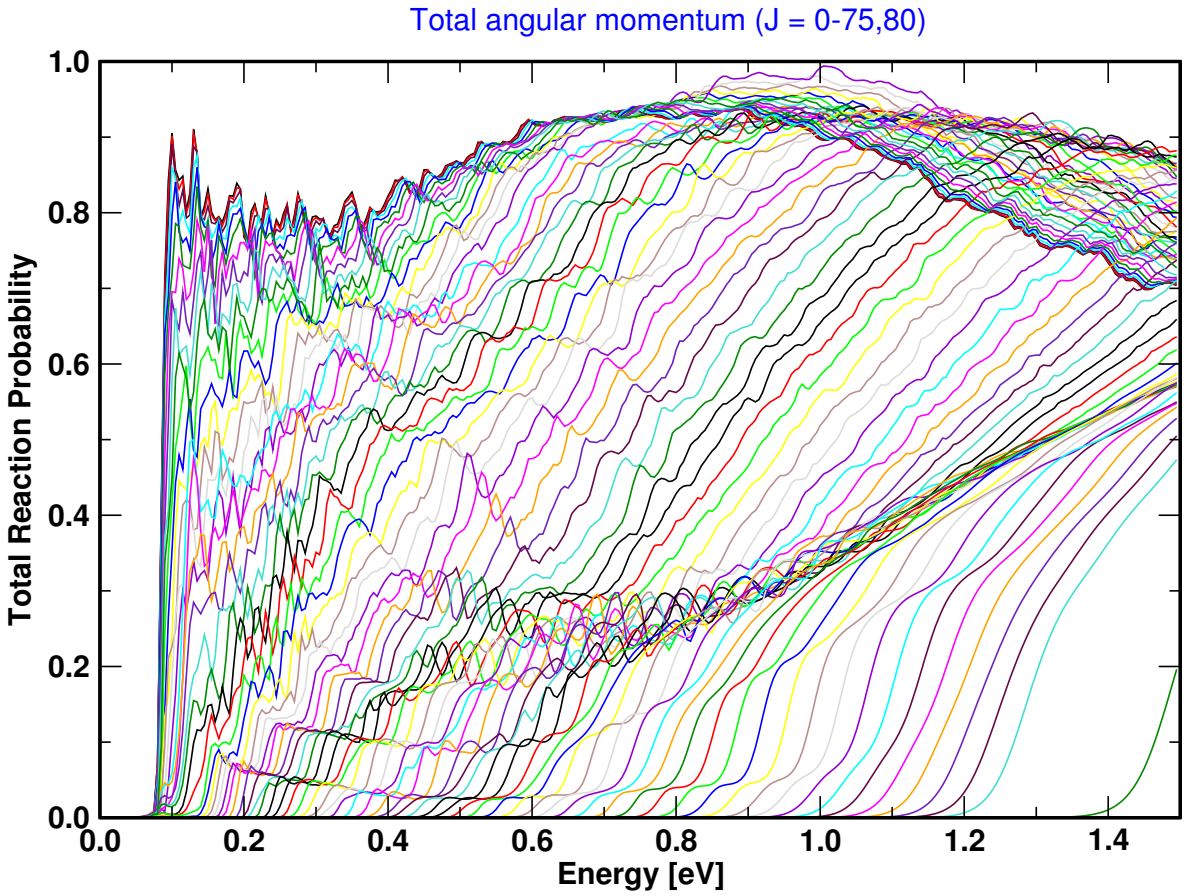

Figure 4.2: The H+HLi reaction probabilities as a function of the total energy for the initial $(v = 0, j = 0)$ state of HLi molecule and for $J = 0 - 75$ and 80, within the CS approximation.

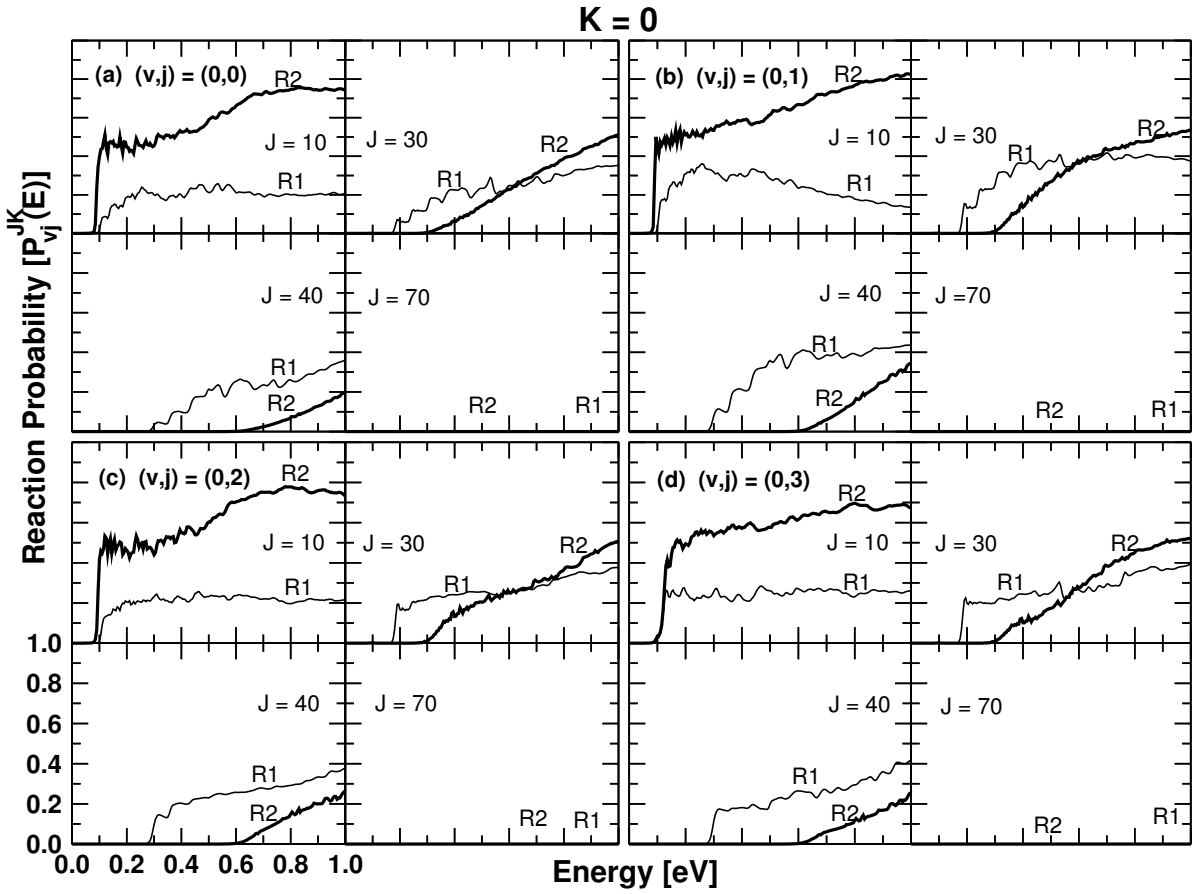

Figure 4.3: Total CS reaction probabilities for the H + HLi(v, j) collisions in three-dimensions and for the total angular momentum $J = 10, 30, 40$ and 70 (indicated in the respective panel) and $K = 0$. The (v, j) levels of the reagent HLi are indicated in each figure. The reaction probabilities for the HLi depletion channel (R1) and the H-exchange channel (R2) are shown as thin and thick solid lines in each panel.

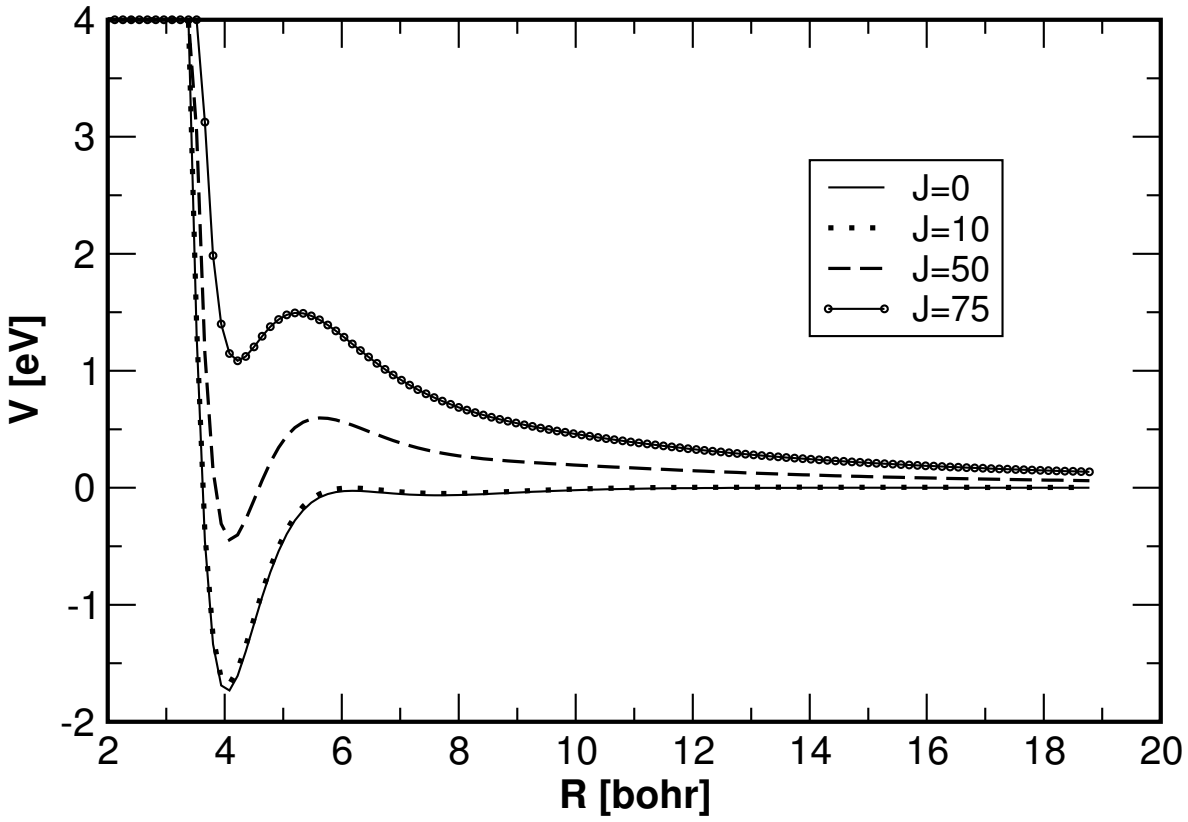

Figure 4.4: Potential energy cuts along R and for $r = r_e$ for different values of J obtained from the *ab initio* DMJ PES of the H+HLi system.

values of J are smaller than the corresponding $J = 0$ results, indicating substantial nonreactive scattering for $J \neq 0$ collisions. Similar features of the probability curves are obtained for $J \neq 0$, $K \neq 0$ collisions. For illustration, we include some of the $J \neq 0$ probability results in Figs. 4.5(a-c) for the corresponding maximum value of K, obtained in the scattering with the reagent HLi in the rotational state j=1,2 and 3, respectively.

In order to assess the partial wave contribution to the probability results at a given energy, we show in Figs. 4.6(a-b) the J-dependence of the degeneracy $(2J+1)$ weighted reaction probability for the R1 and R2 channels, respectively, for four representative values of the total energy indicated in each panel. The weighted probability value for a given energy initially increases with J due to the $(2J + 1)$ degeneracy factor and then decreases at higher values of J, due to the shift of the reaction threshold caused by the centrifugal barrier. It can be seen that the partial wave contribution increases with increasing total energy, E. The J_{max} value for a given energy is less for the H-exchange channel compared to the HLi depletion channel. For example, $J_{max} \sim 40, 50$ for the former compared to $J_{max} \sim 50, 70$ for the latter at 0.50 eV and 0.98 eV, respectively. The oscillatory structures (mostly at low energies) in the probability curves in Figs. 4.6(a-b) are associated with the resonances of the H+HLi system.

The cumulative reaction probabilities (CRPs) calculated using Eq. (2.123) for the R1 and R2 channels in H + HLi ($v = 0, j = 0 - 3$) collisions are shown in Figs. 4.7(a-b). The line type for different j value is indicated in the panel. It can be seen that for the HLi depletion channel (cf. Fig. 4.7(a)) the CRP values show a mild increase with rotational excitation at low energies, however, at high energies the reactivity of all j states are nearly identical. This trend is reversed for the H-exchange channel (cf. Fig. 4.7(b)) in which case the reactivity exhibits a slight decrease which becomes more prominent at high energies. A close look at the CRP results in Figs. 4.7(a-b) indicates that the reactivity of the HLi depletion channel is more at high energies. The resonance

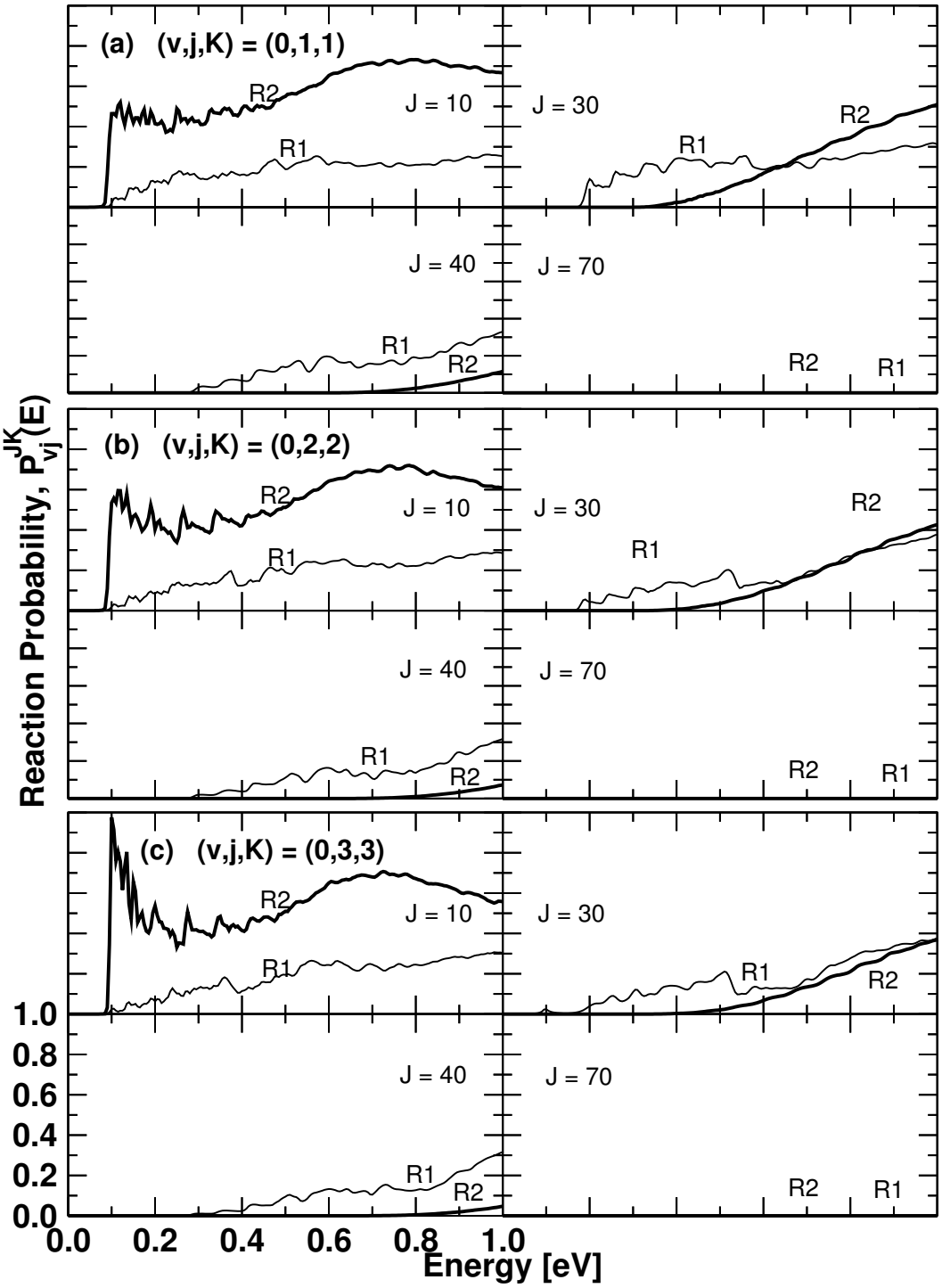

Figure 4.5: Same as in Fig. 4.2, for nonzero values of K included in the figure.

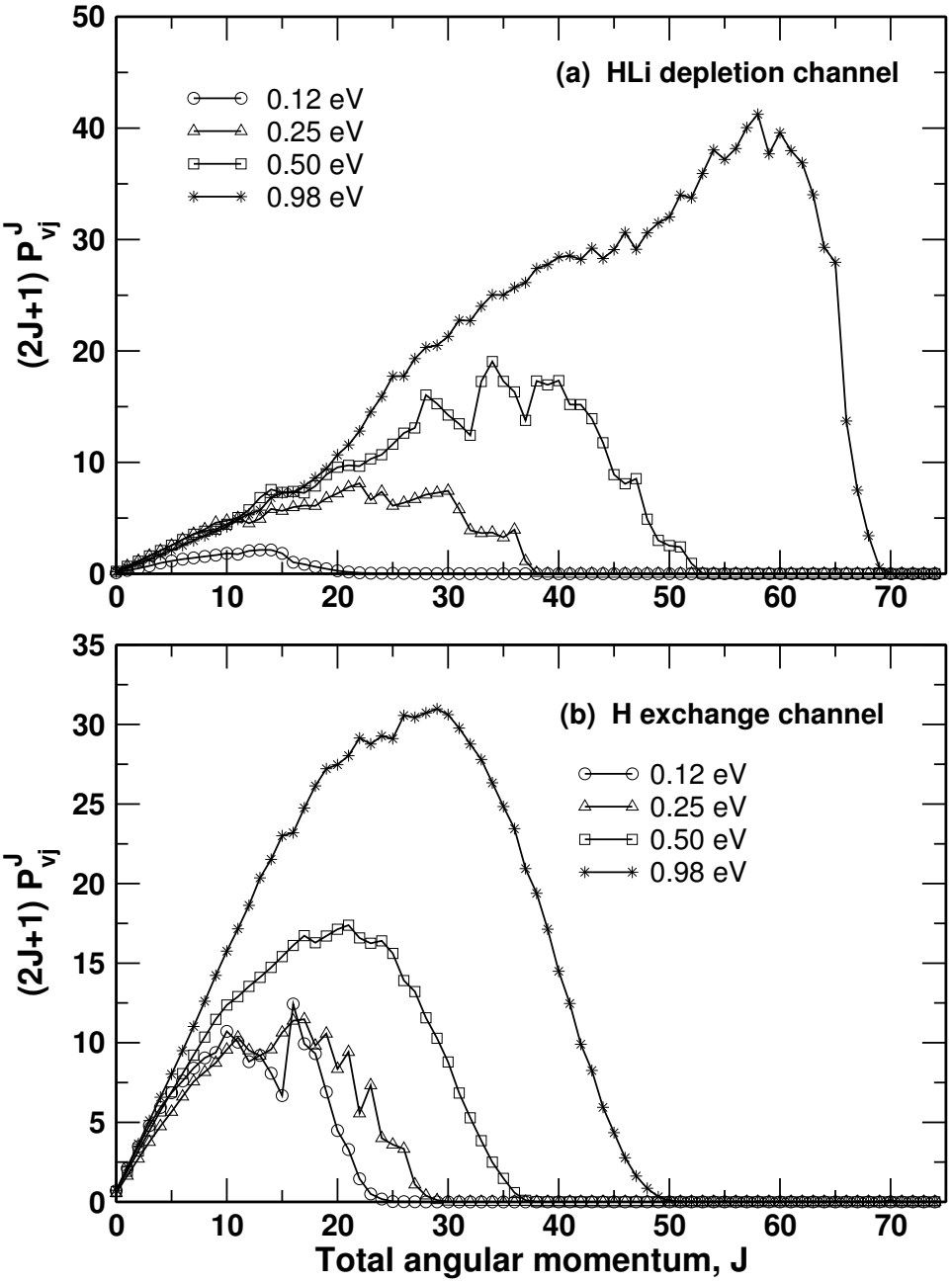

Figure 4.6: Weighted CS partial wave contributions to the CRP and integral cross sections of the R1 (panel a) and R2 (panel b) channels at various values of the total energy (indicated in each panel).

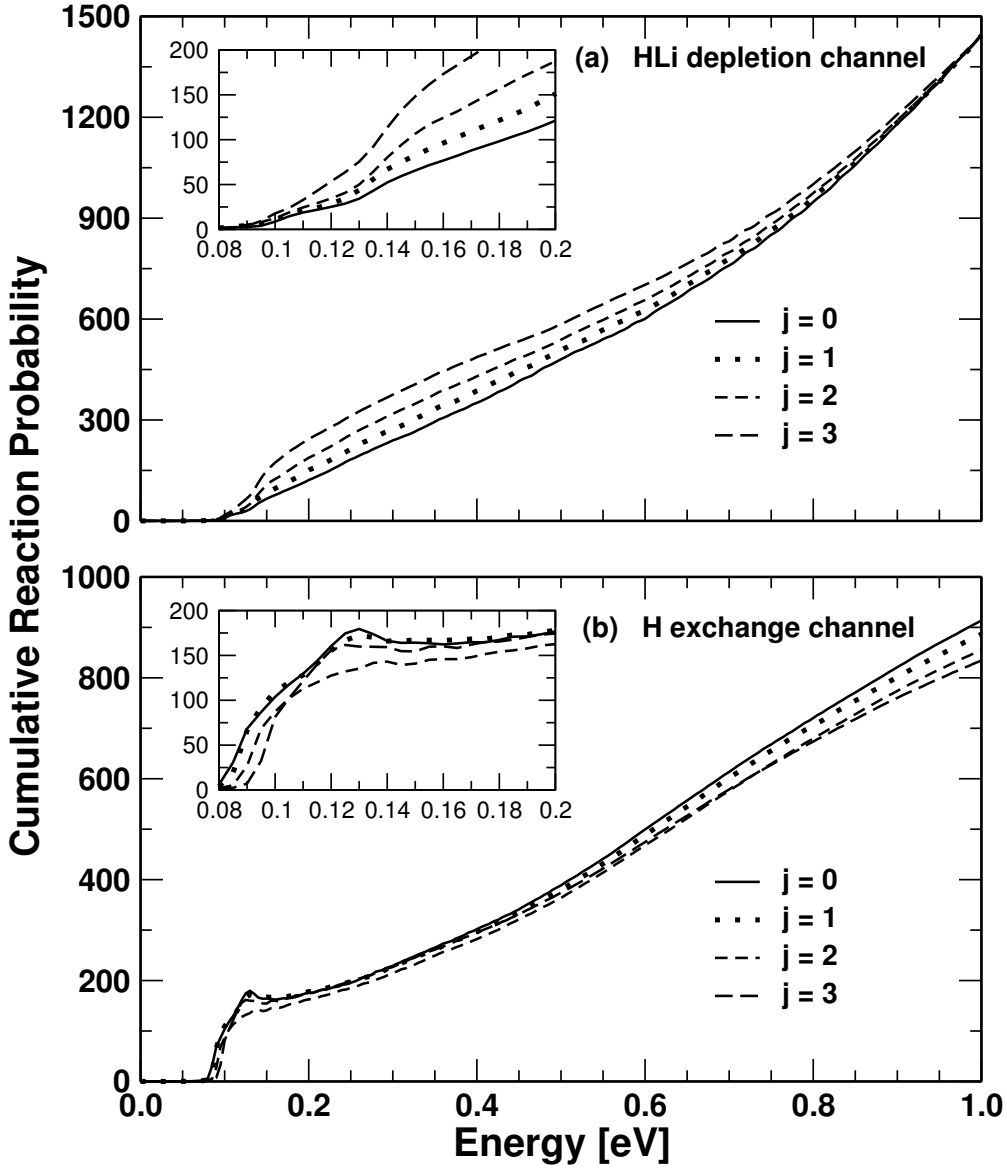

Figure 4.7: Cumulative reaction probabilities for the R1 (panel a) and R2 (panel b) channels as a function of the total energy in the H + HLi ($v = 0, j$) collisions. The CRP curves for various values of j are indicated in each panel. The CRP values are shown on an enlarged scale in the inset of the respective panels in order to clearly reveal the resonance oscillations at low energies.

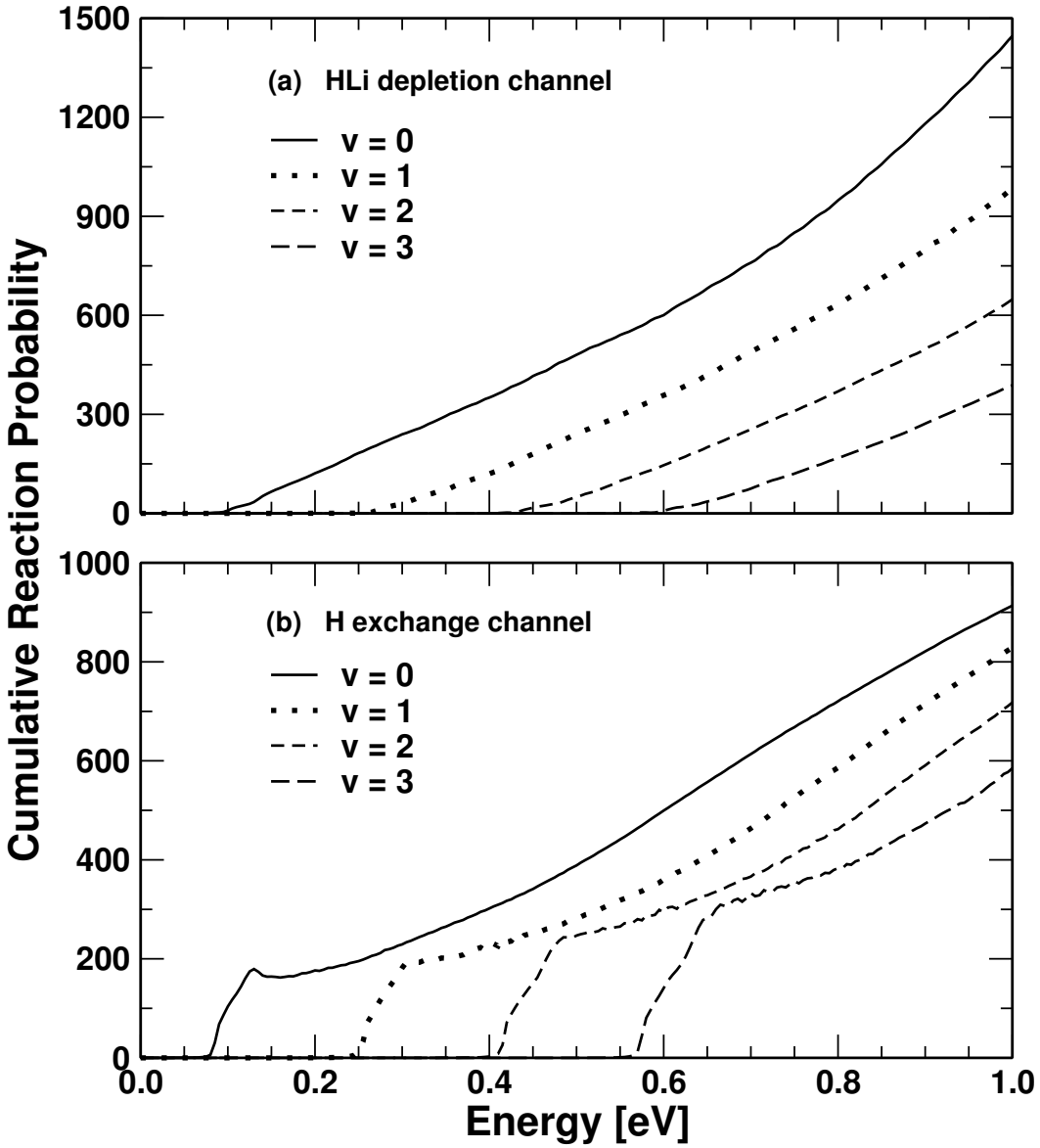

Figure 4.8: Same as in Fig. 4.7, for H + HLi $(v, j = 0)$ collisions. The CRP curves for various values of v are indicated in each panel.

features of the reaction probability results (cf. Figs. 4.3 & 4.5) mostly average out with different partial wave contribution in the CRP results of Figs. 4.7(a-b). Mild resonance oscillations in the CRP results can be seen only at low energies near the onset of the reaction (cf. inset of Figs. 4.7(a-b)).

The CRP results obtained with the vibrationally excited reagent HLi ($v = 0 - 3, j = 0$) are plotted in Figs. 4.8(a-b) for the R1 and R2 channels, respectively. It can be seen from Figs. 4.8(a-b) that the CRP values for a given energy decreases with increasing vibrational excitation for both the R1 as well as R2 channels. The onset of the reaction for each channel shifts monotonically to the higher total energy with vibrational excitation. This shift of the onset is a combined effect due to the initial vibrational energy of HLi and the centrifugal energy. Figs. 4.8(a-b) also reveal that the overall CRP for the HLi depletion channel is more at high energies compared to the H-exchange channel.

4.3.1.2 Integral Reaction Cross Sections

The initial state selected and channel specific reaction cross sections as a function of the collision energy in H + HLi (v, j) scattering are shown in Figs. 4.9(a-b) and Figs. 4.10(a-b). These cross sections represent integral cross sections, i.e., weighted sum of the reaction probabilities over different partial wave contributions and are calculated by Eq. (2.122) [102].

The reaction cross sections shown in Figs. 4.9(a-b) are obtained with the reagent HLi in the $v = 0$ and $j = 0 - 3$ level. The line types for different j values are indicated in each panel. It can be seen from Fig. 4.9(a) that the cross section for the HLi depletion channel increases with the rotational excitation of HLi at low energies (upto ~ 0.5 eV) and then reaches a value of ~ 10 Å^2 at high energies. The reaction cross sections for both the R1 and R2 channels are generally large near the onset and then decreases with increasing collision energy. This is a characteristic of a barrierless reaction [102].

For HLi ($v = 0, j = 0$) the cross section results show a mild increase at higher collision energies (cf. Fig. 4.9(a)). The weak resonance oscillations in the CRP results (shown in the inset of Fig. 4.7(a)) at low energies become somewhat more prominent in the cross section results of Fig. 4.9(a) due to a contribution from the π/k_{vj}^2 factor of Eq. (2.122). A similar feature (although much weaker) is also seen in the cross section results for the R2 channel of Fig. 4.9(b). In this case the cross section values are much larger near the onset, and at high energies they are consistently smaller than the HLi depletion channel. At high energies, the cross section values for the H-exchange channel decreases slightly with increasing j, which can be seen from the inset of Fig. 4.9(b).

The effect of reagent vibrational excitation on the reaction cross section is depicted in Figs. 4.10(a-b). The line types in each plot are indicated in the respective panel. The reaction cross sections for both the HLi depletion channel (cf. Fig. 4.10(a)) as well as H-exchange channel (cf. Fig. 4.10(b)) are generally large near the onset of the reaction. This is also revealed by the classical trajectory results of Kim *et al.* [92] for the HLi depletion channel. While the cross sections for the R1 channel decrease with increasing reagent vibration (cf. Fig. 4.10(a)), those for the R2 channel show a mild increase (cf. inset of Fig. 4.10(b)). A large decrease in the reaction cross section beyond the onset in Fig. 4.10(b) implies a substantial nonreactive scattering at high energies. Except near the onset, the vibrational excitation of the reagent HLi has only a minor effect on the cross sections for the R2 channel. Due to the reason stated for Figs. 4.9(a-b), mild resonance oscillations of the CRP results of Figs. 4.8(a-b) also show up somewhat prominently at low collision energies in Figs. 4.10(a-b).

4.3.1.3 Thermal Rate Constants

The initial state (v, j) specific thermal rate constants for the R1 and R2 channels upto 4000 K calculated within the CS approximation are shown in Figs. 4.11(a-b). The rate constants initially increase with temperature and then decrease. For the depletion channel (R1) (cf. Fig. 4.11(a)) the rate constants show an increase with the rotational

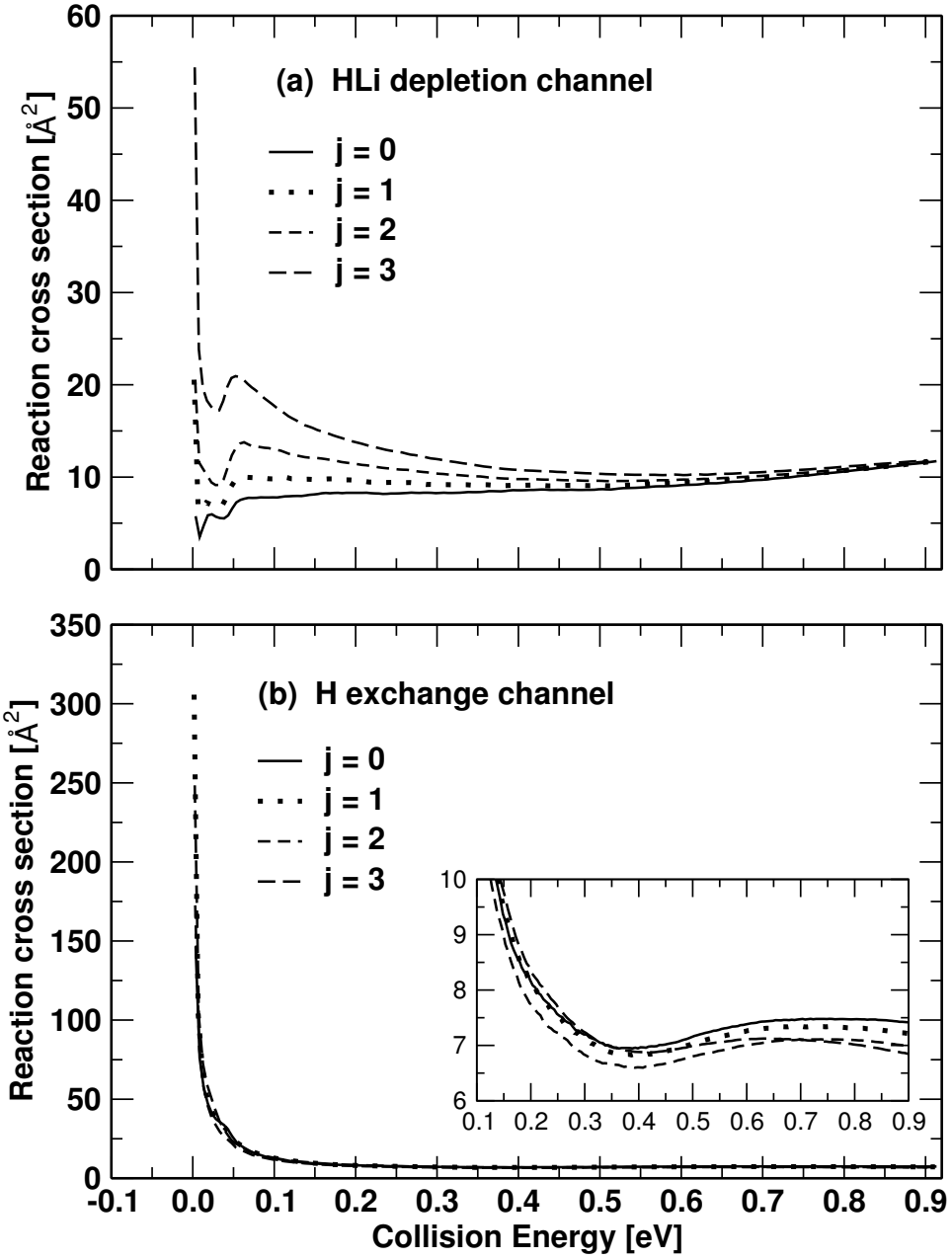

Figure 4.9: Initial state $(v = 0, j)$ selected integral reaction cross sections as a function of the (H, HLi) collision energy for the R1 (panel a) and R2 (panel b) channels. The cross sections for various j values of the reagent HLi are indicated in each panel. The reaction cross sections for the R2 channel at high energies are shown on an enlarged scale as inset in panel (b) in order to clearly reveal the differences.

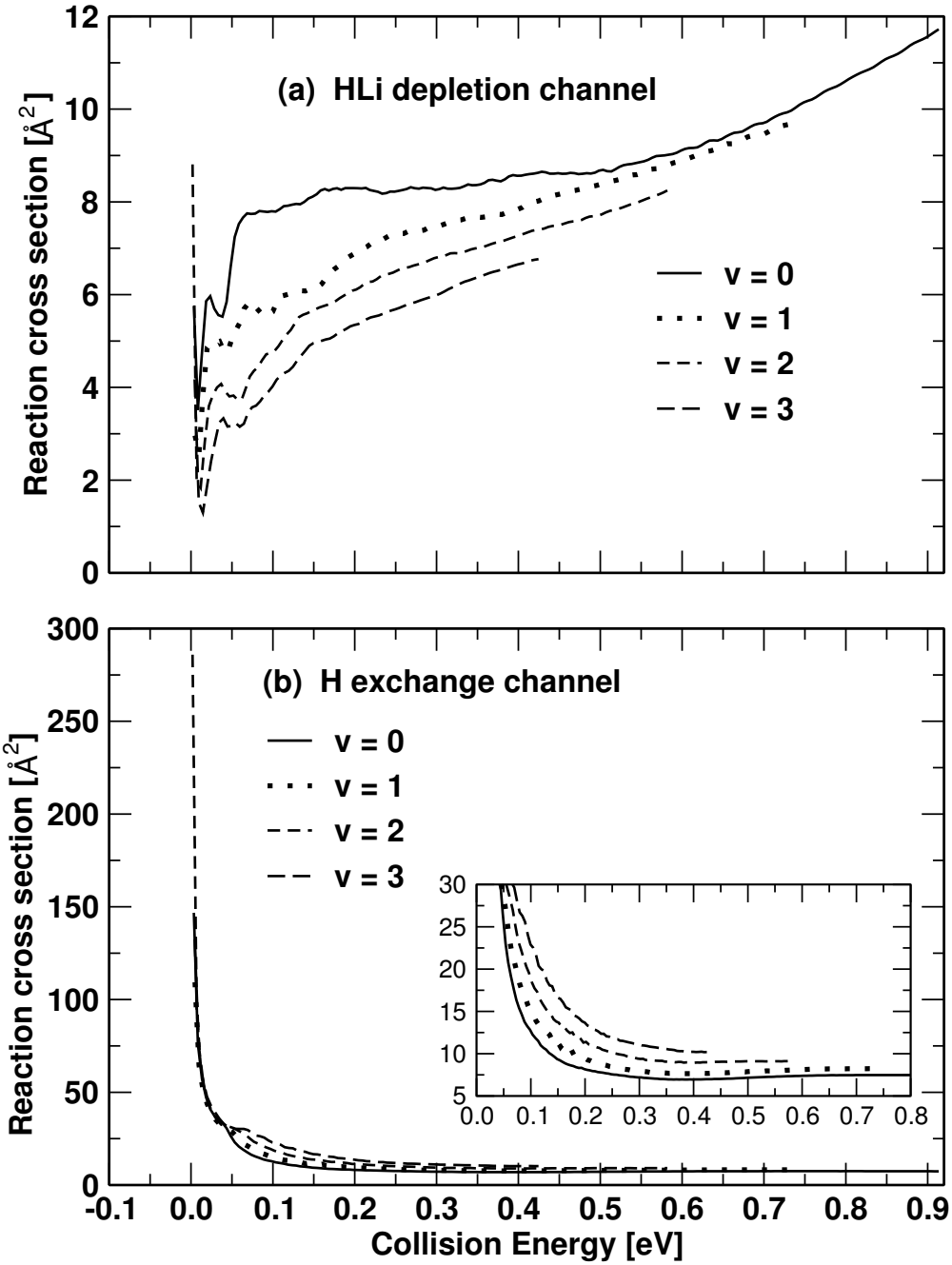

Figure 4.10: Same as in Fig. 4.9, for various v values (indicated in each panel) and $j = 0$ of the reagent HLi.

excitation of HLi at low and moderate temperatures and then approach nearly to the same value at very high temperatures. In contrast, the rate constants for the exchange channel (R2) (cf. Fig. 4.11(b)) decrease with increasing rotational excitation of the HLi molecule and finally approach to nearly the same value at high temperatures. It can be seen from Fig. 4.11(b) that the decrease in the rate constant from $j = 0$ to $j = 1$ and also from $j = 2$ to $j = 3$ is not very significant compared to the same from $j = 0, 1$ to $j = 2, 3$. The effect of vibrational excitation of the HLi molecule on the thermal rate constant is shown in Figs. 4.12(a-b), for the R1 and the R2 channel, respectively. It can be seen that the vibrational excitation of HLi causes a decrease of the rate constant for both the channels. The rate constants for the vibrationally cold HLi ($v = 0$) are much larger than those for the vibrationally hot ones [102]. This indicates that the cold HLi molecules may be efficiently depleted by reactive encounter with H atom at relatively low temperatures [61, 102].

It can be seen from Fig. 4.11 and Fig. 4.12 that the thermal rate constants for the R1 channel are lower than those of the R2 channel. This is in accord with the cross section results presented in Fig. 4.9 and Fig. 4.10, where it is seen that the cross sections for the R2 channel are much larger than those for the R1 channel at low collision energies. The cross sections for the R1 channel is higher only at high energies because of more partial wave contributions. Arrhenius plots [$\ln k(T)$ vs 1000/T] of the above rate constant results are shown in Figs. 4.13 and 4.14. The rate constants of the R1 and R2 channels are shown in panel a and b, respectively, in the above figures. A substantial deviation of the rate constant results from Arrhenius behavior can be seen from the plots. This is consistent with the absence of a barrier in H+HLi reaction [102].

The rate constants for the depletion channel for the reagent HLi ($v = 0, j = 0$) shown above are fitted to the functional form, $k(T) = aT\exp(-bT)$, as suggested by Stancil *et al.* [61] in their kinetic model of lithium reactions in the primordial gas clouds. This yields the value $a = 9.03 \times 10^{-15}$ cm^3 molecule^{-1} s^{-1} K^{-1} and $b = 0.0011$ K^{-1}.

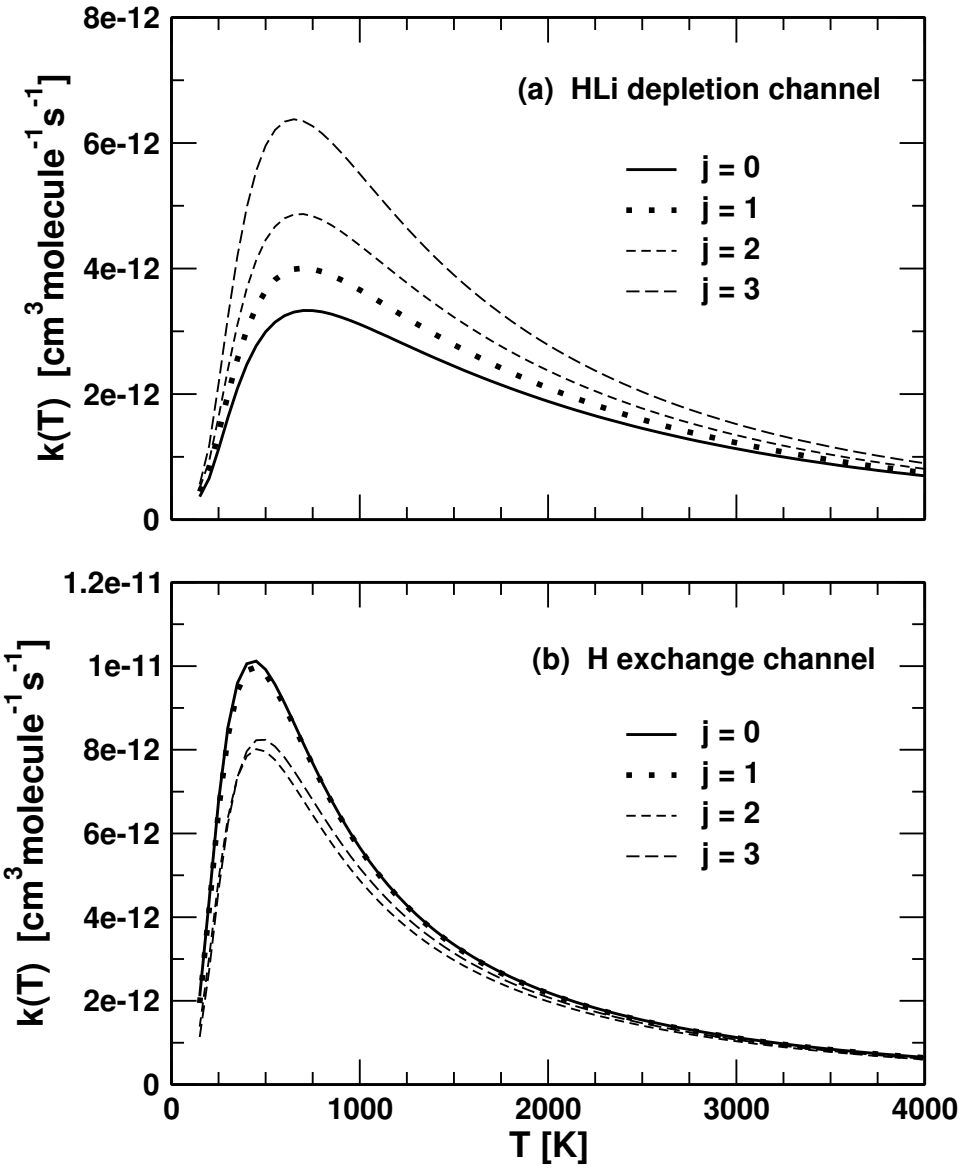

Figure 4.11: Initial $(v = 0, j)$ state selected thermal rate constants calculated from the CS model for the R1 (panel a) and for the R2 (panel b) channels. Thermal rate constants for vibrationally-selected and for various j values of the reagent HLi are indicated in each panel.

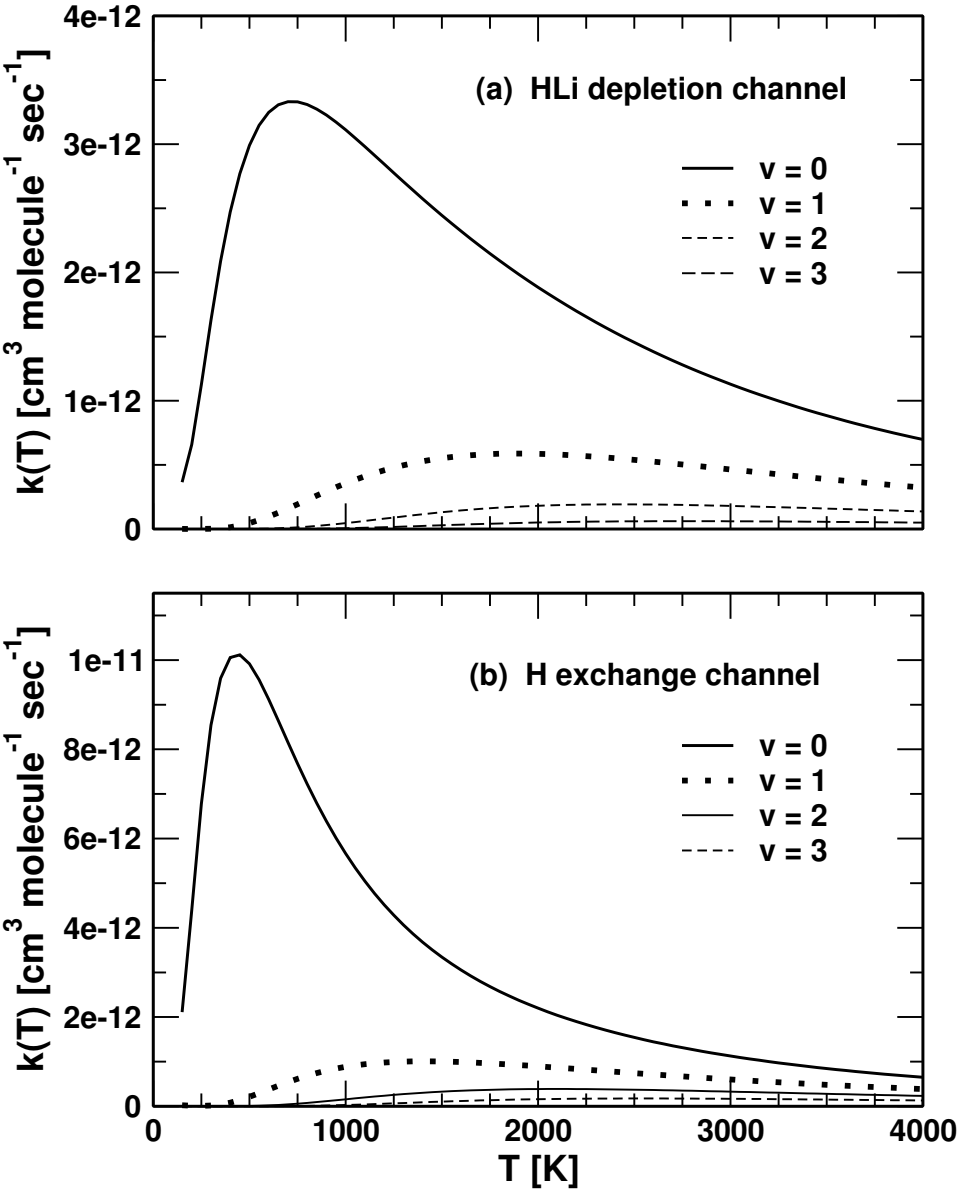

Figure 4.12: Same as in previous Fig. 4.11, for various values of v (indicated in each panel) and $j = 0$ of the reagent HLi in (H, HLi) collisions.

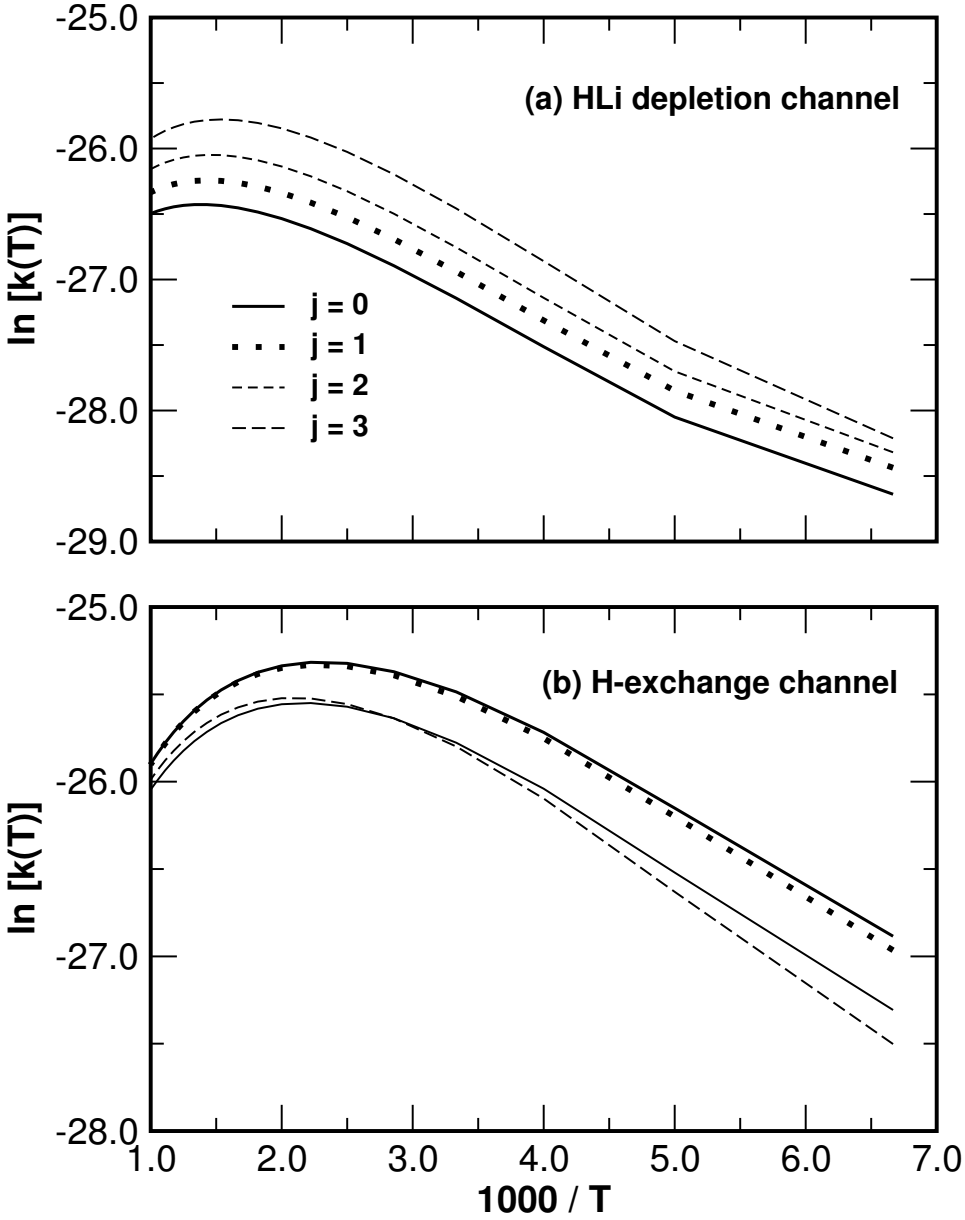

Figure 4.13: Arrhenius plots of the rate constants (cf. Figs.4.11) for the R1 and R2 channels are shown in panel a and b, respectively.

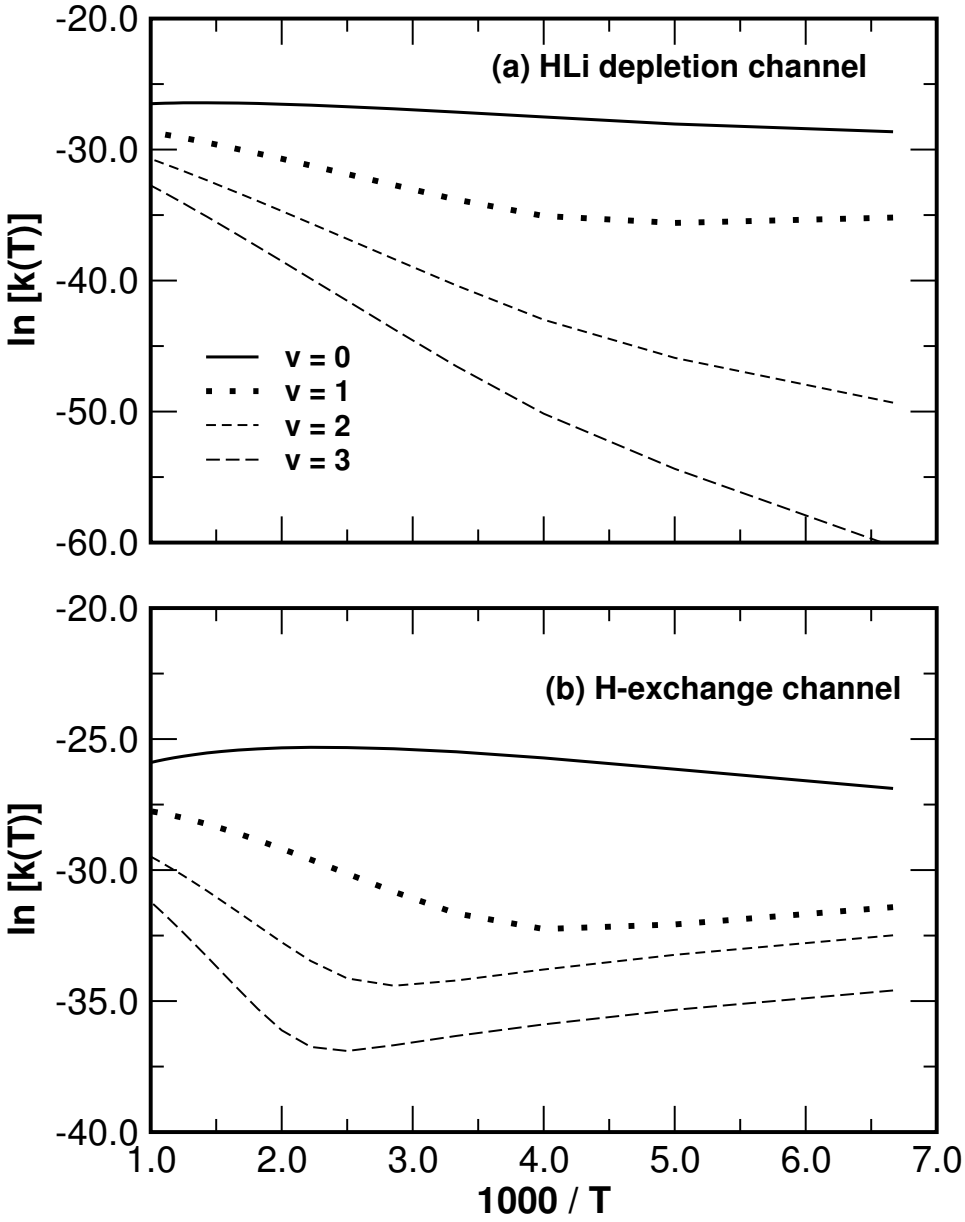

Figure 4.14: Same as in Fig. 4.13, for various values of v and $j = 0$ of the reagent HLi (cf. Fig. 4.12).

These may be compared with $a = 6.6 \times 10^{-14}$ cm^3 molecule^{-1} s^{-1} K^{-1} and $b = 0$ estimated by Stancil *et al.* [61] and with $a = 8.4 \times 10^{-13}$ cm^3 molecule^{-1} s^{-1} K^{-1} and $b = 0.0004$ K^{-1} estimated by Dunne *et al.* [91]. We note that the latter values result from a fit to the initial state averaged thermal rate constant while our values represent the results of a fit to the initial state specific thermal rate constant.

4.3.2 CS versus JS models: Reaction Cross Section and Thermal Rate Constant

The initial state-selected and energy resolved reaction probabilities for all partial waves are also computed (from the $J = 0$ reaction probability results by the energy-shifting, as stated in Eq. (2.127)) [102] using the standard [95] as well as the uniform [97] JS approximations for the H+HLi system. It can be seen from Fig. 4.15 that the resonance structures which occurs in the reaction probabilities for $J = 0$ survive even in case of $J \neq 0$ reaction probabilities calculated by the JS approximations [102]. Summing up the contributions from all these partial waves yields the integral reaction cross sections and a further averaging of the latter yields thermal rate constants. Thermal rate constants upto 4000 K are calculated for the both channels (R1 and R2) using the both standard as well as uniform JS approximations.

We now discuss the rate constant results obtained by the standard JS approximation. The crucial quantity to be determined here is the rotational constant B of the possible transient species. In order to apply the standard JS equation for the rate constant [Eq. (2.130)], we determined B by optimizing the geometry of the possible transient species of the H+HLi system at the MP2 level of theory employing a cc-pVTZ basis set of Dunning [213]. The calculations are performed with the Gaussian 03 program package [214]. At this level of theory we found a more stable $C_{\infty v}$ "transition state" of the HHLi species with an imaginary frequency of $429.776i$ cm^{-1}. The H-H and H-Li distances at the transition state are 1.612Å and 1.736Å, respectively. The value

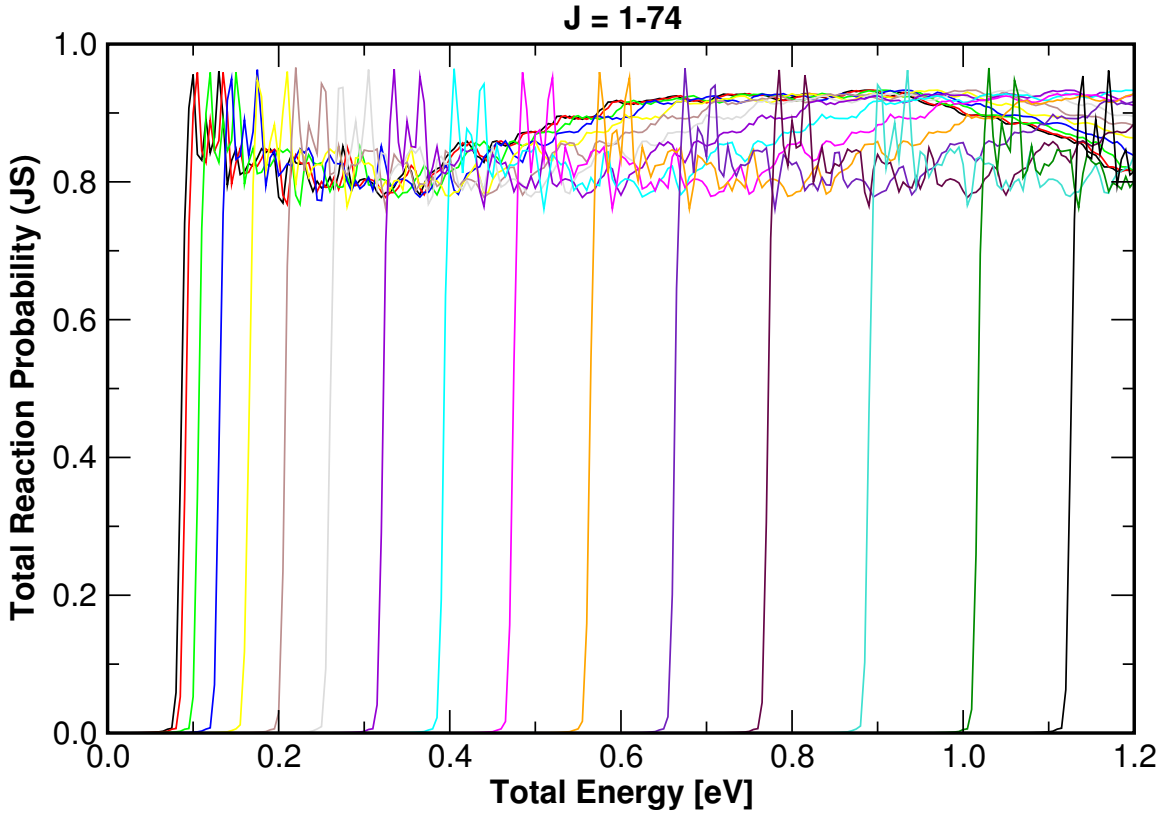

Figure 4.15: The initial state-selected total reaction probabilities as a function of the total energy for the H + HLi ($v = 0, j = 0$) collision for various J values, within the standard JS approximation.

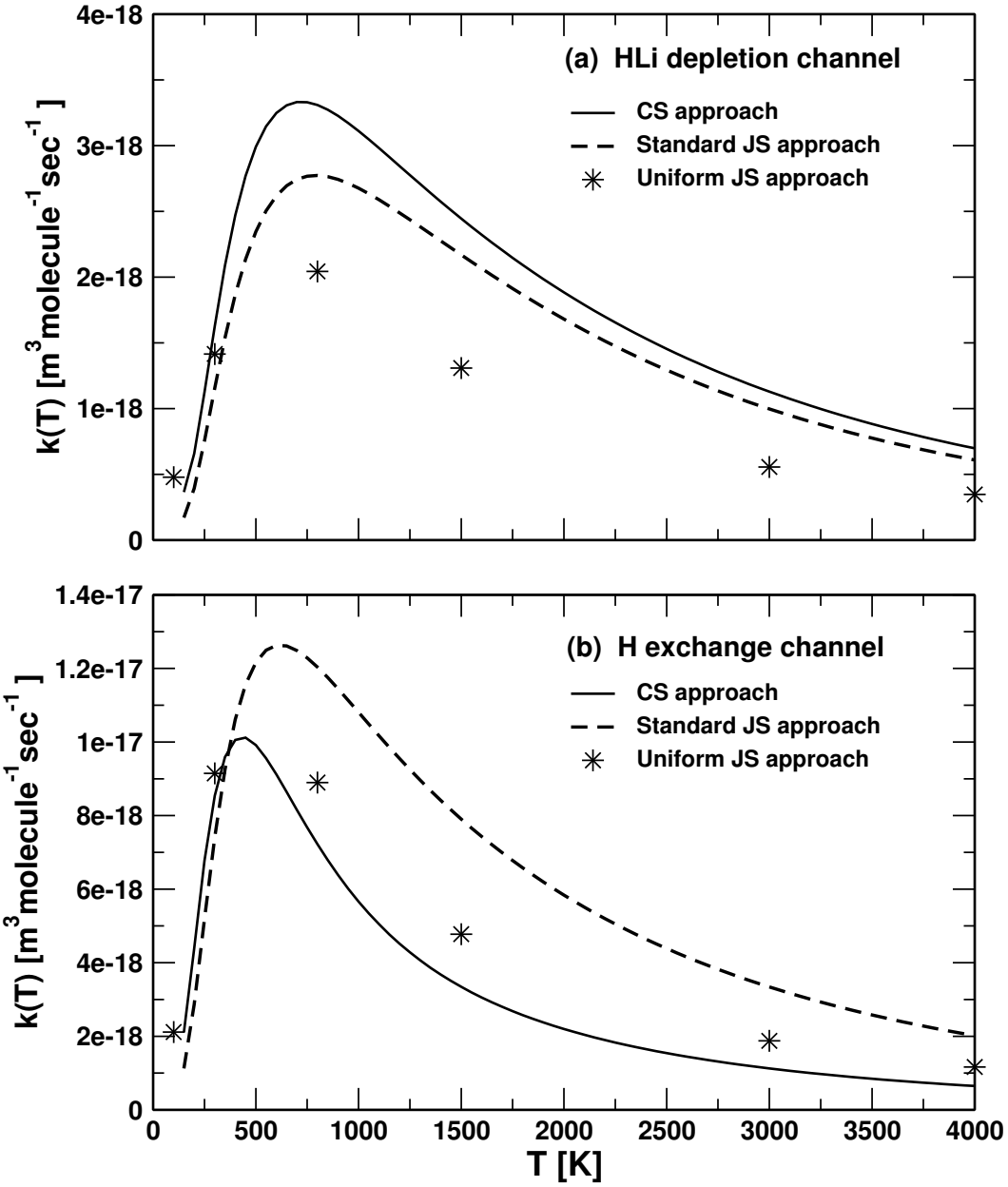

Figure 4.16: Thermal rate constants for the H + HLi ($v = 0, j = 0$) collisions obtained by the CS approach (solid line), standard JS approach (dashed line) and the uniform JS approach (asterisks) for the R1 (panel a) and R2 (panel b) channels.

Table 4.2: The temperature and J dependence of the rotational constant B, used in the rate constant calculations using the uniform JS approximation.

	$B(T)$ $\times 10^3$ eV					
Range of J values	100 K	300 K	800 K	1500 K	3000 K	4000 K
0 - 8	0.0513	0.1614	0.2803	0.3841	0.4973	0.5372
9 - 16	0.0109	0.1279	0.2122	0.2860	0.3713	0.4075
17 - 28	0.0170	0.1834	0.3034	0.3660	0.4231	0.4477
29 - J_{max}	0.0444	0.1532	0.2130	0.2746	0.3540	0.3916

of B for this transient species is found to be $\sim 1.874\times10^{-4}$ eV. The latter is used to determine the rate constant for all temperatures in the standard JS approximation. In the next step, the temperature as well as the J dependence of the rotational constant are calculated using Eq. (2.132), and the J-dependent probability values obtained from the CS calculations. In this way, the variation of B with temperature as well as J is incorporated in the rate constant equation [Eq. (2.135)] of the uniform JS scheme. The B values are calculated for six different temperatures and in the range of J values, 0-8, 9-16, 17-28 and 29-J_{max} and are used to determine the rate constants using the uniform JS equation [Eq. (2.135)]. The resulting B values are given in Table 4.2. Using these B values the thermal rate constants are evaluated in this scheme.

The rate constant results obtained with the above schemes for the R1 and R2 channels in the H + HLi ($v = 0, j = 0$) collisions are shown in Figs. 4.16(a-b), respectively, along with the corresponding CS results. The CS, standard JS and uniform JS results are shown by the solid line, dashed line and asterisks, respectively. Apparently, the uniform JS is a better approximation to the CS results for the exchange channel R2, whereas, the standard JS appears to be a good approximation to the CS results for the depletion channel R1. At low temperatures, both the JS approximations reproduce the CS results reasonably well for both the channels [102].

To this end, we mention that although the CS model worked quite satisfactorily for many bimolecular chemical reactions [138, 162, 163, 211, 215, 216], the inclusion of

the Coriolis coupling terms in the Hamiltonian has also been found to be very crucial for some reactions [49–51, 163]. The CS model sometimes underestimates the reaction cross sections and reaction rates. The variation of reaction cross section with reagent rotational excitation has been found to follow an opposite trend compared to the exact quantum mechanical results for the H+D_2 reaction [163]. Therefore, an estimate of the exact quantum mechanical cross sections and rates including the CC terms in the Hamiltonian is valuable in order to assess the accuracy of the CS model for the H+HLi reaction. Such a study is also undertaken and is discussed in the section below.

4.3.3 Coriolis-coupled Reaction Dynamics

In this section, we present and discuss the effect of CC on the initial state-selected integral reaction cross sections and temperature dependent rate constants for both the R1 and R2 channels and compare them with the same obtained using the JS [95,97] and the CS [98,99] approximations. The CC reaction probabilities are reported for collision energies upto 0.75 eV [103]. The reaction cross sections and thermal rate constants are calculated by averaging these probability results over all partial wave contributions.

4.3.3.1 Computational Details

The properties of the initial WP and the grid parameters used for the numerical calculations are listed in Table 4.1. The initial state-selected integral reaction cross sections are calculated using Eq. (2.122) for a specified rovibrational state of HLi molecule. The WP is propagated for a total of $\sim$ 276 fs using the CP scheme. The norm of the WP typically comes down to 2.2×10^{-3} at the end of the time propagation. Therefore, all major dynamical events are expected to be over within this time period. It is well known that the stability of the CP scheme depends on the maximum allowed energy on the grid. For the potential energy, one generally sets a cut-off value to control the stability. The angular kinetic energy on the grid depending on the j_{max} $(= N_\gamma - 1)$ and J is usually large. Very large values of this kinetic energy are unphysical and the

relevant wavefunction does not contain any components corresponding to them. In the present application the maximum permitted value of the angular kinetic energy is therefore truncated gradually above a reasonable value [193]. All the calculations reported here are carried out with HLi in its vibrational and rotational ground state ($v = 0, j = 0$). Each WP propagation upto 276 fs on a single processor takes nearly 60 hours of CPU time in a IBM P690 machine. The maximum allowed value of K (K_{max}) is considered upto 4. For instance, $K = 3$ state can couple with the $K = 2$ and $K = 4$, whereas $K = 4$ state can couple only with $K = 3$ not with $K = 5$ since $K_{max} = 4$. Similarly, $K = 0$ state can couple only with $K = 1$ because only positive values of K are considered here. The parity is included in the dynamical calculation, which is decided by the $(-1)^{J+p}$ value.

The convergence of the CC reaction probability results upto the total energy $E \sim 0.84$ eV (collision energy ~ 0.75 eV) and for each J and K values is explicitly checked with respect to the numerical parameters given in Table 4.1. Partial wave contribution upto $J = 30$ is required to obtain the converged cross section results. This can be estimated from the J dependence of the degeneracy weighted reaction probabilities for the channel R1 and R2 shown in Figs. 4.17(a-b), respectively. It can be seen from the figure that the partial wave contribution increases with increasing energy. Typically, we find about 10% error in the reaction probability results for some energies at higher J (>18) values.

4.3.3.2 Reaction Probabilities

The initial state-selected and energy resolved reaction probability as a function of the total energy E are plotted in Fig. 4.18 for the total angular momentum, $J = 1$ and for $K = 0, 1$. The reaction probabilities for the HLi depletion (R1) and the H-exchange (R2) channels are shown in panel (a) and (b), respectively. In each panel, the CC reaction probabilities are shown and compared with the CS results for each values of J and K. The latter are distinguished in terms of different line types in panel (b).

The initial and most probable collision energy of the GWP is chosen to be 0.55 eV and the total energy is measured relative to the minimum of the HLi potential [see Fig. 3.6]. The reaction probabilities pertinent to a channel is calculated by integrating the reactive flux flowing into it (cf. Eq. (2.113)). The CC reaction probabilities reported here are calculated at an energy interval of 0.005 eV and summed over all open vibrational (v') and rotational (j') levels of the product molecule at a given energy. The channel specific reaction probability results for $J = 0$ [101] and for $J \neq 0$ [102] indicated a sharp resonance structure at low energies (near the onset) for both the channels. The resonances are found to be less pronounced at high energies. Also the signature of resonances gradually disappears for higher values of J. We characterized some of these resonance structures in a subsequent study, for $J = 0$ [104] as well as for $J \neq 0$ [105] including the CC. These are discussed in Chapter 5.

The CS calculations are carried out for a fixed value of the K quantum number, whereas in the exact (CC) calculations K is a variable quantity and is allowed to vary between 0 to $min(J, K_{max})$. A comparison of the two probability results (CS vs. CC) in Figs. 4.18(a-b) reveals no noticeable effects of CC on the resonance oscillations in the reaction probability curves. Resonance oscillations are only mildly quenched in the CC results. However, as observed before and also revealed by the present results that the resonances tend to become broader when CC is included in the dynamics. The reaction probabilities for the H-exchange channel are generally higher than the HLi depletion channel over the studied energy range. The resonances in the CC results do survive at lower energies near the onset of the reaction even for higher values of J. The DMJ PES [91] does not have a barrier and therefore, H+HLi reaction does not have a threshold on this PES, this is observed in the $J = 0$ reaction probabilities [101]. However, for $J \neq 0$ collisions, the reaction acquires a threshold energy due to the presence of a centrifugal barrier. All CC results reveal that the H-exchange channel is dominant over the HLi depletion channel even for the higher values of J [103].

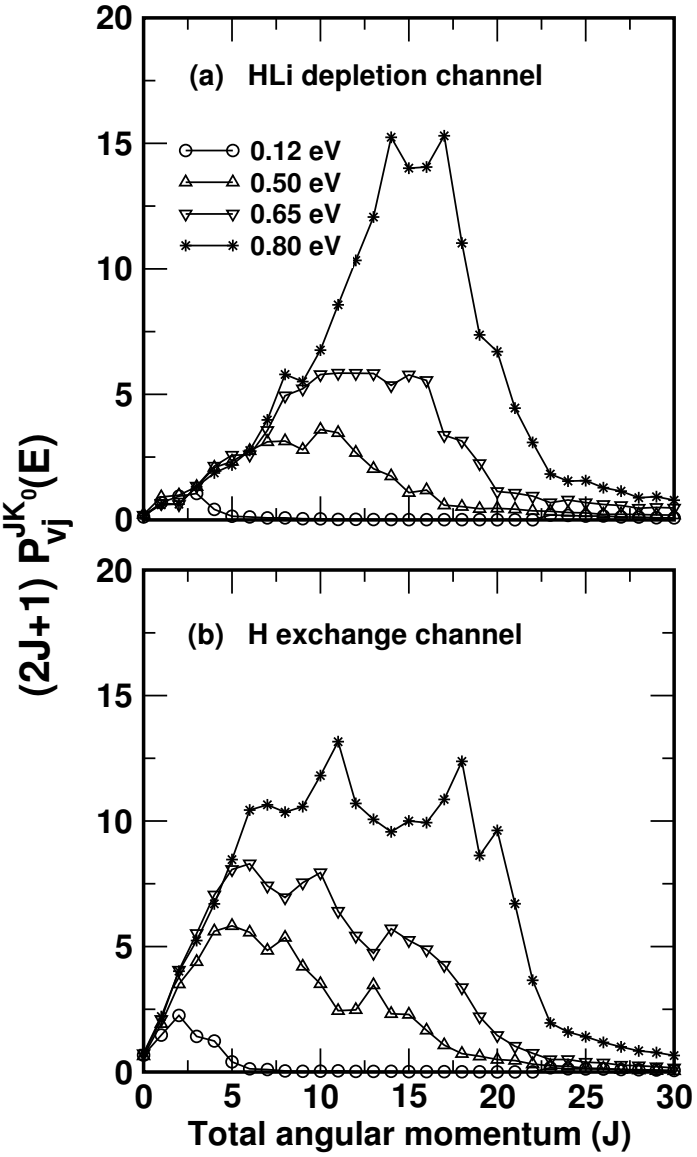

Figure 4.17: Weighted CC partial-wave contributions to the cumulative reaction probability and integral reaction cross sections of the R1 (panel a) and R2 (panel b) channels at various values of collision energy (indicated in panel a).

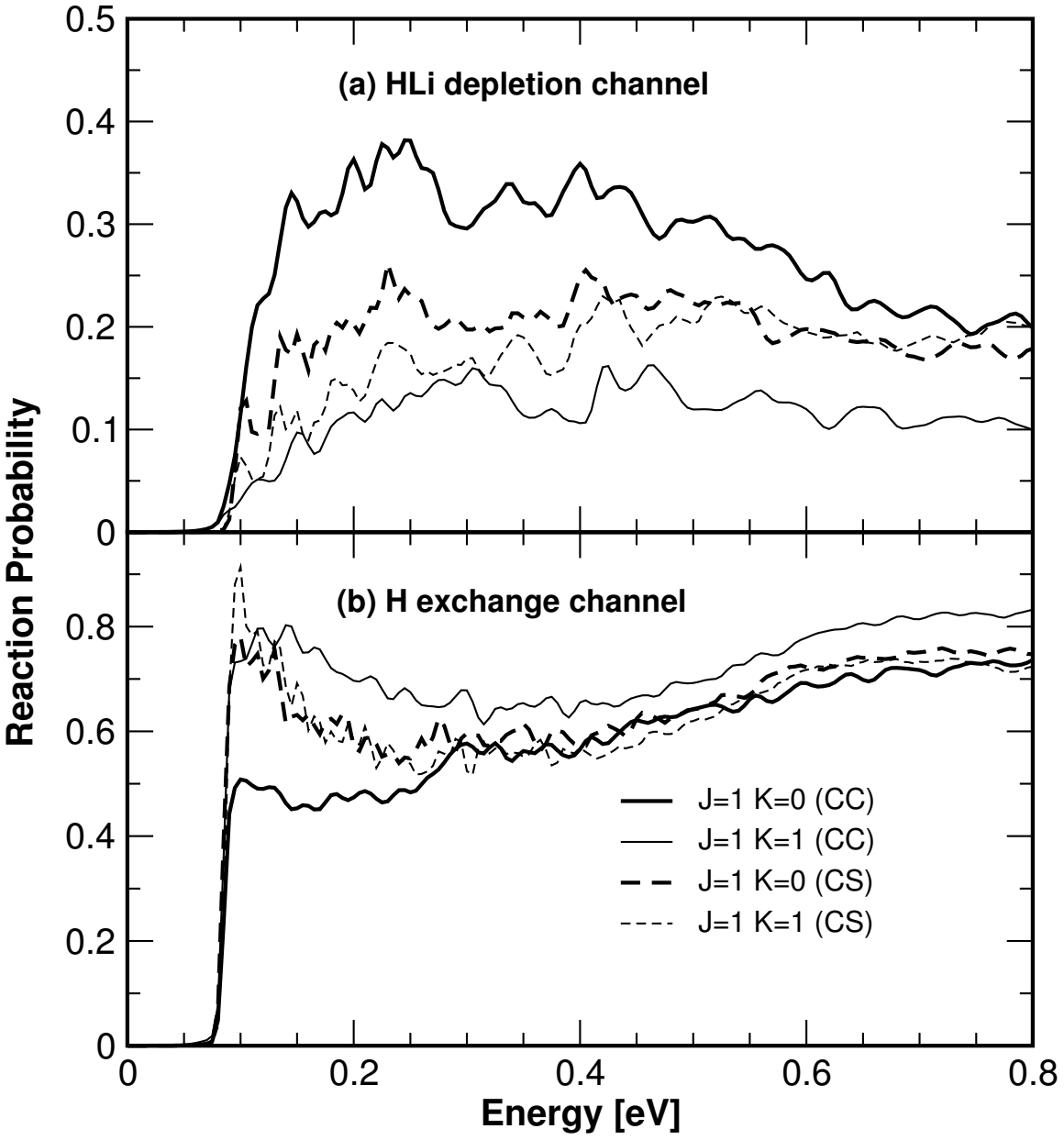

Figure 4.18: The H+HLi ($v = 0, j = 0$) reaction probabilities as a function of the total energy (H-HLi translational + HLi rovibrational) for the total angular momentum $J = 1$ and for $K = 0, 1$ calculated using the CC and the CS model for the HLi depletion (panel a) and H-exchange (panel b) channels. The different line types are identified in panel b. The energy is measured relative to the minimum of the HLi potential which sets the interaction potential to zero for $R \to \infty$.

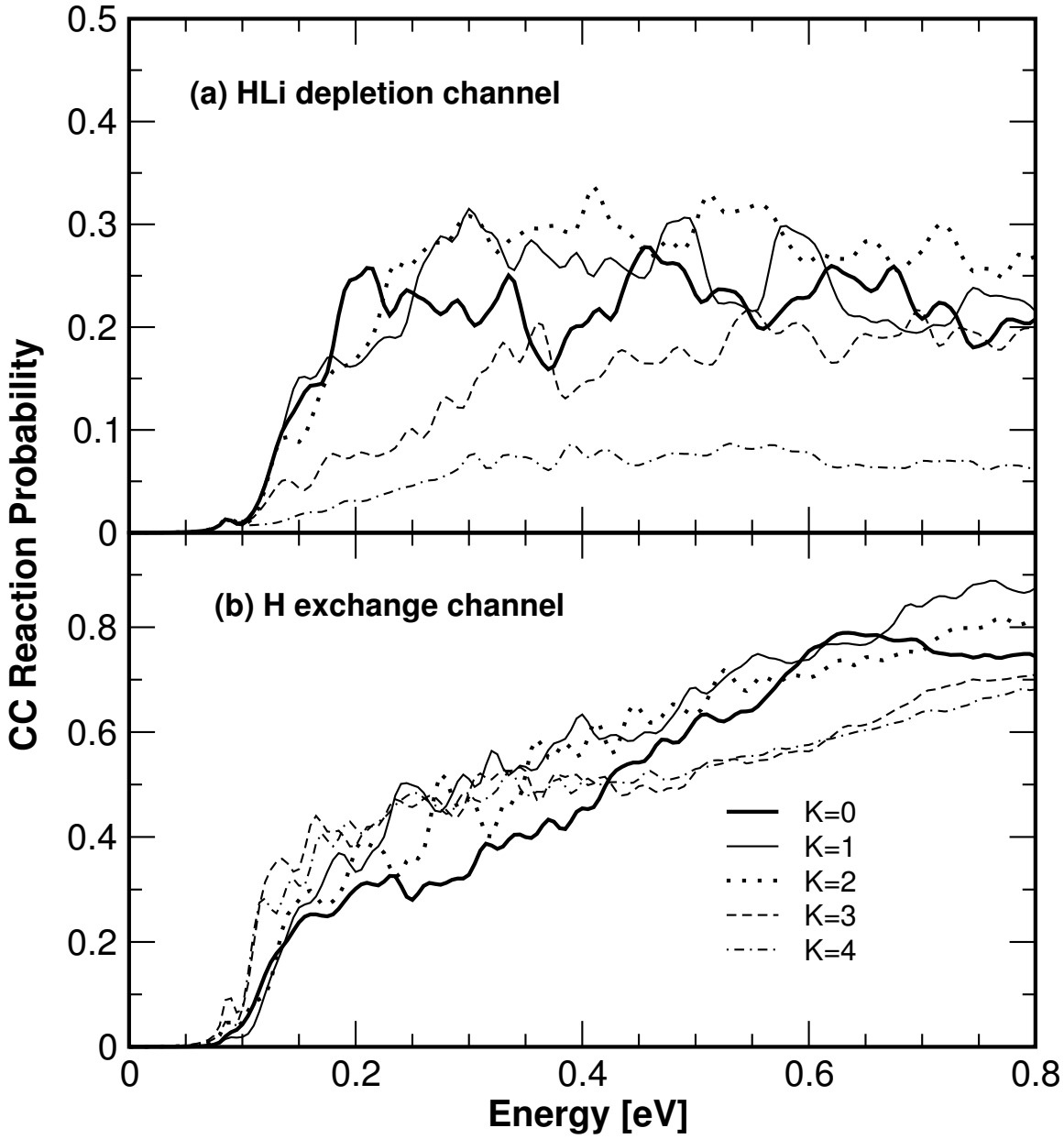

Figure 4.19: Same as in Fig. 4.18, only CC reaction probabilities are shown for $J = 4$ and $K = 0 - 4$. The meaning of different line types is given as legend in panel b.

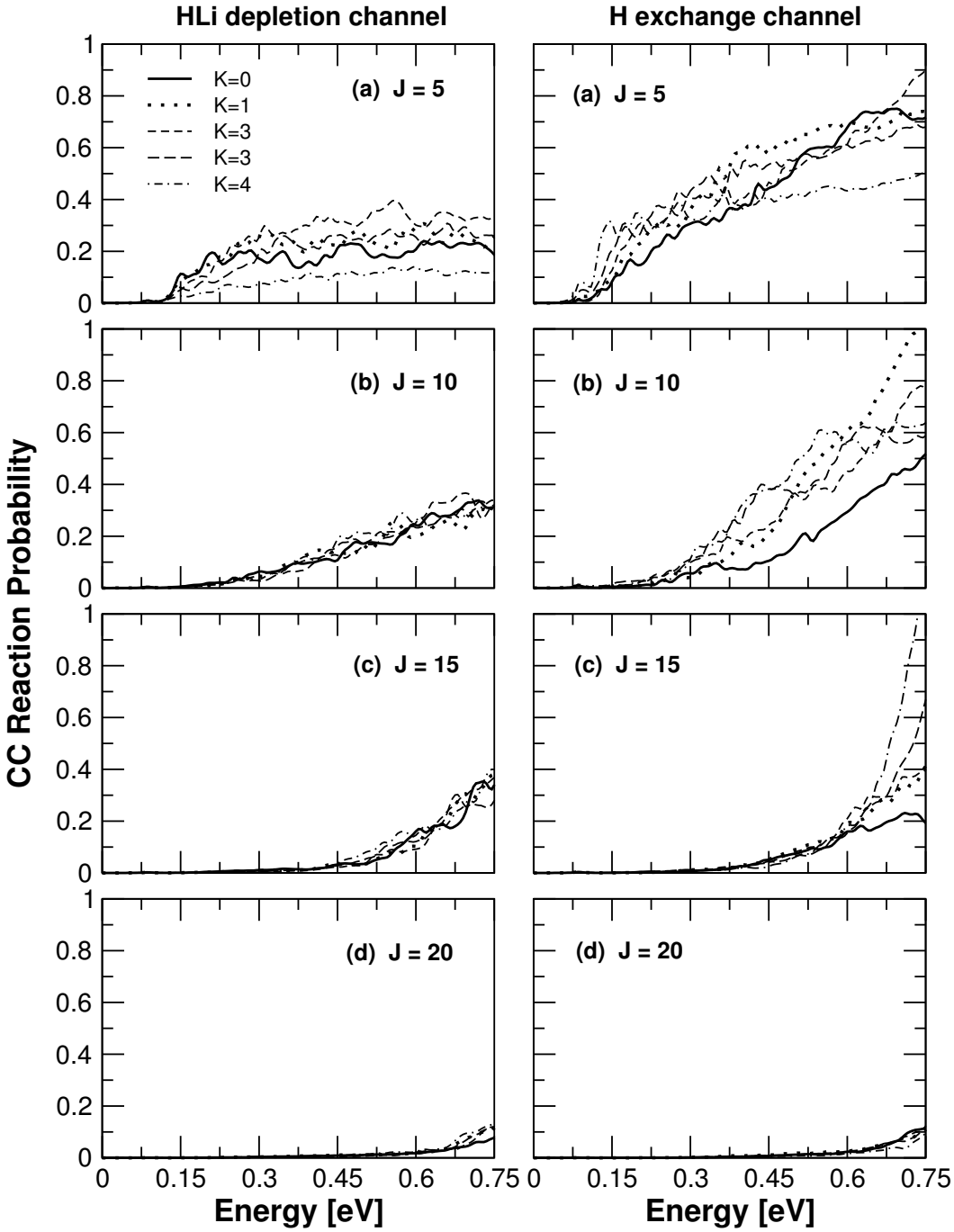

Figure 4.20: Same as in Fig. 4.18, the CC reaction probabilities are shown for different J values (indicated in each panel) and $K = 0 - 4$. The different line types are identified in panel a (upper left corner) and the probabilities for the R1 and R2 channels are shown in the left and right column of the figure, respectively.

The CC reaction probabilities for both the R1 and R2 channels are shown in Figs. 4.19(a-b), respectively, for $J = 4$ and for $K = 0 - 4$. The probability curves are identified in panel (b). It can be seen that the R2 channel is preferred over the R1 channel at this higher value of J and also weak resonance oscillations in the probability curves still survives.

In Fig. 4.20 we show the CC reaction probabilities for various values of the total angular momentum, $J = 5, 10, 15$ and 20, for $K = 0-4$. The identity of the probability curves is given in panel (a) at the upper left corner of the figure. The probabilities for the channel R1 and R2 are shown in the left and right column of the figure, respectively. It can be seen that the reaction path R2 is generally preferred over R1 within the reported energy range. For $J = 5$ the reaction probability curves show some resonance oscillations which survive at low energies for both the channels. These resonance oscillations are gradually lost with increasing values of J (cf. Figs. 4.20(c-d)). This is consistent with our earlier observations that the resonances tend to become broader with increasing J. The onset of the reaction also shifts to higher energies with increasing J, because of an increase in the height of the centrifugal barrier.

4.3.3.3 Reaction Cross Sections and Thermal Rate Constants

The initial state-selected and channel specific integral reaction cross section, as a function of collision energy in H + HLi ($v = 0, j = 0$) scattering is shown in Fig. 4.21. These cross sections are obtained by summing up different partial wave contributions with appropriate weight to the reaction probability using Eq. (2.122). The cross sections for both the R1 and R2 channels obtained in the CC and CS models are shown, and distinguished by different line types (indicated in the panel) in Fig. 4.21. For a clearer representation, the cross sections at low collision energies are shown in an enlarged scale and included as an inset in Fig. 4.21. It can be seen from Fig. 4.21 that the CS results are generally larger than the CC results for both the channels at low collision energies. The overall pattern of variation of the cross section results is similar

in both the models. This indicates no dramatic influence of the CC on the reaction mechanism. The weak resonance features seen in the CS results near the onset of both the channels are absent in the CC results. The reaction cross section values are much larger near the onset of both the channels R1 and R2 and suddenly decrease to lower values with increasing collision energy. This is consistent with the characteristics of a barrierless reaction [3]. A large decrease in the reaction cross section beyond the onset implies a substantial flow of WP flux to the NR channel.

The initial state-selected thermal rate constants for the R1 and R2 channels up to 1200 K calculated using Eq. (2.124) are shown in Fig. 4.22. Both the CC and CS rate constants are plotted and the convergence of the results in the given temperature range is explicitly checked. The curves are identified by labeling each of them in the panel. We note that these represent the initial state-selected rate constants pertinent to HLi ($v = 0, j = 0$). The CS results are modified slightly compared to our earlier results [Sec. 4.3] as a more exact expression of the vibrational and rotational partition functions are used here [see Eqs. (2.126c) and (2.126d)]. The behavior of the rate constant curves are analogous to those reported by Defazio *et al.* [93] obtained using the state-to-state reaction probability and a JS approximation. It can be seen from Fig. 4.22 that the CS rate constants are smaller than the CC rate constants at low temperatures: upto $\sim$ 650 K for the R1 channel and upto $\sim$ 300 K for the R2 channel. At high temperatures, the CS results are consistently larger than the CC results and the differences is more in case of R2 than R1 channel. The Coriolis terms, therefore, effectively reduces the reaction rate constants at higher temperatures for both the R1 and R2 channels. The pattern of variation of the rate constant results with temperature reveals a substantial deviation from the Arrhenius behavior for both the channels within this temperature range. This point is also discussed at length by Defazio *et al.* [93]. The convergence of the present rate constant results is improved compared to our previous CS results. A close look at the values of the reaction rate for both the channels clearly indicates that the R2 channel is preferred over the R1 channel in the given temperature range.

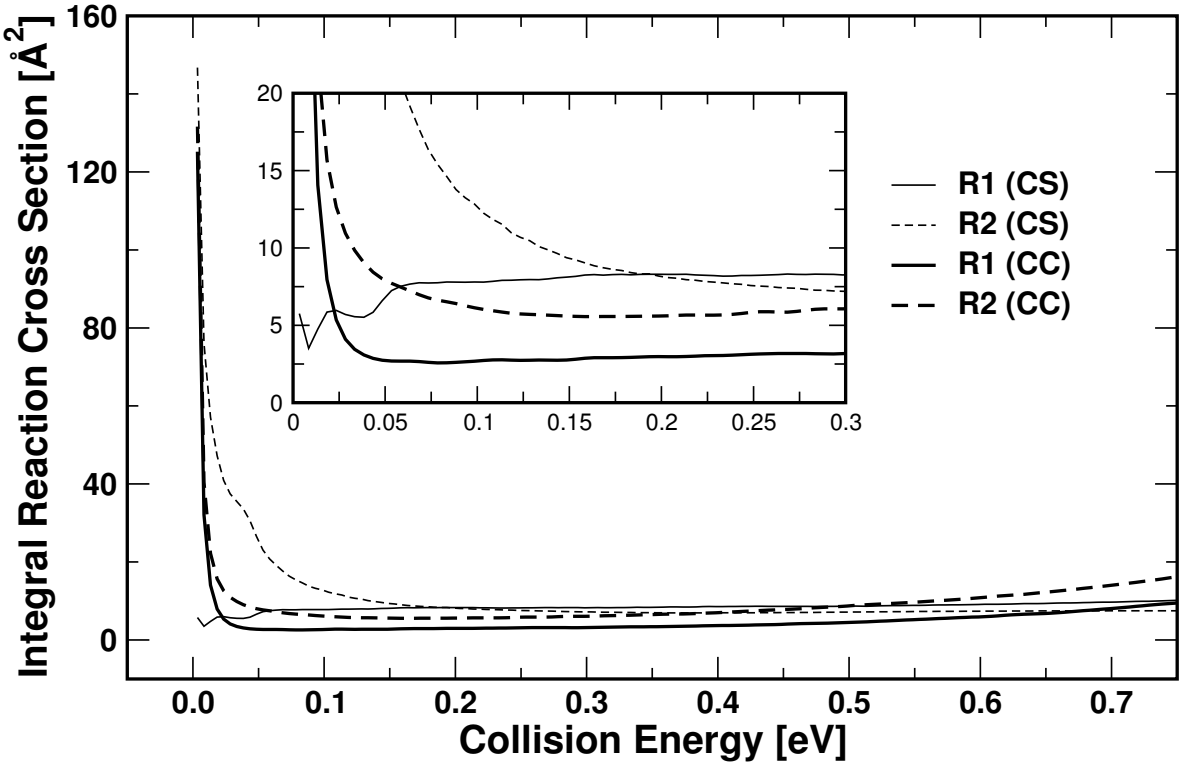

Figure 4.21: Initial state-selected integral reaction cross sections for the H+HLi ($v = 0, j = 0$) collisions as a function of the (H,HLi) collision energy for the R1 and R2 channels, obtained from the CC and CS models, are shown in the panel. The different line types are identified by suitably labeling them in the panel. The cross sections are shown in an enlarged scale (as inset) in panel in order to clearly reveal the effects of CC on the reaction dynamics.

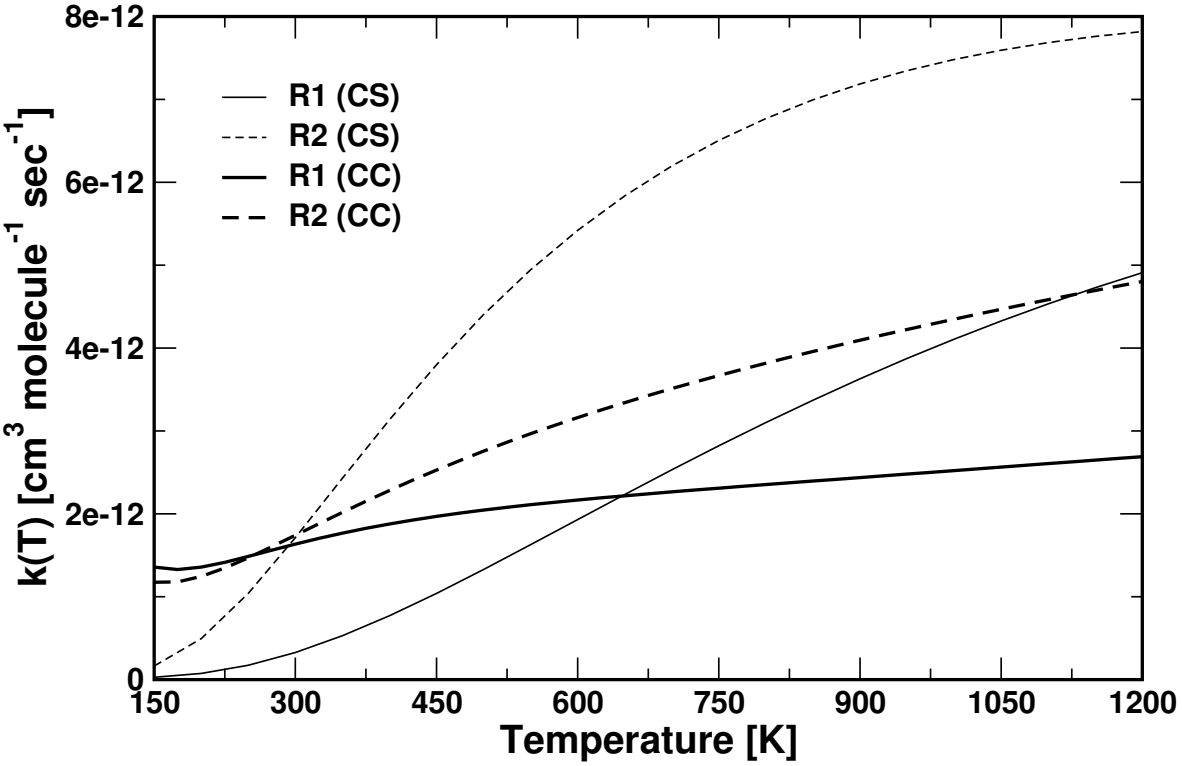

Figure 4.22: Initial state-selected thermal rate constants for the H+HLi ($v = 0, j = 0$) reaction. The rate constant results for both the R1 and R2 channels calculated using the CC and CS models are shown in the panel. Different rate constant curves are identified by labeling them in the panel.

Table 4.3: The present CC rate constant results for the HLi depletion channel fitted to the functional form $k(T) = aT\exp(-bT)$. The numerical values of the fit parameters a and b are listed along with the available literature results.

Method	a [cm^3 molecule^{-1} s^{-1} K^{-1}]	b [K^{-1}]
CC (present)	7.35×10^{-15}	0.0004
JS (Standard)	7.17×10^{-15}	0.0010
JS (Uniform)	6.62×10^{-15}	0.0013
CS (revised)	2.19×10^{-15}	0.0006
Stancil *et al.* [61]	6.60×10^{-14}	0.0000
Dunne *et al.* [91]	8.40×10^{-13}	0.0004

At lower temperature the two rate constants are very close to each other. We do not extrapolate them to ultracold conditions as the present cross section results are not obtained in such conditions.

The initial state-selected thermal rate constants for the depletion reaction R1 shown above are fitted to the functional form, $k(T) = aT\exp(-bT)$, as before. The values of a and b obtained from the present fits are given in Table 4.3. The given parameters represent the rate constants well, beyond room temperature. It can be seen from Table 4.3 that the fit parameters obtained from the CC results are larger than those obtained from the CS results for the R1 channel and very close to the JS results. The empirical results of Stancil *et al.* [61] and also the QCT results of Dunne *et al.* [91] are also given in the table. The difference between our results and that of the latter authors is presumably due to the initial state-averaged nature of their rate constant data.

4.4 Summary

We presented a detailed theoretical investigation of the channel specific cross section and thermal rate constant of the H+HLi scattering dynamics. The results obtained within the various approximate schemes like JS and CS models (as stated in Chapter 2) are discussed. Finally, we presented the results obtained from full-dimensional calcu-

lations (including the Coriolis terms) and compared them with those from the reduced dimensional calculations.

The reaction cross sections are obtained by summing up the partial wave contribution upto $J = 74$ to the initial state-selected reaction probabilities in the JS and CS models [102]. It is found that the H-exchange channel (R2) dominates over the HLi depletion channel (R1) at low and moderate collision energies. At high energies the depletion channel (R1) is preferred. For a given collision energy the number of partial waves necessary to obtain the converged reaction cross section is more for the R1 than for the R2 channel. The reaction is intrinsically barrierless, however, for higher values of J the centrifugal barrier adds a small threshold to the reaction. The cross section results for both the channels exhibit a large value near the onset of the reaction. While the cross section for the R1 channel show an increase with the rotational excitation of HLi at low energies, the cross section for the R2 channel exhibits a slight decrease. The cross section for the R1 channel decreases and that for the R2 channel slightly increases with the vibrational excitation of the reagent HLi at low collision energies. The resonance oscillations seen in the reaction probability curves mostly average out with many partial wave contributions and show up as very mild oscillations in the CRP results only at low collision energies. These oscillations in turn appear somewhat prominently in the cross section results due to the contribution from the π/k_{vj}^2 factor in Eq. (2.122).

The thermal rate constant for both the R1 as well as the R2 channels deviates substantially from the Arrhenius behavior. While the rate constants for the R1 channel increase with the rotational excitation of HLi, the same for the R2 channel show a decrease at low temperatures. With vibrational excitation of HLi the rate constants show a consistent decrease over the entire temperature range for both the channels [102]. The latter supports the conjecture that the cold HLi molecules can be depleted efficiently by reactive encounter with H atom at relatively low temperatures [61].

Both the standard as well as uniform JS approximations reproduce the CS results reasonably well for both the channels, at low temperatures [102]. These approximations underestimate the rate constant for R1 channel and overestimate for R2 channel when compared with the CS results at high temperatures [cf. Fig. 4.16].

The effect of CC on the initial state-selected integral reaction cross sections and thermal rate constants obtained from full-dimensional calculations is reported. The calculations of reaction probability are carried out upto $J = 30$, required to obtain the converged reaction cross sections upto a collision energy of ~ 0.75 eV. The coupling between the neighboring K states are considered upto $K_{max} = 4$. The resonance oscillations in the reaction probability curve tend to become broader on inclusion of the CC terms. The integral reaction cross sections are generally lower in the CC model when compared to the same obtained from the CS model, for both the R1 and R2 channels. The integral reaction cross sections of the H-exchange channel R2 are larger than those of the HLi depletion channel R1. The cross sections does not have a threshold indicating the feature of a barrierless reaction which is again reflected in substantial deviation of the thermal rate constant results from the Arrhenius behavior [102, 103]. The rate constants for both the channels are very close to each other at low temperatures and the exchange rate is more than the depletion rate at high temperatures. The CC lowers the rate constant of both the channels at high temperatures when compared to the CS results.

Chapter 5

Resonances in the H+HLi Scattering

5.1 Introduction

The phenomenon of *resonance* is ubiquitous in a wide range of physical and chemical processes. Resonances are the most delicate and important results of quantum scattering theory [217]. They play an important role in a wide variety of atomic and molecular processes [218,219]. They originate due to the formation of metastable quasibound intermediates during a collision event and drive the subsequent scattering process through an indirect path. Therefore, the study of resonances in a chemical reaction is very important to understand the structure of the reactive transition state and hence the reaction mechanism [217, 220–223].

The resonances are generally identified by either a scattering theory approach or a bound-state like approach. In a scattering theory approach, the resonances are identified from the energy dependence of the scattering matrix, whereas in the latter resonances are treated as a quasibound complex and they are calculated by monitoring the unimolecular dissociation of it. Moreover, in a bound-state like approach the time au-

tocorrelation function is recorded and a Fourier transform of this function to the energy domain yields peaks at distinct energies that are directly attributable to the resonances. The width of these peaks gives an estimate of their lifetimes and their eigenvectors can be calculated by the spectral quantization algorithm [224–228].

The existence and characteristics of short-lived reactive resonances have been the subject of much discussion over the years. The studies provided the much needed insight into the dynamical origin of complex formation. More specifically, the existence of resonances leads to the oscillations in the energy dependence of reaction probability curves. It is possible to identify and characterize them efficiently by the time-dependent quantum mechanical method in large scale molecular calculations [2, 3, 37, 40, 229, 230]. The resonance properties, such as eigenenergy and lifetime, provide sensitive probes of the PES near the saddle point. Sadeghi and Skodje [225] classified them as, (1) conventional reactive resonances, (2) threshold anomalies, and (3) barrier resonances. The conventional reactive resonances are generally characterized by a single quantized resonant periodic orbit [1, 225]. They generally exhibit a large probability build up along the high amplitude asymmetric stretch coordinate. Near the vibrational thresholds of either the reactant or the product channel, one generally observes the peaks in the pseudospectrum [231]. These peaks are usually narrow and the corresponding eigenfunctions possess long tail in either of the two channels. These are referred to as threshold resonances [231]. A resonance state can also be associated with any local maximum of a vibrational adiabatic potential curve [131, 225, 231]. These are the barrier resonances and associated with single quantized periodic orbit dividing surface defining the maximum of the dynamical barrier. The eigenfunctions of the barrier resonances exhibit the build up of probability density near the periodic orbit dividing surface [1, 225, 231]. The authors [225, 226] have identified nearly 13 high-energy transition state (TS) resonances for the collinear H+H_2 chemical reaction through a hypothetical TS spectrum by using a TDWP approach. The classification of the resonances is also discussed in a recent review by Fernández-Alonso and Zare [221] for the

$H+H_2$ reaction. Valentini and coworkers have reported the Feshbach resonances in the state-resolved integral cross sections for the $H+H_2$ [232] and $D+H_2$ [233] reactions by carrying out the theoretical calculations along with the experimental studies. The first fully converged (total angular momentum J upto 31) three-dimensional calculations by Zhang and Miller [234] on these reactions show a dramatic blurring of the resonance peaks in the reaction cross section.

The dynamics at the TS is studied by using a spectra associated with Franck-Condon (FC) transitions directly to the interaction region. In the experimental studies, the FC transitions mostly involve either the photodissociation process or the photodetachment of an electron [17, 235]. In theoretical calculations, the spectral intensity, $I(E)$, can be simulated by using either time-independent or time-dependent methods [219, 221, 224, 236, 237]. Using a time-dependent formulation of FC spectra, the reaction dynamics is mapped out through a set of "pseudospectra" which are not related to any physical transitions between electronic surfaces. The peaks in the pseudospectrum, $I(E)$ vs E plot, are directly considered as the resonance states (either bound or quasibound) of the TS complexes. The intensity of a spectral peak may be enhanced or suppressed as desired by altering the location, symmetry, and shape of the initial WP, while its position (resonant energy) and width (lifetime) remains unaltered.

Skodje *et al.* [238, 239] have presented a combined experimental and theoretical investigations of the A+BC type of reaction and provide evidence for the existence of a TS resonance localized in the strong interaction region of the PES. They have found a step-like feature in the measured cross-section for the F+HD reaction which is just above the reaction threshold energy where quantum-mechanical tunneling dominates. This finding is also revealed by the theoretical results of Takayanagi *et al.* [240], who reported the cumulative reaction probability for the total angular momentum $J = 0$. Skodje *et al.* [238] have further investigated the origin of this peak using various theoretical tools including a time-independent, time-dependent and a spectral quantization

methods, and finally concluded that the peak is due to a TS resonance, which is localized about the collinear A$\cdots$B$\cdots$C geometry.

In this chapter we examine the resonances in H+HLi scattering both for the total angular momentum $J = 0$ [104] as well as $J \neq 0$ [105]. The findings of this chapter are related to those in Chapters 3 and 4, where the signature of resonances is observed in terms of oscillations in the reaction probability curves. The resonances here are identified by examining a set of pseudospectrum calculated by Fourier transforming the time autocorrelation function of suitably located initial WPs in the interaction region of the DMJ PES [91]. Eigenfunctions of these resonances are calculated by using the spectral quantization algorithm [225–228] and they are also characterized in terms of their line-width and decay lifetimes. We find that the resonances are generally narrow at low energies and tend to be broad at high energies, in par with the more direct nature of the scattering at high energies. A schematic illustration of the above technique is presented in Fig. 5.1. The hypothetical initial state is represented in terms of a GWP (pertinent to the triatomic LiH_2 complex, marked 1). This is subjected to a FC transition to the final Born-Oppenheimer ground electronic PES (marked 2) of H+HLi. The unimolecular decay of the GWP is monitored on this final state and the pseudospectrum (marked 3) is calculated by Fourier transforming the time autocorrelation function of the WP.

In addition to the $J = 0$ resonances we also calculate them for $J \neq 0$ by the CS and CC models [98, 99, 117, 128, 129]. This allows us to show more clearly the effect of three-body rotation on the scattering resonances. Our findings reveal that the resonance structures are generally blurred for higher values of J and they disappear at the highest value of the partial wave. The results of the resonance calculations of the CS model are compared with those of the CC model in order to reveal the importance of the latter on the reaction dynamics.

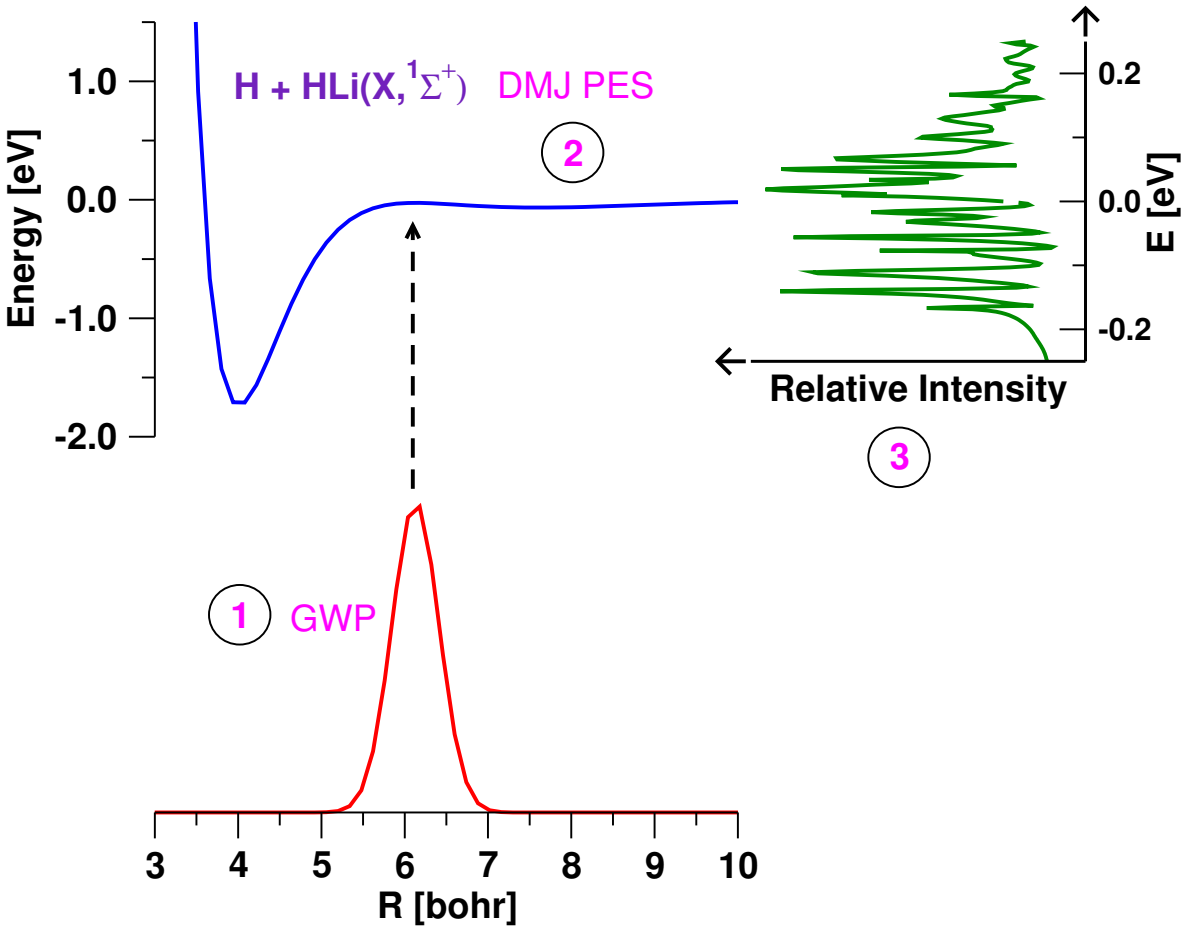

Figure 5.1: A schematic representation - (1) probing the initial GWP from its hypothetical initial state to (2) the interaction region of the (final) BO adiabatic PES of the H+HLi system, and (3) the recorded time-autocorrelation function is then Fourier transformed to get the pseudospectrum - as a function of energy.

5.2 Methodology and Computational Details

In the following, the calculation of resonances in H+HLi scattering by a TDWP approach is described [37,217,218,220,224]. The DMJ PES [91] is used for the system and calculations are reported for $J \geq 0$. In the time-dependent approach, the pseudospectrum pertinent to a FC transition of a hypothetical initial state (as sketched in Fig. 5.1) to the (final) BO adiabatic PES of the H+HLi system is calculated [40, 223, 230]. The spectral intensity is given by the time-dependent version of the golden rule equation:

$$I(E) \approx \left| \int_0^\infty C(t) e^{\frac{iEt}{\hbar}} dt \right|^2 , \tag{5.1}$$

where, $C(t)$ is the autocorrelation function of the system at time t, defined as

$$C(t) = \langle \Psi(t=0) | \Psi(t) \rangle. \tag{5.2}$$

This is calculated by propagating the hypothetical initial state $|\Psi(0)\rangle$ on the adiabatic (final) DMJ PES of the H+HLi system with the aid of the TDSE [Eq. (2.1)]. The solution of TDSE for an explicitly time-independent Hamiltonian is given in Eq. (2.2).

The initial state $|\Psi(t=0)\rangle$ representing the quasibound species in H+HLi scattering is defined in terms of a GWP constructed in terms of the BF Jacobi coordinates of the H+HLi reactants; R (distance of H atom from the center of mass of HLi diatom), r (HLi internuclear distance) and γ (the angle between $\vec{R}$ and $\vec{r}$). In this set of coordinates the initial GWP is given by

$$\begin{aligned} |\Psi(R, r, \gamma, t=0)\rangle &= N\sqrt{w(n)} \exp\left[-\frac{(R-R_0)^2}{2\delta_R^2} - \frac{(r-r_0)^2}{2\delta_r^2} \right] \\ &\quad \times \left\{ \exp\left[-\frac{(\gamma-\gamma_0)^2}{2\delta_\gamma^2} \right] + \exp\left[-\frac{(\gamma-\pi+\gamma_0)^2}{2\delta_\gamma^2} \right] \right\}. \end{aligned} \tag{5.3}$$

This GWP is initially located in the interaction region of the DMJ PES at R_0, r_0 and γ_0. The quantity N in Eq. (5.3), is the normalization constant of the GWP. The width

parameters of the GWP along R, r and γ are defined as δ_R, δ_r and δ_γ, respectively. These initial parameters are suitably varied in order to selectively choose a particular average energy of the GWP and to map out all the scattering resonances in a given energy window with appreciable intensity. The choice of these initial parameters for a few GWPs used in the present study is listed in Table 5.1.

The Hamiltonian, $\hat{H}$ [in Eq. (2.2)], of the H+HLi scattering system, is written in terms of the reactant channel BF Jacobi coordinates (R, r, γ) without a mass scaling for the total angular momentum $J \neq 0$. This can be written analogous to that the scaled one in Eq. (2.32) as [37, 98, 99]

$$\hat{H} = -\frac{\hbar^2}{2}\left(\frac{1}{\mu_R}\frac{\partial^2}{\partial R^2} + \frac{1}{\mu_r}\frac{\partial^2}{\partial r^2}\right) + \frac{\hat{l}^2}{2\mu_R R^2} + \frac{\hat{j}^2}{2\mu_r r^2} + V(R, r, \gamma), \tag{5.4}$$

where, the quantity μ_R and μ_r are the reduced masses of the (H,HLi) and HLi systems, given as

$$\mu_R = \frac{m_{\rm H}(m_{\rm H} + m_{\rm Li})}{2m_{\rm H} + m_{\rm Li}}, \tag{5.5}$$

$$\mu_r = \frac{m_{\rm H} m_{\rm Li}}{m_{\rm H} + m_{\rm Li}}. \tag{5.6}$$

All other quantities appearing in Eq. (5.4) are defined in Chapter 2.

The physical wavefunction of the H+HLi system corresponding to the particular total angular momentum J and its SF z-component can be expressed in terms of the BF Jacobi coordinates and the three Euler angles as [117]

$$|\Psi^{JM}(R, r, \gamma, \theta, \phi, \delta, t = 0)\rangle = \frac{1}{Rr}\sqrt{\frac{2J+1}{8\pi^2}} \sum_{K=-J}^{J} F^J_{K,M}(\theta, \phi, \delta)|\Psi(R, r, \gamma, t = 0)\rangle \tag{5.7}$$

where, M is the quantum number for the projection of J on the SF z-axis and K is the quantum number for the projection of $\boldsymbol{j}$ (and also of J) on the BF z axis. $F^J_{K,M}$

denotes the parity adapted angular function written in terms of the Wigner rotation matrix elements, $D^J_{K,M}$, [see Eq. (2.27) and also Appendix A.1] [151,153]

$$F^J_{K,M}(\theta,\phi,\delta) = [2(1+\delta_{K,0})]^{-1/2}\left[D^J_{K,M} + (-1)^{J+K+p} D^J_{-K,M}\right]. \tag{5.8}$$

As stated in previous chapters, the action of the time-evolution operator on $|\Psi(t=0)\rangle$ is carried out by dividing the total propagation time T into N steps of length Δt. The exponential operator at each time step Δt is then approximated by a second-order SO method [172] [Eq. (3.3)] in the $J=0$ as well as in the CS calculations, and by the CP method [183] [Eq. (2.102)] in the CC calculations. The FFT method [112] is used to evaluate the action of the radial kinetic energy operator and the DVR method [117,125,129] to evaluate the action of the angular kinetic energy operator on the wavefunction.

The time autocorrelation function, $C(t)$, is calculated at each time step t and Fourier transformed to calculate the spectral intensity (cf. Eq. (5.1)). The peaks in pseudospectrum are correspond to the bound or quasibound states of the scattering system. The peak maxima yield the energy eigenvalues of the bound or quasibound levels and their eigenfunction are calculated by projecting the time-evolved WP on the desired eigenstates n of energy E_n,

$$\Psi_n(E) = \int_0^T e^{iE_n t/\hbar}\Psi(t)dt. \tag{5.9}$$

As illustrated in the previous chapters, we solve Eq. (2.2) with the aid of a mixed grid/basis set method in order to calculate the wavefunction at time t. A 128×64 spatial grid is used in the $R \times r$ plane with 1.0 $a_0 \leq R \leq$ 18.78 a_0 and 1.0 $a_0 \leq r \leq$ 8.56 a_0. The nodes of a 64-point GLQ [212] are used for the grid along the Jacobi angle γ. We used 48-point GLQ for the angular grid (γ) in the full-dimensional (CC) calculations.

We construct the γ grid (in the CS approximation) by diagonalizing the $\cos\gamma$ matrix in the basis of the associated Legendre polynomials for each value of K. The resulting diagonal elements define the nodes of a n-point GLQ [212] and the DVR-FBR trans-

Table 5.1: Parameters for the different choices of the initial Gaussian wave packet used in time evolution.

GWP	R_0 (a_0)	r_0 (a_0)	γ_0 (rad)	δ_R (a_0)	δ_r (a_0)	δ_γ (rad)	$\langle E \rangle$ (eV)
1	5.562	2.861	0.31416	0.40	0.20	0.15	0.0282
2	6.130	3.711	0.31416	0.40	0.20	0.15	0.1104
3	5.562	2.861	0.31416	0.28	0.14	0.10	0.1965
4	5.562	2.861	1.09956	0.30	0.18	0.10	0.4188
5	7.129	4.056	0.31416	0.40	0.21	0.15	0.5266
6	6.975	4.245	0.31416	0.30	0.18	0.10	0.6790
7	6.975	4.245	0.31416	0.28	0.15	0.10	0.7450
8	7.961	4.660	0.31416	0.40	0.20	0.15	1.0749
9	7.961	4.660	0.31416	0.28	0.15	0.10	1.1961
10	7.950	4.668	0.31416	0.28	0.14	0.10	1.2285

formation matrix is given by eigenvector matrix U. The quadrature weights associated with the grid point n, $w_n^{1/2}$, are calculated by using Eq. (2.68) [41]. As we mentioned before that the projection quantum number K also adds to the overall dimensionality in addition to three BF Jacobi coordinates, the problem becomes four dimensional when the CC terms are included. In the latter the DVR points along γ are chosen as those for $K = 0$, however, we used appropriate transformation matrix corresponding to a particular value of K.

The WP is time-evolved for a total of $\sim$1.103 ps with a time step Δt=0.1347 ps. The last ten points of the grid along both R and r were covered with a damping function [see Eq. (3.6)] [114] in order to avoid any unphysical reflexion or wraparound of the high energy components of the WP which reach the finite sized grid boundaries at longer times.

The pseudospectral intensity [Eq. (5.1)] when plotted as a function of energy gives rise to peaks at the energy eigenvalues of the resonances. The intensity of the peaks describe the extent of overlap of the initial GWP with the corresponding quasibound state. The energy eigenvalues of the resonances can further be accurately determined by fitting the spectral peaks to a line-shape function [241]. We in the following typically

use a Gaussian line-shape function of the type

$$Y(E) = Y_0 + \frac{A}{\Gamma\sqrt{\pi/2}} e^{\frac{-2(E-E_0)^2}{\Gamma^2}}. \tag{5.10}$$

The line-width lifetime, τ, of the resonances are estimated from the full width at the half-maximum (FWHM), Γ, of the above Gaussian function. The two are related through,

$$\tau = \frac{\hbar}{\Gamma}. \tag{5.11}$$

Some of the spectral peaks are better fitted to a Lorentzian function given by,

$$Y(E) = Y_0 + \frac{2A}{\pi} \frac{\Gamma}{4(E-E_0)^2 + \Gamma^2}. \tag{5.12}$$

5.3 Results and Discussion

The H+HLi reactive scattering dynamics is indirect in nature and proceeds through resonance formation at low energies. At high energies the scattering becomes more direct and the reaction probability curves reveal signatures of very broad resonances (cf. Chapter 3). Below, we describe the resonances of the H+HLi system calculated by applying the methodology discussed in Sec. 5.2. In particular, we focus here on the low-energy resonances and identify and characterize them in terms of their eigenfunctions and life-times. Since we start with a real initial WP [Eq. (5.3)], we utilize the prescription to calculate, $C(2t) = \langle \Psi(t)^* | \Psi(t) \rangle$, from the time-dependent WP at time t [242, 243]. This helps to increase the energy resolution ($\Delta E = 2\pi\hbar/T$) in the eigenvalue spectrum by effectively doubling the propagation time, T.

5.3.1 Wave Packet Dynamics

In order to illustrate the time-dependent dynamics of the quasibound complex in the H+HLi scattering, we show the snapshots of the WP probability density ($|\langle \Psi | \Psi \rangle|$) superimposed on the potential energy grid at various times (indicated in each panel) in

Fig. 5.2. The probability densities are plotted both in the (R, r) (integrated over γ) and (R, γ) (integrated over r) planes. We note that the WP probability density in the last two panels of each set are plotted for fixed values of either γ or r as indicated in the respective panel. The initial WP (at, $t = 0$) in Fig. 5.2 corresponds to the GWP No. 5 of Table 5.1. It can be seen from the plots that in about 8.62 fs the quasibound complex moves towards small r and approaches to the potential well. It also spreads to some extent along γ. In about 20 fs it slides down the attractive valley and then acquires complex structures along all three coordinates at longer times. The asymmetry of the system is indicated by the more build up of the probability density in the reactant channel. The WP probability density (indicated in each panel) decreases in time due to the absorption of the time-evolved WP at the grid edges. The probability density decreases to 2.2×10^{-4} at $\sim$ 1.103 ps, indicating that the dynamical processes are essentially over by this time.

For the sake of clear understanding of nuclear dynamics, we show some more WP snapshots at various times (indicated in each panel), in Figs. 5.3 and 5.4 for the GWP No. 2 ($\langle E\rangle$=0.1104 eV). The probability density of WP is plotted both in the (R, r) and (R, γ) planes by averaging it over γ and r, respectively. It can be seen from Fig. 5.4 that the quasibound complex gets the HLiH configuration quickly in about $\sim$ 70 fs from its stationary HHLi configuration.

5.3.2 Resonances for $J = 0$

In Fig. 5.5, the eigenvalue spectrum of the quasibound states (for $E < 0$) calculated with the aid of Eq. (5.1) and using the GWP (No. 2) with an initial average energy, $\langle E\rangle$=0.1104 eV, is shown. The intensity in arbitrary units is plotted as a function of the energy of the quasibound states. The peaks in the spectrum correspond to the resonances of the H+HLi system. In calculating this spectrum the WP is time evolved for

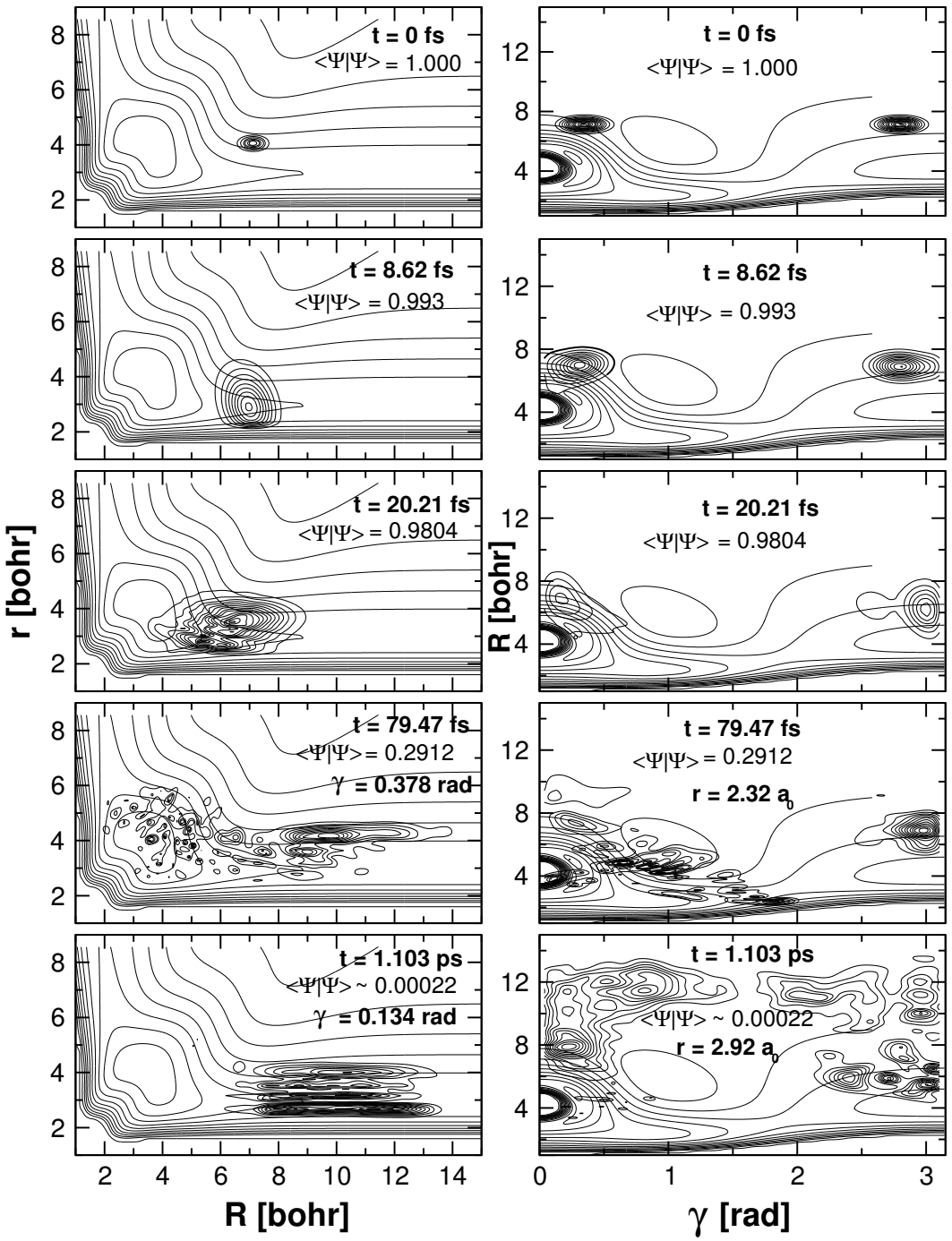

Figure 5.2: Probability density contours of GWP No. 5 superimposed on the potential energy contours at various times t (indicated in each panel) illustrating the unimolecular decay of the quasiboundcomplex in H+HLi scattering, plotted both in the (R, r) and (R, γ) planes (see text for further illustration). The total probability density ($|\langle\Psi|\Psi\rangle|$) of the WP retained on the grid at different times is also included in each panel.

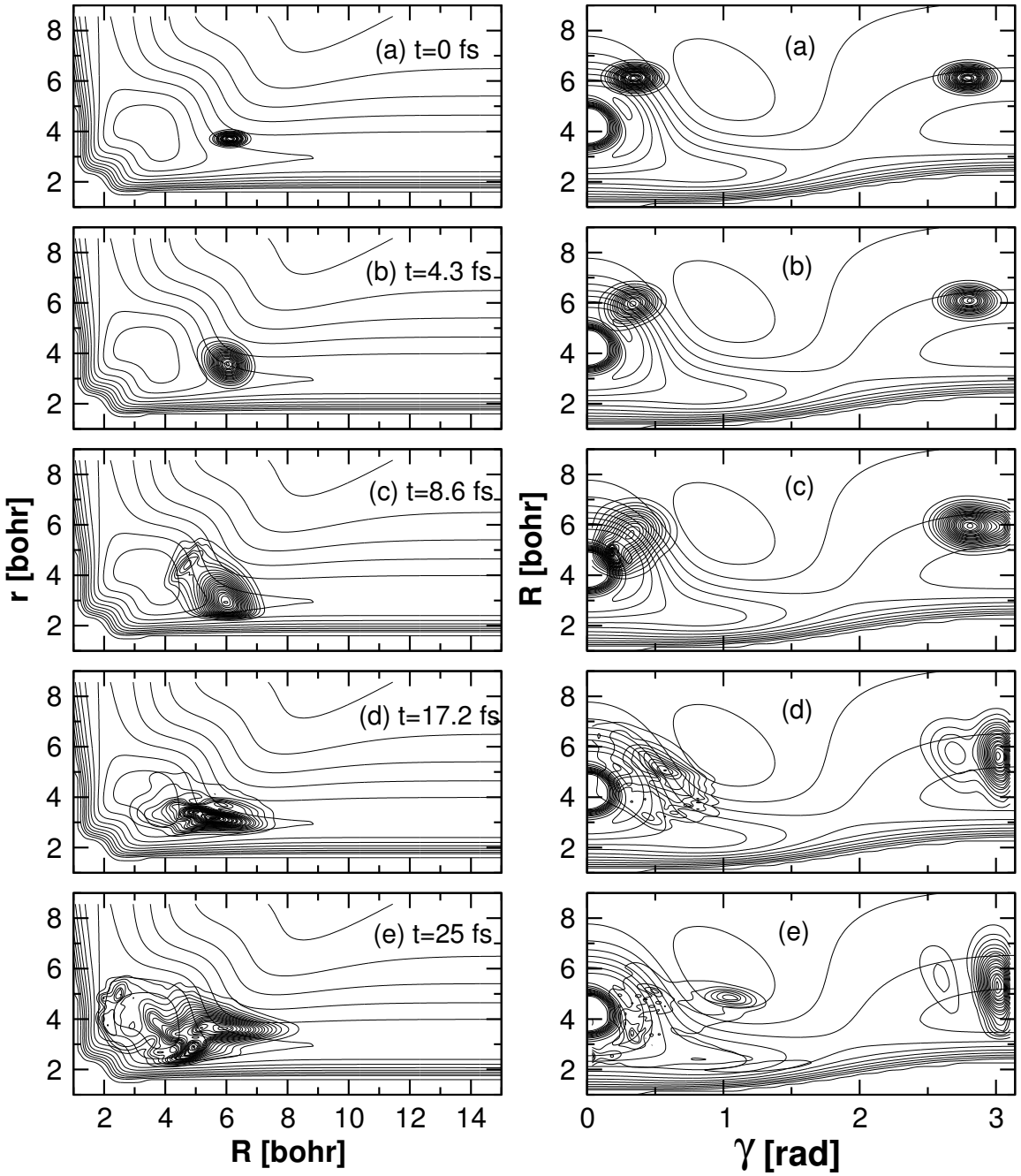

Figure 5.3: Probability density contours of GWP No. 2 superimposed on the potential energy contours at various times t (indicated in each panel) plotted both in the (R, r) and (R, γ) planes.

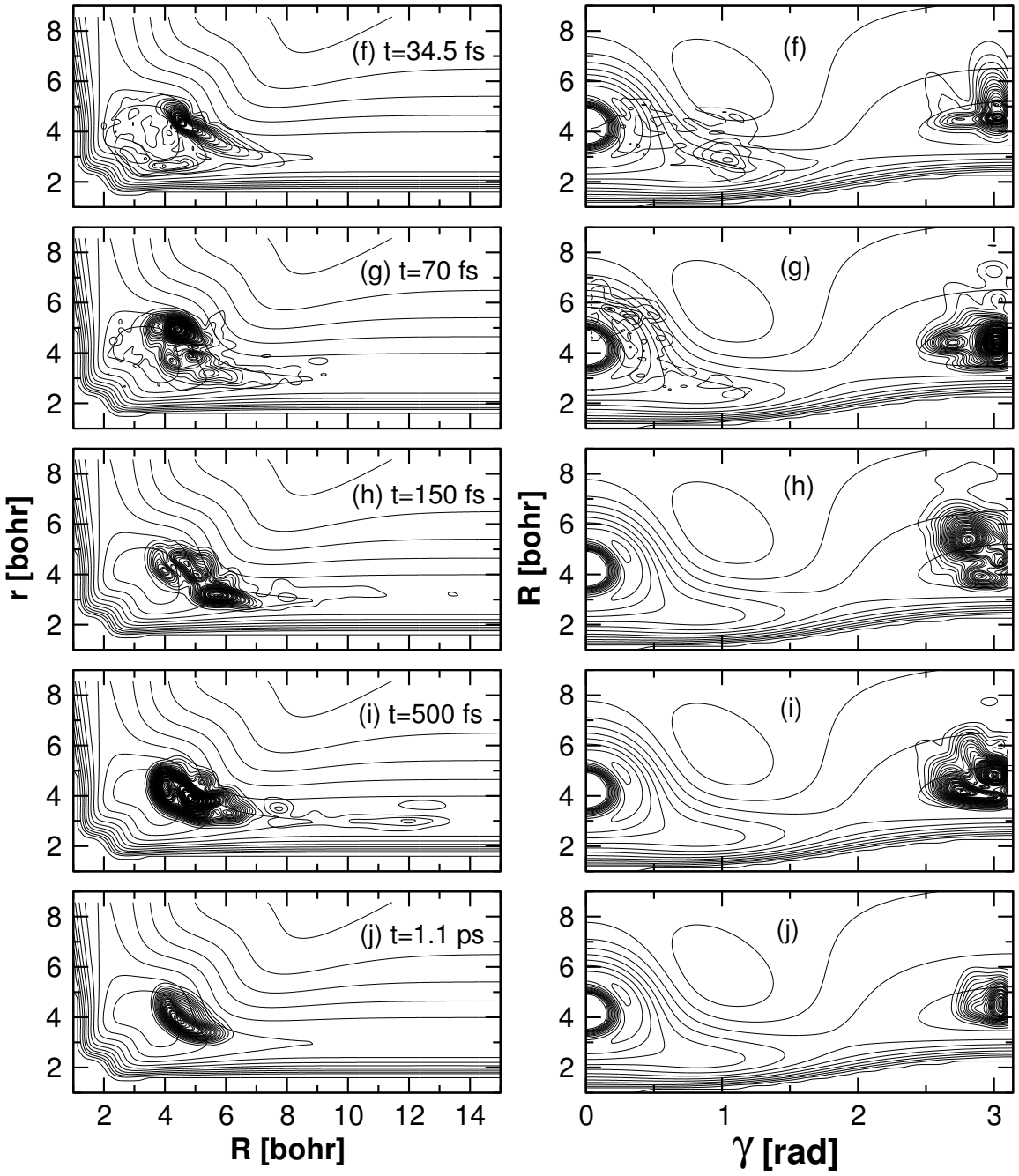

Figure 5.4: Same as in Fig. 5.3 for longer times t (indicated in each panel) and the norm ($|\langle\Psi|\Psi\rangle|$) of the WP on the grid at the end of time step is 1.9×10^{-3}.

1.103 ps which leads to an energy resolution of 1.874×10^{-3} eV (considering the Fourier transform of $C(2t)$). It can be seen that, there exists seven quasibound states for $E < 0$. The decay of the absolute value of time autocorrelation of this GWP (No. 2) is shown in Fig. 5.6. We have carried out a few more WP calculations by further lowering the initial average energy of the GWP. We, however, did not find any additional states in the energy window of Fig. 5.5. The peaks are well resolved, except the fourth one which has a shoulder and appears in all other calculations.

In Fig. 5.7(a), we show the eigenvalue spectrum calculated using the GWP (No. 5 of Table 5.1) shown in Fig. 5.2. This has an initial average energy, $\langle E\rangle$=0.5266 eV. The peaks in the spectrum correspond to the resonances of the H+HLi system which lie within the energy range of the GWP. The energy resolution in the spectrum is 1.874×10^{-3} eV. It can be seen that resonances at low-energies are better resolved with this GWP. The energy corresponding to the peak maxima describes the energy eigenvalue of the resonances. The lifetime of the resonances can be extracted from the corresponding peak width. We note that, irregularity seen in the eigenvalue spectrum can be attributed to the overlapping nature of the quantal resonances in H+HLi system, presence of nearby vibrational thresholds and also to the possible background contributions arising from the direct scattering of the WP. The behavior of the time autocorrelation function for the same GWP is also included in the panel as an insert. The latter shows an initial sharp decrease followed by recurrences of steadily decreasing amplitude. The regular pattern changes to a more complex oscillatory one at longer times. The time interval between successive recurrences can be connected to the periods of the unstable classical periodic orbits corresponding to the quantal resonances [244].

In Fig. 5.7(b), we show the resonances obtained with the GWP No. 8 with high average energy of $\langle E\rangle$=1.0749 eV. It can be seen that with this GWP some of the high-energy resonances are resolved. The energy resolution in the spectrum is same as in Fig. 5.7(a). In contrast to the spectrum in Fig. 5.7(a), the one in Fig. 5.7(b) reveals

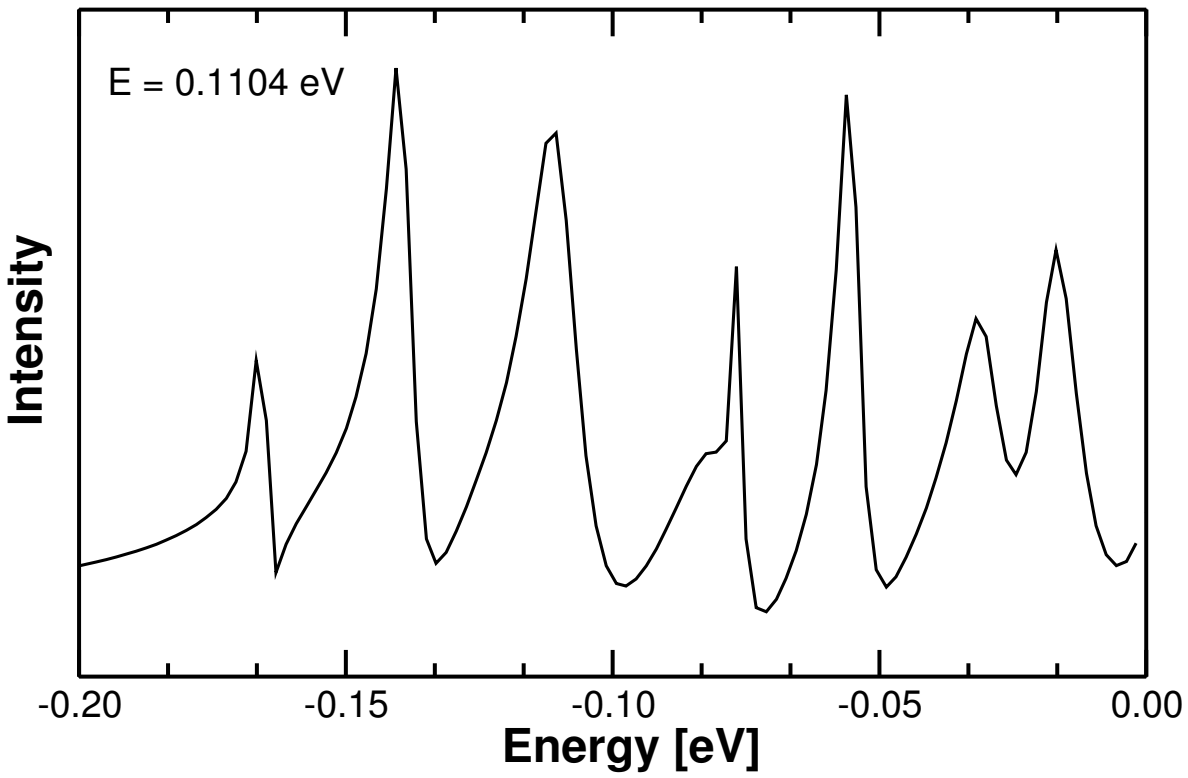

Figure 5.5: The pseudospectrum of the quasibound states in H+HLi scattering, for energy $E < 0$ (average energy of initial GWP is 0.1104 eV). The intensity (in arbitrary units) is plotted as a function of the energy of the quasibound states. The zero of energy corresponds to asymptotically separated H correspond to the quasibound states of H+HLi system in the given energy window.

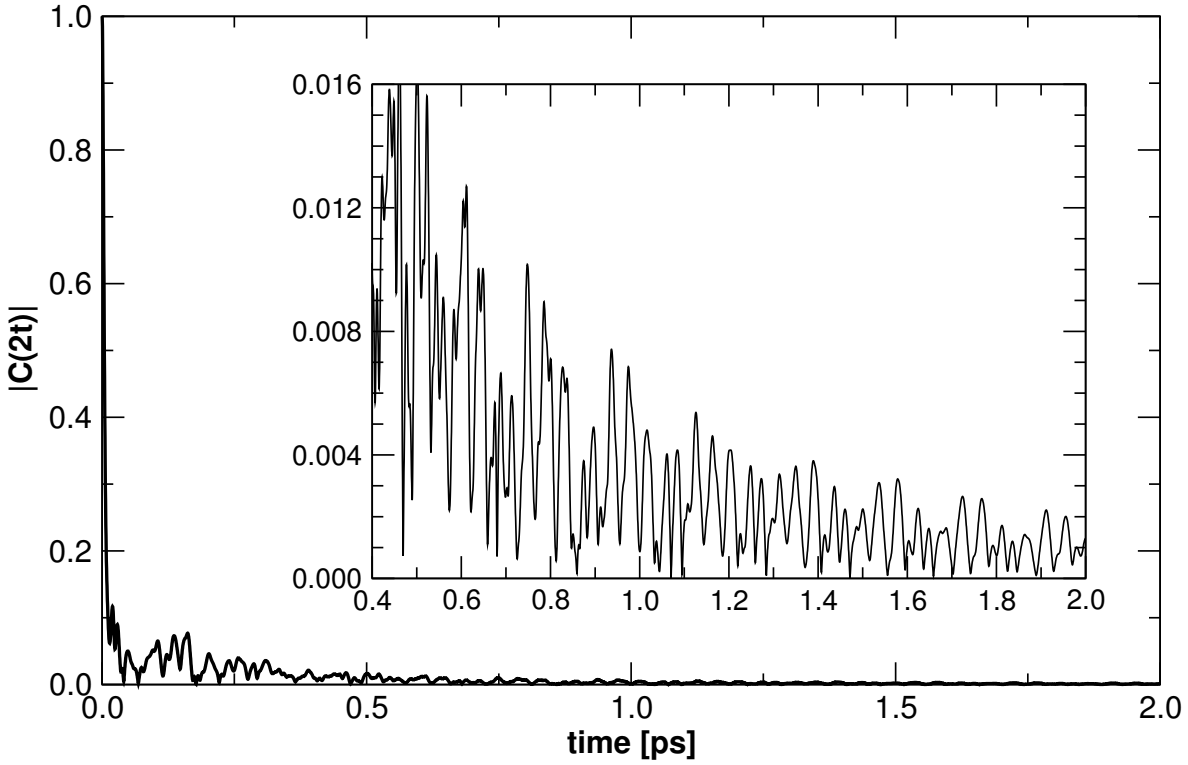

Figure 5.6: The decay of the absolute value of autocorrelation function $|C(2t)|$ in time, corresponding to the pseudospectrum shown in Fig. 5.5. The magnified picture of the time autocorrelation function is shown as an inset.

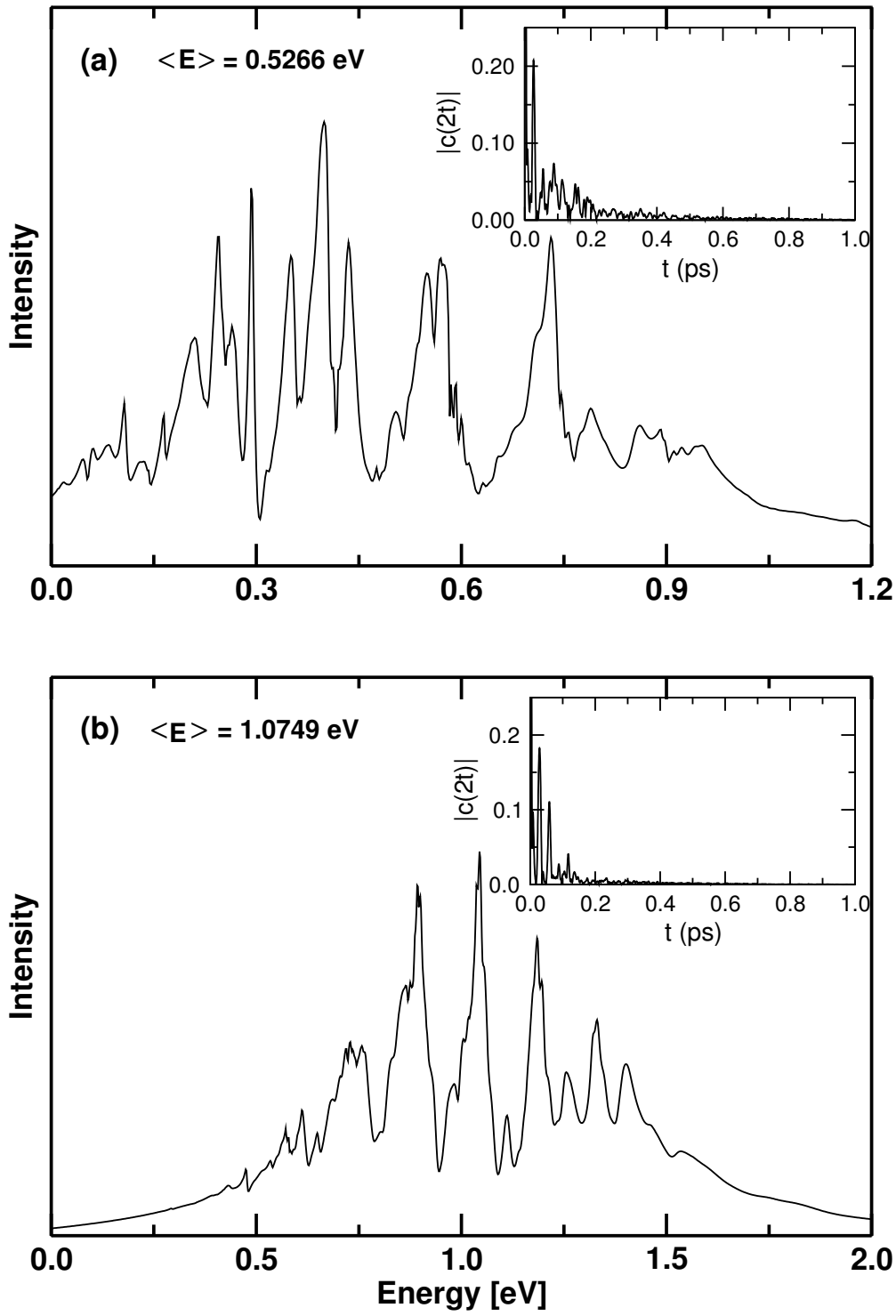

Figure 5.7: Same as in 5.5, for the quasibound states with energy $E > 0$. The two spectra in panel (a) and (b) differ in terms of the location and average energy (indicated in each panel) of the initial GWP. The decay of the absolute value of the corresponding autocorrelation function $|C(2t)|$ in time, is shown as an insert in the respective panels.

Table 5.2: Vibrational energies of the diatomic molecules LiH and H_2 for the $j = 0$ level and for the total angular momentum $J = 0$.

Vibrational level	LiH Vibrational energy (eV)	H_2 Vibrational energy (eV)
0	0.08656	0.27087
1	0.25519	0.78768
2	0.41815	1.27547
3	0.57549	1.73442
4	0.72721	2.16492
5	0.87333	2.56841
6	1.01383	2.94189
7	1.14870	3.27277

that resonances are less pronounced and more broad in the high energy region. The latter is consistent with much wider oscillations seen in the high energy part of the reaction probability curves. The behavior of the time autocorrelation function of this high energy WP is also included in the panel as an insert. The energy eigenvalues of 31 quasibound states of the H+HLi system extracted from ten different WP calculations (cf. Table 5.1) are listed in Table 5.3.

In order to illustrate the resemblance of the above quantal resonances with the oscillations in the reaction probability curves, we in Fig. 5.8 superimpose the reaction probabilities of the H + HLi$(v = 0, j = 0) \longrightarrow H_2(\Sigma v', \Sigma j')$ + Li (R1) and HLi$(\Sigma v', \Sigma j')$ + H (R2) reactions on the pseudospectrum of Fig. 5.7(a). The reaction probability values of (R1), (R2) and the pseudospectrum of Fig. 5.7(a) are shown by the long dashed, short dashed and solid lines, respectively. It can be seen from Fig. 5.8 that both the peaks and dips in the reaction probability curves can be identified with the peaks in the pseudospectrum. We have given the vibrational energies of the HLi and H_2 diatoms in Table 5.2 in order to indicate the threshold energies where a new vibrational channel opens up.

Each features of the quasibound spectrum can be associated with a stationary wavefunction. Therefore, in order to better understand the nature of the quasibound com-

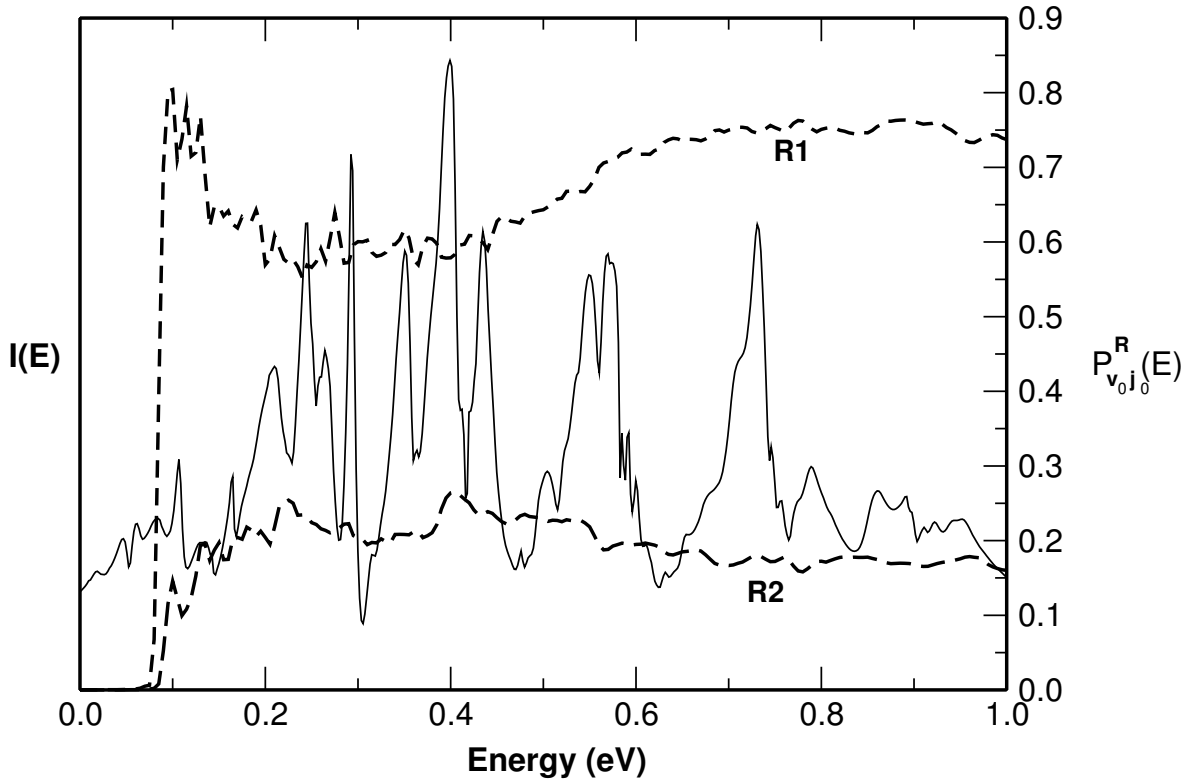

Figure 5.8: The pseudospectrum of Fig. 5.7(a) superimposed with the reaction probability of the depletion (R1) and formation (R2) channels of Fig. 3.9 (indicated in long and short dashed line, respectively) in order to illustrate the commonality of the spectral peaks with the oscillations in reaction probability curves.

plexes in H+HLi scattering, we have calculated their eigenfunctions through spectral quantization i.e., by Fourier transforming a time-evolved WP at precisely the energies of the spectral peaks (cf. Eq. (5.9)). The resulting eigenfunctions of 31 resonances superimposed on the potential energy grid are shown in Figs. 5.9 to Figs. 5.13 as contour level diagrams. The full three-dimensional ($3D$) visualization of the eigenfunctions is a difficult task, therefore, we have attempted to identify and assign them by inspecting suitable cuts in the (R, r) and (R, γ) plane, for fixed or average values of γ and r, respectively. We have also examined the cuts in the (r, γ) plane in order to check the assignments of the resonance states, but we do not show those plots here.

In Figs. 5.9(a-g), the eigenfunctions of the quasibound states of Fig. 5.5 are shown. These quasibound states and all the latter ones shown in this paper are assigned (whenever possible) by examining their nodal pattern along R, r and γ. They are identified in terms of three quantum numbers n_R, n_r and n_γ representing the number of nodes along these coordinates, respectively. The eigenfunction in Fig. 5.9(a) does not have any nodes along any of these coordinates. Therefore, it may be identified as (0,0,0) in that order, representing the lowest quasibound state of the H+HLi system. Furthermore, from the contour diagram in the (R, γ) plane it can be seen that this state has a build up of probability density only around $\gamma = \pi$, revealing a HLiH configuration of the corresponding quasibound complex. The eigenfunction in Fig. 5.9(b) has one node along R which is better visible from the contour plot in the (R, γ) plane. Therefore, it may be assigned as a (1,0,0) state. It can be seen from the (R, γ) plots that all the quasibound states of Figs. 5.9(a-g) correspond to the HLiH configuration of the quasibound complex. The quasibound state in Fig. 5.9(c) has one node along R, one along r (better visible in the (r, γ) plane) and no node along γ and may be assigned as a (1,1,0) state. The quasibound state in Fig. 5.9(d) is the first bend excited state of the H+HLi system, containing one node along γ. It may be assigned as a (0,0,1) state. The bending frequency of the complex is $\sim$90 meV. The remaining quasibound states in Fig. 5.9(e-g) may be assigned as (1,0,1), (1,1,1) and (2,1,0), respectively, in that order.

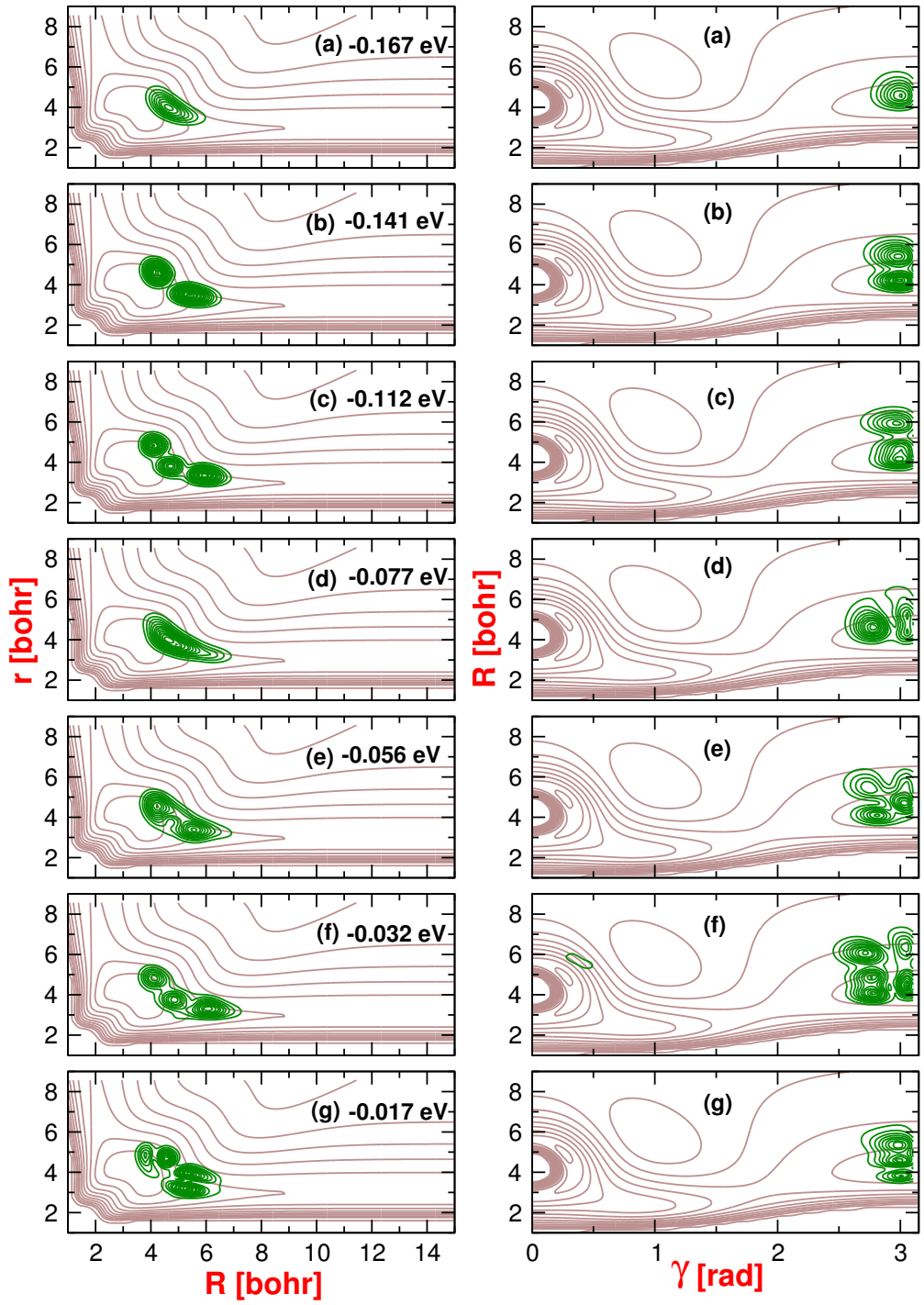

Figure 5.9: Probability density contours of the quasibound eigenfunctions with eigenenergies $E < 0$ obtained through spectral quantization (Eq. (5.9)) and superimposed on the potential energy contours of the H+HLi system. The energy eigenvalues of the quasibound states are indicated in the respective panel and the contour diagrams are plotted both in the (R, r) and (R, γ) planes for fixed or average values of γ and r.

The assignments of the above seven quasibound states are included in Table 5.3.

Eigenfunctions of 24 more quasibound states of the H+HLi system are shown in Figs. 5.10(a-g),5.11(h-m),5.12(n-s) and 5.13(t-x). The energy eigenvalue of these states and their possible assignments are also included in Table 5.3. It can be seen from Figs. 5.10 to Figs. 5.13 (panels (a-x)) that the eigenfunctions exhibit a mixed local and hyperspherical mode behavior. The eigenstates in Figs. 5.12(r-s) and Figs. 5.13(t-x) reveal a heavy build up of probability density near $\gamma = 0^\circ$ and therefore correspond to the HHLi geometrical arrangement of the quasibound complex. We also note that we tried optimizing the TS species in the H+HLi reaction and found a linear TS in the MP2 level of theory employing a cc-pVTZ basis set [213] (this is discussed in Chapter 4). The apparent hyperspherical mode pattern can be seen only in the eigenstates of the HLiH quasibound complex. The corresponding wavefunctions show a heavy build up of probability density along the asymmetric stretch coordinate. We mention that a consistent and unambiguous assignment of all the states in Figs. 5.10 to Figs. 5.13 (panels (a-x)) is difficult and cumbersome. We have repeatedly examined the convergence behavior of these eigenfunctions by computing them with different initial wave packets. The positions and widths of these quasibound states are found to be independent of the choice of the initial wave packet, only intensities are altered with different initial conditions. Invariance of the results with different initial packets supports that the corresponding states are not merely an artifact due to background or of the reflection principle [219]. We approximately assigned these states in terms of (n_R, n_r, n_γ) and included in Table 5.3. A blank entry in Table 5.3 indicates that the corresponding quantity cannot be unambiguously determined. A close look at the assignments in Table 5.3 reveals that the bend excited states upto the second quanta appear in the pseudospectra.

In the light of the work of Sadeghi and Skodje on the collinear D+H_2 resonances [225], the H+HLi resonances shown in Figs. 5.10 to Figs. 5.13 may further be classified into (i) conventional reactive resonances (ii) threshold anomalies and (iii) barrier

Table 5.3: Eigenvalues (E_n), assignments and the line-width and decay lifetime of 31 resonances in the H+HLi scattering. A blank entry indicates the corresponding quantity could not be determined unambiguously.

E_n (eV)	Assignments (n_R, n_r, n_γ)	Line-width lifetime (fs)	Decay lifetime (fs)
-0.167	(0,0,0)	270	266
-0.141	(1,0,0)	133	128
-0.112	(1,1,0)	51	59
-0.077	(0,0,1)	272	262
-0.056	(1,0,1)	-	150
-0.032	(1,1,1)	47	45
-0.017	(2,1,0)	66	65
0.010	(0,0,2)	167	162
0.019	(2,2,0)	47	41
0.034	(1,-,1)	-	116
0.046	(2,-,0)	60	62
0.062	(3,2,0)	26	30
0.067	(1,2,1)	53	47
0.100	(2,2,1)	58	68
0.106	(4,3,0)	103	107
0.149	(1,1,2)	32	28
0.168	(4,2,0)	-	70
0.244	(5,3,0)	55	50
0.293	(6,3,0)	104	98
0.350	(-,3,0)	45	39
0.363	(6,4,0)	-	39
0.397	(-,3,0)	42	36
0.412	(5,2,0)	47	38
0.435	(5,3,0)	51	43
0.549	(0,3,0)	33	28
0.591	(2,3,0)	72	76
0.600	(3,3,0)	63	47
0.731	(0,4,0)	48	40
0.746	(2,4,0)	82	72
0.756	(3,4,0)	38	36
0.861	(0,5,0)	38	27

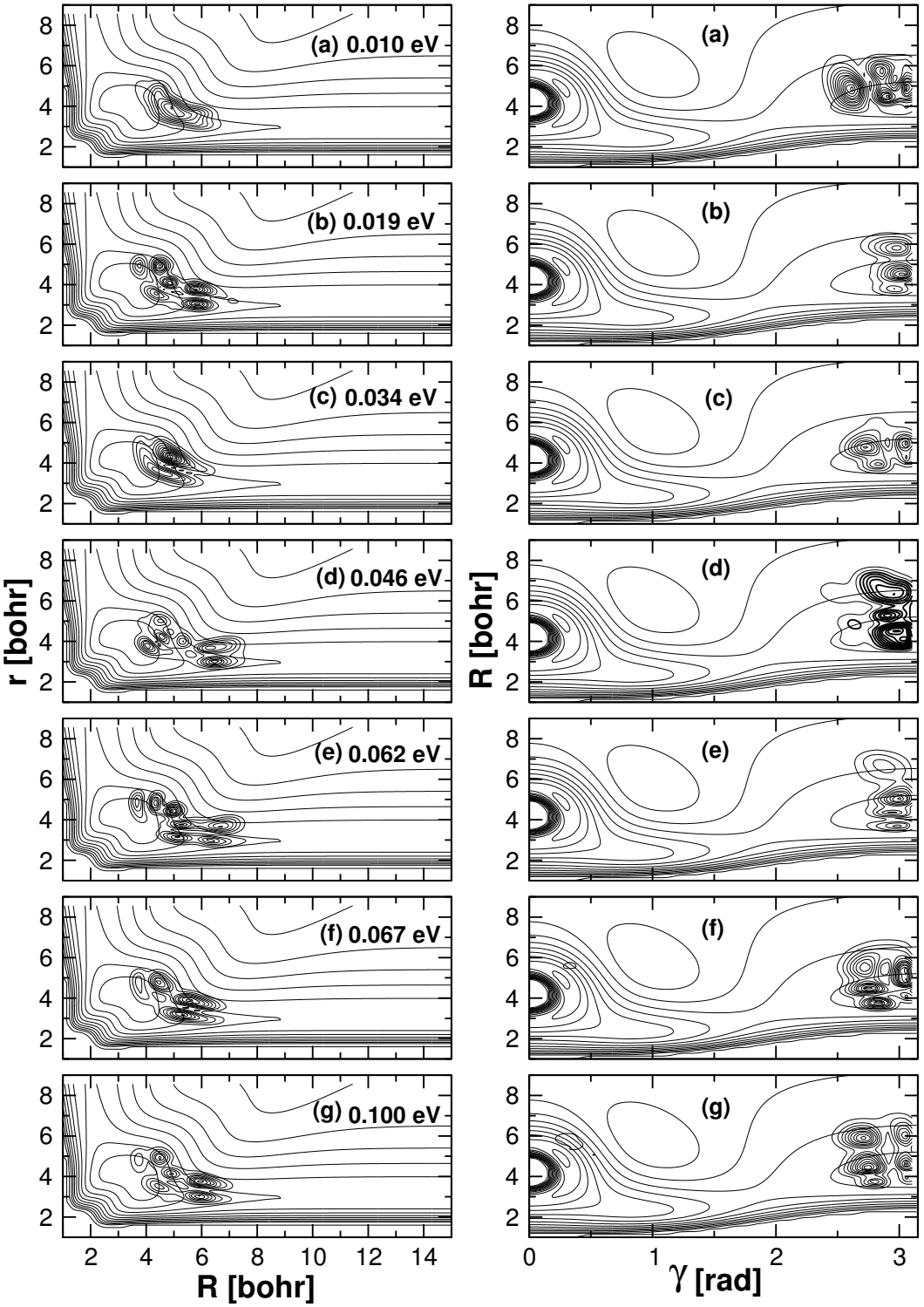

Figure 5.10: Same as in Fig. 5.9, for the quasibound states of H+HLi with eigenenergies $E > 0$.

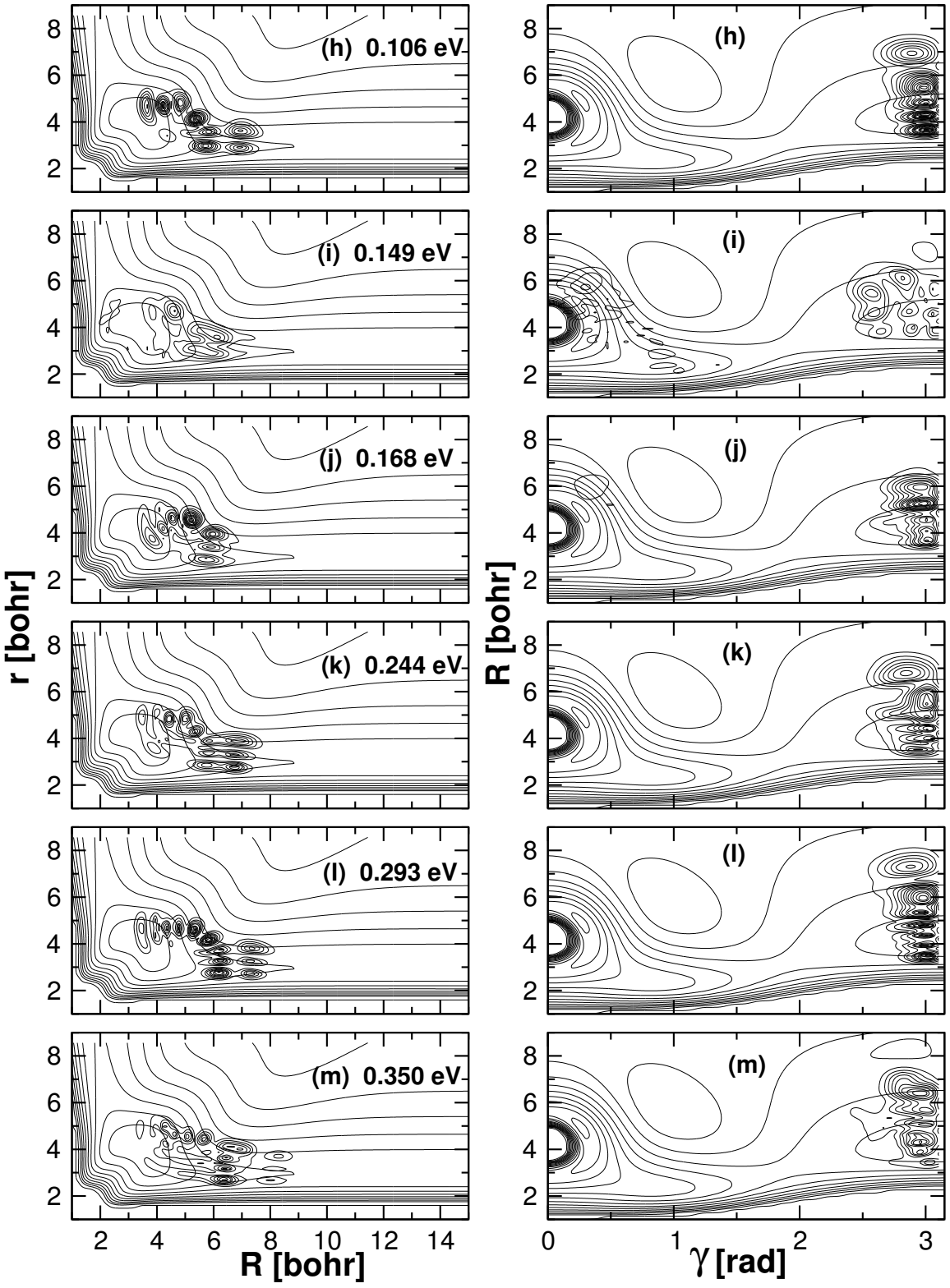

Figure 5.11: (contd.)

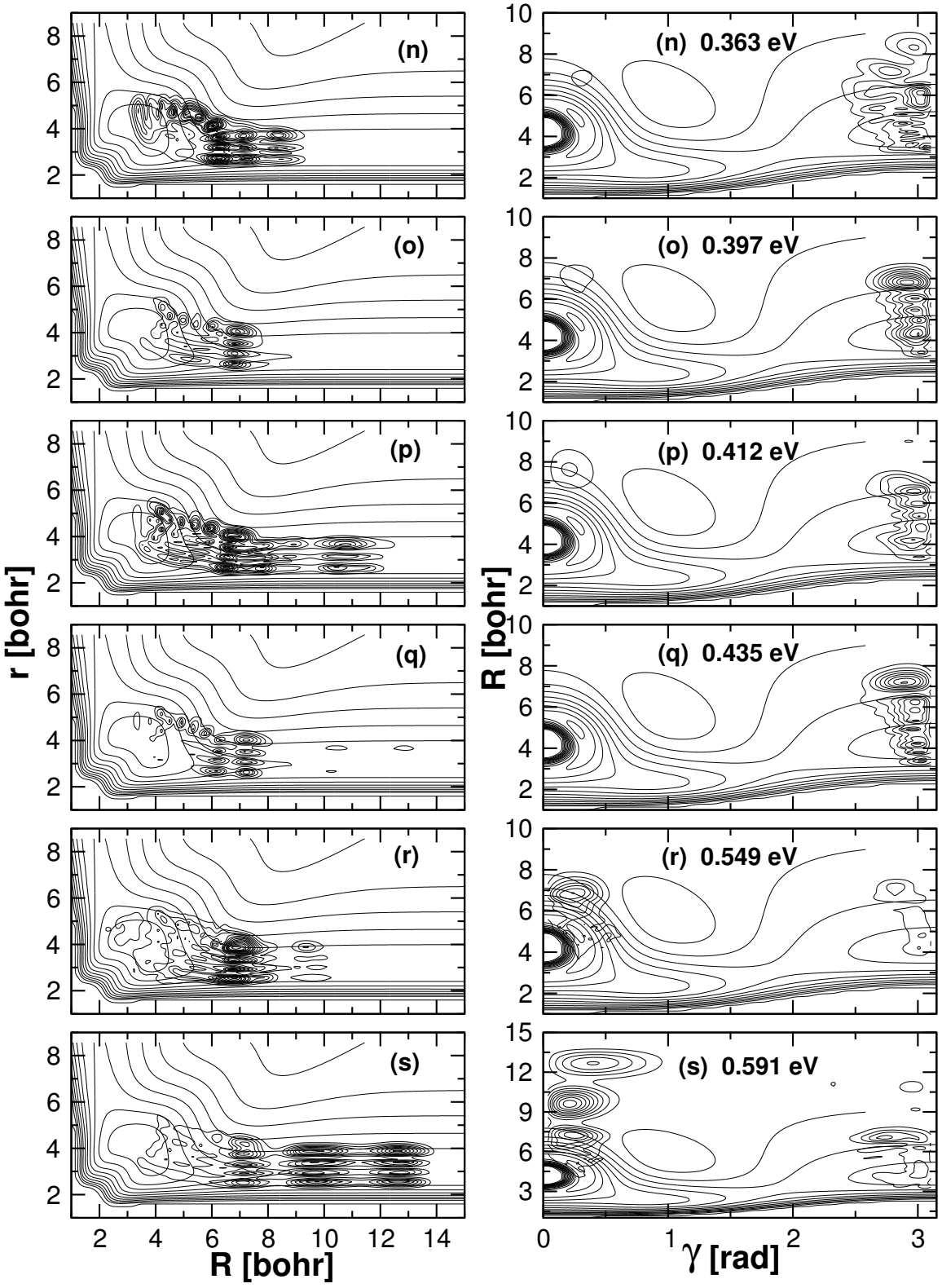

Figure 5.12: (contd.)

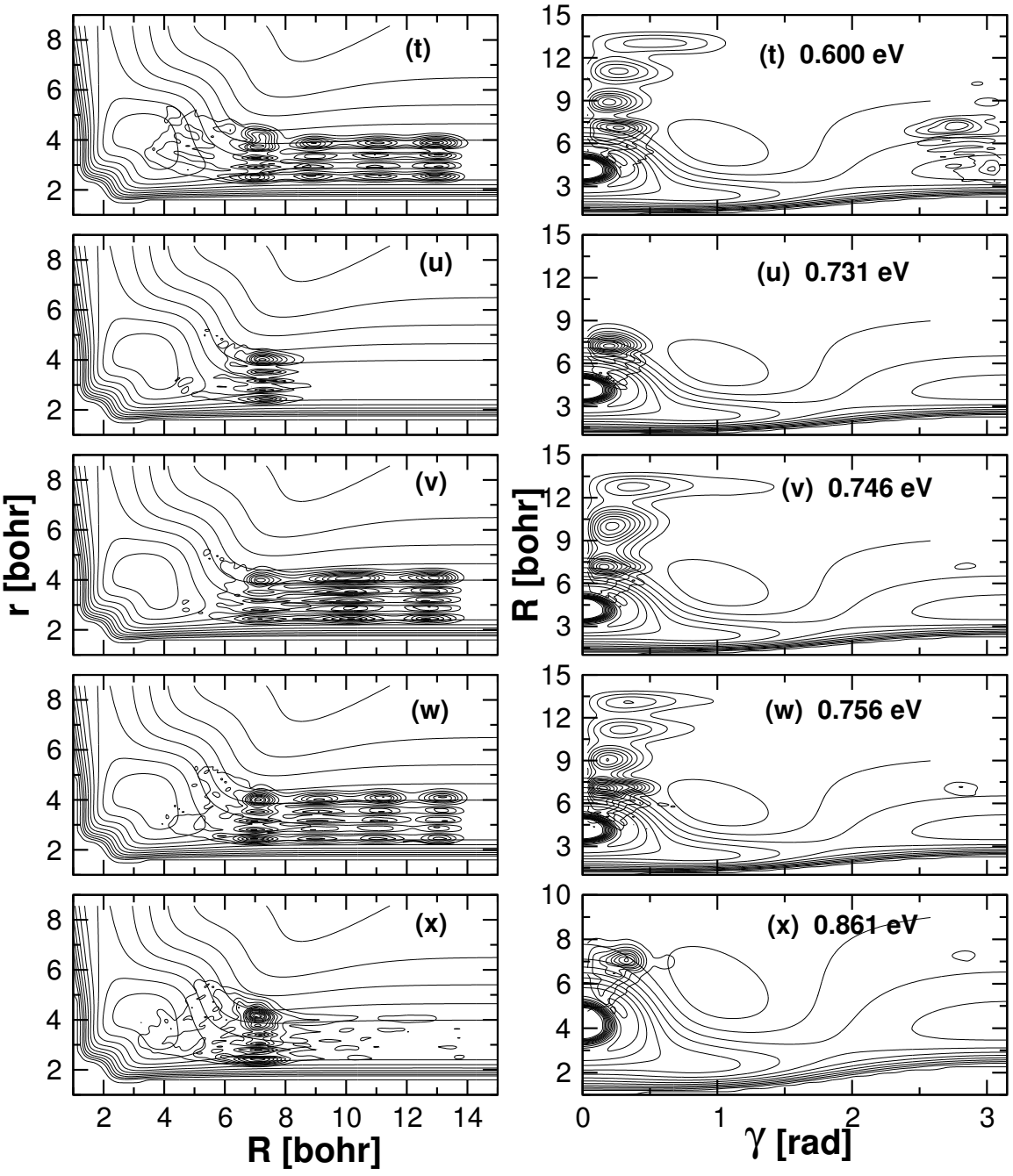

Figure 5.13: (contd.)

resonances (see Sec. 5.1). A close look at the eigenfunctions in Figs. 5.10 to Figs. 5.13 (panels (a-x)) reveals that they can be classified into the above three categories. For example, the states represented in Figs. 5.10(a), (c), (d) and (f), and Figs. 5.11(i-j) may be classified into conventional reactive resonances. The states represented in Figs. 5.12(p) and (r), and Figs. 5.13(u) and (x) may be characterized as threshold resonances associated with the vibrational level $v = 2$ (0.418 eV), 3 (0.575 eV), 4 (0.727 eV) and 5 (0.873 eV) of the LiH molecule, respectively [cf. Table 5.2]. The rest of the states in Figs. 5.10 to Figs. 5.13 (a-x) may be characterized as more subtle barrier resonances. We note that the barrier resonances in the H+HLi system are quantized in the reactant channel only.

The lifetime of the resonances are extracted from the line-width measurements; by fitting the spectral peaks to a line-shape function using a nonlinear least square method. In the present case we used either a Gaussian (Eq. (5.10)) or a Lorentzian (Eq. (5.12)) line-shape function to obtain a possible best fit of the individual peaks observed in the pseudospectrum. It has been pointed out by Sadeghi and Skodje [226] that the spectral peaks due to conventional reactive resonances are well represented by a Lorentzian line-shape, whereas, the peaks due to barrier resonances usually deviates more from a true Lorentzian line-shape. These authors also proposed a new line-shape formula to fit the spectral peaks of the barrier resonances [226]. In Figs. 5.14(a-b) we show two typical peaks (indicated by the asterisks) along with their fit (solid line) to the Gaussian [Eq. 5.10] and Lorentzian [Eq. (5.12)] line-shape function, respectively. The energy eigenvalue and the line-width lifetime of the corresponding resonances are indicated in the respective panel. The deviation of the peaks from a true line-shape function often introduces substantial error in the lifetime measurements. This deviation is mainly caused by the background contributions to the spectral peak arising from the direct scattering of the WP and also from the presence of nearby vibrational thresholds. The line-width lifetime of 31 resonances are reported in Table 5.3.

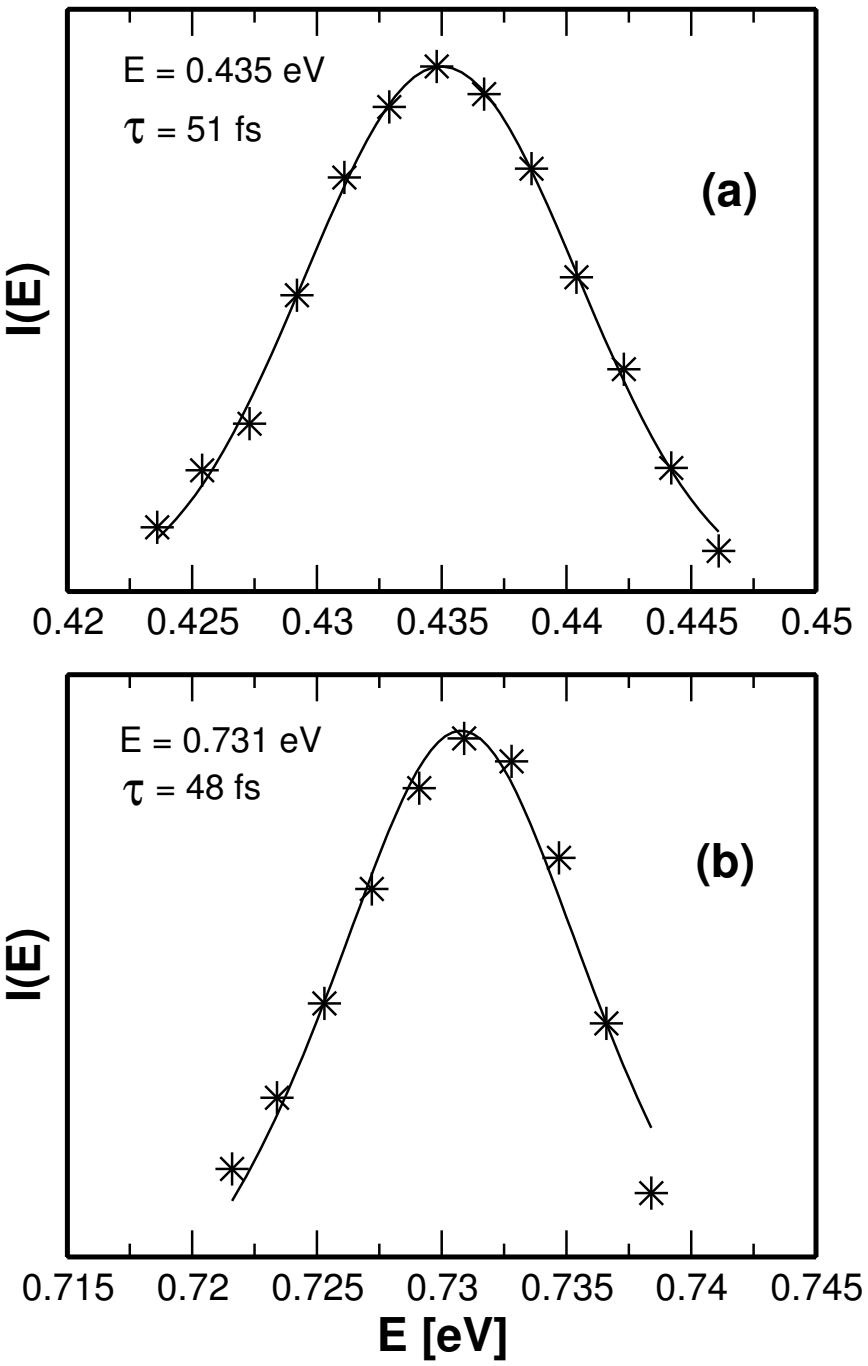

Figure 5.14: Gaussian and Lorentzian line shapes for two typical spectral peaks centered at E=0.435 eV and E=0.731 eV, shown by the solid curve in panel (a) and (b), respectively. The peaks obtained from the time-dependent WP calculations are shown by the asterisks.

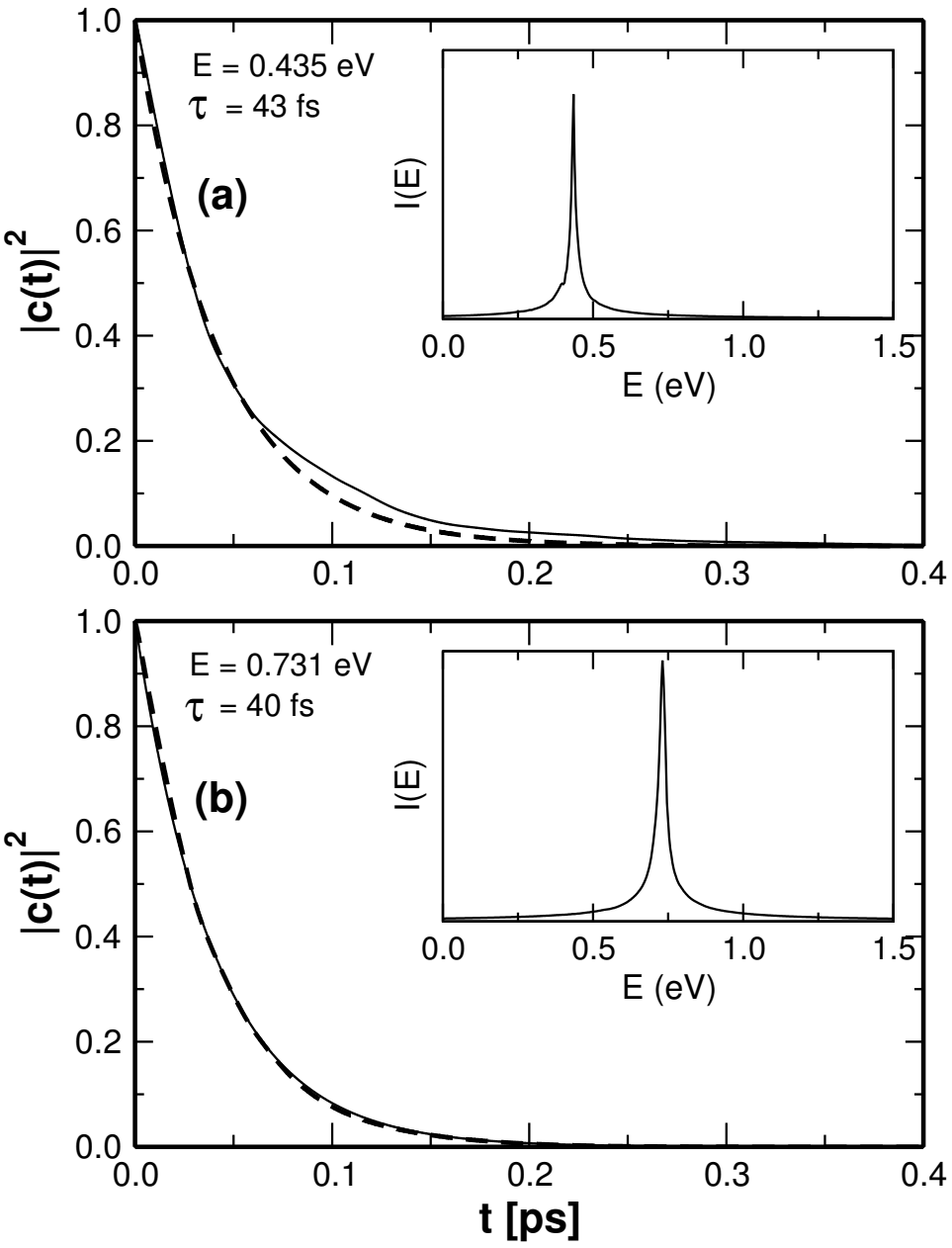

Figure 5.15: Time-dependence of the survival probability ($|C(t)|^2$) (dashed curve) of the quasibound states of Fig. 5.14 are plotted in the panel (a) and (b). An exponential fit of the survival probability is shown by the solid curve in each panel. A Fourier transform of the corresponding autocorrelation function is shown as an insert in panel (a) and (b).

In order to further verify the accuracy of the above lifetime measurements through the line-shape analysis, we have carried out another series of WP calculations using the eigenstate of the resonances as the initial wavefunction, $|\Psi(R, r, \gamma, t = 0)\rangle = |\Psi_n\rangle$, in the WP propagation. The decay dynamics of the initial state is then monitored and its survival probability, $Q(t) = |C(t)|^2$, is calculated in time. Since the initial state in this case is supposed to be fully trapped in the resonance state, the contribution from the direct scattering in the dynamics is expected to be minimized. This would then greatly reduce the background contribution and $Q(t)$ would exhibit the behavior of a pure decaying exponential, $\sim \exp(-t/\tau)$. Therefore, by fitting the short time decay profile to this exponential by a linear least square procedure the lifetime, τ, of the resonances can be extracted. This is applied to all 31 resonances reported in Table 5.3. For example, we show in Figs. 5.15(a) and (b) the decay profiles of the two resonances of Figs. 5.14(a) and (b), respectively. $Q(t)$ resulting from the WP calculations are shown by the solid lines and their exponential fits are shown by the dashed lines. It can be seen that the fits agree very well to the observed decay profiles. A slight discrepancy between the two in Fig. 5.15(a) is possibly arising from the numerical errors accumulated during the WP propagation. We also note that for some of the resonances we carried out a biexponential fit of their decay curve, in order to minimize the contribution of the overlapping partner in their decay lifetime.

In order to clearly demonstrate that the background contribution is minimized in the decay lifetime measurements, we in Figs. 5.15(a) and (b), include the Fourier transform of the corresponding $|C(t)|$ as an insert. A well resolved appearance of the peaks (when compared to the same obtained from the pseudospectrum as shown in Figs. 5.14(a) and (b) by asterisks) approaching to the shape of a true line-shape function indicate that the initial state in these situations are fully trapped in the resonance state and the resonance scattering dominates over the direct scattering. An examination of the two lifetime values reported in Table 5.3 reveals that the line-width lifetime values are usually larger than the corresponding decay lifetime for most of the resonances. Except

for a few resonances the agreement between the two is satisfying.

5.3.3 Resonances for $J \neq 0$

5.3.3.1 Pseudospectrum: CS Approximation

In Fig. 5.16 we show the pseudospectra obtained for different values of J and for $K = 0$ for the H+HLi collisions. The spectra are obtained within the CS approximation. This illustrates how the spectrum changes with increasing value of the total angular momentum. The spectrum in panel (a) is already discussed in a previous section (cf. Figs. 5.5). Two important features are reflected in the spectra of Figs. 5.16(a-d); (1) the band origin (0-0 line) moves up in the energy axis and (2) the spectrum becomes diffuse and the resonances structures are gradually lost when J increases (see panel (a-d)). These can be partly understood from the J-dependence of the PES presented as a function of R and for $r = r_e$ in Fig. 4.4 of chapter 4. It can be seen from Fig. 4.4 that the minimum of the PES moves to the higher energies with increasing J. This explains the shift of the 0-0 line in the spectrum to a higher energy value. The cuts of the PESs for $J = 0$ and $J = 10$ are nearly identical (cf. Fig. 4.4), however, the 0-0 line shifts $\sim$0.043 eV to the higher energy for $J = 10$ relative to that for $J = 0$. This is due to a finite increase in anharmonicity of the PES for higher values of J. The second feature stems from the increasing value of the centrifugal potential. This adds a barrier to the PES and the height of the barrier increases with increasing J (cf. Fig. 4.4). Therefore, the quantum tunnelling becomes an increasingly important mechanism for the decay of the low-lying quasibound levels supported by the PES. It is clear from Fig. 5.16(d) that the resonance structures are completely lost for higher values of J and note that the average energy of the initial GWP is shifted from $\sim$0.11 eV (shown in panel (a)) to $\sim$1.34 eV (shown in panel (d)). This is also obvious from the respective time autocorrelation functions, $|C(2t)|$, vs t plot shown as an insert in each panel of Figs. 5.16(a-d). One can see that the quasiperiodic recurrences rapidly disappears with increasing J values. Therefore, it seems that the WP moves to the reagent and product asymptotes more rapidly for

higher values of the partial wave.

In Fig. 5.17(a-c) we show the effect of increasing the K values on the pseudospectrum for $J = 10$. These spectra are also calculated within the CS approximation. In this case also the 0-0 line shifts to the higher energy when K value increases. For example, the 0-0 line shifts by ~ 0.026 eV from $K = 0$ (cf. Fig. 5.16(b)) to $K = 1$, by ~ 0.03 eV from $K = 1$ to $K = 4$ and by ~ 0.04 eV from $K = 4$ to $K = 8$. The overall structure of the spectrum also becomes somewhat more diffuse with increasing K value.

5.3.3.2 Pseudospectrum: Effects of Coriolis coupling

The impact of the CC in the nuclear dynamics is illustrated by the results shown in Fig. 5.18(a-c). The calculations are carried out for $J = 2$ and $K = 0, 1, 2$ and the corresponding pseudospectra are plotted in panel a, b, and c, respectively. The CS and CC results are shown by the dotted and solid lines, respectively. In the CC calculations the K grid is chosen to vary from 0 to J_{max} and the coupling between the adjacent K and $K \pm 1$ states in this range is considered. The calculations are started with even spectroscopic parity [defined by $(-1)^{J+p}$; p=0(1) represents even(odd) parity]. It can be seen that the energy eigenvalue of the quasibound levels shifts further to the higher energy in the CC results. It is also obvious from the figure that the resonances become broader when the CC is considered. This is also reflected in the decay of the corresponding autocorrelation function shown as an insert in each panel of Fig. 5.18. The quasiperiodic recurrences gradually disappears in the CC results with increasing K value. The energy eigenvalue of the resonances obtained from the spectra shown in Fig. 5.18 are given in Table 5.4.

Results obtained from both the CS and CC calculations are included in the Table 5.4. The linewidth life-time of the prominent resonances are calculated by fitting the corresponding peaks to a Lorentzian line-shape function. In Fig. 5.19, we show two typical spectral peaks (indicated by the asterisks) along with their Lorentzian fit (solid

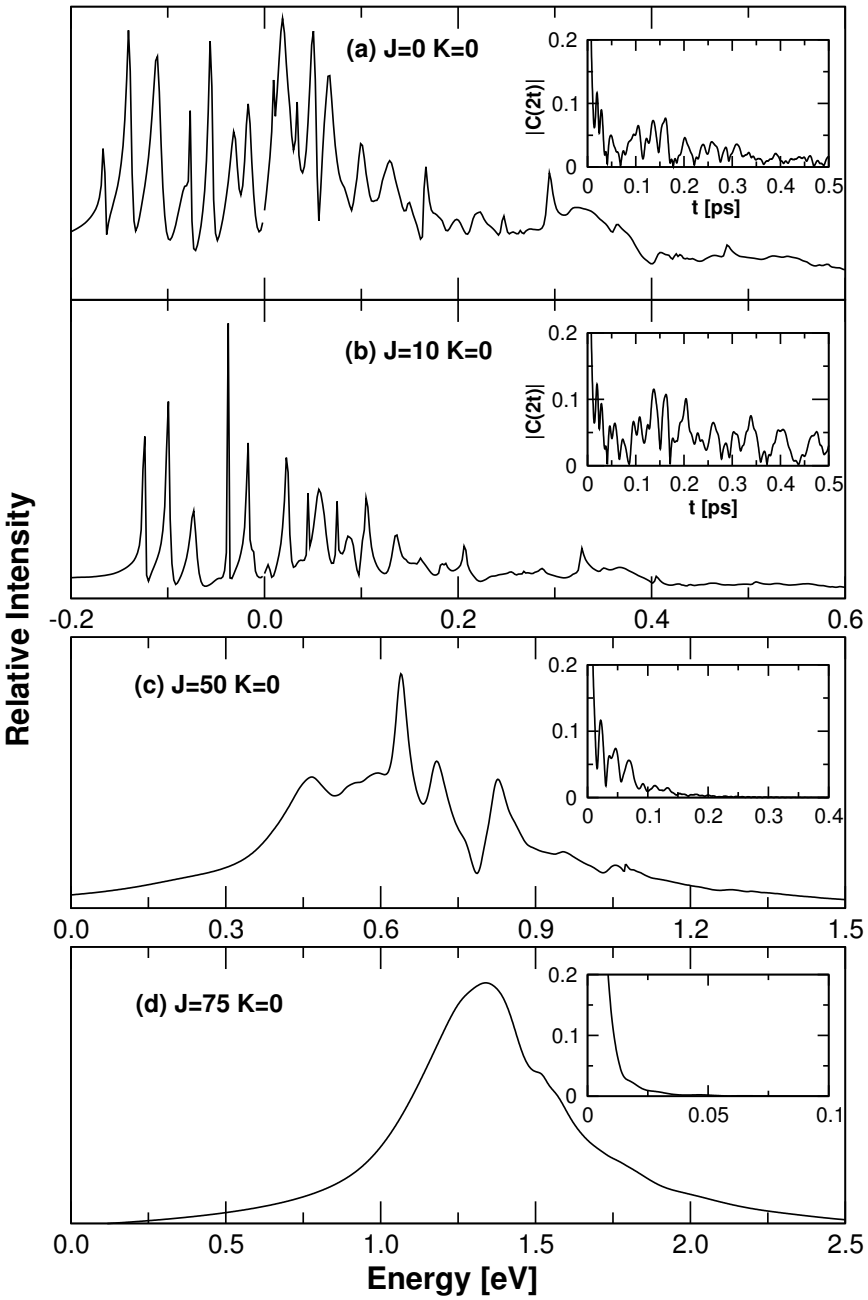

Figure 5.16: The pseudospectra for the quasibound levels of the ground electronic state of H+HLi for increasing values of J (indicated in each panel) and for $K = 0$ (see the text for details). The intensity (in arbitrary units) is plotted as a function of the energy of the quasibound levels. The zero of energy corresponds to asymptotically separated H and HLi fragments. The time-dependence of the corresponding autocorrelation function $|C(2t)|$ is shown as an insert in the respective panels.

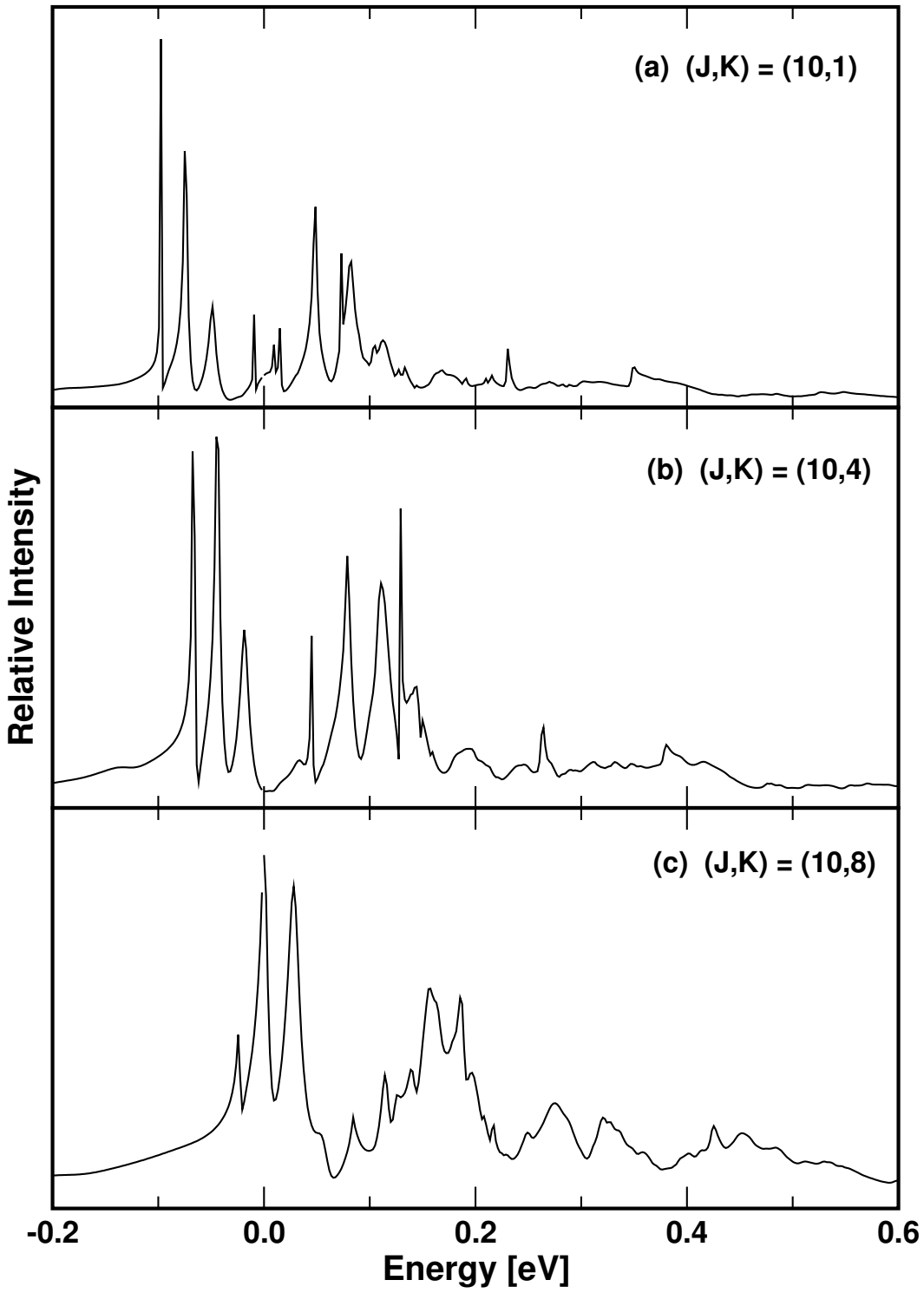

Figure 5.17: Same as in 5.16, for J=10 and K=1, 4, and 8 shown in panel (a), (b) and (c), respectively.

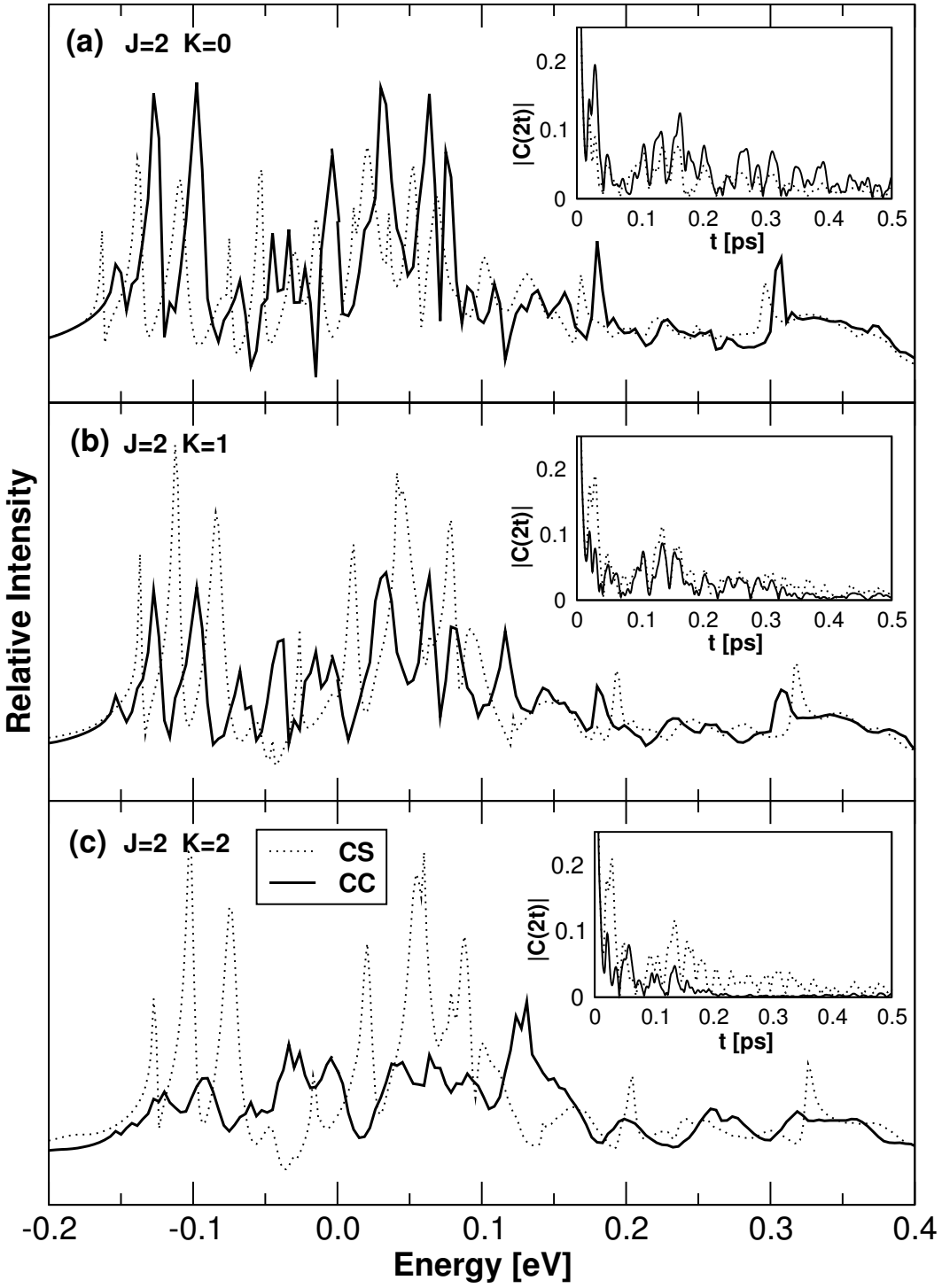

Figure 5.18: Same as in 5.16, obtained for J=2 and K=0, 1 and 2 plotted in the panel a, b and c, respectively. The CS and CC results are shown by the dotted and solid lines, respectively.

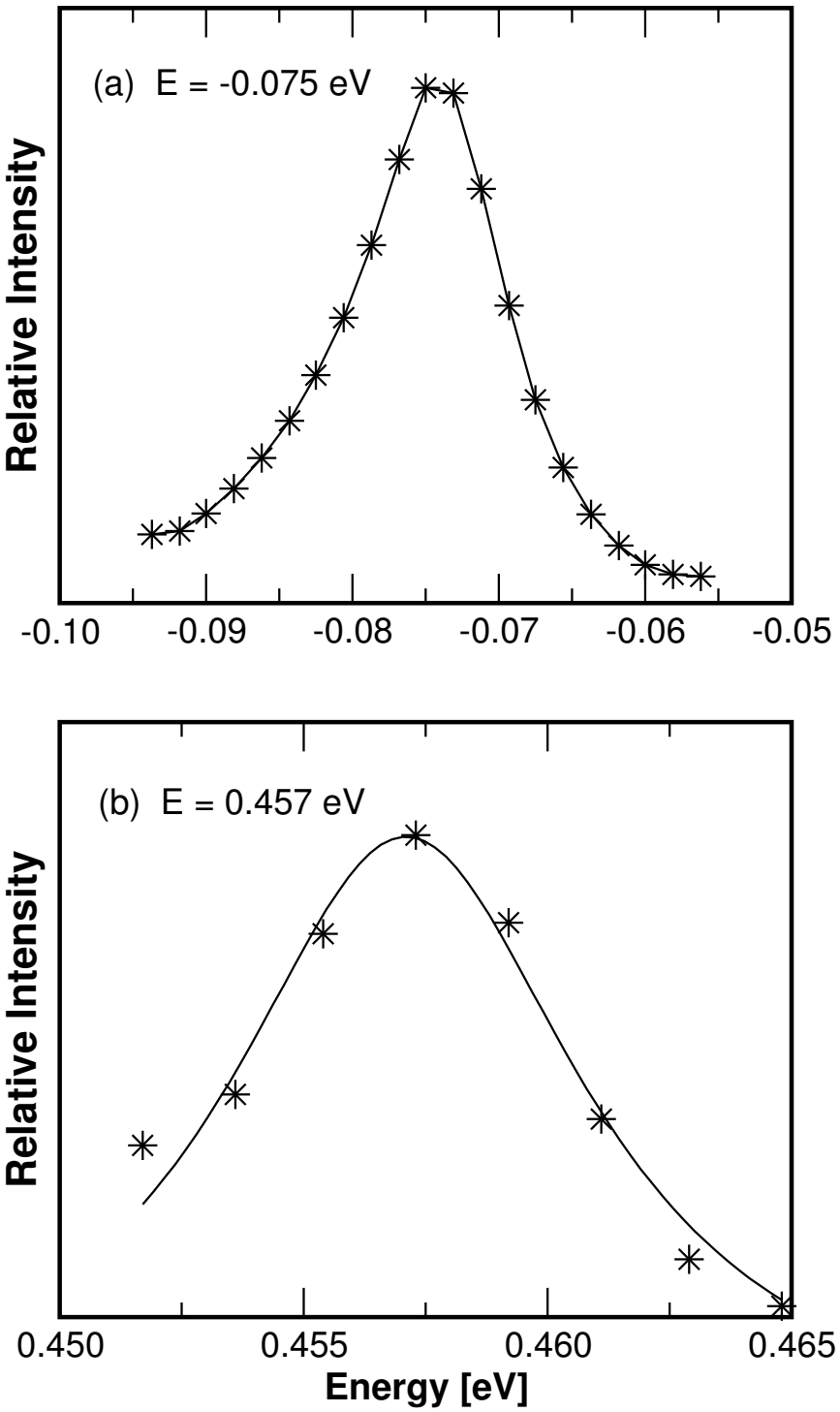

Figure 5.19: Lorentzian line-shapes for two typical spectral peaks shown by the solid curve. The peaks obtained from the time-dependent WP calculations are shown by the asterisks.

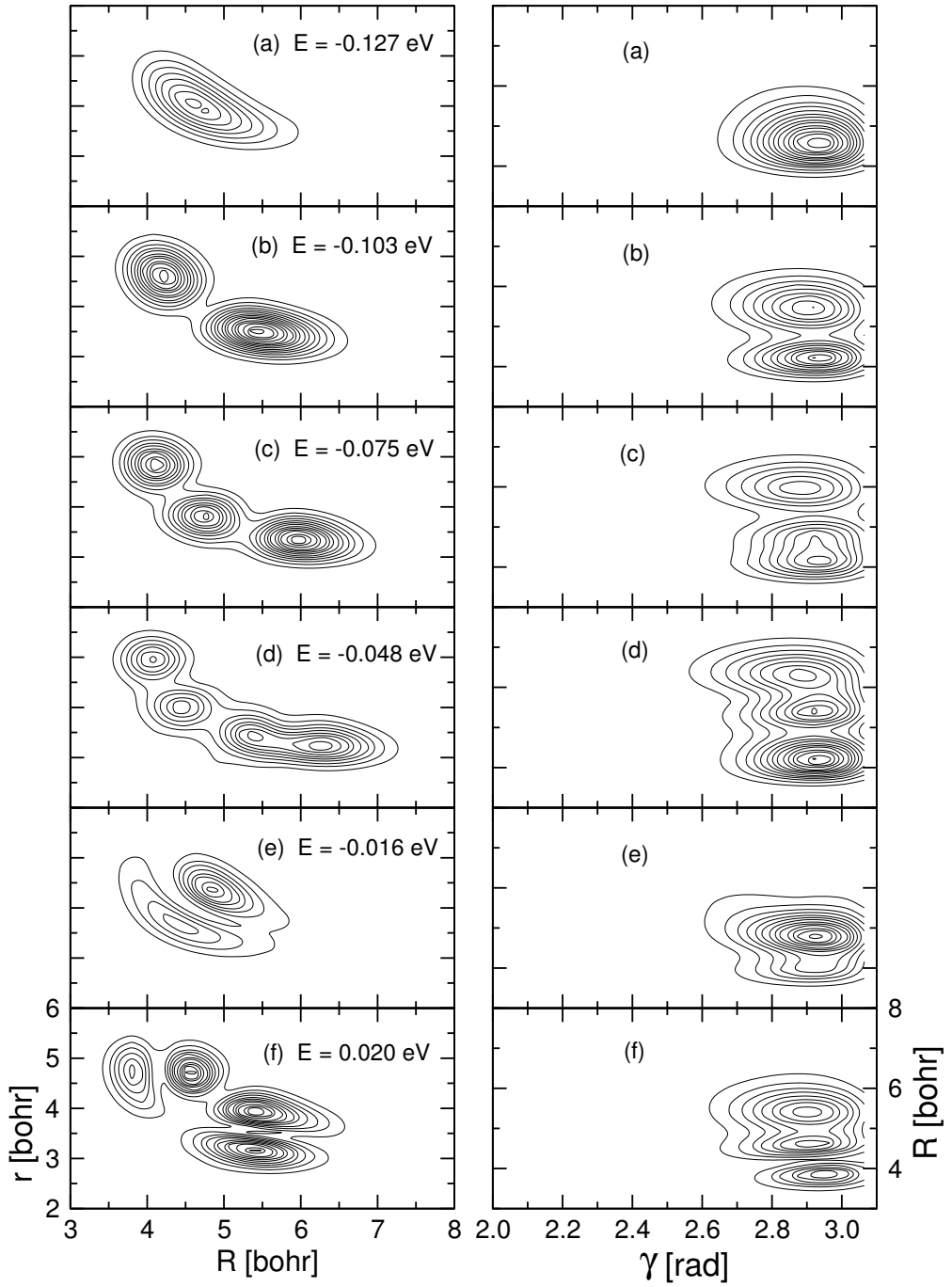

Figure 5.20: Probability density contours of the quasibound eigenfunctions obtained through spectral quantization for the H+HLi system. The energy eigenvalues of the quasibound states are indicated in the respective panel and the contour diagrams are plotted both in the (R, r) and (R, γ) planes averaged over the values of γ and r, respectively.

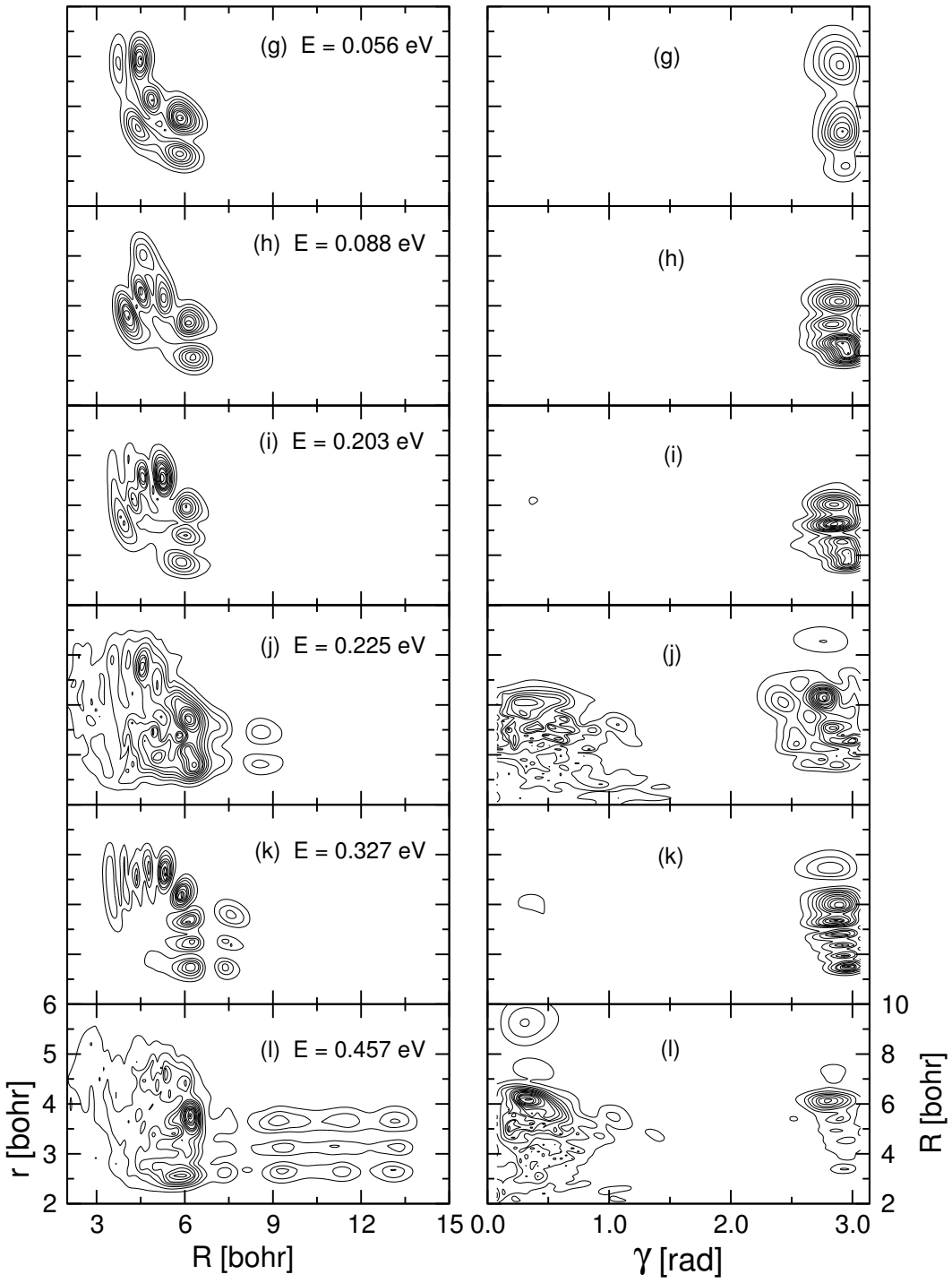

Figure 5.21: Same as in Fig. 5.20 for higher energies.

Table 5.4: Eigenvalues (E_n) and the line-width lifetime of the resonances in H+HLi scattering for $J = 2$ and $K = 0 - 2$ calculated using CS and CC methods. A blank entry indicates the corresponding quantity could not be determined unambiguously.

$J=2$ $K=0$				$J=2$ $K=1$				$J=2$ $K=2$			
CS		CC		CS		CC		CS		CC	
E_n (eV)	τ_n (fs)	E_n (eV)	τ_n (fs)	E_n (eV)	τ_n (fs)	E_n (eV)	τ_n (fs)	E_n (eV)	τ_n (fs)	E_n (eV)	τ_n (fs)
-0.164	-	-0.153	40	-0.138	553	-0.154	56	-0.127	56	-0.153	33
-0.139	100	-0.127	77	-0.113	94	-0.128	74	-0.103	92	-0.142	38
-0.111	54	-0.098	56	-0.085	52	-0.099	45	-0.075	51	-0.121	20
-0.078	54	-0.071	130	-0.058	20	-0.068	51	-0.048	19	-0.093	22
-0.054	12	-0.045	67	-0.027	155	-0.041	49	-0.016	111	-0.061	60
-0.030	49	-0.035	-	0.010	85	-0.016	41	0.020	86	-0.034	54
-0.015	7	-0.023	27	0.045	32	-0.004	-	0.056	34	-0.027	77
0.020	26	-0.004	-	0.078	112	0.032	27	0.079	360	-0.004	-
0.035	278	0.032	44	0.094	29	0.062	83	0.088	44	0.045	11
0.051	79	0.063	68	0.123	-	0.082	52	0.104	28	0.067	37
0.069	60	0.077	-	0.180	118	0.116	70	0.163	9	0.089	9
0.102	65	0.092	-	0.194	107	0.145	23	0.203	9	0.129	27
0.131	30	0.108	17	0.248	130	0.182	-	0.225	37	0.201	22
0.152	39	0.128	18	0.281	34	0.199	20	0.243	17	0.260	27
0.169	178	0.138	43	0.319	86	0.235	18	0.255	36	0.274	26
0.200	34	0.156	28	0.346	17	0.260	25	0.300	19	0.320	16
0.223	38	0.181	12	0.431	38	0.310	45	0.327	131	0.358	19
0.250	118	0.229	33	0.502	20	0.340	6	0.440	37	0.431	12
0.297	89	0.253	-	0.523	30	0.382	12	0.457	74	0.480	17
0.328	8	0.272	-			0.426	53	0.513	17	0.499	38
0.368	14	0.306	-			0.464	17	0.563	13	0.524	19
0.413	20	0.315	-			0.492	72	0.606	30	0.563	26
0.429	24	0.373	26			0.557	19				
0.481	89	0.421	29			0.597	28				
0.530	21	0.450	31								
0.581	69	0.489	535								

line). The life-time (τ) of the resonance is calculated from a Lorentzian fit of the spectral peak. The linewidth life-times of the resonances are also included in Table 5.4. A close look at the data recorded in Table 5.4 reveals that the resonances are tend to become broader when the CC is considered in the dynamics, although a uniform pattern does not emerge from the given results.

In order to discuss the nature of some of the eigenfunctions of the resonances for $J \neq 0$ and $K \neq 0$, in relation to their counterpart for $J = 0$ and $K = 0$, we calculate the eigenfunctions of a few resonances (for $J = 2$ and $K = 2$) by Eq. (5.9) [105]. The resulting eigenfunctions of 12 resonances are shown in Figs. 5.20(a-l). The probability density ($|\Psi_n(E)|^2$) contours of the eigenfunctions are plotted in the (R, r) and (γ, R) planes for average values of γ and r, respectively. As discussed in a previous section (Sec. 5.3.2), the eigenstates in Fig. 5.20 can be assigned in terms of the number of nodes $n_R,\ n_r$ and n_γ along R, r and γ coordinates, respectively. These eigenfunctions may be compared with the corresponding ones for $J = 0$ and $K = 0$ presented in Figs. 5.9 to Figs. 5.13. It can be seen that the eigenvalue of the (0,0,0) [according to the (n_R, n_r, n_γ) specification] level for $J = 2$ and $K = 2$ shifts by ~ 0.04 eV to the higher energy when compared with the same for $J = 0,\ K = 0$ (cf. Fig. 5.9(a)). Similarly the eigenvalue of the (1,0,0) (panel b) level also shifts by ~ 0.038 eV to the higher energy compared with its $J = 0,\ K = 0$ counterpart (cf. Fig. 5.9(b)). A similar shift can be observed for the eigenvalue of the (1,1,0) level. It can be seen that the quanta of energies for the motion along the R and r coordinates remain almost same for both $J = 0,\ K = 0$ and $J = 2,\ K = 2$ results. The eigenstates in Fig. 5.20(d) and 6(e) are not observed in the $J = 0,\ K = 0$ calculations. The one in Fig. 5.20(f) can be assigned to a (2,1,0) level is also ~ 0.037 eV above to the corresponding one for $J = 0,\ K = 0$. It is to be noted that like in the $J = 0,\ K = 0$ case the quasibound complexes discussed above also correspond to a linear ($\gamma = \pi$) HLiH configuration. With increase in the energy eigenvalues, the resonances acquire a much more complex nodal pattern (cf. Figs. 5.21(g-l)) for $J = 2,\ K = 2$, compared to those for $J = 0,\ K = 0$. A close look

at the lifetime of the low-lying eigenstates discussed above reveal that the resonances tend to have shorter lifetime for $J \neq 0,\ K \neq 0$. For example the (0,0,0) level has a lifetime of $\sim$ 270 fs in the case of $J = 0,\ K = 0$. This can be compared with the values of $\sim$ 56 fs and $\sim$ 33 fs obtained in the present CS and CC calculation, respectively (cf. Table 5.4). Similarly, a substantial reduction of the lifetime (compared to that for $J = 0,\ K = 0$, cf. Table 5.3) of the (1,0,0) level can be observed in both the CS and CC results. The CS results [105] reproduce the same lifetime for the (1,1,0) level as that found in the case of $J = 0,\ K = 0$ [104]. However, the CC results predict substantial reduction of the lifetime by $\sim$ 30 fs in this case. In case of the (2,1,0) level the CS results predict a higher lifetime compared to that found in the $J = 0,\ K = 0$ results, but the CC calculations yield a shorter lifetime.

5.4 Summary

In the present Chapter, we have presented the systematic analysis of a TDWP approach (in related to those in Chapter 2) to calculate the resonances in H+HLi scattering for the total angular momentum $J \geq 0$, employing the *ab initio* DMJ PES [91] of the system. The signature of these resonances are observed in terms of oscillations in the reaction probability vs. energy curves (cf. Chapter 3 and 4). The resonances are identified here by examining a set of pseudospectrum calculated by locating a suitable WPs initially in the interaction region of the DMJ PES. The resonances are characterized by calculating their eigenfunctions and both the line-width as well as decay lifetimes. These are assigned based on the number of nodes in their eigenfunctions along R, r and γ grid. They are further classified into the conventional reactive resonances and more subtle barrier or threshold states, by examining the nodal progression in their eigenfunctions. The resonances are usually broad at high energies in par with the observed direct nature of the scattering. Lifetime analysis of the 31 resonances of the H+HLi system reveal that they can survive as long as $\sim$ 250 fs, in the case of $J = 0$ [104].

The effects of three-body rotation on the resonances ($J \neq 0$) in the H+HLi scattering are investigated by carrying out the calculations using both the CS and the CC model [105]. These are generally observed that the quasibound levels shift to the higher energies and also the corresponding resonances tend to become broader with increasing contributions of the three-body rotation in the nuclear dynamics. The CC model makes the resonances even broader compared to the CS model. The height of the centrifugal barrier increases with increasing value of the partial wave and quantum tunnelling becomes an important mechanism for the decay of the low-lying quasibound levels of the PES.

Chapter 6

Future Directions

The reactive scattering dynamics of H+HLi system is theoretically studied in the present thesis. The theoretical approach is based on a TDWP method and an *ab initio* PES of the ground electronic state of the system. The dynamical observables reported include the state-selected reaction probabilities, integral reaction cross sections and thermal rate constants. The reaction dynamics is systematically examined starting from a reduced dimensional to the full-dimensional model. The commonly employed approximate methods to treat reactive scattering problems are also considered and the results from various calculations are compared with the full-dimensional results to judge their validity. The important quantum mechanical phenomenon of resonances is examined in detail.

The main findings of the present work on the H+HLi reaction dynamics on the *ab initio* DMJ PES are:

1. The H exchange reaction path (R2) is more favored over the HLi depletion path (R1) at low and moderate collision energies, and the reverse holds at high collision energies and for higher values of the total angular momentum J.

2. The resonance oscillations observed in the reaction probability results average out on inclusion of the contributions from various partial waves.

3. The reaction does not reveal a threshold and the overall variation of reaction cross section is consistent with the characteristics of a barrierless reaction.

4. The variation of initial state-selected thermal rate constants within the temperature range (150-1200 K) shows substantial deviations from the Arrhenius behavior which is again indicating the feature of a barrierless reaction.

5. The sharp resonances (lifetime upto $\sim$ 250 fs) observed for the zero total angular momentum become broad for the nonzero values of the three body rotation. The resonance energies for $J \neq 0$ shifts to the higher energies compared to those for $J = 0$. At very large values of J (e.g. > 70) the resonances disappear.

The initial state-selected reaction dynamics is examined in this thesis. It will be important and worthwhile to study the state-to-state reaction dynamics to understand the microscopic energy disposal mechanisms in this reaction in greater detail. Furthermore, the latter will enable to calculate the differential reaction cross sections and help to understand the forward / backward nature of the scattering. It is worthwhile to point out that molecular beam experiments will be valuable for this reaction which will further add to the trustworthiness of the theoretical predictions and the accuracy of the underlying PES.

Since the lithium hydrogen collisions form an important part of the chemistry of the interstellar clouds, it is also important to investigate these collisions at ultracold conditions. This aspect of the study is currently in progress. The ionic members of the lithium-hydrogen family of reactions are also considered and are being studied at present with the accurate theoretical approach developed here. Many of the reactions in this family are believed to be perturbed by the nonadiabatic interactions with the excited electronic states. A detailed study of the role of excited electronic states on the reaction dynamics is planned for the future. Finally, we note that as large scale computational resources become more powerful and accessible, issues like improved

software design and massively parallel algorithms to be addressed in order to better deal with the expensive exact quantum dynamical simulations.

Bibliography

[1] E. Pollak, in *Theory of Chemical Reaction Dynamics*, edited by M. Baer (CRC, Boca Raton, 1985).

[2] D. C. Clary, *The theory of Chemical Reaction Dynamics* (Reidel, Boston, 1986).

[3] R. D. Levine and R. B. Bernstein, *Molecular Reaction Dynamics and Chemical Reactivity* (Oxford University, Oxford, 1987).

[4] J. N. Murrell and S. D. Bosanac, *Introduction to the Theory of Atomic and Molecular collisions* (John Wiley, Chichester, 1989).

[5] S. K. Adhikari and K. L. Kowolski, *Dynamical Collision Theory and Its Applications* (Academic, New York, 1991).

[6] *Modern Trends in Chemical Reaction Dynamics: Experiment and Theory, Part I*, edited by X. Yang and K. Liu (World Scientific, Singapore, 2004).

[7] A. H. Zewail, *Femtochemistry - Ultrafast Dynamics of the Chemical Bond* (World Scientific, Singapore, Vol. I-II, 1994).

[8] R. B. Bernstein, *Chemical Dynamics via Molecular Beam and Laser Techniques* (Clarendon Press, Oxford, 1982).

[9] B. Friedrich and D. R. Herschbach, Nature (London), **353**, 412 (1991).

[10] B. Freidrich, D. P. Pullman and D. R. Herschbach, J. Phys. Chem. **95**, 8118 (1991).

[11] J. J. Valentini, Y. T. Lee, and D. J. Auerbach, J. Chem. Phys. **67**, 4866 (1977).

[12] H. W. Cruse, P. J. Dagdigian, and R. N. Zare, Faraday Discuss. Chem. Soc. **55**, 277 (1973); R. N. Zare, Faraday Discuss. Chem. Soc. **67**, 7 (1979).

[13] A. Laubereau, S. F. Fischer, K. Spanner, and W. Kaiser, Chem. Phys. **31**, 335 (1978).

[14] M. Noll and J. P. Toennies, Chem. Phys. Lett. **108**, 297 (1984).

[15] J. R. Heath, S. C. O'Brien, Q. Zhang, Y. Liu, R. F. Curl, H. W. Kroto, F. K. Tittel, and R. E. Smalley, J. Am. Chem. Soc. **107**, 7779 (1985).

[16] A. H. Zewail, Science, **242**, 1645 (1988).

[17] M. Dantus, R. M. Bowman, and A. H. Zewail, Nature, **343**, 737 (1990); L. R. Khundkar and A. H. Zewail, Ann. Rev. Phys. Chem. **41**, 15 (1990).

[18] I. W. M. Smith, Nature **343**, 69 (1990).

[19] S. C. Althorpe, F. F.-Alonso, B. D. Bean, J. D. Ayers, A. E. Pomerantz, R. N. Zare, and E. Wrede, Nature, **416**, 67 (2002).

[20] M. Karplus, R. N. Porter, and R. D. Sharma, J. Chem. Phys. **43**, 3259 (1965).

[21] L. M. Raff and D. L. Thompson, in *Theory of Chemical Reaction Dynamics*, edited by M. Baer (CRC Press, Boca Raton, Florida, Vol. III, 1985), pp.1-121.

[22] J. M. Bowman and G. C. Schatz, Ann. Rev. Phys. Chem. **46**, 169 (1995), and references therein.

[23] W. H. Miller, Adv. Chem. Phys. **25**, 69 (1974); Adv. Chem. Phys. **30**, 77 (1975); J. Phys. Chem. A **105**, 2942 (2001).

[24] E. J. Heller, J. Chem. Phys. **62**, 1544 (1975).

[25] *Atom-Molecule Collision Theory: A Guide for the Experimentalists*, edited by R. B. Bernstein (Plenum, New York, 1979).

[26] Y. Huang, S. S. Iyengar, D. J. Kouri, and D. K. Hoffman, J. Chem. Phys. **105**, 927 (1996).

[27] *Molecular Collision Dynamics*, edited by J. M. Bowman (Springer-Verlag, Berlin, 1983).

[28] *Dynamics of Molecular Collisions*, edited by W. H. Miller (Plenum, New York, 1979).

[29] *The Theory of Chemical Reaction Dynamics*, edited by M. Baer (CRC Press, Boca Raton, Florida, Vol.I-IV, 1985).

[30] G. C. Schatz, Chem. Rev. **87**, 81 (1987).

[31] D. C. Clary, Mol. Phys. **53**, 3 (1984).

[32] D. C. Clary, Science, **279**, 1879 (1998).

[33] H. Eyring and M. Polanyi, Z. Phys. Chem. **B12**, 279 (1931); *Potential Energy Surfaces and Dynamics Calculations*, edited by D. G. Truhlar (Plenum, New York, 1981).

[34] N. Sathyamurthy, Comput. Phys. Rep. **3**, 1 (1985).

[35] B. R. Johnson and N. W. Winter, J. Chem. Phys. **66**, 4116 (1977).

[36] P. Siegbahn and B. Liu, J. Chem. Phys. **68**, 2457 (1978); D. G. Truhlar and C. J. Horowitz, J. Chem. Phys. **68**, 2466 (1978); J. Chem. Phys. **71**, 1514 (1979).

[37] (a) *Dynamics of Molecules and Chemical Reactions*, edited by R. E. Wyatt and J. Z. H. Zhang (Marcel Dekker, New York, 1996); (b) J. Z. H. Zhang, *Theory and Application of Quantum Molecular Dynamics* (World Scientific, Singappore, 1999).

[38] D. G. Truhlar and B. C. Garrett, Ann. Rev. Phys. Chem. **35**, 159 (1984).

[39] D. M. Neumark, Ann. Rev. Phys. Chem. **43**, 153 (1992).

[40] N. Balakrishnan, C. Kalyanaraman, and N. Sathyamurthy, Phys. Rep. **280**, 79 (1997).

[41] M. Beck, A. Jäckle, G. A. Worth, and H. -D. Meyer, Phys. Rep. **324**, 1 (2000), and references therein.

[42] G. Nyman and H.-G. Yu, Rep. Prog. Phys. **63**, 1001 (2000).

[43] H. Nakamura, Ann. Rev. Phys. Chem. **48**, 299 (1997).

[44] S. C. Althorpe and D. C. Clary, Ann. Rev. Phys. Chem. **54**, 493 (2003).

[45] T. Peng and J. Z. H. Zhang, J. Chem. Phys. **105**, 6072 (1996).

[46] D. J. Kouri, D. Hoffmann, T. Peng, and J. Z. H. Zhang, Chem. Phys. Lett. **262**, 519 (1996).

[47] S. C. Althorpe, D. J. Kouri, and D. K. Hoffman, J. Chem. Phys. **106**, 7629 (1997); J. Chem. Phys. **107**, 7816 (1997); J. Phys. Chem. A **102**, 9494 (1998); S. C. Althorpe, J. Chem. Phys. **114**, 1601 (2001).

[48] E. M. Goldfield and S. K. Gray, Comput. Phys. Commun. **98**, 1 (1996), and references therein.

[49] A. J. H. M. Meijer and E. M. Goldfield, J. Chem. Phys. **108**, 5404 (1998); **110**, 870 (1999).

[50] E. M. Goldfield and A. J. H. M. Meijer, J. Chem. Phys. **113**, 11055 (2000);

[51] T. E. Carroll and E. M. Goldfield, J. Phys. Chem. A **105**, 2251 (2001).

[52] W. H. Miller, Ann. Rev. Phys. Chem. **41**, 245 (1990), and references therein.

[53] B. Jackson, Ann. Rev. Phys. Chem. **46**, 251 (1995).

[54] V. Mohan and N. Sathyamurthy, Comput. Phys. Rep. **7**, 213 (1988).

[55] J. Broeckhove and L. Lathouwers, *Time Dependent Methods for Quantum Dynamics* (NATO ASI Ser. **B229**, Plenum Press, New York, 1992).

[56] D. G. Truhlar, Comput. Phys. Commun. **84**, 78 (1994).

[57] S. Lepp and J. M. Shull, Astrophys. J. **280**, 465 (1984).

[58] (a) A. Dalgarno and S. Lepp, in *Astrochemistry*, edited by S. P. Tarafdar and M. P. Varshni (Dordrecht, Reidel, 1987), p. 109; (b) J. H. Black, in *Molecular Astrophysics*, edited by T. W. Hartquist (Cambridge University Press, Cambridge, 1988), p. 473.

[59] (a) A. Dalgarno and J. L. Fox, in *Unimolecular and Bimolecular Reaction Dynamics*, edited by C. Y. Ng, T. Baer, and I. Powis (Chichester, Wiley, 1994), 1; (b) M. Signore, *et al.* , Astrophys. J. Suppl. Ser. **92**, 535 (1994).

[60] V. K. Dubrovich, Astron. Lett. **19**, 53 (1993); R. Maoli, F. Melchiorri, and D. Tosti, Astrophys. J. **425**, 372 (1994).

[61] P. C. Stancil and A. Dalgarno, Astrophys. J. **479**, 543 (1997); P. C. Stancil, S. Lepp, and A. Dalgarno, Astrophys. J. **458**, 401 (1996).

[62] E. Bodo, F. A. Gianturco, and R. Martinazzo, Phys. Rep. **384**, 85 (2003).

[63] T. J. Martínez, Chem. Phys. Lett. **272**, 139 (1997).

[64] H. S. Lee, Y. S. Lee, and G. -H. Jeung, J. Phys. Chem. A, **103**, 11080 (1999).

[65] J. -J. Chen, Y. -M. Hung, D. -K. Liu, H. -S. Fung, and K. -C. Lin, J. Chem. Phys. **114**, 9395 (2001).

[66] R. J. Marsh, A. J. McCaffery, and M. A. Osborne, J. Phys. Chem. A, **107**, 9511 (2003).

[67] F. A. Gianturco, S. Kumar, S. K. Pathak, M. Raimondi, and M. Sironi, Chem. Phys. **215**, 239 (1997); E. Bodo, S. Kumar, F. A. Gianturco, A. Famulari, M. Raimondi, and M. Sironi, J. Phys. Chem. A **102**, 9390 (1998).

[68] E. Bodo, F. A. Gianturco, R. Martinazzo, A. Forni, A. Famulari, and M. Raimondi, J. Phys. Chem. A **104**, 11972 (2001); A. Satta, E. Bodo, R. Martinazzo, and F. A. Gianturco, J. Chem. Phys. **117**, 177 (2002).

[69] A. J. McCaffery, Phys. Chem. Chem. Phys. **6**, 1637 (2004).

[70] S. Bililign, B. C. Hattaway, T. L. Robinson, and H. G. Jeung, J. Chem. Phys. **114**, 7052 (2001).

[71] A. Grimpe, C. Figl, J. Grosser, O. Hoffmann, and F. Rebentrost, J. Phys. B: At. Mol. Opt. Phys. **38**, 135 (2005).

[72] T. J. Martínez and R. D. Levine, Chem. Phys. Lett. **259**, 252 (1996).

[73] T. J. Martínez and R. D. Levine, J. Chem. Phys. **105**, 6334 (1996).

[74] E. Teller, J. Phys. Chem. **41**, 109 (1937); E. R. Davidson, J. Am. Chem. Soc. **99**, 397 (1977); H. Köppel, W. Domcke, and L. S. Cederbaum, Adv. Chem. Phys. **57**, 59 (1984); F. Bernardi, M. Olivucci, and M. Robb, Chem. Soc. Rev. **25**, 321 (1995); W. Domcke and G. Stock, Adv. Chem. Phys. **100**, 1 (1997).

[75] T. J. Martínez, Chem. Phys. Lett. **272**, 139 (1997).

[76] J. N. Murrell, T. G. Wright, and S. D. Bosanac, J. Mol. Str. (Theochem), **591**, 1 (2002).

[77] E. Bodo, F. A. Gianturco, R. Martinazzo, and M. Raimondi, Chem. Phys. **271**, 309 (2001); R. Martinazzo, E. Bodo, F. A. Gianturco, and M. Raimondi, Chem. Phys.

287, 335 (2003); R. Martinazzo, G. F. Tantardini, E. Bodo, and F. A. Gianturco, J. Chem. Phys. **119**, 11241 (2003).

[78] E. Bodo, F. A. Gianturco, and R. Martinazzo, J. Phys. Chem. A **105**, 10994 (2001).

[79] N. Bulut, F. Gogtas, and S. Akpinar, Chem. Phys. **407**, 298 (2005).

[80] B. K. Taylor and R. J. Hinde, J. Chem. Phys. **122**, 074308 (2005).

[81] A. Laganá, R. T. Pack, and G. A. Parker, J. Chem. Phys. **99**, 2269 (1993); W. Zhu, D. Wang, and J. Z. H. Zhang, Theor. Chem. Acc. **96**, 31 (1997).

[82] M. Paniagua, and A. Aguado, M. Lara, and O. Roncero, J. Chem. Phys. **111**, 6712 (1999); C. Sanz, O. Roncero, M. Paniagua, and A. Aguado, Chem. Phys. Lett. **351**, 295 (2002).

[83] P. F. Weck and N. Balakrishnan, J. Chem. Phys. **122**, 154309 (2005).

[84] Y. Sun, R. S. Judson, and D. J. Kouri, J. Chem. Phys. **90**, 241 (1989).

[85] P. Hobza and P. von R. Schleyer, Chem. Phys. Lett. **105**, 630 (1984).

[86] C. H. Wu, J. Chem. PHys. **71**, 783 (1979).

[87] A. I. Boldyrev and J. Simons, J. Chem. Phys. **99**, 4628 (1993).

[88] J. Senekowitsch and P. Rosmus, J. Chem. Phys. **86**, 6329 (1987).

[89] A. I. Boldyrev and W. von Niessen, Chem. Phys. **155**, 71 (1991).

[90] N. J. Clarke, M. Sironi, M. Raimondi, S. Kumar, F. A. Gianturco, E. Buonomo, and D. L. Cooper, Chem.Phys. **233**, 9 (1998).

[91] L. J. Dunne, J. N. Murrell, and P. Jemmer, Chem. Phys. Lett. **336**, 1 (2001).

[92] K. H. Kim, Y. S. Lee, T. Ishida, and G.-H. Jeung, J. Chem. Phys. **119**, 4689 (2003).

[93] P. Defazio, C. Petrongolo, P. Gamallo, and M. Gonzaález, J. Chem. Phys. **122**, 214303 (2005).

[94] S. K. Gray and G. G. Balint-Kurti, J. Chem. Phys. **108**, 950 (1998).

[95] J. M. Bowman, Adv. Chem. Phys. **61**, 115 (1985); J. Phys. Chem. **95**, 4960 (1991); Theor. Chem. Acc. **108**, 125 (2002).

[96] S. L. Mielke, G. C. Lynch, D. G. Truhlar, and D. W. Schwenke, J. Phys. Chem. **98**, 8000 (1994).

[97] D. H. Zhang and J. Z. H. Zhang, J. Chem. Phys. **110**, 7622 (1999).

[98] R. T. Pack, J. Chem. Phys. **60**, 633 (1974).

[99] P. McGuire and D. J. Kouri, J. Chem. Phys. **60**, 2488 (1974).

[100] R. S. Judson, D. J. Kouri, D. Neuhauser, and M. Baer, Phys. Rev. A **42**, 351 (1990); A. Baram, I. Last, and M. Baer, Chem. Phys. Lett. **212**, 649 (1993).

[101] R. Padmanaban and S. Mahapatra, J. Chem. Phys. **117**, 6469 (2002).

[102] R. Padmanaban and S. Mahapatra, J. Chem. Phys. **121**, 7681 (2004); *Erratum,* J. Chem. Phys. **122**, 029902 (2005).

[103] R. Padmanaban and S. Mahapatra, J. Phys. Chem. A (submitted).

[104] R. Padmanaban and S. Mahapatra, J. Chem. Phys. **120**, 1746 (2004).

[105] R. Padmanaban and S. Mahapatra, J. Theor. Comp. Chem. (in press).

[106] D. H. Zhang, M. Yang, and S. -Y. Lee, J. Chem. Phys. **117**, 10067 (2002), and references therein.

[107] D. H. Zhang and J. Z. H. Zhang, J. Chem. Phys. **99**, 5615 (1993); J. Chem. Phys. **100**, 2697 (1994).

[108] J. Z. H. Zhang, J. Dai, and W. Zhu, J. Phys. Chem. A, **101**, 2746 (1997), and references therein.

[109] S. Y. Lin and H. Guo, J. Chem. Phys. **117**, 5183 (2002).

[110] D. Neuhauser, M. Baer, R. S. Judson, and D. J. Kouri, J. Chem. Phys. **90**, 5882 (1989); **93**, 312 (1990).

[111] D. Neuhauser, Chem. Phys. Lett. **200**, 173 (1992).

[112] D. Kosloff and R. Kosloff, Comput. Phys. Commun. **30**, 333 (1983); J. Comput. Phys. **52**, 35 (1983).

[113] D. Neuhauser and M. Baer, J. Phys. Chem. **93**, 2872 (1989); J. Chem. Phys. **90**, 4351 (1989); J. Chem. Phys. **91**, 4651 (1989). D. Neuhauser, M. Baer, R. S. Judson, and D. J. Kouri, Comput. Phys. Commun. **63**, 460 (1991).

[114] S. Mahapatra and N. Sathyamurthy, J. Chem. Soc. Faraday Trans. **93**, 773 (1997).

[115] M. S. Child, Mol. Phys. **96**,4412 (1999).

[116] Á. Vibók and G. G. Balint-Kurti, J. Phys. Chem. **96**, 7615 (1992); **96**, 8712 (1992).

[117] A. R. Offer and G. G. Balint-Kurti, J. Chem. Phys. **101**, 10416 (1994).

[118] D. Neuhauser, J. Chem. Phys. **100**, 9272 (1994).

[119] N. Balakrishnan and G. D. Billing, J. Chem. Phys. **101**, 2785 (1994); Chem. Phys. Lett. **233**, 145 (1995).

[120] G. D. Billing and N. Marković, J. Chem. Phys. **99**, 2674 (1993); N. Marković and G. D. Billing, J. Chem. Phys. **100**, 1085 (1994).

[121] J. Z. H. Zhang and D. H. Zhang, J. Chem. Phys. **101**, 1146 (1994).

[122] J. Z. H. Zhang and D. H. Zhang, Chem. Phys. Lett. **232**, 370 (1995); Y. Zhang, D. Zhang, W. Li, Q. Zhang, D. Wang, D. H. Zhang, and J. Z. H. Zhang, J. Phys. Chem. **99**, 16824 (1995).

[123] R. Chen and H. Guo, Comput. Phys. Commun. **119**, 19 (1999).

[124] B. Poirier, Chem. Phys. **308**, 305 (2005).

[125] J. V. Lill, G. A. Parker, and J. C. Light, Chem. Phys. Lett. **89**, 483 (1982); J. C. Light, I. P. Hamilton, and J. V. Lill, J. Chem. Phys. **82**, 1400 (1985); J. P. Hamilton and J. C. Light, J. Chem. Phys. **84**, 306 (1986).

[126] R. M. Whitnell and J. C. Light, J. Chem. Phys. **90**, 1774 (1989).

[127] Z. Bačić and J. C. Light, Ann. Rev. Phys. Chem. **40**, 469 (1989).

[128] F. Le Quéré and C. Leforestier, J. Chem. Phys. **92**, 247 (1990); C. Leforestier, J. Chem. Phys. **94**, 6388 (1991).

[129] G. C. Corey and D. Lemoine, J. Chem. Phys. **97**, 4115 (1992).

[130] D. T. Colbert and W. H. Miller, J. Chem. Phys. **96**, 1982 (1992).

[131] T. Seideman and W. H. Miller, J. Chem. Phys. **96**, 4412 (1991); J. Chem. Phys. **97**, 2499 (1992).

[132] C. Leforestier and W. H. Miller, J. Chem. Phys. **100**, 733 (1994).

[133] U. Manthe and W. H. Miller, J. Chem. Phys. **99**, 3411 (1993).

[134] A. Veil and C. Leforestier, and W. H. Miller, J. Chem. Phys. **108**, 3489 (1998), and references therein.

[135] I. Last, M. Gilibert and M. Baer, J. Chem. Phys. **107**, 1451 (1997); T. Takayanagi, Y. Kurosaki and A. Ichihar, J. Chem. Phys. **112**, 2615 (2000).

[136] S. Mahapatra, Phys. Chem. Chem. Phys. **2**, 671 (2000).

[137] S. Mahapatra and N. Sathyamurthy, J. Chem. Phys. **105**, 10934 (1996); J. Chem. Phys. **107**, 6621 (1997).

[138] S. Y. Lin and H. Guo, J. Phys. Chem. A **108**, 2141 (2004).

[139] C. L. Russell and D. E. Manolopoulos, J. Chem. Phys. **110**, 177 (1999).

[140] K. Drukker and G. C. Schatz, J. Chem. Phys. **111**, 2451 (1999); X. Liu, J. J. Lin, S. A. Harich, and X. Yang, Phys. Rev. Lett. **86**, 408 (2001).

[141] P. Defazio, C. Petrongolo, and C. Oliva, M. González, and R. Sayos, J. Chem. Phys. **117**, 3647 (2002).

[142] F. Dong, S.-H. Lee, and K. Liu, J. Chem. Phys. **115**, 1197 (2001).

[143] M. H. Alexander, G. Capecchi, and H.-J.Werner, Science, **296**, 715 (2002).

[144] S. Ghosal and S. Mahapatra, J. Chem. Phys. **121**, 5740 (2004).

[145] G. A. Parker, A. Laganá, S. Crocchianti, and R. T. Pack, Chem. Phys. Lett. **324**, 466 (2000).

[146] R. Kosloff, J. Phys. Chem. **92**, 2087 (1988); Ann. Rev. Phys. Chem. **45**, 145 (1994), and references therein.

[147] G. G. Balint-Kurti, F. Gögtas, S. P. Mort, A. R. Offer, A. Laganá, and O. Garvasi, J. Chem. Phys. **99**, 9567 (1993).

[148] A. M. Arthurs and A. Dalgarno, Proc. R. Soc. Lond. A **256**, 540 (1960).

[149] C. F. Curtiss and F. T. Adler, J. Chem. Phys. **20**, 249 (1952); C. F. Curtiss, J. Chem. Phys. **21**, 2045 (1953); J. Chem. Phys. **49**, 1952 (1968).

[150] J. H. Van Vleck, Rev. Mod. Phys. **23**, 213 (1951).

[151] E. P. Wigner, *Group Theory* (Academic Press, New York, 1959); R. N. Zare, *Angular momentum* (John Wiley & Sons, New York, 1988).

[152] (a) W. A. Lester, Jr. in *Modern Theoretical Chemistry, vol. 1*; (b) *Dynamics of Molecular Collisions, Part A*, edited by W. H. Miller (Plenum Press, New York and London, 1976).

[153] A. R. Edmonds, *Angular Momentum in Quantum Mechanics* (Princeton University,Princeton, 1960).

[154] M. E. Rose, *Elementary Theory of Angular Momentum* (Wiley, New York, 1957).

[155] E. U. Condon and G. H. Shortley, *The Theory of Atomic Spectra* (Cambridge University Press, Cambridge, 1935).

[156] R. T. Pack and G. A. Parker, J. Chem. Phys. **87**, 3888 (1987).

[157] J. Tennyson and B. T. Sutcliffe, J. Chem. Phys. **77**, 4061 (1982); J. Mol. Spectrosc. **101**, 71 (1983).

[158] G. G. Balint-Kurti and A. Brown, in *Theory of Chemical Reaction Dynamics*, edited by A. Laganá and G. Lendvay (NATO ASI, Kluwer Academic Publishers, The Netherlands, Vol. II, 2004), pp. 149-185.

[159] J. Tennyson and J. R. Henderson, J. Chem. Phys. **91**, 3815 (1989).

[160] G. C. Schatz and A. Kuppermann, J. Chem. Phys. **65**, 4642 (1976).

[161] J. Z. H. Zhang, J. Chem. Phys. **94**, 6047 (1991).

[162] A. Jäckle, M.-C. Heitz, and H.-D. Meyer, J. Chem. Phys. **110**, 241 (1999).

[163] S. Sukiasyan and H.-D. Meyer, J. Chem. Phys. **116**, 10641 (2002).

[164] A. Aguado, M. Paniagua, M. Lara, and O. Roncero, J. Chem. Phys. **107**, 10085 (1997).

[165] S. K. Gray and G. G. Balint-Kurti, J. Chem. Phys. **108**, 950 (1998); S. K. Gray, C. Petrongolo, K. Drukker, and G. C. Schatz, J. Phys. Chem. A **103**, 9448 (1999);

S. K. Gray, G. G. Balint-Kurti, G. C. Schatz, J. J. Lin, X. Liu, S. Harich, and X. Yang, J. Chem. Phys. **113**, 7330 (2000), and references therein.

[166] D. H. Zhang and J. Z. H. Zhang, J. Chem. Phys. **103**, 6512 (1995); D. H. Zhang and S.-Y. Lee, J. Chem. Phys. **110**, 4435 (1999).

[167] J. Mazur and R. J. Rubin, J. Chem. Phys. **31**, 1395 (1959).

[168] A. Goldberg, H. M. Schey and J. L. Schwarts, Am. J. Phys. **35**, 177 (1967).

[169] E. A. McCullogh and R. E. Wyatt, J. Chem. Phys. **51**, 1253 (1969); **54**, 3578 (1971); **54**, 3592 (1971).

[170] A. Askar and A. S. Cakmak, J. Chem. Phys. **68**, 2794 (1978).

[171] J. A. Fleck, Jr.. J. R. Morris and M. D. Feit, Appl. Phys. **10**, 129 (1976).

[172] M.D. Feit, J. A. Fleck, Jr., and A. Steiger, J. Comput. Phys. **47**, 412 (1982); M.D. Feit and J. A. Fleck, Jr. J. Chem. Phys. **78**, 301 (1983); J. Chem. Phys. **80**, 2578 (1984).

[173] J. W. Cooley and J. W. Tuckey, Math. Computation, **19**, 297 (1965).

[174] H. J. Nussbaumer, *Fast Fourier Transform and Convolution Algorithms* (2nd ed., Springer, Verlag, Berlin, 1982).

[175] P. N. Swarztrauber, in *Parallel Computations*, edited by G. Rodrigue (Academic, New York, 1982).

[176] R. Kosloff, in *Numerical Grid Methods and Their Applications to Scrödinger's Equation*, edited by C. Cerjan (NATO ASI Ser. C412, Kluweru Academic Publishers, Dordrecht, The Netherlands, 1993), pp. 97-116; pp. 175-193.

[177] D. O. Harris, G. G. Engerholm, and W. D. Gwinn, J. Chem. Phys. **43**, 1515 (1965).

[178] A. S. Dickinson and P. R. Certain, J. Chem. Phys. **49**, 4209 (1968).

[179] F. J. Lin and J. T. Muchkerman, Comput. Phys. Commun. **63**, 538 (1991).

[180] O. Sharafeddin and J. Z. H. Zhang, Chem. Phys. Lett. **204**, 190 (1993).

[181] J. C. Light, R. M. Whitnell, T. J. Park, and S. E. Choi, in *Supercomputer Algorithms for Reactivity, Dynamics and Kinetics of Small Molecules*, edited by A. Laganá (NATO ASI se. C277, Kluwer Academics Publishers, Dordrecht, 1989), pp. 187-213.

[182] G. C. Corey, J. W. Tromp, and D. Lemoine, in *Numerical Grid Methods and Their Applications to Schrödinger's Equation*, edited by C. Cerjan (NATO ASI se. C412, Kluwer Academic Publishers, The Neterlands, 1993), pp. 1-23.

[183] H. Tal-Ezer and R. Kosloff, J. Chem. Phys. **81**, 3967 (1984).

[184] V. A. Mandelshtam and H. S. Taylor, J. Chem. Phys. **103**, 2903 (1995).

[185] D. Neuhauser, J. Chem. Phys. **103**, 8513 (1995).

[186] T. J. Park and J. C. Light, J. Chem. Phys. **85**, 5870 (1986).

[187] S. K. Gray and D. E. Manolopoulos, J. Chem. Phys. **104**, 7099 (1996).

[188] C. C. Marston and G. G. Balint-Kurti, J. Chem. Phys. **91**, 3571 (1989); G. G. Balint-Kurti, C. L. Ward, and C. C. Marston, Comput. Phys. Commun. **67**, 285 (1991).

[189] S. Adhikari and S. P. Bhattacharyya, Phys. Lett. A, **172**, 155 (1992); Proc. Indian Acad. Sci. (Chem. Sci.), **106**, 553 (1994).

[190] C. Leforestier, R. Bisseling, C. Cerjan, M. D. Feit, R. Friesner, A. Guldberg, A. Hammerich, G. Jolicard, W. Karrlein, H.-D. Meyer, N. Lipkin, O. Roncero, and R. Kosloff, J. Comput. Phys. **94**, 59 (1991).

[191] C. C.-Tannoudji, B. Diu, and F. Laloë, *Quantum Mechanics* (John Wiley & Sons, New York, Hermann, Vol. I, 1977).

[192] E. Merzbacher, *Quantum Mechanics* (John Wiley & Sons, 2nd Ed., New York, 1970), p. 475.

[193] F. Gögtas, G. G. Balint-Kurti, and A. R. Offer, J. Chem. Phys. **104**, 7927 (1996).

[194] R. C. Mowrey, J. Chem. Phys. **99**, 7049 (1993).

[195] W. H. Miller, J. Phys. Chem. **102**, 793 (1998), and references therein.

[196] N. Balakrishnan and N. Sathyamurthy, Chem. Phys. Lett. **240**, 119 (1995).

[197] D. H. Zhang, J. Z. H. Zhang, Y. C. Zhang, D. Y. Wang, and Q. G. Zhang, J. Chem. Phys. **102**, 7400 (1995); C. Kalyanaraman, D. C. Clary, and N. Sathyamurthy, J. Chem. Phys. **111**, 10910 (1999).

[198] D. A. McQuarrie, *Statistical Mechanics* (University of California, Davis, 2000).

[199] J. M. Bowman and H. M. Shnider, J. Chem. Phys. **110**, 4428 (1999).

[200] M. Bittererová, J. M. Bowman, and K. Peterson, J. Chem. Phys. **113**, 6186 (2000), and references 13-20 therein.

[201] S. K. Gray, E. M. Goldfield, G. C. Schatz, and G. G. Balint-Gurti, Phys. Chem. Chem. Phys. **1**, 1141 (1999).

[202] K. Nobusada and H. Nakamura, J. Phys. Chem. A **103**, 6715 (1999).

[203] U. Manthe, W. Bian, and H. -J. Werner, Chem. Phys. Lett. **313**, 647 (1999).

[204] Q. Sun, J. M. Bowman, G. C. Schatz, J. R. Sharp, and J. N. L. Cornor, J. Chem. Phys. **92**, 1677 (1990).

[205] A. Laganá, R. T. Pack, and G. A. Parker, J. Chem. Phys. **99**, 2269 (1993).

[206] K. Moribayashi and H. Nakamura, J. Phys. Chem. **99**, 15410 (1995).

[207] J. Qi and J. M. Bowman, Chem. Phys. Lett. **276**, 371 (1997).

[208] B.-H. Yang, H.-T. Gao, and K.-L. Han, J. Chem. Phys. **113**, 1434 (2000).

[209] N. Balakrishnan, J. Chem. Phys. **119**, 195 (2003).

[210] J. N. Murrell, S. Carter, S. C. Farantos, P. Huxley, and A. J. C. Varandas, *Molecular Potential Energy Functions* (John Wiley, Chichester, 1984).

[211] D. M. Charutz, I. Last, and M. Baer, J. Chem. Phys. **106**, 7654 (1997); D. H. Zhang, J. C. Light, and S. -Y. Lee, J. Chem. Phys. **109**, 79 (1998).

[212] W. H. Press, B. P. Flannery, S. A. Teukolsky, and W. T. Vetterling, *Numerical Recipes: The art of Scientific Computing* (Cambridge University Press, Cambridge, 1986), p. 125.

[213] T. H. Dunning, Jr., J. Chem. Phys. **90**, 1007 (1989).

[214] M. J. Frisch *et al.* , GAUSSIAN 03, Revision B.05, Gaussian, Inc., Pittsburgh, PA, 2003.

[215] A. Jäckle and H.-D. Meyer, J. Chem. Phys. J. Chem. Phys. **105**, 6778 (1996); **109**, 2614 (1998).

[216] B. Maiti, C. Kalyanaraman, A. N. Panda, and N. Sathyamurthy, J. Chem. Phys. **117**, 9719 (2002).

[217] J. R. Taylor, *Scattering Theory* (Wiley, New York, 1972).

[218] (a) G. C. Schatz and A. Kuppermann, Phys. Rev. Lett. **35**, 1266 (1975); (b) E. Pollak and M. S. Child, Chem. Phys. **63**, 23 (1981); (c) B. C. Garrett, D. W. Schwenke, R. T. Skodje, D. Thirumalai, T. C. Thompson, and D. G. Truhlar, ACS Symposium Ser. **263**, 375 (1984); (d) W. H. Miller and J. Z. Zhang, J. Chem. Phys. **95**, 12 (1991); (e) D. A. V. Kliner, D. E. Adelman, and R. N. Zare, J. Chem.

Phys. **94**, 1069 (1991); (f) J. Chang, N. J. Brown, M. D'Mello, R. E. Wyatt, and H. Rabitz, J. Chem. Phys. **97**, 6226 (1992).

[219] R. Schinke, *Photodissociation Dynamics* (Cambridge University, Cambridge, 1993).

[220] N. Moiseyev, Phys. Rep. **302**, 211 (1998).

[221] K. Liu, Ann. Rev. Phys. Chem. **52**, 139 (2001); F. Fernández-Alonso and R. N. Zare, Ann. Rev. Phys. Chem. **53**, 67 (2002).

[222] S. -D. Chao and R. T. Skodje, Theor. Chem. Acc. **108**, 273 (2002).

[223] A. Kuppermann, in *Potential energy surfaces and dynamical calculations*, edited by D. G. Truhlar (Plenum, New York, 1981), p. 375; J. C. Polanyi and A. H. Zewail, Acc. Chem. Res. **28**, 119 (1995); A. H. Zewail, in *Femtochemistry*, edited by J. Manz and L. Wöste (VCH, Weinheim, 1995), Vol. 1, p. 15.

[224] E. J. Heller, J. Chem. Phys. **68**, 3891 (1978); Acc. Chem. Res. **14**, 368 (1981).

[225] R. Sadeghi and R. T. Skodje, J. Chem. Phys. **98**, 9208 (1993); **99**, 5126 (1993).

[226] R. Sadeghi and R. T. Skodje, J. Chem. Phys. **105**, 7504 (1993).

[227] R. T. Skodje, R. Sadeghi, H. Köppel, and J. L. Krause, J. Chem. Phys. **101**, 1725 (1994).

[228] S. Mahapatra and N. Sathyamurthy, J. Chem. Phys. **102**, 6057 (1995); B. Maiti, S. Mahapatra, and N. Sathyamurthy, J. Chem. Phys. **113**, 59 (2000).

[229] J. Manz, in *Femtochemistry and Femtobiology*, edited by V. Sundström (World Scientific, Singapore, 1997).

[230] S. Mahapatra, N. Chakrabarti, and N. Sathyamurthy, Int. Rev. Phys. Chem. **18**, 235 (1999).

[231] R. S. Friedman and D. G. Truhlar, Chem. Phys. Lett. **183**, 539 (1992).

[232] J.-C. Nieh and J. J. Valentini, Phys. Rev. Lett. **60**, 519 (1988).

[233] J.-C. Nieh and J. J. Valentini, J. Chem. Phys. **92**, 1083 (1990).

[234] J. Z. H. Zhang and W. H. Miller, Chem. Phys. Lett. **153**, 465 (1988); Chem. Phys. Lett. **159**, 130 (1989); J. Chem. Phys. **91**, 1528 (1989).

[235] S. Buelow, G. Radhakrishnan, H. Reisler, C. Wittig, and G. Hancock, J. Phys. Chem. **90**, 1015 (1986); B. A. Collings, J. C. Polanyi, M. A. Smith, A. Stolow, and A. W. Tarr, Phys. Rev. Lett. **59**, 2551 (1987).

[236] G. C. Schatz, J. Chem. Phys. **94**, 6157 (1990).

[237] S. K. Gray, J. Chem. Phys. **96**, 6543 (1992).

[238] R. T. Skodje, D. Skouteris, D. E. Manolopoulos, S.-H. Lee, F. Dong, and K. Liu, J. Chem. Phys. **112**, 4536 (2000); Phys. Rev. Lett. **85**, 1206 (2000).

[239] K. Liu, R. T. Skodje, and D. E. Manolopoulos, Phys. Chem. Commun. **4**, 2002.

[240] T. Takayanagi and Y. Kurosaki, J. Chem. Phys. **109**, 8929 (1998); T. Takayanagi and A. Wada, Chem. Phys. Lett. **348**, 524 (2001).

[241] M. D. Feit and J. A. Fleck, Jr., Appl. Opt. **19**, 1154 (1980).

[242] V. Engel, Chem. Phys. Lett. **189**, 76 (1992).

[243] U. Manthe, H. -D. Meyer, and L. S. Cederbaum, J. Chem. Phys. **97**, 9062 (1992).

[244] M. S. Child and E. Pollak, J. Chem. Phys. **73**, 4365 (1980); E. Pollak, J. Chem. Phys. **74**, 5586 (1981).

[245] J. Manz and H. H. R. Schor, Chem. Phys. Lett. **107**, 542 (1984); T. C. Thompson and D. G. Truhlar, Chem. Phys. Lett. **101**, 235 (1983).

Appendix A

Appendix

A.1 Explicit expression for d^J_{KM}

The expression for the reduced rotation matrix is given by Wigner [151, 154] as

$$\begin{aligned} d^J_{KM}(\theta) &= \sqrt{(J+K)!(J-K)!(J+M)!(J-M)!} \\ &\quad \times \sum_v \frac{(-1)^v}{(J-K-v)!(J+M-v)!(v+K-M)!v!} \\ &\quad \times [\cos(\theta/2)]^{2J+M-K-2v} [-\sin(\theta/2)]^{K-M+2v}, \end{aligned} \tag{A.1}$$

where the summation index, v, covers all integer and the non-negative factorial arguments.

A.2 Matrix elements of the l^2 operator in the BF basis

The orbital angular momentum operator l can be expressed in terms of total angular momentum operator $\boldsymbol{J}$ and rotational angular momentum operator $\boldsymbol{j}$ as [37, 151]

$$l^2 \equiv (J-j)^2 = (J^2 + j^2 - 2\hat{J}_z\hat{j}_z) - (\hat{J}_+\hat{j}_- + \hat{J}_-\hat{j}_+). \tag{A.2}$$

The matrix elements of the orbital angular momentum l^2 in the parity-adapted BF angular momentum basis, (Y_{jK}^{JMp} in Eq. (2.27)), are defined by

$$W_{K'K}^{JMpj} = \langle Y_{jK'}^{JMp} | \boldsymbol{l^2} | Y_{jK}^{JMp} \rangle. \tag{A.3}$$

One has to know that the action of the total angular momentum operator on Y_{jK}^{JMp} functions to obtain an explicit expression for the matrix elements of the orbital angular momentum l^2. It is worth emphasizing here that the projection of the total angular momentum on the SF and the BF axes are satisfying the *normal* and *anomalous* commutation relations, respectively [150, 151]. These are given by, for example,

$$[J_X, J_Y] = iJ_Z \tag{A.4}$$

$$[J_x, J_y] = -iJ_z. \tag{A.5}$$

Thus, the action of raising and lowering operators (also referred as *ladder operators*) of the total angular momentum $\hat{J}_\pm = \hat{J}_x \pm i\hat{J}_y$ in the BF frame behave like the operators $\hat{J}_\mp = \hat{J}_X \mp i\hat{J}_Y$ in the SF frame.

In the BF coordianate system the action of $\hat{J}_\pm$ operators on the normalized rotation matrix leads to following relation

$$\hat{J}_\pm \tilde{D}_{KM}^J = \sqrt{J(J+1) - K(K \mp 1)} \tilde{D}_{K\mp1,M}^J = \lambda_{JK}^\mp \tilde{D}_{K\mp1,M}^J. \tag{A.6}$$

Using the above relation, one can evaluate the rotation matrix elements in the BF coordinate system

$$\begin{aligned} \hat{J}_\pm \hat{j}_\mp Y_{jK}^{JM} &= (\hat{J}_\pm \tilde{D}_{KM}^J)(\hat{j}_\mp P_{jK}) \\ &= (\lambda_{JK}^\mp \tilde{D}_{K\mp1,M}^J)(\lambda_{jK}^\mp P_{jK\mp1}) \\ &= \lambda_{JK}^\mp \lambda_{jK}^\mp Y_{jK\mp1}^{JM}. \end{aligned} \tag{A.7}$$

As in the BF frame $J_z = j_z$, the action of $\hat{J}_z \hat{j}_z$ on parity adapted BF angular

momentum functions is written as

$$\hat{J}_z\hat{j}_z Y^{JMp}_{jK} = \hbar K \hat{J}_z Y^{JMp}_{jK} = \hbar^2 K^2 Y^{JMp}_{jK}. \tag{A.8}$$

For the parity adapted BF angular momentum function Eq. (A.7) can be rewritten as

$$\hat{J}_\pm\hat{j}_\mp Y^{JMp}_{jK} = \frac{1}{\sqrt{2(1+\delta_{K0})}}\left[\lambda^\mp_{JK}\lambda^\mp_{jK}Y^{JM}_{jK\mp1} + (-1)^P\lambda^\pm_{JK}\lambda^\pm_{jK}Y^{JM}_{j-K\mp1}\right]. \tag{A.9}$$

Using the relaion of Eq. (A.8), the matrix element of Eq. (A.3) is then written as,

$$\begin{aligned} W^{JMpj}_{K'K} &= \left[J(J+1)+j(j+1)-2K^2\right]\delta_{K',K} \\ &\quad -\langle Y^{JMp}_{jK'}|\hat{J}_+\hat{j}_- + \hat{J}_-\hat{j}_+|Y^{JMp}_{jK}\rangle \end{aligned} \tag{A.10}$$

Therefore, using the definition of l^2 in Eq. (A.10), the matrix element corresponding to the second bracket, can be written as

$$\begin{aligned} (\hat{J}_+\hat{j}_- + \hat{J}_-\hat{j}_+)Y^{JMp}_{jK} &= \frac{1}{\sqrt{2(1+\delta_{K0})}}[\lambda^-_{JK}\lambda^-_{jK}Y^{JM}_{jK-1} + (-1)^P\lambda^+_{JK}\lambda^+_{jK}Y^{JM}_{j-K-1}) \\ &\quad +\lambda^+_{JK}\lambda^+_{jK}Y^{JM}_{jK+1} + (-1)^P\lambda^-_{JK}\lambda^-_{jK}Y^{JM}_{j-K+1}] \end{aligned} \tag{A.11}$$

By separating the $K=0$, one can rewrite the above equations as [37]

$$\begin{aligned} (\hat{J}_+\hat{j}_- + \hat{J}_-\hat{j}_+)Y^{JMp}_{jK} &= \lambda^+_{JK}\lambda^+_{jK}\sqrt{(1+\delta_{K0})}Y^{JMp}_{jK+1} \\ &\quad +\lambda^-_{JK}\lambda^-_{jK}(1-\delta_{K0})\sqrt{(1+\delta_{K1})}Y^{JMp}_{jK-1}, \end{aligned} \tag{A.12}$$

which leads the matrix element in Eq. (A.3) to that in Eq. (2.39) in BF frame.

List of Publications

1. Time-dependent wave packet dynamics of the H+HLi reactive scattering,
   R. Padmanaban and S. Mahapatra, J. Chem. Phys. **117**, 6469 (2002).

2. Resonances in three-dimensional H+HLi scattering:
   A time-dependent wave packet dynamical study,
   R. Padmanaban and S. Mahapatra, J. Chem. Phys. **120**, 1746 (2004).

3. Quantum wave packet dynamics of H+HLi scattering:
   Reaction cross section and thermal rate constant,
   R. Padmanaban and S. Mahapatra, J. Chem. Phys. **121**, 7681 (2004); Erratum: **122**, 029902 (2005).

4. Resonances in H+HLi scattering for nonzero total angular momentum ($J > 0$):
   A time-dependent wave packet approach,
   R. Padmanaban and S. Mahapatra, J. Theor. Comput. Chem. (in press).

5. Coriolis-coupled wave packet dynamics of H+HLi reaction,
   R. Padmanaban and S. Mahapatra, J. Phys. Chem. A. (submitted).

6. Time-dependent wave packet dynamics of the H+HLi^+ reaction,
   R. Padmanaban and S. Mahapatra, (manuscript under preparation).

Posters/Papers Presented in Symposia

1. Poster presented in "Trends in Theoretical Chemistry"(**TTC 2002**), IACS, Kolkata, January 17-19, 2003.

2. Poster presented in "6th National Symposium on Chemistry"(**VI NSC**), IIT Kanpur, Kanpur, February 6-8, 2004.

3. Poster presented in "**Chemfest 2004**"in School of Chemistry, University of Hyderabad, Hyderabad. March 17, 2004.

4. Poster presented in "Symposium in Theoretical Chemistry"(**TCS 2004**), BARC, Mumbai, December 9-12, 2004.

5. Flash presentation in "**Chemfest 2005**"in School of Chemistry, University of Hyderabad, Hyderabad. February 19, 2005.

6. Poster presented in "2nd Asian Pacific Conference on Theoretical & Computational Chemistry"(**APCTCC2**), Chulalongkorn University, Bangkok, Thailand, May 2-6, 2005.